UNIVERSITY OF SOUTHAMPTON

FACULTY OF ENGINEERING AND ENVIRONMENT

AERODYNAMICS AND FLIGHT MECHANICS

Extending the Capability of Large Eddy Simulations to Model Dispersion in Urban Areas

by

VINCENZO SESSA

FINAL THESIS

Supervisor:

Dr. Xie ZHENG-TONG

Co-supervisors:

Dr. Thomas T GLYN

Prof. Ian CASTRO

April 18, 2020

UNIVERSITY OF SOUTHAMPTON

FACULTY OF ENGINEERING AND ENVIRONMENT

AERODYNAMICS AND FLIGHT MECHANICS

Extending the capability of Large Eddy Simulations to model dispersion in urban areas

ABSTRACT

A synthetic turbulence and temperature fluctuation generation method was developed in Large–Eddy Simulations (LES) to investigate the effects of inflow turbulent conditions, thermal stratification and wind direction on flow and dispersion over a rural–to–urban transition region. The modelling approach was validated by comparing predictions of mean velocity, turbulent stresses and point–source dispersion against data from a wind tunnel experiment. The depth of the internal boundary layer (IBL) that developed from the leading edge of the block array was determined using the wall–normal turbulent stress method that I developed in this study. The method allowed the location of the interface to be more clearly defined by using a power law formula of similar form to those derived in previous studies. The development of the IBL was analysed in relation to the dispersion from a ground–level point source within the urban array. It was found that the vertical transport of pollutant was constrained by the presence of the IBL so leading to trapping of material in the canopy layer. The effects of weakly stable stratification (i.e. with the Richardson number $R_i \leq 1$) on turbulence and line source dispersion were investigated over the same rural–to–urban transition region. Vertical profiles of wall–normal turbulent stress showed that the height and the growth rate of the IBL were sensitive to the thermal stability and the turbulent kinetic energy (TKE) prescribed at the inlet. Furthermore, it was found that increasing the stable stratification level reduced the vertical transport of pollutant which increased the volume–averaged concentration within the canopy. The transport of pollutant below and above the canopy was analysed for a mean wind direction inclined at angles to the main streets (i.e. 15° and 45°) of the urban array. The natural ventilation below the canopy due to wind variation was found to be greatly improved at the 45° compared to the normal wind direction (i.e. 0°). For $R_i = 0.2$ the effects of wind direction on turbulence and dispersion were found to dominate the effects of weak thermal stratification. Lastly, an LES study of a field experiment confirmed that dispersion scenario is greatly sensitive to variations of wind direction which may produce large concentration differences even in the far–field.

Acknowledgements

This thesis is dedicated to my family and their continuous support of my hopes and aspirations. Words can not express how grateful I am to my father, my mother, my sister and my brothers for all the sacrifices that you have made on my behalf. I would also like to thank to my beloved girlfriend who supported me in the last stage of this experience.

I would like to express my sincere gratitude to my supervisor Dr. Zheng-Tong Xie for his support, patience, motivation and immense knowledge. His guidance helped me in all the time of research, presentation, publication and writing of this PhD thesis. Without his support I would not be in the position that I am today.

I gratefully acknowledge the funding received from Dstl and University of Southampton towards my PhD research. In particular Dr. Steven Herring for his insightful comments and encouragement, but also for the hard questions which incentivised me to widen my research from various perspectives.

I thank my fellow officemates for the stimulating discussions, for the long days we were working together before deadlines, and for all the fun we have had in the last four years.

Lastly, I am deeply grateful to Dr Glyn Thomas, Prof Ian P Castro, Mr Timothy Foat, Vladimir Fuka for their comments, support and collaboration.

Contents

List of Figures

List of Tables

Research Thesis: Declaration of Authorship

Print name: *Vincenzo Sessa*

Title of thesis: *Extending the capability of Large Eddy Simulations to model dispersion in urban areas*

I declare that this thesis and the work presented in it are my own and has been generated by me as the result of my own original research.

I confirm that:

1. This work was done wholly or mainly while in candidature for a research degree at this University;

2. Where any part of this thesis has previously been submitted for a degree or any other qualification at this University or any other institution, this has been clearly stated;

3. Where I have consulted the published work of others, this is always clearly attributed;

4. Where I have quoted from the work of others, the source is always given. With the exception of such quotations, this thesis is entirely my own work;

5. I have acknowledged all main sources of help;

6. Where the thesis is based on work done by myself jointly with others, I have made clear exactly what was done by others and what I have contributed myself;

7. Parts of this work have been published as:

Sessa, V., Z.-T. Xie, and S. Herring (2019). *'Thermal stratification effects on turbulence and dispersion in internal and external boundary layers'.* In: Boundary-Layer Meteorology, Accepted.

Sessa, V., Z.-T. Xie, and S. Herring (2018). *'Turbulence and dispersion below and above the interface of the internal and the external boundary layers'.* In: Journal of Wind Engineering and Industrial Aerodynamics 182, pp. 189–201.

Sessa, V., Z.-T. Xie, and S. Herring (2018). *'Dispersion in a stable boundary layer over a change in surface roughness'.* 13^{th} UK Conference on Wind Engineering, Leeds, UK.

Sessa, V., Z.-T. Xie, and S. Herring (2018). *'Stable stratification effects in a spatially–developing urban boundary layer'.* 10^{th} International Conference on Urban Climate, New York, USA.

Sessa, V. & Z.-T. Xie (2017). *'Dispersion within and above an array of blocks in a spatially developing boundary layer'.* EACWE, Liege, Belgium.

Sessa, V., Fuka, V., and Z.-T. Xie (2016). *'Flows within and above an array of blocks in a spatially developing boundary layer'.* 12^{th} UK Conference on Wind Engineering, Nottingham, UK.

Signature: Date:

1 Introduction

The aim of this PhD research is to improve our understanding of the mechanisms of air pollution dispersion over rural–to–urban areas under various meteorological conditions, e.g. thermal stratification and wind directions. In order to achieve this goal, numerical simulations were developed and used. These were a valuable tool to make accurate predictions, to gain deep insight into physical phenomena, and to improve design.

Figure 1.1: Example of smoke pollution released from industrial chimneys showing a serious environmental issue. (www.gettyimages.co.uk)

Air pollution in urban areas is of increasing concern. Chemicals or other materials if released or misused can cause death, serious injury, long lasting health effects and damage to the environment. The far–field dispersion can be well predicted using a Gaussian model, whereas it is extremely challenging to accurately predict near–field dispersion. The accurate modelling of pollutant dispersion from localized sources at short range is essential to undertake important decisions such as rescue and mitigation procedures.

The major advantages of numerical modelling compared to experimental or field studies are the lower costs and the capability of producing a large amount of data in a relatively short time. Numerical models are used to estimate the concentration of air pollutants emitted from sources such as industrial plants, vehicular traffic or accidental chemical releases.

They are also used to predict concentrations for different scenarios (i.e. changes in source's size/emission), to improve design. However, most of the current prediction tools in urban areas have limited application to ideal conditions (Wang et al., 2018; Cushman-Roisin, Gualtieri, and Mihailovic, 2008) (i.e. non-buoyant flow over a flat surface). Thus it is essential to provide numerical models able to compute the flow and dispersion of contaminant particles and gases within and around buildings, including the effects of nearby urban morphology for different meteorological conditions.

The concentration near the source may rapidly change, firstly because of the turbulence generated in urban areas, and secondly because the concentration plume is generally smaller than the size of background turbulent structures. In the attempt to address these issues, several numerical approaches have been developed to improve basic understandings and predictive capability. For example, large–eddy simulation (LES), which is the numerical approach used in this thesis, has received increasing consideration both because of its ability to describe turbulence in detail and relatively low computational cost.

1.1 Atmospheric boundary layer

Whilst the atmosphere is more than $100km$ thick, the instabilities, which create meteorological patterns and turbulent mixing, approximately occupy the first $10km$ from the ground, forming the so called troposphere. The part of the troposphere closest to the ground, where the atmosphere is affected by the ground surface, is called the atmospheric boundary layer (ABL) and it extends for roughly $1km$. The mechanical contact between the wind against the land surface generates a friction which causes a wind velocity gradient (Cushman-Roisin and Beckers, 2005). Excluding the thermal interaction, the ABL is characterized by neutral stratification and the wind speed assumes a logarithmic profile generally limited to the lowest $100m$, within the 'surface layer' of the ABL:

$$u_y = \frac{u^*}{\kappa}\left[ln\left(\frac{y}{y_0}\right)\right] \tag{1.1}$$

where u^* is the friction velocity related to the wall shear stress, κ the Von Karman constant and y_0 the surface roughness (assuming the $y - axis$ along the vertical direction). For regions with great plan area density, such as vegetation and buildings, the wind profile is also related to the zero plane displacement d because the mean flow is not able to penetrate into the surface (Drew, Barlow, and Lane, 2013):

$$u_y = \frac{u^*}{\kappa}\left[ln\left(\frac{y-d}{y_0}\right)\right]. \tag{1.2}$$

The roughness length y_0 is equivalent to the height at which the wind speed theoretically becomes zero, whereas d is usually defined as the centre of the body forces (Stull, 1988). Hence, giving a wind–speed observation at a certain height, the values of y_0 and d are adjusted in order to fit the velocity profile to Eq. 1.2.

1.1.1 Surface roughness

Different approaches are used for the characterization of y_0 and d. For example, Davenport et al. (2000) suggested a detailed definition of the relation between y_0 and the urban or industrial land use (Table 1.1.1). The effective terrain roughness was classified in five urban categories ranging from the lowest value of $0.1m$ to the highest value of $2.0m$, depending on building density and height variation.

Table 1.1: Surface roughness y_0 related to the urban/industrial site (Davenport et al., 2000)

Category	y_0	Urban/industrial site
Roughly open	$\mathcal{O}(0.1m)$	Moderately open country with occasional obstacles at relative separations of at least 20 obstacle heights
Rough	$\mathcal{O}(0.25m)$	Scattered buildings and/or industrial obstacles at relative separations of 8 to 12 obstacle heights. Analysis may need displacement length, d
Very rough	$\mathcal{O}(0.5m)$	Area moderately covered by low buildings and/or industrial tanks at relative separations of 3 to 7 obstacle heights. Analysis requires displacement length, d
Skimming	$\mathcal{O}(1.0m)$	Densely built-up area without much obstacle height variation. Analysis requires displacement length, d
"Chaotic"	$\mathcal{O}(2.0m)$	City centres with mixture of low-rise and high-rise buildings. Analysis by wind tunnel advised.

The estimation of y_0 and d depends on the shape, size, density and height of the roughness elements (Davenport et al., 2000) and this is proved by using morphometric methods in wind tunnel, numerical and analytical studies (Bottema, 1997; Wieringa, 1992). Morphometric methods are based on the morphology of the urban area and frequently do not require high instrumentation costs. For example, Counehan (1971) used a relationship to estimate the roughness length based on the total plan area and the average building height. Davenport et al. (2000) argued that many other building parameters are to be used (i.e. frontal area index, width and density) because the roughness parameters change locally. However, Britter and Hanna (2003) suggested to use a single averaged value of the roughness length as it was found that wind flow and plume dispersion rates are relatively insensitive to small variations of y_0.

1.1.2 Smooth and rough surfaces

Over a rough wall, it is typically assumed that the shear stress is dominated by the form drag (the force acting opposite the relative motion) generated by the roughness elements whereas for a smooth wall, the viscosity effects are relevant. However, both smooth and rough–wall boundary layers have a similar outer regions.

The surface roughness may be evaluated by considering at least two characteristic lengths: the height of the roughness elements and their spacing (Garratt, 1994). The former is involved in the definition of smooth and rough surfaces in the aerodynamic sense. Assuming the depth of the viscous sublayer δ_1, where viscous processes are dominant, and the height of the roughness element h_τ, a surface is aerodynamically smooth when $h_\tau << \delta_1$ whereas it is aerodynamically rough when $h_\tau >> \delta_1$. By increasing the wind speed, the viscous sublayer δ_1 decreases, therefore a surface may vary from being aerodynamically smooth to aerodynamically rough.

Following Garratt (1994) and several experiments of flow over flat plates, for $u^* h_\tau / \nu < 5$ a surface is aerodynamically smooth whilst for $u^* h_\tau / \nu > 75$ it is aerodynamically rough. Similarly, Snyder and Castro (2002) demonstrated in the laboratory that over a surface comprised of a staggered array of vertical fences, the viscous effects were significant for a roughness Reynolds number $Re^* = y_0 u^* / \nu$ equal or below unity. On the contrary, for a roughness Reynolds number of at least 2, but perhaps close to 5, the viscous effects were negligible.

The inner layer is characterized by the wall's characteristics. For example, the viscous length-scale is defined as the important scaling factor for smooth walls, while additional parameters such as the height of the roughness elements, lateral and longitudinal element dimensions and inter–obstacle spacing are required for the characterization of rough or very rough walls (Barlow and Coceal, 2008). In urban environments, the ground surface is usually considered a very rough wall, so that the viscous sublayer may be replaced by a roughness sublayer (Coceal et al., 2014) which provides the dominant mechanism for generating near–wall turbulence.

1.1.3 Roughness and inertial sublayers

The structure of the flow over a rough surface is generally divided into a *roughness sublayer* (RSL) where the flow is governed by the individual roughness elements and the velocity is spatially inhomogeneous, and an *inertial sublayer* (ISL) where the wind flow only varies with the height as it appears horizontally homogeneous (which also represents one assumption for the application of the logarithmic wind function) (Britter and Hanna, 2003). The basic hypothesis of a local equilibrium between production and dissipation (Monin-Obukhov Similarity Theory, MOST) is only valid in the inertial sublayer as it is assumed that the turbulent structures are simply transported (Monin and Obukhov, 1954).

The interface between the two layers is sensitive to the surface roughness elements but usually the depth of the roughness sublayer is 2–5 times the mean height of the elements

(Giometto et al., 2016). In some cases (i.e. during unstable atmospheric conditions), the depth of the RSL can be 10 to 15 times the mean building height (Barlow and Coceal, 2008). In a very rough wall regime, the RSL may dominate over the ISL in terms of turbulence intensity and, as a consequence, the ISL may not form (Barlow and Coceal, 2008).

The general assumption is that the mean velocity profile is logarithmic in the inertial sublayer whereas the behaviour is no longer logarithmic in the roughness sublayer. However, some authors (e.g., Coceal et al., 2014; Barlow and Coceal, 2008; Macdonald, 2000) have concluded that by using a spatial average of the mean velocity, the profile may assume a logarithmic form in the RSL.

Nevertheless, because of the great spatial variability of the flow within the roughness sublayer, there is still no comprehensive theory for its vertical structure (Giometto et al., 2016). Several numerical and experimental approaches have been developed for the parametrization of the flow within this region. For instance, it has been identified that obstacle height variability, obstacle shape, building arrangement and other geometric features may have a significant impact on turbulent characteristics and scalar dispersion (Boppana, Xie, and Castro, 2010; Cheng and Porte-Agel, 2016; Davidson et al., 1996).

1.2 Urban environments

Because of increasing urbanization, scientists are strongly focussed on urban air quality, wind flow and sources of pollutants within and beyond the urban area. The city scale is usually defined by the diameter of the average urban region (Britter and Hanna, 2003). This area, having large obstacles, is characterised by a strong drag force that distinguishes the city area from the surrounding rural region. In urban environments, wind characteristics and local turbulence intensity have an explicit influence on people mobility and comfort. Temperature, weather and wind conditions also play a dominant role in the exchange processes between indoor–outdoor building environments. Building materials affect the rate of heat transfer through the building walls, so the indoor air quality and energy use. On the contrary, the outdoor air quality is sensitive to the type, number, location and intensity of pollutant sources within and beyond the city. Transport and dispersion of pollutants are driven by urban turbulence, for this reason it is currently observed and analysed with great interest.

1.2.1 Urban turbulence

Urban turbulence is the result of all the instabilities occurring in environmental flows. One advantage for environmental systems is that the turbulence is an extremely efficient agent of dispersion and dilution, but in the meantime, it is a phenomenon beyond any easy description.

The parameter which characterises the level of turbulence is the Reynolds number, defined as the ratio between the amount of the flow kinetic energy and the work of viscous forces:

$$Re = \frac{\rho_0 UL}{\mu} \tag{1.3}$$

where ρ_0 is the density of the fluid, U a characteristic velocity value, L a characteristic length of the geometry and μ the dynamic viscosity of the fluid.

Turbulent flows occur at high Reynolds numbers and are characterized by irregularity or randomness, being rotational and dissipative. For large Reynolds number the inertial forces are dominant over the viscous forces, therefore the flows exhibit complex spatial patterns and much temporal variability (Cushman-Roisin, Gualtieri, and Mihailovic, 2008). Another important characteristic of a turbulent flow is its ability to transport and mix fluid much more effectively than a comparable laminar flow. This observation applied to the transport and mixing of momentum and heat in flows is of great practical importance as it is the major motivation for the study of turbulent flows (Pope, 2000).

The first measurements and observations of turbulence over urban and suburban areas looked at the effect of human activity in the urban area and its surroundings on the turbulent velocity components, from day to night. For example, Clarke et al. (1978) showed that in the St. Louis area, during the night, the turbulence intensity in the residential zone was roughly double that of the rural region, whereas during the day, it was approximately 30% higher. It was concluded that, particularly during the night, human activities in the city centre not only generate more turbulence than in rural regions but also sustain the air instability by adding heat to the atmosphere.

The feature which characterises the urban turbulence compared to the surrounding area is the extension of the roughness sublayer due to the surface morphology as it governs the dynamics at the city scale region and beyond. Fig. 1.2 shows a schematic of the atmospheric boundary sublayers over a typical urban area: the urban canopy sublayer, the roughness sublayer and the inertial sublayer. The surface layer, which includes the roughness and inertial sublayers, extends up to the outer region.

The inertial sublayer is analysed with the standard atmospheric boundary layer formulas (Eq: 1.2) because that region exhibits some statistical homogeneity. The urban canopy layer is the lower part of the roughness sublayer with a depth equal to the mean building height or the zero plane displacement d (Castro et al., 2017). In this region the flow is governed by local obstacles as well as the arrangements of the streets, the plan area density, trees, vegetation and other topographic features. As a consequence, within the urban canopy layer the flow is spatially inhomogeneous with a complex three dimensional structure. Lastly, in the upper region of the roughness sublayer, the flow is still inhomogeneous and affected by the characteristic length of the roughness elements. Within this layer turbulence intensity and turbulent diffusion are sensitive to the wake regions forming behind the roughness elements (Barlow and Coceal, 2008).

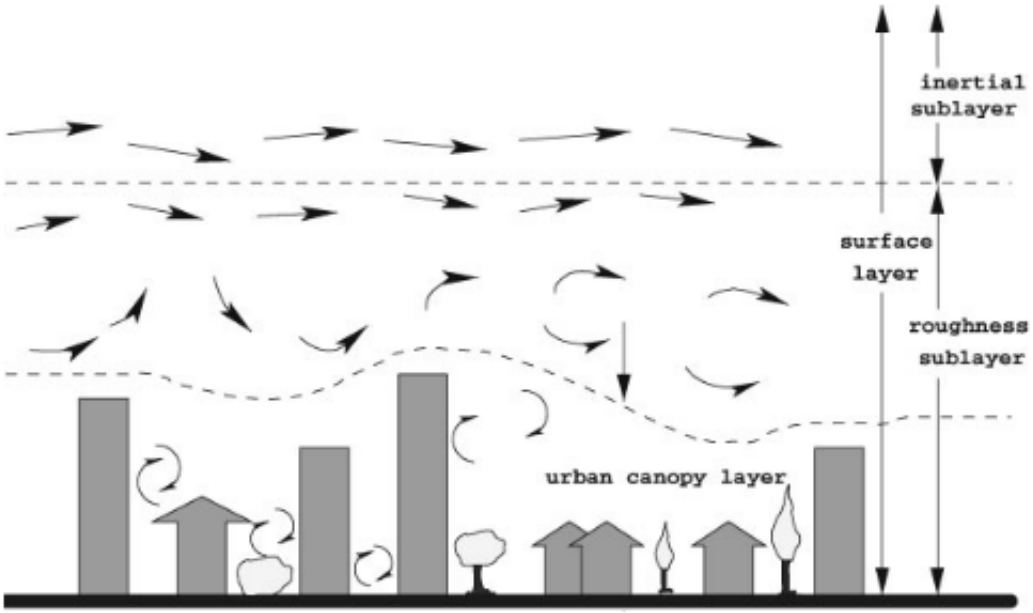

Figure 1.2: Separation of the atmospheric boundary sublayers over a typical urban area (Britter and Hanna, 2003)

1.2.2 Urban internal boundary layer

Urban roughness is heterogeneous consisting of different types of surfaces (e.g. Antoniou et al., 2016; King et al., 2017; Vasaturo et al., 2018; Tolias et al., 2018). A change in surface roughness, such as exists at the edge of the city, or at the junction between the central business district (CBD) and an area of surrounding low–rise buildings, leads to a region of transitional flow as the turbulent boundary layer takes time to adapt to the new wall condition (e.g. Smits and Wood, 1985; Cheng and Castro, 2002; Barlow, 2014; Cao and Tamura, 2007; Hanson and Ganapathisubramani, 2016). This transitional flow results from the development of an internal boundary layer (IBL) above the roughness elements (i.e. Fig. 1.3). It is challenging to identify the interface between the IBL and the approaching boundary layer. The interface may have a crucial effect on scalar exchange. To gain a deeper understanding of dispersion from a ground level source downstream of a change in surface roughness, it is necessary to analyse the development of the IBL.

Barlow (2014) reviewed observations and modelling studies of turbulent boundary layers approaching a rural–to–urban transition region (rough–to–very rough surface change) and found that on the city scale an IBL began to form at the junction between the smoother rural and the rougher urban surfaces. However, on the neighbourhood scale, and close to the ground, the flow was continuously adjusting to changes in roughness and that locally generated IBLs were in equilibrium with the underlying surfaces. This meant that multiple changes in roughness could lead to overlapping local IBLs and, as a consequence, the IBL assumed a non-homogeneous 3-dimensional structure extending up to $2-5$ times the mean

building height (Barlow and Coceal, 2008). These findings were supported by those of Hanson and Ganapathisubramani (2016), who analysed boundary layer development across a rougher–to–smoother surface change and identified an IBL with two regions: an energetic region near the wall in which the flow had adapted to the new wall condition and an outer region in which the flow retained characteristics of the upstream condition.

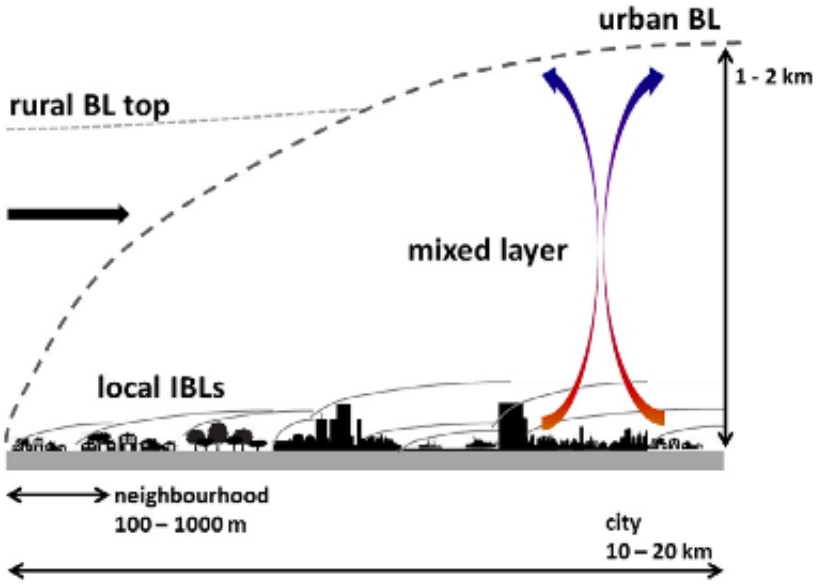

Figure 1.3: Schematic layout of the urban internal boundary layer forming at the rural-to-urban transition region (Barlow, 2014) including the overlapping of local internal boundary layers due to several changes of surface roughness.

The strength of the step change in roughness between two regions may be described by the roughness length ratio (y_{01}/y_{02}), where y_{01} and y_{02} are the upstream and downstream roughness lengths respectively. Alternatively, Jackson (1976) used atmospheric and wind tunnel data to demonstrate that the growth rate of the IBL is essentially driven by the rougher surface and is not related to the roughness length ratio, or to the ratio of boundary layer thickness to roughness element height. This conclusion is supported by work conducted by Townsend (1965) and Schofield (1975), who showed that if $(y_{01}/y_{02}) < 1$ (a change from smoother to a rougher wall) only y_{02} is important in estimating the growth of the IBL.

Bradley (1968) conducted the first atmospheric experiments on IBL development due to an increase in surface roughness. His observations showed that the growth rate of the IBL was independent of wind speed and could be described well by Elliot's formula (Elliott, 1958) which also indicates that the IBL development is independent of the roughness length ratio:

$$\frac{\delta_{IBL}}{y_{02}} = a \left(\frac{X}{y_{02}} \right)^{P} \tag{1.4}$$

where X is the distance from the step change, δ_{IBL} is the depth of the IBL, and P and a are the exponent and the coefficient of the power–law formula respectively.

Elliott (1958) found that the coefficient a varied from 0.6 to 0.9 and that $P = 0.8$ for $X/y_{02} > 1000$. His work has been further confirmed by Wood (1982) and Pendergrass and Arya (1984). Elliott (1958) emphasised that the exponent $P = 0.8$ in Eq. 1.4 was only valid for $X/y_{02} \geq 1000$ as it relied upon assumptions of constant stress and a logarithmic profile that were only valid downstream of that point. He showed that closer to the roughness transition point the development of the IBL could be fitted with a similar power law relationship, but with a lower exponent P and greater coefficient a.

The development of the IBL close to the transition point was examined by Cheng and Castro (2002) who performed an experimental study of the flow field immediately downstream of a roughness transition in which they fitted their experimental results for the IBL at distances of $X/y_{02} < 1000$ by applying Eq. 1.4 using an exponent $P = 0.33$ and a coefficient $a = 10.56$. This confirmed Elliott's finding that the exponent P decreased while the coefficient a increased as X/y_{02} was reduced. In their work Cheng and Castro (2002) defined the IBL height as the location where the velocity was 99% of that for upstream roughness at the same height. As noted above, this led to significant scatter in the derived IBL height due to the difficulty of measuring 1% differences experimentally.

1.2.3 Urban dispersion

The dispersion of pollutants within and above urban canopies is a $3D$–complex phenomenon sensitive to wind direction, thermal stratification, source location, type of source, building configuration, plan area density and so forth. The analysis of dispersion in urban areas at the city scale is usually conducted by applying the Gaussian plume model, which is considered the simplest mathematical model and also the most commonly used in operational modelling (Britter and Hanna, 2003).

The spatial distribution of the mean scalar concentration C from a continuous point–source release is given by the classic Gaussian plume equation with ground reflection (Hertwig et al., 2018):

$$C(x,y,z) = \frac{Q}{2\pi U_p \sigma_y \sigma_z} exp\left(-\frac{z^2}{2\sigma_z^2}\right)\left[exp\left(-\frac{(y-h_Q)^2}{2\sigma_y^2}\right) + exp\left(-\frac{(y+h_Q)^2}{2\sigma_y^2}\right)\right] \quad (1.5)$$

where U_p is a representative wind speed, Q is the constant mass emission rate, h_Q is the release height and σ_y, σ_z are the dispersion coefficients. If the source is located on the ground then the release height $h_Q = 0$ and Eq. 1.5 is reduced to the Gaussian plume equation without ground reflection.

The Gaussian plume/puff model assumes that the pollutant dispersion has a Gaussian distribution or, in other words, a normal probability distribution. Frequently applied both for

continuous, buoyant air pollution plumes or non–continuous air pollution puffs, the Gaussian model is used in combination with empirical correlations for evaluating the growth of the plume dimensions with the distance from the source location. Several computational fluid dynamic models have been implemented for dispersion prediction in urban areas (e.g., Xie, Hayden, and Wood, 2013; Hertwig et al., 2018) as well as significant experimental data (e.g., Vincont et al., 2000; Marucci and Carpentieri, 2020; Davidson et al., 1996; Theurer et al., 1996; Brixey et al., 2009) from ground–level sources have been produced.

For example, Davidson et al. (1996) carried out wind tunnel tests of pollutant dispersion over staggered and aligned arrays of obstacles from ground–level sources. It was concluded that the lateral profile of the plumes followed a Gaussian distribution assuming a self–similarity even below the canopy height. In contrast, the plume vertical profile was not self–similar and the reflected Gaussian plume model was used in order to match the experimental results. Moreover, it was found that the vertical dimension of the plume was sensitive to the height of the building canopy.

Similar conclusions were achieved by MacDonald, Griffiths, and Cheah (1997) who performed wind tunnel experiments over a regular array of cubes. After two rows of obstacles downstream of the source location, the lateral distribution of the plume was of a Gaussian type whereas the vertical profile was well approximated by the reflected Gaussian model. It was further noticed that the width of the plume was in a direct relationship with the building width–to–height aspect ratio. However, the mechanisms of pollutant dispersion were found to be greatly sensitive to the urban configuration and eventually to the building height variations.

Further on this aspect, Boppana, Xie, and Castro (2010) used LES to simulate dispersion over two different urban–like geometries: an array of equal height cubes and an array with random heights. It was found that large amounts of pollutant were trapped in the wake regions of the obstacles while lower amounts were observed in front. The weak–front pollutant pattern was more evident for the uniform height array. For example, in Fig. 1.4 (Boppana, Xie, and Castro, 2010), greater pollutant concentration was found in the wake regions behind the obstacles and lower pollutant concentration in the front obstacle regions, for the uniform (a) than the random (b) height building array. In addition, the surface flux of the scalar was found to be higher for the random height array than the uniform height array, with the highest values closer to the tallest buildings, probably due to the higher turbulence intensity.

Recently, Fuka et al. (2018) simulated scalar dispersion from a ground–level point source within an array of uniform height buildings and within an array with one periodically repeated tall building. It was found that the scalar plume was mainly transported upwards if the source was located between two obstacles in a recirculation zone. Differently, if the source was placed in a street parallel to the wind direction, the flow channelling caused the plume to be mainly horizontally advected.

However, Theurer et al. (1996) and Belcher (2005) showed that far from a continuous release (far–field), the exact location of the source and details of the street network in the given locations did not substantially affect the scalar plume characteristics. On the contrary, close

to the source (near–field) the building configuration and the exact location of the realising point were found to be relevant in the accurate prediction of scalar dispersion (Theurer et al., 1996; Xie and Castro, 2009).

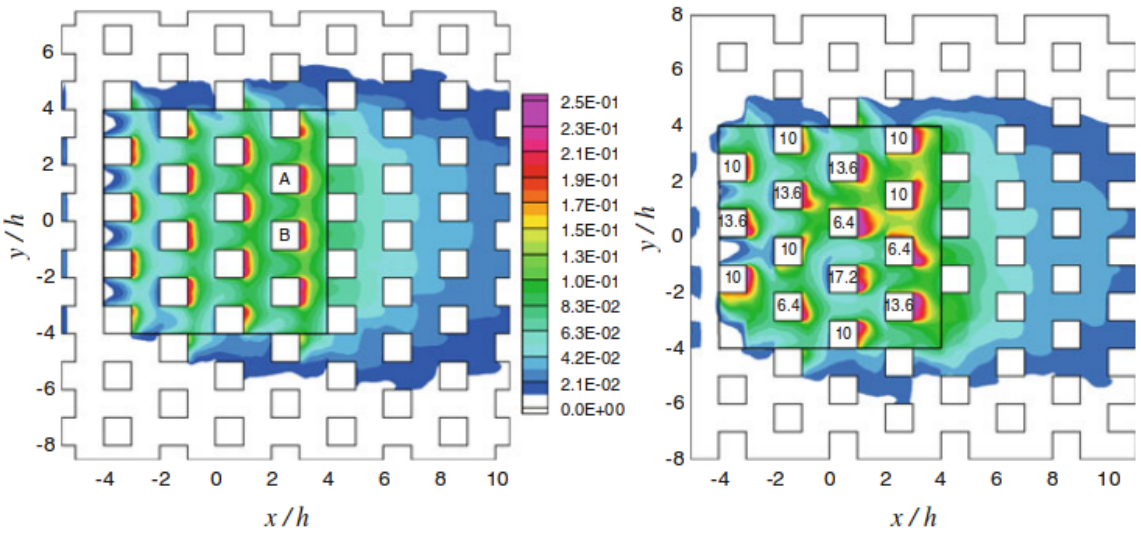

(a) C10S (b) RM10S

Figure 1.4: Pollutant concentration within the canopy at the height $z/h = 0.3$. (a) C10S: uniform obstacles, (b) RM10S: random height obstacles (Boppana, Xie, and Castro, 2010)

1.3 Wind direction effects on turbulence and dispersion

Several studies investigated the influence of the street network and building morphology on dispersion in urban areas. However, the understanding and the ability to predict pollutant dispersion under real atmospheric conditions, including thermal stratification and wind direction effects, is still at its infancy.

Most of the literature, including experimental tests and numerical simulations, focuses on square or rectangular arrays of blocks arranged in regular patterns, so the prevailing wind direction is normal to the front faces of the obstacles or in–line with the main streets. Nevertheless, in real situations, the mean wind flow is never constant in either direction or magnitude and the conditions simulated in experiments are rarely achieved. As a consequence, when numerical results are compared with field measurements, inevitable discrepancies are found.

Reduced–scale experiments and numerical studies could reproduce the flow fields at full scale as long as the Reynolds number in reduced-scale models exceeds a critical value. This hypothesis known as 'Reynolds number independence' states that the normalized flow field remains invariant with increasing Reynolds number above the critical value. Castro and Robins (1977) conducted wind tunnel tests to study flows across a single cube at different

Reynolds numbers and found that Reynolds number independence is achieved at $Re_C \sim 4000$ based on the free–stream velocity and the cube's height. Uehara, Wakamatsu, and Ooka (2003) obtained a similar $Re_C \sim 3500$ for Reynolds number independence of atmospheric boundary layer flows over a single cube.

Xie and Castro (2006) showed that the use of LES is feasible at high Reynolds number (i.e. Reynolds number independence) and sufficient mesh resolution (i.e. $h/16$ with mean building height h) because the surface drag is dominated by pressure forces over geometries comprising sharp–edged obstacles. Therefore, viscous forces become negligible and the LES issues (i.e. near wall–region and subgrid–scale modelling) are less relevant. These conclusions were obtained by assuming the mean flow direction normal to the front face of the obstacles. Claus et al. (2012) found that for few wind directions and building arrangements, Reynolds number independence is less certain. However, Lim, Castro, and Hoxey (2007) analysed the flow around a cube oriented at 45° concluding that the classical approach of scaling up from wind tunnel test is perfectly acceptable for turbulent flows where no concentrated vortex regions exist.

Britter and Hanna (2003) showed that the surface drag may vary substantially if the prevailing wind direction is not in–line with the streets but rather aligned at prominent angles to the obstacle faces. The roughness length y_o used in the wind logarithmic law (Eq. 1.2) as well as the zero–plane displacement d clearly differ for changes in the prevailing wind direction. The flow within the canopy, the boundary layer thickness and therefore the mechanisms of pollutant dispersion are greatly sensitive to wind direction and magnitude so the accurate prediction of such phenomena is obviously harder for real test cases. The key for progress is to consider wind variation effects on arrays of obstacles arranged in regular patterns and analyse the effects on the mean flow and turbulent statistics. In this way, general conclusions might be applicable to more complex circumstances.

To this end, Claus et al. (2012) simulated turbulent flows for various wind directions over arrays of cubes in order to analyse the mean flow differences within the canopy and wind direction effects on global properties. In Fig. 1.5 Claus et al. (2012) showed flow vectors within the canopy of staggered (a, c) and square (b, d) arrays by simulating the wind directions $\phi = 0°$ (a, b) and $\phi = 27°$ (c, d). It was found that the recirculation regions behind the obstacles were evident and not dissimilar to the staggered array for both wind directions (a, c). On the contrary, for the uniform array the local flow direction was much more sensitive to wind direction. In fact, the flow pattern at $\phi = 27°$ (d) was clearly different from the one at $\phi = 0°$ (b), particularly behind the obstacles. Moreover, it was found that the total surface drag could vary of up to 300% when different wind directions were considered. Similarly, the roughness length y_0 differed by a factor of 4 when the wind direction was rotated by 45°. It was concluded that locally the flow pattern within the canopy is sensitive to wind directions although mainly directed along the streets. However, in a few case studies, the near–surface average flow direction (averaged in time and over an horizontal plane covering the entire domain) was found to be visibly non–sensitive to wind variations.

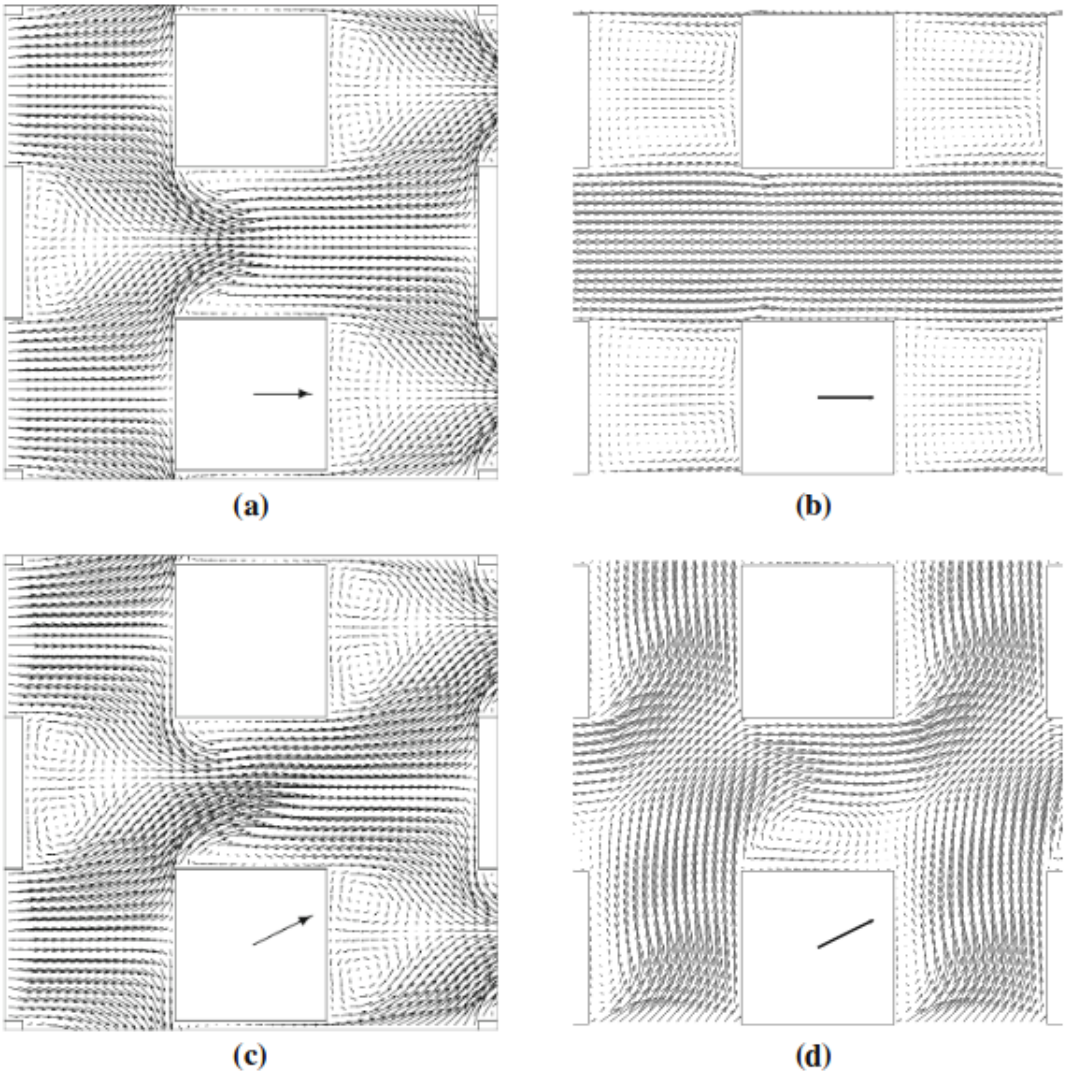

Figure 1.5: Flow vectors at the height $y/h = 0.5$ within the canopy for staggered (a, c) and square (b, d) arrays at wind direction $\phi = 0°$ (a,b) and $\phi = 27°$ (c,d) (Claus et al., 2012)

Similar results were found by Xie (2011) where two different wind directions (90° and 51°) caused similar average wind directions near the ground, confirming that the inhomogeneous canopy flow is more strongly influenced by the canopy morphology than the wind direction. To this regard, Bezpalcova (2007) conducted an important study on the effects of wind variations on dispersion over urban geometries. A rectangular array of obstacles was used in the wind tunnel to reproduce the Mock Urban Setting Test (MUST) performed in the Utah desert. It was found that the flow within the canopy was driven by the shape of the obstacle so that, when considering a non–aligned wind direction, the flow below the container canopies oriented quickly in the parallel direction to the streets, along the length of the obstacles.

Wind variations coupled with canopy morphology lead to significant effects on dispersion, especially when the source is located within the canopy. For example, Xie (2011) observed

that the maximum street–level concentration varied by a factor of 2 for the 51° wind direction compared to the 0°. The conclusions of that analysis and those of several other relevant studies (e.g., Claus et al., 2012; Bezpalcova, 2007) suggest that canopy morphology and prevailing wind direction must be both accounted for the accurate prediction of pollutant dispersion.

1.4 Stable and unstable thermal stratification

Another atmospheric parameter usually neglected, which has large effects on turbulent integral length scales (e.g., Boppana, Xie, and Castro, 2014; Park and Baik, 2013; Lienhard V and Van Atta, 1990; Flores and Riley, 2011; Grachev et al., 2008) and on dispersion (e.g., Xie, Hayden, and Wood, 2013; Tomas, Pourquie, and Jonker, 2016; Sini, Anquetin, and Mestayer, 1996), is the atmospheric thermal stratification.

The contact between the lower atmosphere and the ground surface generates a thermal interaction due to solar radiation which is absorbed immediately below the earth surface. In turn, the surface emits its heat upward (in lower frequencies), which is retained in great part by the atmosphere. This state of convection vanishes during the night, generating as a consequence, vertical thermal stratification. Turbulence and vertical stratification hold the troposphere in a permanent state of chaos that is still hard to analyse.

1.4.1 Flux Richardson number

Turbulent kinetic energy (TKE) is considered the most relevant parameter in micro–meteorology because it represents a measure of turbulence intensity. Physical processes such as advection, buoyant production/consumption, mechanical shear production and turbulent transport play a role in the TKE budget equation:

$$\frac{\partial k}{\partial t} + \overline{u_j}\frac{\partial k}{\partial x_j} = -\frac{1}{\rho_0}\frac{\partial \overline{u_i' p'}}{\partial x_i} - \frac{1}{2}\frac{\partial \overline{u_j' u_j' u_i'}}{\partial x_i} + \nu\frac{\partial^2 k}{\partial x_j^2} - \overline{u_i' u_j'}\frac{\partial \overline{u_i}}{\partial x_j} - \nu\frac{\overline{\partial u_i' \partial u_i'}}{\partial x_j \partial x_j} - \frac{g}{\rho_0}\overline{\rho' u_i'}\delta_{i2} \tag{1.6}$$

Assuming that each term of the TKE equation (Eq. 1.6) is certainly important, we may focus on: the second term on the left–hand side which is the advection of kinetic energy k due to the mean velocity $\overline{u_j}$; the second term on the right–hand side which is the turbulent transport of TKE with velocity fluctuations u_j' and u_i'; the fourth term on the right–hand side which is the mechanical shear contribution (implicitly negative) or, in other words, the production of kinetic energy due to the Reynolds stresses $\overline{u_i' u_j'}$ related to the velocity gradient $\frac{\partial \overline{u_i}}{\partial x_j}$. The last term on the right–hand side is the buoyant production/consumption of kinetic energy due to density differences ρ' induced by temperature variations.

The capability of the flow to maintain turbulence or become turbulent is determined by the balance between all of these processes. In particular, thermal stability is due to the interaction between buoyancy and wind shear. Assuming for example a stable–stratified atmosphere in

urban environment, the mechanical turbulence generated by the wind shear over the buildings is generally suppressed by the restoring force of gravity. In this case, the buoyant term in the TKE equation is negative (consumption of energy) whereas the shear term is the production of energy. The ratio between the buoyancy and the shear terms is called the flux Richardson number R_f (Stull, 1988):

$$R_f = \frac{(\frac{g}{\theta_v})(\overline{v'\theta'_v})}{(\overline{u'_i u'_j})\frac{\partial \overline{U_i}}{\partial x_j}} \tag{1.7}$$

where in the buoyancy term ($\overline{v'\theta'_v}$), v' is the vertical velocity fluctuation, θ'_v the temperature fluctuation and g is the gravity acceleration. The turbulent shear stress $\overline{u'_i u'_j}$ is expressed as a production in the TKE equation with a negative sign because it is implicitly negative. In Eq. 1.7 the minus is dropped by convention so the denominator is always negative. Therefore, in stable–stratified conditions the flux Richardson number is always positive because the buoyancy term is negative. For unstable flows, the buoyancy term is positive so the flux Richardson number is negative, for neutral flows is zero because the buoyant term is zero or negligible compared to the mechanical shear.

1.4.2 Gradient Richardson number

The flux Richardson number is a widely used parameter for stable thermal conditions (e.g., Pardyak, Monti, and Fernando, 2002; Venayagamoorthy and Koseff, 2016). It may be used to evaluate whether a turbulent flow becomes laminar but not the opposite. The reason is that turbulent correlations $\overline{v'\theta'_v}$ do not pertain to laminar flows. To overcome this problem, alternative ratios were introduced, based on the proportionality between of a few terms of the TKE equation, as described below.

According to the eddy diffusivity theory (Sutton, 1932), the turbulent correlation -$\overline{v'\theta'_v}$ is similar in form to the kinematic flux term (i.e. $\overline{VU}$, the vertical kinematic advective flux of U–momentum), apart from the fact that the perturbations are used instead of the mean values. Thus, it is reasonable to expect the value -$\overline{v'\theta'_v}$ to be proportional to the gradient $\frac{\partial \overline{\theta_v}}{\partial y}$ (e.g. -$\overline{v'\theta'_v} \simeq \frac{\partial \overline{\theta_v}}{\partial y}$). Similarly, the turbulent shear stresses $-\overline{u'v'}$ and $\overline{w'v'}$ may be linked to $\frac{\partial \overline{U}}{\partial y}$ and $\frac{\partial \overline{W}}{\partial y}$ respectively (e.g. $-\overline{u'v'} \simeq \frac{\partial \overline{U}}{\partial y}$ and $\overline{w'v'} \simeq \frac{\partial \overline{W}}{\partial y}$), where y is the vertical direction. If these proportionals are assumed, then the gradient Richardson number Rg may be defined as follows (Stull, 1988):

$$Rg = \frac{(\frac{g}{\theta_v})\frac{\partial \overline{\theta_v}}{\partial y}}{\left[\frac{\partial \overline{U}}{\partial y}\right]^2 + \left[\frac{\partial \overline{W}}{\partial y}\right]^2} \tag{1.8}$$

Local measurements of wind shear and temperature gradient suggest a critical Richardson number of $R_c \cong 0.25$ and a number indicating the termination of turbulence of $R_T \cong 1$.

A laminar flow becomes turbulent when $Rg < R_c$ while a turbulent flow becomes laminar when $Rg > R_T$.

1.4.3 Bulk Richardson number

The gradient Richardson number has been successfully applied in several studies (e.g., Balsley, Svensson, and Tjernstr, 2008; Silva et al., 1999) and is the formulation of the Richardson number usually referred in literature. However, local temperature and velocity gradients are difficult to measure accurately. Frequently, the meteorologists prefer to approximate the gradients by using observations made at discrete intervals, yielding to the third and last formulation of the Richardson number.

By approximating $\overline{\frac{\partial \theta_v}{\partial y}}$ to $\frac{\Delta \overline{\theta_v}}{\Delta y}$, $\overline{\frac{\partial U}{\partial y}}$ to $\frac{\Delta \overline{U}}{\Delta y}$ and $\overline{\frac{\partial W}{\partial y}}$ to $\frac{\Delta \overline{W}}{\Delta y}$, the ratio called bulk Richardson number Ri is defined as follows (Stull, 1988):

$$Ri = \frac{g \Delta \overline{\theta_v} \Delta y}{\overline{\theta_v} \left[(\Delta \overline{U})^2 + (\Delta \overline{W})^2 \right]} \tag{1.9}$$

where Δy is a characteristic vertical length–scale. Because of the simplicity to calculate, this form is the most widely used in meteorology and engineering applications (e.g., Xie, Hayden, and Wood, 2013; Zoumakis and Kelessis, 1991). The finite differences in velocities are computed from the ground to the top of the domain while the discrete temperature intervals are calculated as the differences between the bulk temperature within the domain and the temperature on the ground. It is often reasonable to replace the bulk temperature with the free–stream temperature at the top of the domain, ensuring that the differences in the resulting Richardson number are negligible. Assuming the last formulation, the bulk Richardson number is always positive for stable–stratified flows, negative for unstable–stratified flows and zero in neutral conditions.

Whether or not expressed in fluxes, gradients or finite differences form, the Richardson number gives information about the stability of the flow and the level of turbulence. Furthermore, for positive Richardson number under stable conditions, low turbulence intensity is expected. On the contrary, for negative Richardson number during unstable conditions, the strong mixing leads to high turbulence intensity.

1.4.4 The Monin-Obukhov length

The scaling parameter used for thermally stratified flows and to quantify the effects of buoyancy on turbulent flows is the Monin–Obukhov length L. It was so called because it is based on the Monin–Obukhov similarity theory (Monin and Obukhov, 1954), but frequently it is simply referred to the Obukhov length. This parameter correlates the mechanical shear term with the buoyancy production or consumption of energy in turbulent flows. Originally, it was defined as (Stull, 1988):

$$L = \frac{-(\overline{u'v'}^2 + \overline{w'v'}^2)^{\frac{3}{4}}}{\kappa \frac{g}{\theta_v}(\overline{v'\theta'_v})} \tag{1.10}$$

where κ is the von Karman constant, ranging from 0.35 and 0.42. Assuming this formulation, the Obukov length indicates the ratio between the shear and the buoyancy processes. However, the total shear stress is also defined as $\tau = \rho u^{*2}$ (where u^* is the friction velocity), so the Obukov length is usually rearranged as follows:

$$L = \frac{-\overline{\theta_v} u^{*3}}{\kappa g(\overline{v'\theta'_v})} \tag{1.11}$$

The Obukhov length is negative during unstable thermal conditions because the buoyancy term in the denominator is a (positive) production of turbulent energy. During stable thermal situations, the Obukhov length L is positive because the buoyancy term is a (negative) consumption of energy. Physically, the Obukhov length is the absolute height above the ground where the contribution of the mechanical shear term to the turbulent kinetic energy equals the contribution of the buoyancy effect. For stable stratified flows, the Obukhov length is always positive, however, if L is very small (close to the wall), it means that the buoyancy effects are relevant because their energy contribution equals the shear production in a region where the latter is supposed to be high. On the contrary, if the Obukhov length is big and far from the wall, it means that the buoyancy effects are almost negligible because they equalize the mechanical energy contribution in a region where the latter is supposed to be low. During unstable situations, the Obukov length assumes similar meaning but (virtually) on the other side of the wall. As a scaling parameter, the Obukhov length has been used to assess the stability effects in the surface layer (e.g., Golder, 1972; Pahlow, Parlange, and Port-Agel, 2001).

1.4.5 Richardson number and Monin-Obukhov length relationship

In Sec. 1.4.1, the flux Richardson number has been defined as the ratio between the buoyancy and shear terms of the TKE Eq. 1.6. In Sec. 1.4.4, the height from the ground where the buoyancy and shear are approximately equal is defined as the Monin-Obukhov length. The dimensionless Obukhov stability parameter y/L, where y is the height above the ground, can be obtained directly from the flux Richardson number (Eq. 1.7) when approximating the wind gradient $\partial\overline{U_i}/\partial x_j$ to $u^*/\kappa y$ (Reible, 2017):

$$\frac{y}{L} = \frac{R_f}{(1 - 5R_f)}; \qquad stable \quad conditions \tag{1.12}$$

$$\frac{y}{L} = R_f; \qquad unstable \quad conditions \tag{1.13}$$

For stable thermal conditions, Eq. 1.12 shows that for $R_f \longrightarrow 0$ then $L \longrightarrow \infty$ and the neutral condition is approached. Whereas for positive values of R_f, the relationship is limited by $R_f = 0.2$ as $L \longrightarrow 0$ and a 'strongly' stratified condition is achieved.

1.4.6 Summary of recent studies on thermal stratification

Nearly two decades ago, Britter and Hanna (2003) suggested that urban flows may be considered as neutral or nearly neutral in urban dispersion models. However, the topic of thermal stratification in urban areas has recently received renewed attention (e.g. Kanda and Yamao, 2016; Boppana, Xie, and Castro, 2013), suggesting that non–neutral atmospheric stratification conditions frequently occur in urban areas and neutral conditions may be the exception rather than the rule (Wood et al., 2010). It has been documented that unstable thermal conditions occur three times more frequently than stable and six times more than neutral conditions over the city of London during the daytime (Wood et al., 2010). Furthermore, at night the number of unstable cases was almost equal to the number of stable cases and four times greater than the number of neutral ones, because of radiative cooling of the surface.

In stable conditions, pollutant concentration may increase and air quality may decrease within the urban canopy because of the reduced dispersion in the vertical direction. Despite the increasing concerns regarding air quality, only a few experimental studies have examined the effects of stable stratification on turbulent structures over smooth, rough (e.g. Ohya, 2001; Williams et al., 2017), and very rough to urban (e.g. Marucci and Carpentieri, 2018a; Marucci, Carpentieri, and Hayden, 2018) surfaces, and the impact on passive scalar dispersion (e.g. Yassin et al., 2005; Kanda and Yamao, 2016). Not surprisingly, only very few numerical studies (e.g. Cheng and Liu, 2011; Xie, Hayden, and Wood, 2013; Boppana, Xie, and Castro, 2013; Tomas, Pourquie, and Jonker, 2016; Huang and Bou-Zeid, 2013) have examined turbulence and dispersion in stably stratified flows over very rough–urban surfaces. Two key problems remain to be addressed.

The first problem is to identify the critical level of stratification which can be interpreted as signalling the start of 'strongly' stratified conditions. Williams et al. (2017) reported that the critical bulk Richardson number, based on the boundary layer thickness, the free stream velocity and the temperature difference across the boundary layer thickness, was 0.10 for a smooth surface and 0.15 for a rough surface with a roughness length in wall units y_0^+ less than 4. This confirms that a rough surface reduces the stratification effect compared to a smooth wall, and also suggests that for a very rough urban surface, which would have a much greater roughness length, the critical Richardson number is likely to be greater than 0.15.

In Chap. 4, stable thermal conditions were investigated for a bulk Richardson number $Ri \leq 1$. Assuming the formulation of Eq. 1.9, we claim that for $Ri \leq 1$, the thermal stability over an urban–like geometry may still be classified as weakly stratified (Britter and Hanna, 2003) because in real wind scenarios the wind speed approaches zero frequently (i.e. near the building walls, during calm–windy day etc.) so that the Richardson number is typically much greater than $Ri = 1$.

The second problem is that the urban surface is always heterogeneous. The change in surface roughness associated with a flow crossing from a rural area into an urban area, or low-rise buildings area into a central business district (CBD) with high-rise buildings, leads to

a region of transitional flow as the turbulent boundary adapts to the new wall condition (e.g. Hanson and Ganapathisubramani, 2016; Cheng and Castro, 2002; Tomas, Pourquie, and Jonker, 2016; Marucci, Carpentieri, and Hayden, 2018; Sessa, Xie, and Herring, 2018). This transitional flow results from the development of an internal boundary layer (IBL) above the roughness elements. To understand how air quality may be impacted, it is necessary to determine to what extent the step change of roughness and the thermal stratification together affect flow and dispersion.

Tomas, Pourquie, and Jonker (2016) investigated the effect of stable stratification on flow and line source dispersion by simulating a smooth–wall boundary layer entering a generic urban area using LES. Although it was only considered a weakly stable condition with a bulk Richardson number of 0.147, it was found that the IBL was 14% shallower than that in neutral conditions and the turbulent kinetic energy was reduced by 21%. It should be noted that the approaching flow was developed over a smooth–wall surface so that the inflow turbulence intensity and integral length scales were not representative of a typical rural boundary layer. This means that the subsequent turbulence and dispersion predictions downstream of the step change in surface roughness were not representative of a true rural–urban surface.

1.5 Research objectives

This work is based on large eddy simulations of turbulence and ground–source dispersion over a rural–to–urban transition region in various meteorological conditions. There are important aspects that will be investigated.

1. Is there an accurate method to evaluate the depth and growth rate of the internal boundary layer (IBL) developing over a change in roughness?

2. Is ground–source dispersion affected by the development of the IBL?

3. To what extent do increasing thermal stratification and inflow turbulence intensity affect the IBL thickness and ground–source dispersion?

Another aspect of this work is the investigation of wind direction effects on ground–source dispersion. The two following questions will be answered.

4. Can we quantify the effects of wind direction on vertical and horizontal transport of pollutant in neutral and stable thermal conditions?

5. What are the limitations of the developed LES model for the simulation of a full–scale field study?

1.6 Thesis outline

In Chapter 2 the LES method was briefly described, including the filtering operation, the sub–grid scale models, the wall function, momentum and transport equations. Following,

the widely–used CFD code OpenFOAM settings were reported, with particular attention to the pre and post–processing of the LES cases simulated. The code implementation contributed by the author for his PhD research was discussed in Sec. 2.11.4.

In Chapter 3, the first part of this study has looked at the development of the internal boundary layer (IBL) over a block array close to a sharp change in surface roughness and its effect on dispersion from a ground level source for ratios of the downstream distance to the roughness length of less than 300.

In Chapter 4, a synthetic turbulence and temperature fluctuation generation method embedded in Large–Eddy Simulations (LES) was developed to investigate the effects of weakly stable stratification (i.e. with the Richardson number $Ri \leq 1$) on turbulence and dispersion following a rural–to–urban transition region.

In Chapter 5, the transport of pollutant below and above the canopy was analysed for a mean wind direction inclined to a different angle (i.e. 15° and 45°) from the main streets of the urban array.

In Chapter 6, a full–scale LES was performed to analyse a field experiment of gas dispersion.

In Chapter 7, final conclusions of this PhD research and comments on future development were given.

2 Methodologies

2.1 Complexity of the urban geometry

Although computational power is increasing, the simulation of most real urban scenarios is still a challenge when large and complex geometries are to be analysed. An affordable solution is then to consider using urban–like arrays of obstacles and large–eddy simulations to compute flow, turbulence and dispersion processes.

The cuboid elements represent either simple buildings or roughness elements, and the analysis of such morphologies is beneficial to the understanding of building aerodynamics, urban meteorology and boundary layer flows. At the neighbourhood scale ($\sim 1km$), real buildings might show statistical homogeneities (i.e. low–rise adjacent buildings oriented in regular patterns), so the modelling assumption of homogeneous buildings may be considered fairly realistic. On the contrary, when modelling at the city scale ($\sim 10km$) the homogeneous assumption is no longer valid because heterogeneous features (i.e. building height, size, shape variation and non–regular patterns) cannot be neglected for the accurate prediction of turbulent flows.

In order to improve the understanding of transport and diffusion of particles and gas within such arrays of obstacles, it is useful to analyse the complex flow patterns due to the interactions of the wind over a single building or groups of buildings. The characteristic regions of the flow around an isolated obstacle are the separation zone at the upwind face, the cavity in the lee of the obstacle, and the recirculation zone at the downwind face. In contrast, over groups of buildings, the flow pattern is affected by the height, width and spacing between the obstacles. Analysis of such flows have been already performed on arrays of staggered cubes, as for example in Xie and Castro (2008), in Xie and Castro (2006), Hanna et al. (2002), and around a surface–mounted cube (Castro and Robins, 1977), whereas the study of flow around aligned cuboid elements (more complex than cubes) in a uniform or non–uniform height array is still very poor.

Urban–like geometries can be characterised by two parameters: the plan area density $\lambda_p = A_p/A_T$ and the frontal area density $\lambda_f = A_f/A_T$, usually called "lambda parameters". A_p is the total building plan area, A_T the building lot area and A_f the total building frontal area. For regular arrays of uniform height obstacles, the frontal area is measured over the first row of buildings. The frontal parameter λ_f is the surface facing the wind flow so that, it is implicitly correlated to the drag force. Typical values for λ_f are 0.1 for moderate building density and 0.3 for urban centres (Britter and Hanna, 2003). However, the lambda parameters λ_p and λ_f are not sufficient to fully characterise urban areas. For example, real urban

areas have great variability of building height which generate large drag forces leading to increases of friction velocity. Therefore, a change of surface roughness due to non–uniform building heights leads to modifications in wind speed and shear stress profiles.

Another geometric unit that can be used to describe an urban area is the street canyon. Street canyons are usually characterised by the aspect ratio, which is defined as the ratio of the height of obstacles to the separation. The street–canyon effect occurs within the roughness sublayer when the aspect ratio of the street leads to flow channelling along the main streets and flow recirculation in the wake of the obstacles (Castro et al., 2017). Hanna et al. (2002) compared a square array of aligned cubes with an array of staggered ones concluding that a street–canyon effect was more prominent for the aligned array because of the higher flow speeds between the obstacles. Castro et al. (2017) observed that when the streets between the intersections in an array of cubes are only h in extent this is inadequate for the establishment of the development of street–canyon flows. Therefore it was proposed a compromise solution block ($h \times 2h \times h$) with h spacing on the basis that the street–canyons should be longer than h and of smaller aspect ratio. The geometry designed by Castro et al. (2017) has been widely tested (e.g. Hertwig et al., 2018; Fuka et al., 2018; Marucci and Carpentieri, 2018a) as part of the DIPLOS project (DIsPersion of LOcalised releases in Street networks; www.diplos.org). The DIPLOS geometry introduces a geometrical asymmetry that is more typical of actual street topologies.

Fig. 2.1 shows the regular urban array of uniform height cuboid elements used for the described LES study. It was assumed cuboid elements with height h, width $2h$ and uniform spacing h in the lateral and normal direction so that, the plan area density measured $\lambda_p = 0.33$. The domain measured $29h \times 12h \times 12h$ and included 48 cuboid elements (12×4). Hanna et al. (2002) compared model simulations with observation and found that flow characteristics were converged after 7 rows of buildings. We used 12 rows of buildings to allow a fully developed turbulent flow and to ensure sufficient model extension to analyse dispersion mechanisms. A sensitivity test was performed on the minimum length of the upstream and downstream extensions, before and after the first and last row of buildings respectively, to avoid buildings perturbations of the prescribed flow characteristics at the inlet and reverse flow at the outlet. It was found that $3h$ extension with no obstacles was the minimum length both upstream and downstream of the array. Castro et al. (2017) performed a sensitivity test of different domain heights ($y = 6h, 8h$ or $10h$) and recommended a top domain of at least six canopy heights in order to capture the most important turbulence features. In this study we used a domain height of $y = 12h$ to capture vertical motions of non–neutral turbulent flows and to analyse the interaction between the internal and the external boundary layers.

By considering a simplified array of regular buildings, this study improves the basic understanding of boundary layers interaction and dispersion mechanisms in neutral and stable thermal conditions. This is a required step before introducing geometric complexities such as building height variations or changes in obstacle's shape which may lead to dynamics that are hard to discern.

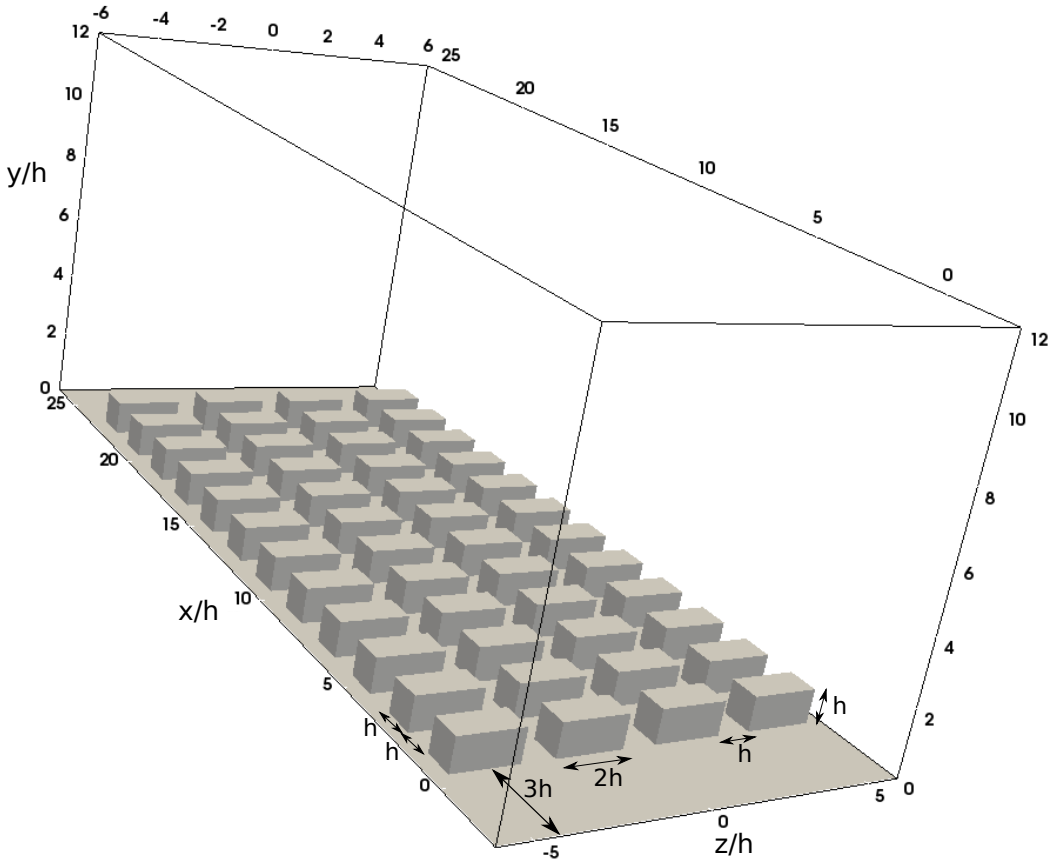

Figure 2.1: A regular array of uniform height cuboid elements.

2.2 Numerical models

In engineering applications the flow field is computed by using several computational approaches (i.e. Reynolds–averaged Navier–Stokes equations RANS, large–eddy simulations LES, direct numerical simulations DNS, hybrid models) which mainly differ for the accuracy of the solution and the required computational cost. From the energy spectrum point of view, Fig. 2.2 gives an overview of the RANS, DNS and LES approach for modelling/resolving the turbulent flow.

The RANS approach is to model all eddy frequencies, DNS resolves the entire turbulent energy spectrum while LES resolves up to the cut–off which is placed in the region of the spectrum where the energy is transferred without significant dissipation from the large scales to the small scales (e.g. inertial sublayer). The remaining energy field is modelled by LES. The difference between RANS and LES averaging process is that the former is performed over time whereas the latter over space.

During the last 30 years the RANS method has been widely used for industrial applications where the short–term tasks always require low–demanding methods. The method combines

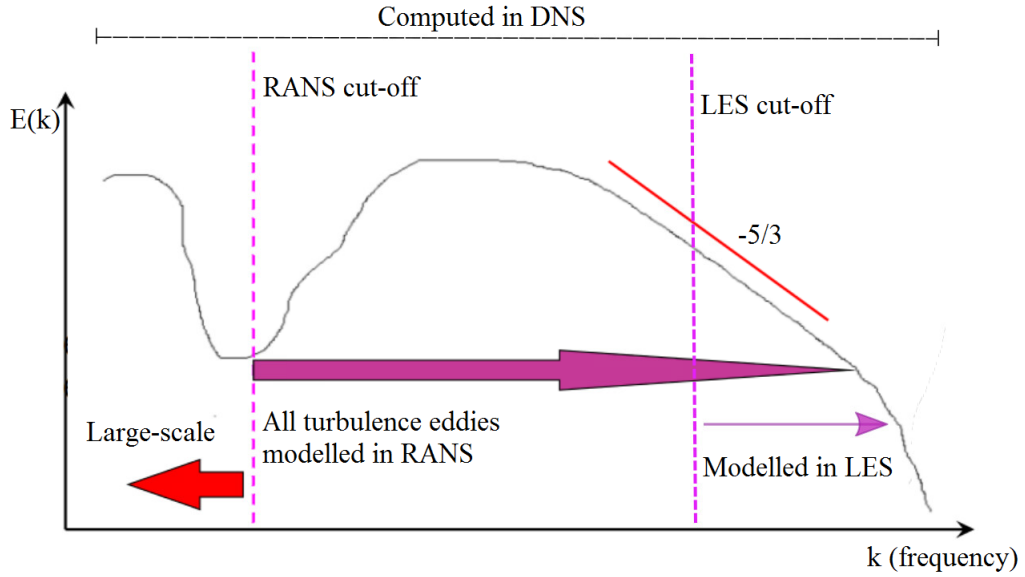

Figure 2.2: RANS, DNS and LES approach of modelling/resolving the energy spectrum

the time–averaged Navier–Stokes equations and a turbulence model (e.g. $k-\varepsilon, k-\omega$) to model the effect of all the scales of motion ensuring a relatively low computational cost.

The DNS approach is to resolve all the scales of motion and represents the most accurate numerical method available. However, the required number of grid points to resolve all the scales of motion is proportional to $Re^{9/4}$ (Piomelli, 2008) hence, the method is hardly used today for large Re–number problems.

LES is a computational method which lies between the RANS and the DNS solution. LES is becoming a mature tool for computing unsteady 3–dimensional flows at high Reynolds number and over complex geometries. Following a filtering operation, in LES the larger–scale motions affected by the geometry are solved explicitly, whereas the smaller scales, showing a universal character, are simply modelled. Because the modelled small scales tend to be homogeneous and isotropic, LES can be more accurate than the RANS approach and more appropriate for $3D$ problems. Moreover, in LES the smaller scales only contribute for a small fraction of the total energy (i.e. less than 10%) while the greater part of the flow information is achieved by resolving the larger scales. This allows the use of a coarser grid resolution if compared to DNS and much less computational time and computer resources. From these considerations, the general goal of the present and future research is to extend the capability of LES in terms of accuracy and efficiency when modelling $3D$ anisotropic turbulent flows over complex geometries.

2.3 Large–Eddy Simulations

Most LES developments since 1963 have focussed on meteorological applications and modelling atmospheric boundary layer flows. In particular, three main methodologies have been

developed based on the flow characteristics and computational resources:

Table 2.1: LES methodologies (Pope, 2000)

Model	Acronym	Resolution
Large-eddy Simulation with near-wall resolution	LES–NWR	The filter and the grid are sufficiently fine to resolve 80% of the energy everywhere
Large–eddy Simulation with near-wall modelling	LES–NWM	The filter and the grid are sufficiently fine to resolve 80% of the energy remote from the wall, but not in the near–wall region
Very–large–eddy Simulation	VLES	The filter and the grid are too coarse to resolve 80% of the energy

Briefly, the LES–NWR requires a very fine grid near the wall, thus considering the relation between the viscous length scale and the Reynolds number, the method is infeasible for high–Reynolds–number flows. Most of the meteorological applications of LES as well as the present research, are conducted by using LES–NWM, which implies that about 80% of the total energy is resolved and only the near–wall energy is modelled, assuming the local equilibrium of the near–wall region. Wall–layer models, also known as approximate boundary conditions are based on equilibrium laws which assume the validity of a law–of–the-wall because the dynamics of the wall–layer region is universal (Piomelli et al., 2003).

2.3.1 Filtering operation

LES methods perform a filtering operation on the Navier–Stokes equations so that the filtered velocity $\overline{U}(x,t)$ is computed explicitly whereas the residual (or subgrid–scale, SGS) component $u'(x,t)$ is modelled. Assuming an homogeneous filter function, the velocity field has the decomposition:

$$U(x,t) = \overline{U}(x,t) + u'(x,t) \tag{2.1}$$

where, if $U(x)$ is a random velocity field defined in one dimension (x) and $G(r)$ is the homogeneous filter associated with wavelength r, the filtered velocity field is given by the convolution (Pope, 2000):

$$\overline{U}(x) \equiv \int_{-\infty}^{+\infty} G(r)U(x-r)\,dr \tag{2.2}$$

The most frequently used filters are the box filter, the Gaussian filter and the sharp spectral filter (Fig. 2.3). The simplest filtering method is the box filter $G(r) = \frac{1}{\triangle}H(\frac{1}{2}\triangle - |r|)$ where $\triangle$ is the filter width, proportional to the grid spacing. The box filter defines $\overline{U}(x,t)$ as the average of $U(x')$ in the interval $x - \frac{1}{2}\triangle < x' < x + \frac{1}{2}\triangle$.

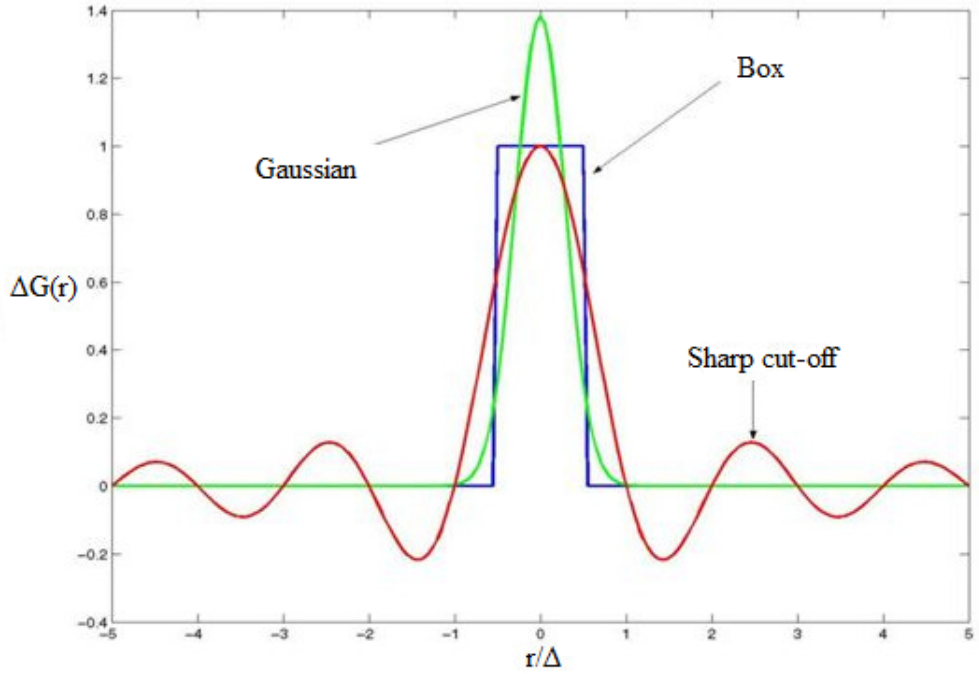

Figure 2.3: Filters $G(r)$: box, Gaussian and sharp spectral filters (Pope, 2000)

The Gaussian filter function is the Gaussian distribution with mean zero whereas the sharp spectral filter function is defined as:

$$G(r) = \frac{\sin(\pi r/\Delta)}{\pi r} \tag{2.3}$$

In Fig. 2.4 it is shown an example of Gaussian filtered velocity $\overline{U}(x,t)$ following the general trend of $U(x)$ where the short length scale fluctuations are removed.

2.3.2 Filtered conservation equations

Assuming spatially uniform filters, the filtered continuity equation is:

$$\overline{\left(\frac{\partial u_i}{\partial x_i}\right)} = \frac{\partial \overline{u_i}}{\partial x_i} = 0 \tag{2.4}$$

whilst the momentum equation in conservative form is:

$$\frac{\partial \overline{u_i}}{\partial t} + \frac{\partial \overline{u_i}\,\overline{u_j}}{\partial x_j} = \nu \frac{\partial^2 \overline{u_i}}{\partial x_j \partial x_j} - \frac{1}{\rho}\frac{\partial \overline{p}}{\partial x_i} \tag{2.5}$$

where $\overline{p}(x,t)$ is the filtered pressure field and the filtered product $\overline{u_i u_j}$ differs from the product of the filtered velocities $\overline{u_i} \cdot \overline{u_j}$ of the Navier–Stokes equations. The difference defines the *residual–stress tensor*:

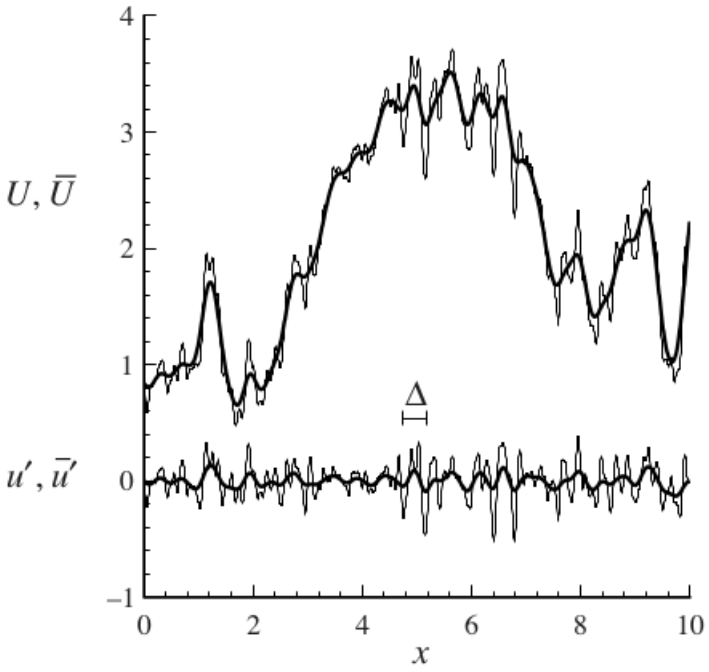

Figure 2.4: Upper curves:velocity field $U(x)$ and the corresponding filtered field $\overline{U}(x,t)$. Lower curves: the residual field $u'(x)$ and the filtered residual field $\overline{u'}(x)$ (Pope, 2000)

$$\tau_{ij}^{R} \equiv \overline{u_i u_j} - \overline{u_i}\,\overline{u_j} \tag{2.6}$$

from which, the *anisotropic residual–stress tensor* is defined as:

$$\tau_{ij}^{r} \equiv \tau_{ij}^{R} - \frac{2}{3} k_r \delta_{ij} \tag{2.7}$$

while the modified filtered pressure includes the isotropic part:

$$\bar{p} \equiv \overline{p} + \frac{2}{3}\rho k_r \tag{2.8}$$

From these definitions, the filtered momentum equation 2.5 can be rewritten as:

$$\frac{\partial \overline{u_i}}{\partial t} + \frac{\partial \overline{u_i}\,\overline{u_j}}{\partial x_j} = \nu \frac{\partial^2 \overline{u_i}}{\partial x_j \partial x_j} - \frac{\partial \tau_{ij}^{r}}{\partial x_j} - \frac{1}{\rho}\frac{\partial \overline{p}}{\partial x_i} \tag{2.9}$$

Closure of the filtered continuity and momentum equations (Eq. 2.4 and Eq. 2.9) is given by modelling the anisotropic residual stress tensor τ_{ij}^{r} by using a subgrid–scale (SGS) model.

2.4 The Smagorinsky model

The simplest and commonly used subgrid–scale (SGS) model is the one proposed by Smagorinsky in 1963. The residual stress tensor is related to the filtered rate of strain by the eddy viscosity $\nu_r(x,t)$ of the residual motions.

$$\tau_{ij}^r = -2\nu_r \overline{S_{ij}} \tag{2.10}$$

where $\overline{S_{ij}} = \frac{1}{2}\left(\frac{\partial \overline{u_i}}{\partial x_j} + \frac{\partial \overline{u_j}}{\partial x_i}\right)$.

The eddy viscosity ν_r is modelled as:

$$\nu_r = \ell_S^2 \overline{S} \tag{2.11}$$

$$= (C_S \Delta)^2 \overline{S} \tag{2.12}$$

where $\overline{S}$ is the characteristic filtered rate of strain and $\ell_S = C_S\Delta$ is the Smagorinsky length scale, related to the filter width Δ through the Smagorinsky coefficient C_S.

The model gives closure to the governing equations and implies that the energy transfer is everywhere from the filtered motions to the residual motions with no backscatter.

2.4.1 Law of the wall

The viscous wall region is a critical issue especially for LES, because the production, dissipation, kinetic energy and Reynolds–stress anisotropy reach the highest value at y^+ less than 20, where y^+ is the distance in wall units (see below) of the centroid of the first cell from the wall (Pope, 2000). A typical criteria is then to increase the grid resolution in the vicinity of solid walls in order to have y^+ of the order of unity.

In that case, the local wall shear stress is obtained from the laminar stress–strain relationships:

$$u^+ = \frac{u}{\hat{u}_\tau}, \quad y^+ = \frac{\rho \hat{u}_\tau y}{\mu}, \quad y^+ = u^+,$$

where $\rho \hat{u}_\tau^2$ is the local shear stress. If the inner–layer eddies are resolved, a constant grid spacing in wall units must be used. Piomelli (2008) suggested that for boundary layer or channel flows, the streamwise grid size must be $\triangle x^+ \simeq 100$ while the lateral grid size $\triangle z^+ \simeq 20$ (where $x_i^+ = x_i u_\tau / \nu$). However, due to the complexity of some geometries or to the near–wall mesh (y^+), which is not fine enough to resolve the viscous sublayer, this criteria is not always satisfied. Indeed, Xie and Castro (2006) showed that for flows over an array of cuboid elements where separation and attachment occur, to obtain the overall surface drag, it is not necessary to resolve the viscous sublayer everywhere. Therefore, it is typically assumed the

centroid of the first cell from the wall, being within the logarithmic region of the boundary layer:

$$\frac{u}{\hat{u}_\tau} = \frac{1}{\kappa} lnE \left(\frac{\rho \hat{u}_\tau y}{\mu} \right) \tag{2.13}$$

where κ is the von Karman constant and E is an empirical value.

2.4.2 Van Driest damping function

Following the definition of eddy viscosity (Eq. 2.12) in Sec. 2.4:

$$\nu_r = (C_S \Delta)^2 \overline{S}, \tag{2.14}$$

the specification of the Smagorinsky length scale $\ell_S = C_S \Delta$ is only reasonable for Δ in the inertial subrange[1] and high Reynolds number. In the near–wall region these assumptions are not valid and the definition of ℓ_S yields, incorrectly, to excessive eddy viscosity and shear stress at the wall. For this reason, where the near–wall mesh is fine enough to resolve the viscous sublayer, it is assumed the van Driest damping function to specify ℓ_S as:

$$\ell_S = C_S \Delta [1 - exp \left(\frac{-y^+}{A^+} \right)] \tag{2.15}$$

where A^+ is a constant. This function damps the Smagorinsky length scale in the viscous sublayer leading to a more correct behaviour near the wall.

The Smagorinsky model supplemented with a wall–damping function is known to give accurate results when applied to simple flow fields. However, the wall function of van Driest form specifies ℓ_S as a function of the wall–unit coordinate y^+. The latter is calculated based on the wall friction velocity u^*, which becomes very small near a flow reattachment point. As a consequence, in that region the damping function is unreasonably applied (Inagaki, Kondoh, and Nagano, 2005).

Another defect of this model is the inaccuracy in regions where free–shear layers exist. The residual eddy viscosity of Eq. 2.12 is a function of the characteristic filtered rate of strain $\overline{S}$. In free–shear layer regions, the rate of strain assumes high values leading to an overestimation of the SGS eddy viscosity ν_r.

[1] The region where, on average, the transfer of energy to the residual motions is balanced by the dissipation

2.5 Dynamic Smagorinsky model

In order to overcome the defect related to the use of a wall–damping function, a new model known as dynamic Smagorinsky was proposed by Germano et al. (1991). By applying the "Germano identity", a stress–tensor L_{ij} is defined as:

$$L_{ij} = T_{ij} - \tilde{\tau}_{ij} = \widetilde{\bar{u}_i \bar{u}_j} - \tilde{\bar{u}}_i \tilde{\bar{u}}_j \tag{2.16}$$

where ($\tilde{}$) denotes the test–filtering operator and $T_{ij} = \widetilde{u_i u_j} - \tilde{\bar{u}}_i \tilde{\bar{u}}_j$ is the sub–test–scale stress.

Applying the Smagorinsky model to T_{ij} and τ_{ij} (Eq. 2.12), L_{ij} is:

$$L_{ij} = -2(C_S \bar{\Delta})^2 M_{ij} \tag{2.17}$$

In the dynamic Smagorinsky model the constant C_S is calculated by the least–square error minimization (Lilly, 1992):

$$(C_S \overline{\Delta})^2 = -\frac{1}{2} \frac{\langle L_{ij} M_{ij} \rangle}{\langle M_{ij} M_{ij} \rangle} \tag{2.18}$$

where $M_{ij} = \left(\frac{\tilde{\bar{\Delta}}}{\bar{\Delta}}\right)^2 |\tilde{\bar{S}}| \tilde{\bar{S}}_{ij} - \widetilde{|\bar{S}| \bar{S}_{ij}}$. The angle brackets denote instantaneous averaging over homogeneous directions, $\tilde{\bar{\Delta}}$ is calculated as $\sqrt{\bar{\Delta}^2 + \tilde{\Delta}^2}$ and usually $\gamma = \frac{\tilde{\bar{\Delta}}}{\bar{\Delta}}$ is set to $\sqrt{3}$. C_S is the function of time and inhomogeneous direction (Germano et al., 1991) and there is no need to give the model parameter or a wall–dumping function. Although the defect of the standard Smagorinsky model is overcome, the dynamic Smagorinsky model still suffers of numerical instability as it is not guaranteed that the SGS eddy viscosity is always positive.

2.6 Mixed–time–scale model

To avoid numerical instabilities and the use of a wall–damping function, another SGS model called mixed–time–scale was proposed by Inagaki, Kondoh, and Nagano (2005). Typically, the residual eddy viscosity ν_t may be expressed in two possible ways:

$\nu_t \propto$ (Velocity scale)$\times$ (Length scale)

or

$\nu_t \propto$ (Velocity scale)$^2\times$ (Time scale).

The standard Smagorinsky model (Eq. 2.12) follows the first formulation, where $\bar{\Delta}|\bar{S}|$ represents the velocity scale and $\bar{\Delta}$ is the length scale. On the contrary, the mixed–time–scale model obeys to the second expression by assuming the SGS turbulent kinetic energy k, where

$\sqrt{k}$ is the velocity scale. The kinetic energy is solved by the k–equation or estimated by filtering a velocity field (e.g. Horiuti, 1993):

$$k_{es} = (\bar{u}_k - \hat{\bar{u}}_k)^2 \tag{2.19}$$

where ($\hat{}$) represents the filtering operator. Near the wall, the use of a damping function is avoided because the estimated kinetic energy approaches zero in the laminar–flow region thus, the SGS eddy viscosity ν_t is ensured to approach zero. The proposed model reads as follows:

$$\nu_t = C_{MTS} k_{es} T_S \tag{2.20}$$

where

$$T_S^{(-1)} = \left(\frac{\bar{\Delta}}{\sqrt{k_{es}}}\right)^{-1} + \left(\frac{C_T}{|\bar{S}|}\right)^{-1} \tag{2.21}$$

is the time scale, defined as the harmonic average of $\left(\frac{\bar{\Delta}}{\sqrt{k_{es}}}\right)^{-1}$ (the characteristic time scale of the small scale turbulence) and $\left(\frac{C_T}{|\bar{S}|}\right)^{-1}$ (the time scale of the large scale turbulence).

The model parameters C_{MTS} and C_T are set to 0.05 and 10 (Inagaki, Kondoh, and Nagano, 2005), respectively. By using the harmonic average, the time scale T_S tends to $\frac{1}{|\bar{S}|}$ near the wall hence, the eddy viscosity $\nu_t \to 0$ as $|\bar{S}|$ is increasing and the use of the dumping function is avoided. Far from the wall, the rate of strain $|\bar{S}|$ tends to zero, however the first term on the right hand side of Eq. 2.21 approaches to zero faster, so that the residual viscosity ν_t is equal to $C_{MTS}\bar{\Delta}\sqrt{k_{es}}$. In this way, the model does not suffer of the zero–divide problem when $|\bar{S}|$ approaches zero away from the wall. In relation to the type of flow and the geometry being considered, the mixed-time–scale model may be in different measure more accurate than the standard Smagorinsky model.

Here, the standard Smagorinsky was used for the LES analysis of the non–buoyant atmospheric boundary layer over a rural–to–urban transition region (further details in Chap. 3). Differently, the mixed-time–scale model was used for the LES analysis of stable thermal effects on the transport of pollutant (further details in Chap. 4) to ensure more accuracy for the evaluation of vertical transport at the canopy region for slightly different thermal conditions.

2.7 Transport equation of a passive scalar

In Chapter 3, scalar dispersion from a ground–level point source is discussed. As mentioned in Sec. 1.2.3, the dispersion analysis is usually conducted by assuming the Gaussian plume/puff model for the scalar concentration. In this work, the scalar concentration values are calculated explicitly by solving the filtered transport equation of a passive scalar:

$$\frac{\partial \overline{C}}{\partial t} + \frac{\partial \overline{u_j}\overline{C}}{\partial x_j} = \frac{\partial}{\partial x_j}\left[(K + K_{SGS})\frac{\partial \overline{C}}{\partial x_j}\right] + S \tag{2.22}$$

where $\overline{C}$ is the filtered mean scalar concentration, K is the molecular diffusivity, K_{SGS} is the subgrid turbulent diffusivity and S is the source term. The subgrid turbulent diffusivity is computed as:

$$K_{SGS} = \frac{\nu_{SGS}}{Sc_{SGS}} \tag{2.23}$$

where Sc_{SGS} is the subgrid turbulent Schmidt number which is assumed to be constant. The molecular Schmidt number Sc is computed from the molecular diffusivity K as:

$$Sc = \frac{\nu}{K} \tag{2.24}$$

where the molecular diffusivity of a generic passive gas K is a constant material property.

2.8 Temperature transport equation

Similarly to the scalar equation, temperature values are computed explicitly by solving the filtered temperature transport equation:

$$\frac{\partial \overline{T}}{\partial t} + \frac{\partial \overline{u_j}\overline{T}}{\partial x_j} = \frac{\partial}{\partial x_j}\left[(d + d_{SGS})\frac{\partial \overline{T}}{\partial x_j}\right] \tag{2.25}$$

where $\overline{T}$ is the filtered mean temperature, d is the thermal diffusivity and d_{SGS} is the subgrid turbulent diffusivity. The latter is computed as:

$$d_{SGS} = \frac{\nu_{SGS}}{Pr_{SGS}} \tag{2.26}$$

where Pr_{SGS} is the subgrid turbulent Prandtl number which is assumed to be constant. The Prandtl number is calculated from the thermal diffusivity d as follows:

$$Pr = \frac{\nu}{d} \tag{2.27}$$

where the thermal diffusivity d is a constant property. The subgrid turbulent and molecular Schmidt and Prandtl numbers are analogous. The first is used in relation to mass transfer while the second in relation to heat transfer. If considering the temperature as a scalar (i.e. gravity $g = 0$), those two numbers assume the same meaning.

2.9 Inflow Boundary Condition Technique

A critical issue when dealing with Large–Eddy Simulation is the generation of realistic and computationally efficient inflow boundary conditions. Assuming the features of urban boundary layer flows are governed by high Reynolds number and fully developed turbulence, if the inflow conditions are poorly defined in terms of temporal and/or spatial correlation, the results are less accurate and the computational cost to achieve a steady state solution rapidly increases.

Several past studies demonstrated that proper generation of inflow boundary conditions is required when LES is applied to wind engineering problems in urban environments (e.g. Vasaturo et al., 2018; Batten, Chakravarthy, and Goldberg, 2004). In fact, inflow turbulence plays the major role in the accurate prediction of particular processes such as the unsteady dispersion of pollutants in a turbulent atmospheric boundary layer (e.g. Sessa, Xie, and Herring, 2018).

Synthetic turbulence methods are based on various stochastic algorithms to generate inflow turbulence fluctuations. The generated coherent fields, including the pre–defined mean flow, are prescribed at the inlet of the computational domain according to different techniques. Because of the practical importance for industrial applications, there are a variety of methods available for generating inflow turbulence for large–eddy simulations. These can further be classified in sub–categories such as the Fourier technique (spectral method), digital filter approach, proper orthogonal decomposition (POD) method, synthetic eddy method (SEM) etc. The two synthetic inflow turbulent methods most frequently used are the synthetic random Fourier method (spectral method) and the synthetic digital filtering method.

The spectral method assumes a given energy spectrum of homogeneous isotropic turbulence and 1-dimensional problems. By using a trigonometric function of wave vectors k_n and energy $E(k_n)$, the velocity components are reconstructed. Applications of the spectral method are limited by the assumptions of isotropic turbulence, 1-dimensional problems and generated fields not correlated in time.

The digital filtering method starts from a series of random data, a filter function and any known types of correlation function to generate velocity components correlated in time and/or space. Differently from spectral method, the digital filtering method is applied to 3-dimensional problems and non–isotropic turbulence. However, the divergence–free constraint is rarely imposed. From an engineering point of view, the digital filtering method is more attractive than the spectral method because of its ability to impose a 2–point spatial correlation directly (Wu, 2017).

Examples of inflow turbulence applications are provided in literature demonstrating the growing interest of LES researchers. Few current methods are able to generate artificial turbulent inflow but only temporal correlations are preserved. For example, Hanna et al. (2002) generated one–dimensional time series of inflow data based on an exponential correlation

function to simulate flows over an array of cubes. Although the method was computationally efficient, the accuracy was seriously limited because no spatial correlation function was set at inlet.

Batten, Chakravarthy, and Goldberg (2004) designed random phases and amplitudes to sum up a set of sine and cosine in order to generate a turbulent fluctuation field able to preserve space/time correlations and second order moments. Keating et al. (2004) used the procedure to simulate a plane channel flow demonstrating that the efficiency failed the expectations.

In this study we used an efficient method of generating turbulence at inlet (Xie and Castro, 2008), embedded in large–eddy simulations within the CFD code OpenFOAM. The method is based on the exponential correlation function (Eq. 2.28) to design a filter (Eq. 2.29) on a set of two–dimensional data.

$$\frac{\overline{u_m u_{m+k}}}{\overline{u_m u_m}} = R_{uu}(k\Delta x) = \exp(-\frac{\pi|k|}{2n}) \tag{2.28}$$

$$u_m = \sum_{j=-N}^{N} b_j r_{m+j} \tag{2.29}$$

where $L = n\Delta x$ is the length scale, Δx is the grid size, r_m is a series of data ($\overline{r}_m = 0$, $\overline{r_m r_m} = 1$) and b_j are the filter coefficients. By using the exponential function Eq. 2.28, the two–dimensional data of the current time step are correlated with the two–dimensional data of the previous time step iteratively:

$$\Psi_\beta(t+\triangle t, y, z) = \Psi_\beta(t, y, z)\exp\left(-\frac{\pi\triangle t}{2T}\right) + \psi_\beta(t, y, z)\left[1-\exp\left(-\frac{\pi\triangle t}{T}\right)\right]^{0.5} \tag{2.30}$$

where T is the Lagrangian time and $\psi_\beta(t, y, z)$ is fully random in time with variance equals to unity. Therefore, the velocity components are calculated by considering the following transformation (Lund, Wu, and Squires, 1998):

$$u_i = \overline{u}_i + a_{ij}\Psi_j \tag{2.31}$$

where

$$[a_{ij}] = \begin{bmatrix} \hat{R}_{11}^{1/2} & 0 & 0 \\ \hat{R}_{21}/a_{11} & (\hat{R}_{22}-a_{21}^2)^{1/2} & 0 \\ \hat{R}_{31}/a_{11} & (\hat{R}_{32}-a_{21}a_{31})/a_{22} & (\hat{R}_{33}-a_{31}^2-a_{32}^2)^{1/2} \end{bmatrix} \tag{2.32}$$

and $\hat{R}_{ij}$ is the Reynolds stress tensor obtained from experimental data and prescribed at inlet. One assumption of the method is that the mean flow is homogeneous in the lateral direction, hence a_{31} and a_{32} vanish in Eq. 2.32 whereas the integral length scales in lateral and vertical

directions are supposed to be constant. In the streamwise direction, the Lagrangian time scale is assumed to be constant so that, considering an axial mean velocity of logarithmic form at inlet, the integral length scale also follows a log–law function.

The required inputs to initialise the method are dimensions and grid size of the virtual patch, axial mean velocity, Reynolds stresses and integral length scales in three directions. Artificial coherent turbulence structures are first generated on the virtual patch of uniform size grid and then interpolated in space to the inlet patch of the computational domain. The generated fields also satisfy a spatial correlation function of exponential form. The use of an exponential function both in time and space is justified by the simpler implementation allowing faster iterations than a Gaussian distribution. To summarise, the method allows spatially and temporally varying turbulence scales on uniform or non–uniform grids to be imposed at inlet.

2.10 IBL height calculation methods

The flow over an array of cuboid obstacles is a complex, anisotropic 3D turbulent flow. If the TKE generated upstream of the leading edge is similar to that produced downstream, then identifying the interface between the internal and external boundary layers may be difficult. For example, some authors (e.g., Cheng and Castro, 2002; Schlichting and Kestin, 1979) have defined the height of the IBL as the point on a log–linear plot where the velocity reaches 99% of that for upstream roughness at the same position. However, this definition is difficult to use because of the uncertainty of measuring differences of 1% experimentally or numerically.

An accurate method for defining the edge of the IBL helps to analyse flow and dispersion mechanisms over roughness transition regions, in particular in some specific scenarios such as in stable stratification (e.g. Kanda and Yamao, 2016). A step change over cuboid elements with uniform height, perpendicular to the flow direction, determines a more visible interface. The interface is more well-defined as greater is the difference between the TKE below and above it.

In Chapter 3 we tested two alternative methods proposed by Antonia and Luxton (1972) (Method I) and Efros and Krogstad (2011) (Method II). Upon validation, we then designed a third method (Method III, Sessa, Xie, and Herring, 2018) to calculate the height of the IBL.

Method I (Antonia and Luxton, 1972) involves plotting the streamwise velocity profile at a series of locations, downstream of the step change in roughness, against the square–root of the height above the ground. According to Method I, the velocity profiles show a discontinuity point between two distinct linear slopes which can be approximated by two straight line segments corresponding to the external and IBLs. The intersection of the segments defines the height of the IBL.

Method II devised by Efros and Krogstad (2011) is similar, but involves plotting the laterally–averaged streamwise Reynolds stress against the height above the ground. The depth of the IBL is again indicated by the intersection of two straight line segments.

Both Method I and Method II are based on the 'knee' point technique which might be open to interpretation in situations where the differences between the boundary layer velocity profiles are small. Nevertheless, they are easy to implement and provide a good indication of the IBL growth rate.

Given that the IBL grows in the vertical direction and a laterally homogeneous flow is assumed above the canopy, then it may be hypothesised that the use of a wall–normal parameter may make identifying the interface easier. Method III (Sessa, Xie, and Herring, 2018) was designed in a similar way to applying Methods I and II. The vertical Reynolds stress profiles were averaged over the lateral direction, normalized by the friction velocity u^*, i.e. $\overline{v'v'}^+$ and plotted against the height from the ground in several streamwise locations. The Reynolds stress profiles for the external and IBL regions were linearly fitted by two straight line segments. Again, the intersection of the segments defined the height of the IBL.

Further details of the three methods are given in Chapter 3, where results are compared and conclusions are drawn.

2.11 OpenFOAM settings

OpenFOAM (OF) was created by Henry Weller in the late 1980*s* at Imperial Collage in London, to develop a powerful and flexible simulation platform based on the $C++$ language. Released for free, this code includes numerical solvers and pre/post–processing utilities for the solution of continuum mechanics problems in computational fluid dynamics (CFD). Differing from many other CFD codes, the syntax of the OpenFOAM (OF) library enables users to create custom solvers with relative ease, such as boundary conditions or turbulent models. As a result, the extensibility qualities of OpenFOAM are, nowadays, appreciated all over the world.

Because of the wide range of applications, utilities and features, in this section the focus is mainly on the typical procedure for the pre/post–processing of incompressible flows by using Large–Eddy Simulations. In particular, the OF settings for the simulation of the turbulent flow over a urban–like geometry are reported. The procedure includes the implementation of three directories (*0, constant, system*) by choosing mesh characteristics, initial and boundary conditions, solvers, processing and post–processing. Results are shown in the following chapters.

Table 2.2: Pre/post-processing in OpenFOAM (OF)

Grid preparation	· OF grid generator/Supported mesh software (Pointwise)
Physical boundary conditions	· Initial boundary conditions · Flow boundary conditions
Flow characteristics	· LES properties · Transport properties · Turbulence properties
Solver	· Inflow method · PISO and PIMPLE algorithms
Discretization schemes	· Interpolation error · Spatial gradient · Time derivative
Computational setup	· CPU settings · Parallel processing · Field averaging
Post–processing	· Visualization · Output

2.11.1 Mesh

Similarly to several CFD codes, OF allows the generation of the geometry grid either by using the code as an integral part of the numerical solution or by importing the mesh already designed from a supported mesh generation software.

2.11.1.1 Mesh characteristics

Pointwise is a mesh generator which covers most of the pre–processing phase before the numerical geometry is exported to any CFD codes. For the accurate mesh generation, few instructions are to be considered. For example, the aspect ratio should be equal to one to ensure best results, as it affects the magnitude of the interpolation error. Local variations in cell size should be minimal and adjacent cell dimensions should not change by more than 20%.

In this study the neutral and non–neutral turbulent flow discussed in Chapter 3 and Chapter 4 respectively were simulated by using the following mesh parameters of the numerical model:

· *Resolution* of $h/16$ in all directions (where h is the height of the cuboid element), inlet patch comprising 192×192 cells and a total number of 16 million of cells for the entire domain;

· 3*D regular (or structured) grid* identified by regular connectivity;

· *Hexahedral (hex) mesh* to ensure the highest accuracy of the solution if compared to other types of cells with same resolution;

· *Aspect ratio* of the mesh obviously equal to one;

· *No refinement* near the wall, because Xie and Castro (2006) showed against DNS results that LES predictions with a resolution of 16 points were accurate and the grid resolution was sufficient to compute the flow. Moreover, as mentioned in Sec. 2.4.1, because of several flow separations and reattachments over an array of obstacles is not necessary or maybe impossible to resolve the viscous sublayer everywhere.

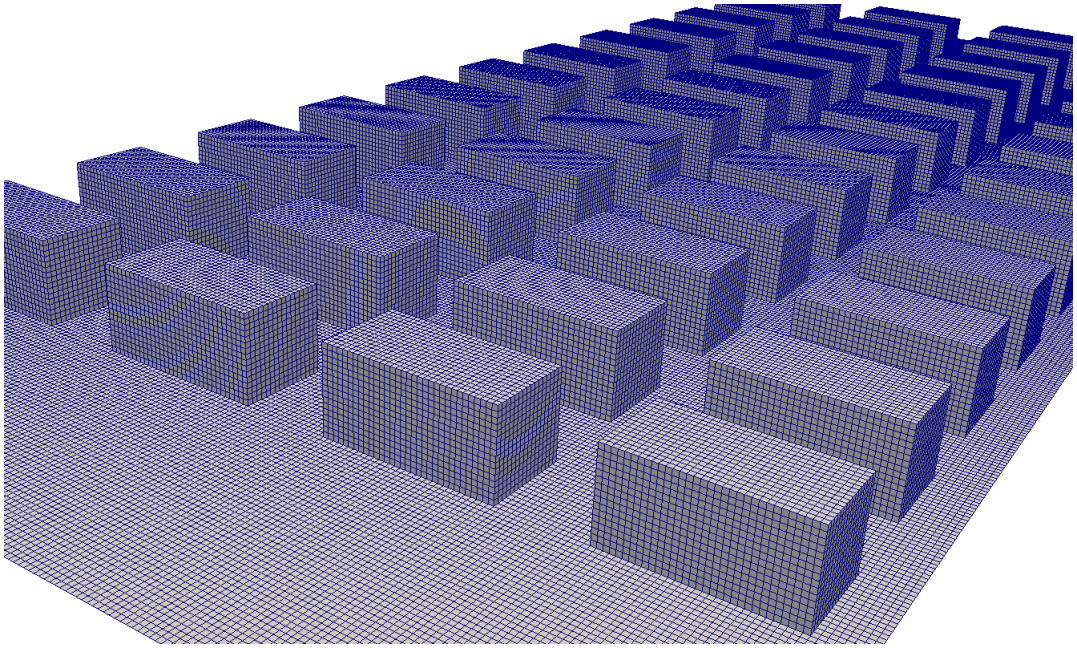

Figure 2.5: Mesh resolution of the regular array of uniform cuboid obstacles.

In Fig. 2.5 the mesh resolution ($h/16$) of the simulated urban–like geometry is shown. The obstacles and the bottom were defined as solid walls, the top of the rectangular domain was assumed at $y = 12h$ as a symmetry plane whereas the side planes were assumed to be cyclic patches.

2.11.2 Physical boundary conditions

The validity of the imported mesh is checked in OpenFOAM by running the command *checkMesh -allTopology -allGeometry*, which analyses the consistency of the mesh, including checks on the bounding box and the topology. The mesh tool reports any failures in the alignment of the cells, dimensions, number of faces, boundary definitions, non–orthogonality etc. If the mesh analysis is successful, the flow is initialised by choosing the boundary conditions for all the computed scalar and non–scalar fields.

2.11.2.1 Velocity boundary condition

The mean velocity profile on the inlet boundary of the numerical domain was assumed to be of logarithmic form and homogeneous in the lateral direction. By fitting wind tunnel data

taken upstream of the leading edge of the urban array (Castro et al., 2017 for neutral and Marucci, Carpentieri, and Hayden, 2018 for non–neutral boundary layer), the velocity values at each height were given to each cell of the inlet patch according to the patch resolution: 192×192. For solid walls, velocity values were fixed to zero in all directions, periodic values for the lateral patches of the domain and *stress–free* (or symmetry) condition at the top patch to ensure that the velocity gradient approached to zero in the top–normal direction. Lastly, for the outlet face, the OF condition *inletOutlet* switching between the *zero–gradient* and the *fixed value to zero* condition according to the flow direction, in order to avoid any reverse flow. Further details are given in Chapter 3.

2.11.2.2 Boussinesq assumption for thermal stratification

For thermally stratified flows, the kinematic density ρ_k for buoyancy force is defined as:

$$\rho_k = \rho[1 - \beta(T - T_{ref})] \tag{2.33}$$

where β is the thermal expansion coefficient and T_{ref} is the reference temperature. Eq. 2.33 is known as the Boussinesq assumption for the buoyancy force in the momentum equations. It states that density differences in thermal stratified flows are negligible except when multiplied by the gravity acceleration g. Ensuring that $|\rho_k - \rho|/\rho \ll 1$, the hypothesis of incompressible flow is still valid. Recalling the filtered momentum equation in Sec. 2.3.2:

$$\frac{\partial \overline{u_i}}{\partial t} + \frac{\partial \overline{u_i}\,\overline{u_j}}{\partial x_j} = \nu \frac{\partial^2 \overline{u_i}}{\partial x_j \partial x_j} - \frac{\partial \tau_{ij}^r}{\partial x_j} - \frac{1}{\rho}\frac{\partial \overline{p}}{\partial x_i} + \frac{F}{\rho} \tag{2.34}$$

the additional term (F/ρ) accounts for the effects due to gravity. F is the gravity body force and according to the Boussinesq assumption $F = \rho_k g$. By substituting:

$$\frac{\partial \overline{u_i}}{\partial t} + \frac{\partial \overline{u_i}\,\overline{u_j}}{\partial x_j} = \nu \frac{\partial^2 \overline{u_i}}{\partial x_j \partial x_j} - \frac{\partial \tau_{ij}^r}{\partial x_j} - \frac{1}{\rho}\frac{\partial \overline{p}}{\partial x_i} + \frac{\rho_k g}{\rho}\delta_{i,2} \tag{2.35}$$

the general expression of momentum conservation for buoyancy–driven flows is derived.

Assuming no gravity ($g = 0$), $\overline{p}$ in Eq. 2.35 is usually defined as the static pressure. Differently, for thermal stratified flows, the static pressure is $\overline{p} = \rho_k g y + \overline{p}_{rgh}$, where y is the height and $\overline{p}_{rgh}$ is the additional pressure term used to define the boundary conditions of the simulated problem. The static pressure gradient was fixed to zero on solid walls, inlet and outlet patches. Symmetry conditions were applied on the top boundary and periodic boundary conditions on the lateral boundaries.

The pressure $\overline{p}_{rgh}$ is then defined within the OF code as follows:

$$\overline{p}_{rgh} = \overline{p} - \rho_k g y \tag{2.36}$$

The gradient of pressure $\overline{p}_{rgh}$ was fixed to zero at inlet and bottom, symmetry conditions were applied at the top, cyclic conditions for the sides and the *totalPressure* condition for the outlet. The latter assumes that $\overline{p}_{rgh} = 0$ at the outlet so that, the static pressure tends to $\rho_k g y$ at the outlet and the total pressure is equal to:

$$\overline{P}_T = 0.5\rho_k \overline{u}^2 + \overline{p} \tag{2.37}$$

2.11.3 Turbulence generator (IBC)

As mentioned above, the syntax of the OF library enables users to create custom solvers with relative ease. In this study, the inflow boundary Condition technique (Sec. 2.9) was implemented within OpenFOAM 1.7 and 2.1, and used to generate synthetic turbulence at the inlet patch. Second–order statistics $\overline{u'u'}, \overline{v'v'}, \overline{w'w'}, \overline{u'v'}$ were interpolated from wind tunnel data (Castro et al., 2017; Marucci, Carpentieri, and Hayden, 2018) taken upstream of the leading edge, and included in the inflow code to generate similar fluctuations and turbulence intensity of the experimental test. Additional inputs were the number of cells in lateral and vertical directions (i.e. 192×192), the integral length scales fixed to the constant value of $1h$ in the same directions and the integral time scale fixed to $2t$ in the streamwise direction. Assuming the prescribed logarithmic mean velocity, the integral length scale in the flow direction also followed a logarithmic profile with a top value of $4h$, obtained from the free–stream velocity of $2m/s$.

The original inflow code assumes that the *PISO* (Pressure Implicit with Splitting of Operator) algorithm is applied as the pressure–velocity solver. PISO implies a first predictor step for the pressure field and two corrector steps for the velocity and pressure fields, where the resulted velocity field from the previously predicted pressure, is adjusted (twice) to satisfy the continuity equation. Compared to other solvers such as the SIMPLE algorithm, which applies two iterations on the pressure and velocity fields at each time step, PISO is considered much faster but less accurate. In order to have the same accuracy as the SIMPLE method, in the PISO loop the time step has to be reduced.

2.11.4 Inflow code implementation

As a part of the author's PhD research and contribution, the inflow turbulent method by Xie and Castro (2008) was implemented in OpenFOAM and developed in order to include:

· Ground–level point source of varying shape, size and location;

· Scalar fluxes, instantaneous and mean concentrations by solving the added transport equation of a passive scalar (Eq. 2.22);

· Heat fluxes, instantaneous and mean temperatures by solving the added temperature transport equation (Eq. 2.35) according to the Boussinesq assumption;

· Temperature fluctuations and incoming stratified flow at the inlet boundary;

Furthermore, the solving loop of the original inflow code was modified from the PISO to the PIMPLE method (defined as the combination of PISO and SIMPLE, more accurate but slower) to overcome the solution instabilities due to buoyancy.

Firstly, the momentum equation is solved with the initial value of the kinematic density ρ_k and the predicted pressure field p. Secondly, the temperature equation is solved for T and the kinematic density ρ_k is updated to the new value. Thirdly, the pressure p_{rgh} is corrected twice according to the continuity equation so that the static pressure p is updated. Fourthly, the scalar equation is solved for C, out of the pressure–velocity loop. More detailed settings for the scalar C and temperature T are given in Chapter 4 and Chapter 5 respectively.

2.11.5 LES properties

The LES method is applied in OF by choosing *LESModel* in the *turbulenceProperties* file within the *constant* folder. The Sub–Grid–Scale model parameters and the damping function are specified in the *LESProperties* file. The filter LES cut–off Δ is the cubic root of the cell volume defined as follows:

$$\Delta = (\Delta x_1 \Delta x_2 \Delta x_3)^{\frac{1}{3}} \tag{2.38}$$

where the subscripts denote the directions of the grid spacing.

For the standard Smagorinsky SGS model, the constant coefficient was fixed to $C_s = 0.1$ and *Van Driest* was the dumping function with $A^+ = 26$ and $C_\triangle = 0.1$. This function is activated where the wall-normal distance y^+ of the nearest cell is within the viscous sublayer otherwise it is non–activated. In order to evaluate y^+, the command *yPlusLES* calculates the wall–normal distance from the centroid of the nearest cell to all solid faces of the domain. For the simulated urban–like geometry, y^+ ranged between 1.31 and 24 with an area–averaged y^+ of 10.16. For the mixed–time–scale SGS model, the fixed parameters were $C_T = 10$ for the harmonic average of the time–scale T_S and $C_{MTS} = 0.05$ for the residual SGS viscosity ν_t.

In the *transportProperties* file, the kinematic viscosity ν is typically defined as well as the bulk velocity if periodic boundary conditions are applied in the streamwise direction.

2.11.6 Discretization schemes

For a fine grid resolution, second–order schemes approach the exact solution faster than lower order methods. However, higher order schemes can affect the accuracy of the solution only if the grid is fine enough, otherwise for a coarser mesh, the accuracy is lower. Linear interpolations and central discretization schemes were chosen to calculate derivatives and gradients. Second–order accurate schemes were considered both in time and space.

Time scheme. The implicit method (backward scheme) was used in this study to calculate numerical approximations to the solution of time–dependent ordinary and partial differential equations. Differently from explicit methods, implicit schemes approach the solution by solving an equation involving both the current state of the system and the later one. The backward method, specified in the *fvSchemes* file of the *system* folder in OF, by using backwards 3–point differences $(n, n-1, n-2)$ is second–order accurate but not bounded. It is named backward scheme because uses informations from already computed time–steps. Within OpenFOAM, if ϕ, ϕ^o and ϕ^{oo} are the generic field at time–steps n, $n-1$ and $n-2$ respectively, the backward formulation is:

$$\frac{\partial}{\partial t}\phi = \frac{1}{\Delta t}(\frac{3}{2}\phi - 2\phi^o + \frac{1}{2}\phi^{oo}) \tag{2.39}$$

where Δt is the time–step and the right–hand side is the 2^{nd} order time discretization of the time derivative at the left–hand side.

Gradient, Laplacian and Divergence schemes. The terms of the momentum equations (Eq.2.5) were discretized by using gradient, laplacian and divergence schemes. In particular, the normal gradients ∇U and ∇p, the diffusion term $\nabla(\nu \nabla U)$ (laplacian term) and the convection term $\nabla(\rho U \cdot U)$ (divergence term) are interpolated in OpenFOAM by using the *Gauss linear* method. This scheme specifies the standard finite volume discretization of Gaussian integration which requires the interpolation of values from cell centres to face centres. *Linear* means that the interpolation is based on linear or central differencing schemes.

2.11.7 Computational setup

The computational domain was simulated by using between 256 and 512 processor cores on the Super–computers Iridis4 and Iridis5 of University of Southampton. The LES simulations were usually conducted on 16 nodes by 16 processors for 24/48 hours slots (real–time). The choice was usually a result of an analysis involving different parameters, such as the computational time, the queuing time, the initialisation and the averaging processes.

For example, it was found that by using 256 cores, one complete flow–pass of the rectangular array was computed in about 1.5 real–time hours whereas by using 512 cores, the computational time was almost halved. However, the required queuing time to submit the job on 512 cores was almost the double that for 256 cores, assuming the same real time of 24 hours. Typically, in order to simulate parallel cases within the limit of data storage on the login node of the Super–computer, the use of 256 cores was found to be the best option.

Similar LES works highlighted that at least 20 flow–passes are required to achieve a fully developed turbulent flow and the second–order statistics are to be averaged over at least 40 flow–passes, or even more in particular cases. In this LES study, the typical initial development was fixed to 40 flow–passes and second–order statistics were averaged over at least 180 flow–passes. The time–step resolution was fixed to 0.02 and the mean Courant number:

$$C_o = U\frac{\triangle t}{\triangle x} \tag{2.40}$$

was about 0.4, where U is the free stream velocity, $\triangle t$ the time–step and $\triangle x$ the grid resolution. The total number of time–steps was typically $\sim$ 150000, corresponding to the OF time of 3000t. The averaging process of 180 flow–passes was equivalent to 3 minutes averaging in the wind tunnel experiment.

2.11.8 Post-processing

The scalar and vector fields computed by OpenFOAM were reconstructed at the end of each parallel simulation and converted to VTK files by using the OF command *foamToVTK*, which allows the output file to be exported to any supported software for visualization and post–processing (i.e. Paraview). Contour plots by using the Q–criterion and/or turbulent fluctuation profiles were typically used to detect any problems in the simulations. The Q-criterion is defined as:

$$Q = \frac{\Omega_{ij}\Omega_{ji} - S_{ij}S_{ji}}{2} \tag{2.41}$$

where Q is the second–scalar invariant of the velocity derivative tensor, S_{ij} and Ω_{ij} are the symmetric and the antisymmetric part respectively.

The Q–criterion is a widely used vortex detector which highlights regions where rotation is dominant over the shear and is useful for the analysis of turbulent flows. Similarly, vorticity contours are typically used to detect the rotation mechanisms at any point in the flow field. For a channel flow with the x–axis the streamwise direction, y in the vertical direction and z in the spanwise direction, the lateral vorticity component is defined as:

$$\omega_z = \left(\frac{\partial v}{\partial x} - \frac{\partial u}{\partial y}\right) \tag{2.42}$$

where u and v are the velocity components in x and y directions respectively. The vorticity ω_z highlights the flow rotation across a plane parallel to the mean flow direction. As an example, in Fig. 2.6 the lateral vorticity ω_z (calculated as in Eq. 2.42) is shown on a plane normal and parallel to the flow direction.

Although the flow over an array of obstacles is purely three dimensional, visible turbulent structures are expected to evolve mainly in the streamwise direction. Assuming a turbulent flow past a change in surface roughness, the lateral vorticity ω_z is useful to qualitatively locate the interface between the internal and the external boundary layers. For example, Fig. 2.6 shows the lateral vorticity over a step change from a rough to a very rough geometry. The deep red color highlights high vorticity values in the canopy region and close to the wall, where the flow dynamics is strongly affected by the roughness morphology. Moving upwards, the vorticity magnitude is decreasing. Such qualitative analysis was found to be

useful to understand the effects of the roughness geometry on the flow immediately and well above the canopy.

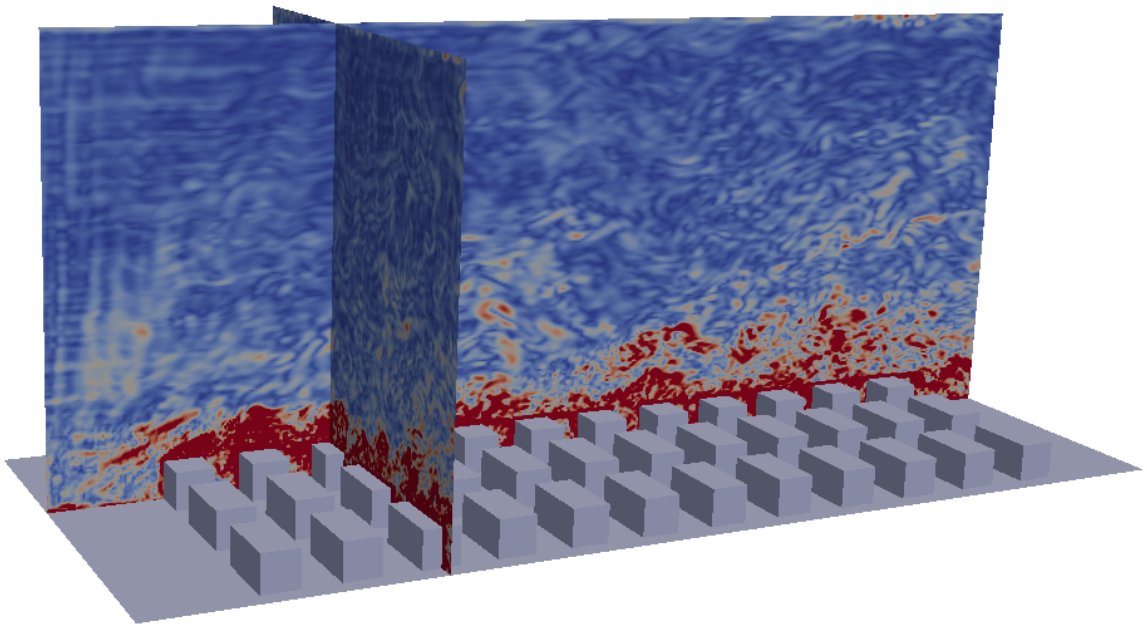

Figure 2.6: Lateral vorticity ω_z over a lateral and longitudinal plane of the regular array of uniform cuboid elements.

3 Turbulence and dispersion in internal and external boundary layers. *Sessa, Xie & Herring, 2018.*

Journal of Wind Engineering and Industrial Aerodynamics, 182, 189–201

This study has looked at the development of the internal boundary layer (IBL) over a block array close to a sharp change in surface roughness and its effect on dispersion from a ground level source for ratios of the downstream distance to the roughness length of less than 300. This was done by comparing a large–eddy simulation (LES) with inflow boundary conditions against a LES with inlet–outlet periodic boundary conditions and data from a wind tunnel experiment. In addition to established methods, an alternative approach based on the vertical Reynolds stress was used to evaluate the depth of the IBL as it developed over the array which enabled the location of the interface to be more clearly defined. It was confirmed that the IBL growth rate close to the change in surface roughness could be described by a power law profile, similar to the power law formula used in previous studies for a ratio of the downstream distance to the roughness length greater than 1000. An analysis of mean concentration and turbulent scalar fluxes suggested that the presence of the IBL constrained the vertical development of the plume from a ground level source and so led to trapping of material in the canopy layer.

3.1 Introduction

Large–Eddy Simulations have demonstrated the capability to model turbulence, dispersion and heat transfer in urban environments (Baker, Walker, and Cai, 2004; Fuka et al., 2018; Hanna et al., 2002; Kanda, Moriwaki, and Kasamatsu, 2004; Xie and Castro, 2006). The majority of LES flow and dispersion studies have focussed on the street–scale below and immediately above the canopy and used simple periodic inlet–outlet boundary conditions. Very few numerical studies have analysed the characteristics of turbulent flow as it passes over a change in roughness. Two which have are those by Michioka et al. (2011) and Tomas et al. (2017). Both of these applied the LES approach using the inflow boundary condition method to compute the flow over arrays of obstacles with various aspect ratios with the aim of better understanding the dispersion mechanisms. However, their focus was limited to examination of the advective and turbulent pollutant fluxes around the array obstacles up to the canopy height, and they did not examine IBL development. To the authors' knowledge there have been no numerical studies or experimental works which have specifically addressed the effects of IBL development on gas dispersion.

In this study we examine LES predictions made using the inflow generator proposed by Xie and Castro (2008), and then identify how the height of the IBL evolves over a pseudo rural–to–urban transition region using a similar approach to those proposed by Efros and Krogstad (2011) and Antonia and Luxton (1972), but based on using the vertical Reynolds stress. This was done with the objective of understanding the extent to which the dispersion of a neutrally buoyant gas from a ground–level point source is influenced by the interaction of the external boundary layer and IBL. The governing equations are briefly described in Sect. 3.2. Details of the numerical settings including geometry, mesh and inflow conditions are given in Sect. 3.3. LES predictions for turbulence and dispersion are discussed in Sect. 3.4. Finally, the conclusions are summarised in Sect. 3.5.

3.2 Governing equations

In LES the filtered continuity and Navier-Stokes equations are written as follows:

$$\frac{\partial \overline{u}_i}{\partial x_i} = 0 \tag{3.1}$$

$$\frac{\partial \overline{u}_i}{\partial t} + \frac{\partial \overline{u}_i \overline{u}_j}{\partial x_j} = -\frac{1}{\rho}\frac{\partial \overline{p}}{\partial x_i} + \frac{\partial}{\partial x_j}\left(\frac{\tau_{ij}}{\rho} + \nu\frac{\partial \overline{u}_i}{\partial x_j}\right) \tag{3.2}$$

where the filtered velocity and pressure fields are $\overline{u}_i$ and $\overline{p}$ respectively, ν is the kinematic molecular viscosity and ρ is the density. The standard Smagorinsky subgrid–scale (SGS) model was applied to determine the isotropic part of the residual stress tensor τ_{ij}:

$$\tau_{ij} = -2\nu_r \overline{S}_{ij} \tag{3.3}$$

where $\overline{S}_{ij} = \frac{1}{2}\left(\frac{\partial \overline{u}_i}{\partial x_j} + \frac{\partial \overline{u}_j}{\partial x_i}\right)$ is the filtered rate of strain and ν_r is the SGS residual viscosity. The SGS residual viscosity ν_r is modelled as:

$$\nu_r = (C_S\Delta)^2\overline{S} \tag{3.4}$$

where $\overline{S}$ is the characteristic filtered rate of strain, the filter width Δ was taken as the cube root of the cell volume and the Smagorinsky coefficient as $C_S = 0.1$. The Van Driest damping function was applied in the near wall region.

The Smagorinsky model supplemented with a wall-damping function is known to be less accurate near a flow-reattachment point or in free–shear layer regions (Inagaki, Kondoh, and Nagano, 2005). However, Castro et al. (2017) compared the performance of the dynamic mixed time scale sub–grid model (Inagaki, Kondoh, and Nagano, 2005) and the standard Smagorinsky over an identical array of uniform blocks and their results revealed only small differences in the spatially averaged mean velocities and turbulence stresses. Based on those results the standard model and wall-damping function were adopted for the simulations reported here.

The filtered transport equation for a passive scalar is:

$$\frac{\partial \overline{C}}{\partial t} + \frac{\partial \overline{u}_j \overline{C}}{\partial x_j} = \frac{\partial}{\partial x_j}\left[(K + K_r)\frac{\partial \overline{C}}{\partial x_j}\right] + S \tag{3.5}$$

where $\overline{C}$ is the filtered scalar concentration and S is a source term. The second term on the left–hand side is the advection term and the first term on the right–hand side is the diffusion term. K is the molecular diffusivity and K_r is the SGS turbulent diffusivity computed as:

$$K_r = \frac{\nu_r}{Sc_r} \tag{3.6}$$

where Sc_r is the subgrid (or turbulent) Schmidt number. Several numerical and experimental studies used a subgrid Schmidt number $Sc_r = 0.7$ to investigate turbulent transport of pollutant (e.g. Zhang, Tejada-Martínez, and Zhang, 2016; Hsu and Liu, 2004; Gualtieri et al., 2010). Chavez et al. (2011) carried out numerical simulations of pollutant transport in urban environments by using a turbulent Schmidt number equal to 0.1, 0.3 and 0.7. They found that variations of Sc_r had less impact on assessing gas dispersion for group of buildings. In this study, a constant Schmidt number $Sc_r = 0.7$ was assumed.

3.3 Numerical settings

The LES model was implemented within the open-source CFD package OpenFOAM version 1.7.1. A second-order backward implicit scheme in time and second–order central difference scheme in space were applied for the discretisation of the terms in Eqs. 2.9 and 2.22. Flow and turbulence within the domain were simulated as a half channel. An efficient inflow turbulence generation method (Xie and Castro, 2008) was used at the inlet, with periodic conditions at the lateral boundaries and a stress–free condition at the top of the domain ($y = 12h$, where $h = 70mm$ is the uniform height of the array element). The Reynolds number based on h and the free stream velocity $U_{ref} = 2m/s$ at $y = 12h$ was approximately $12,000$. The averaged CFL (Courant-Friedrichs-Lewy) number was 0.2, based on a time step resolution of $0.0014s$. Flow and second-order statistics were initialized for $40s$ and then averaged over $180s$ (180 flow–passes).

3.3.1 Geometry, mesh and resolution

Although computational power is increasing, the simulation of most real urban scenarios still represents a challenge, especially when large and complex geometries have to be analysed. As mentioned in Sec. 2.1, in studies to improve the understanding of building aerodynamics it is therefore usual to represent urban configurations in their simplest form as an array of cuboid elements in regular or non–regular patterns (e.g., Hanna et al., 2002; Xie and Castro, 2006).

The array of regular cuboid elements modelled in this paper represents part of a larger array used in a wind tunnel experiment designed to simulate a neighbourhood scale region in

which statistical homogeneities should exist. The section of the array modelled is shown in Fig. 3.1 where the street units parallel to the x axis are $1h$ long and referred to as 'short streets' hereinafter. Street units parallel to the z axis are $2h$ long and referred to as 'long streets'. The rectangular array includes 48 aligned blocks with h spacing, which considering the single block unit leads to a plan area density of $\lambda_p = 0.33$.

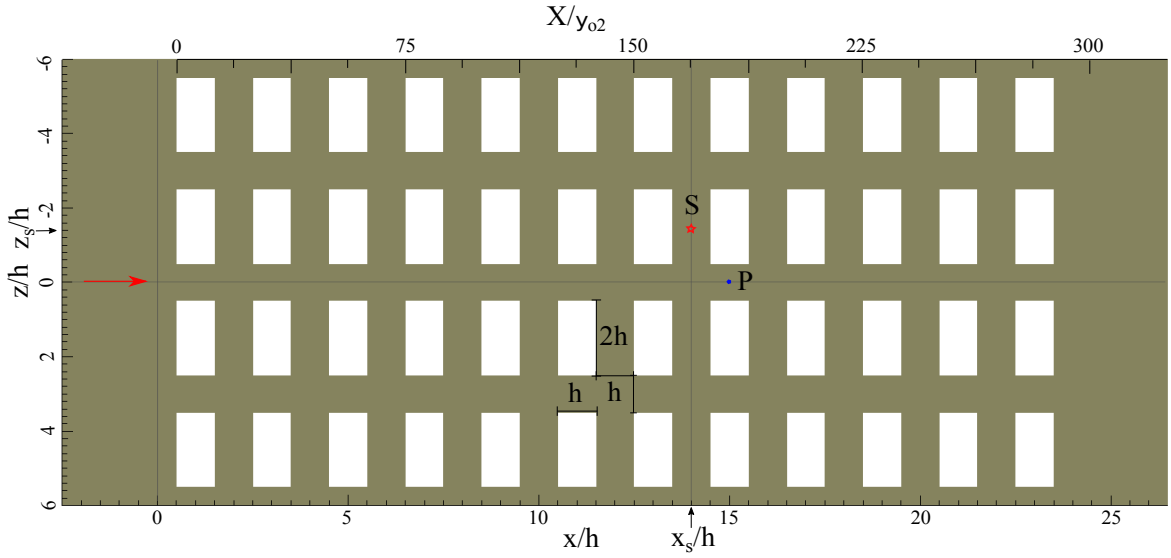

Figure 3.1: The array configuration: dimensions of buildings and streets, the coordinate system, the flow direction, the distance from the leading edge X/y_{02}, the position x_s and z_s of source S and measurements location P.

The dimensions of the modelled domain were $29h \times 12h \times 12h$ within a uniform Cartesian grid of resolution $\triangle = h/16$. Simulations by Castro et al. (2017) at this resolution yielded LES results for turbulence that agreed well with higher resolution direct numerical simulation data. The top boundary was placed at $y = 12h$, which is very close to the boundary layer height in the wind tunnel. Computations were made for the 0° wind direction by assuming that the mean wind flow was perpendicular to the front face of the cuboid elements as indicated in Fig. 3.1.

3.3.2 Scalar source

A passive scalar was released from a ground–level point source within the array of cuboid elements. The shape and size of the point source were identical to that reported in Fuka et al. (2018). The source was positioned at the middle of a long street after the seventh row of buildings (Fig. 3.1) where the downstream flow would be fully developed (Hanna et al., 2002). Because the modelling used a uniform grid, the shape of the source only approximated the source used in the experiment. The diameter was represented by 4 cells and so measured $0.25h$, while the height was one cell ($h/16$). A constant scalar flux release rate was set for each cell inside the source volume.

3.3.3 Inflow conditions

The simulation of flow over a rural–to–urban transition region requires a continuous specification of inlet turbulence. This was achieved by using the inflow turbulence method developed by Xie and Castro (2008) to generate a synthetic turbulent inflow with exponential–form correlations in time and space. The used inflow method proved to reconstruct energy–containing region and inertial sublayer of the spectra in high fidelity. Moreover, (Bercin, Xie, and Turnock, 2018) showed that the use of exponential-form correlation functions as a model approximation is more advisable than that of Gaussian-form.

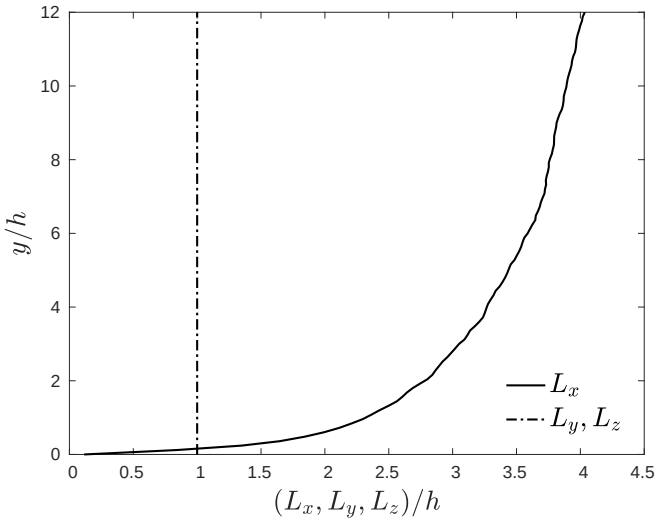

Figure 3.2: Vertical profiles of prescribed integral length scales at the LES inlet $x = -2.5h$.

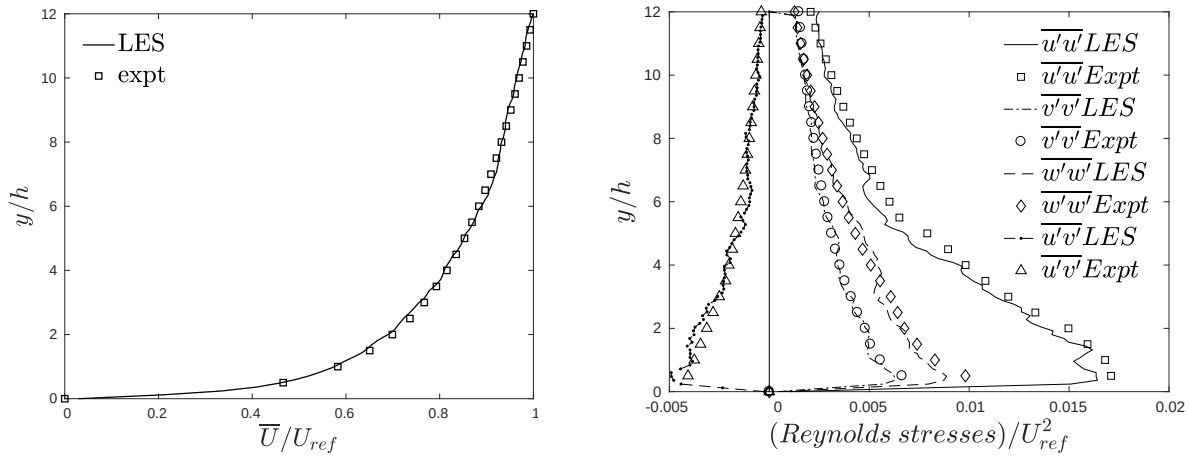

(a) (b)

Figure 3.3: (a) Vertical profiles of laterally averaged mean velocity from LES at inlet and prescribed mean velocity from experiments. (b) Vertical profiles of prescribed Reynolds stresses at the LES inlet and experimental values.

The generated turbulence satisfied the prescribed integral length scales and Reynolds stress-

tensor values. The integral length scales L_x, L_y and L_z in the streamwise, vertical and lateral directions respectively were estimated from data presented in Castro, Cheng, and Reynolds (2006) and shown in Fig. 3.2. Xie and Castro (2008) performed LES for different length scale combinations imposed at inlet (i.e. L_x, L_y and L_z factored by 0.5, 1 or 2). It was found that the results of mean velocity and turbulent stresses within or immediately above the canopy were insensitive to the precise inflow length scales.

The prescribed mean velocity and Reynolds stresses were obtained from the wind tunnel experiment reported in Castro et al. (2017) by assuming lateral homogeneity. Fig. 3.3a shows the prescribed mean velocity profile. Castro et al. (2017) fitted the profile in the usual log–law form $U = \frac{u^*}{\kappa} \ln\left(\frac{y-d}{y_0}\right)$ with $y_{01} = 1.8mm$, $d = 0$ and by assuming $\kappa = 0.41$. They also estimated that the friction velocity u^* is $0.067U_{ref}$ at $7h$ upstream of the array. This is consistent with the peak Reynolds shear stress measured at the same location.

3.4 Results

The turbulence and dispersion predictions produced using the inflow method were compared against LES predictions made using periodic boundary conditions at the inlet and outlet and the wind tunnel experiment data reported in Castro et al. (2017). The Reynolds numbers of the flows over the array were similar in all three cases.

A representative atmospheric boundary layer profile was generated in the experiment by a set of Irwin spires at the entry of the working section and an array of thin 2D plates (height $\sim 0.3h$) placed upstream of the cuboid array. As mentioned, the experimental and LES value of the upstream roughness length was $y_{01} = 1.8mm$ whereas the roughness length of the array of cuboid elements was $y_{02} = 5.6mm$ as in Castro et al. (2017). This meant that an IBL was created from the leading edge of the array which developed in the downstream direction.

The development of the IBL was captured by the simulation made using the turbulence inflow generation method with prescribed turbulence statistics (§ 3.3.3), but was not by the simulation based on using periodic boundary conditions (PBC) at the inlet and outlet. This was because the PBC simulation effectively modelled the array as a single repeated unit of an infinite domain. One might therefore expect the inflow boundary condition (IBC) simulation to give a more accurate prediction of flow characteristics measured in the experiment, not only within the IBL but also above it when compared to the PBC simulations.

3.4.1 Flow and turbulence

For a simulation to accurately predict the dispersion of a pollutant it must accurately predict the turbulence statistics of the flow. This was assessed by examining the mean velocity and second–order statistics in the middle of the short streets (e.g. position P of Fig. 3.1) normalized by the reference velocity.

For the IBC case the results were averaged at the four locations equivalent to point P in Fig. 3.1 after the seventh row of cuboids at $x = 15h$. Whereas the PBC results produced by Castro et al. (2017) were averaged over all equivalent locations within the array. The experimental data were averaged in time over 3 minutes, but not in space. The wind tunnel errors were assumed to be 2% for $\overline{U}$, 10% for $\overline{u'u'}$ and 5% for $\overline{v'v'}$ and $\overline{w'w'}$, respectively.

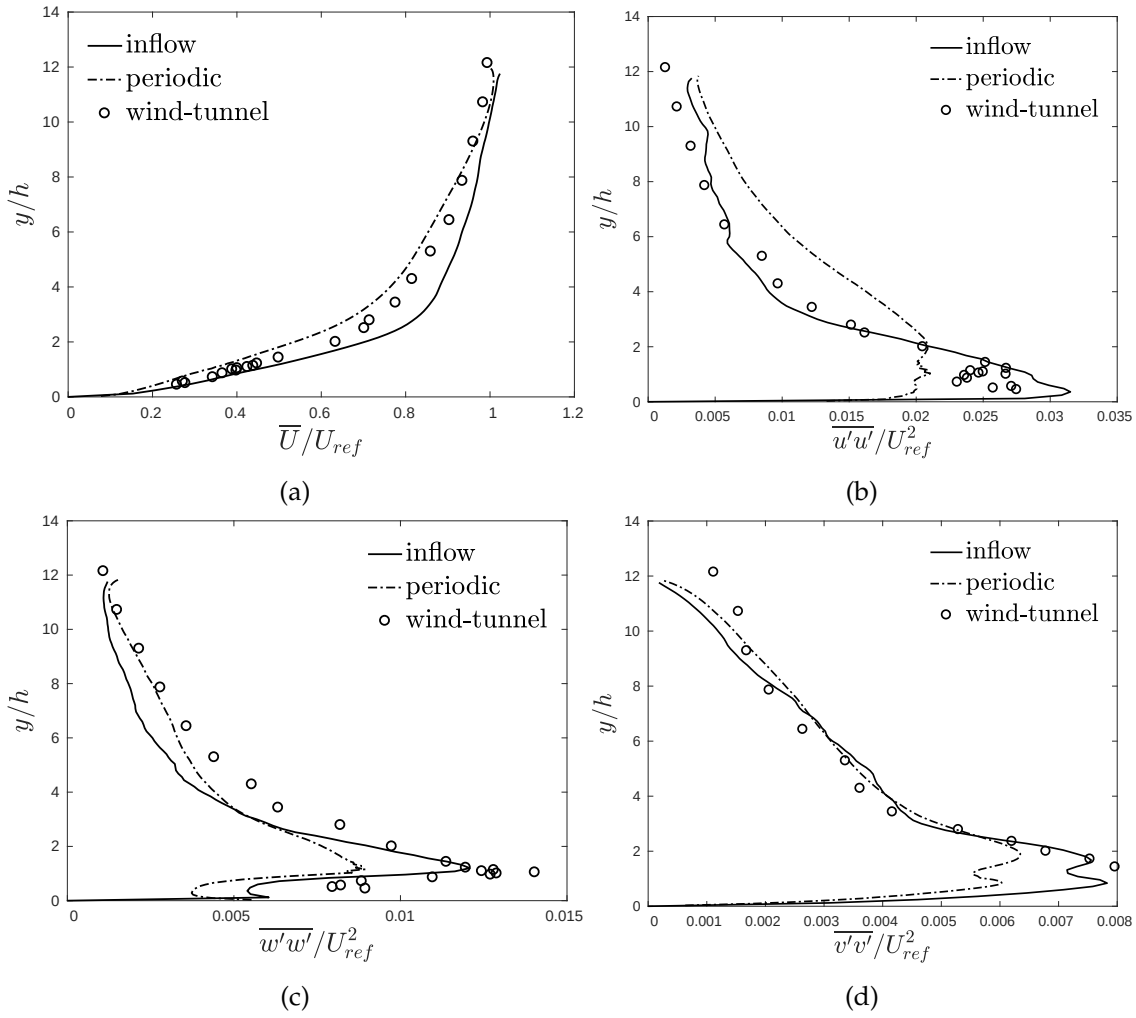

Figure 3.4: (a) IBC and wind tunnel mean velocity profiles measured at $x = 15h$ and spanwise averaged for position P in Fig. 3.1. Periodic mean velocity values were averaged at all similar points across the array. Corresponding profiles of streamwise normal stress (b), lateral normal stress (c) and vertical normal stress (d).

The IBC predictions for mean velocity (Fig. 3.4a) were found to be in good agreement with the experimental data below the canopy and up to $y = 2h$. Above that height, the IBC results slightly over–predicted while the PBC under–predicted the mean velocity. Fig. 3.4b shows that the streamwise Reynolds stress was predicted more accurately by the IBC simulation than the PBC. The peak stress occurred at the canopy height and was successfully captured by the IBC. The Reynolds stress profile above the canopy was also well predicted. The PBC simulation under-predicted the peak streamwise stress at the canopy height, and

over–predicted the streamwise stress for $y/h > 3$. The lateral Reynolds stress, $\overline{w'w'}$, was well predicted by the IBC below and immediately above the canopy as shown in Fig. 3.4c, but at greater heights it under-predicted the stress compared to the wind tunnel data. The vertical stress (shown in Fig. 3.4d) was well predicted by both IBC and PBC simulations. Nevertheless, the inflow method gave more accurate results immediately above the canopy height. Close to the top of the domain, both LES computations underestimated the vertical stress because the vertical velocity gradient was fixed to zero by the symmetric boundary condition.

The results show that imposing inflow turbulence using IBC captured the transition from a rough to a very rough wall and led to predicted Reynolds stresses that were in better agreement with experimental results below and immediately above the canopy than those obtained from the PBC approach. This confirmed that the IBC method provided a better approach to predicting the characteristics of the flow below and immediately above the canopy.

3.4.2 Growth of the internal boundary layer

The transition from the relatively smooth surface ahead of the array to the much higher roughness of the array itself causes an IBL to develop from the leading edge of the obstacles. The IBL increases in depth as it develops downstream through the array and the flow within it is characterised by having greater turbulent kinetic energy (TKE) than that in the external boundary layer above it. As TKE is the primary driver of dispersion, it is expected that the location of the interface between the internal and external boundary layers will have an important influence on the dispersion of material from a source within the array.

Three methods were used to determine the interface between the internal and external boundary layers along the length of the array in the IBC simulation. Method I was that developed by Antonia and Luxton (1972). Fig. 3.5 shows the result of applying method I using normalized velocity profiles obtained by averaging over 48 lateral positions, for nine streamwise locations (a vertical offset is imposed for ease interpretation). The regions related to the internal and external boundary layers were then linearly fitted to a residual error of less than 2%.

The first velocity profile was taken at $x = -2.5h$ ($3h$ upstream of the leading edge LE of the array in Fig. 3.1) where the mean velocity profile approaching the urban array is shown. There is no IBL at that point, and the profile shows no vertical discontinuity. At the second location, at $x = 2h$ ($1.5h$ downstream of the leading edge) the profile is distinctly different and has two linear fits, whose intersection identifies the edge of the IBL ($x = 2h$, $y = 1.8h$). Following the same approach, the edge of the IBL can be identified for a further 7 downstream locations and the evolution of the interface derived.

Method II was that developed by Efros and Krogstad (2011) based on plotting the streamwise Reynolds stress component normalized by the friction velocity u^*, i.e. $\overline{u'u'}^+$, against the height normalized by the domain height H. Method II was applied by calculating the

streamwise stress profile at the same x-locations and averaged over 48 lateral positions as previously. The profiles within the external and IBL were then linearly fitted to a residual error less than 5%. The edge of the IBL was again found at each location and its growth with downstream distance is shown in due course.

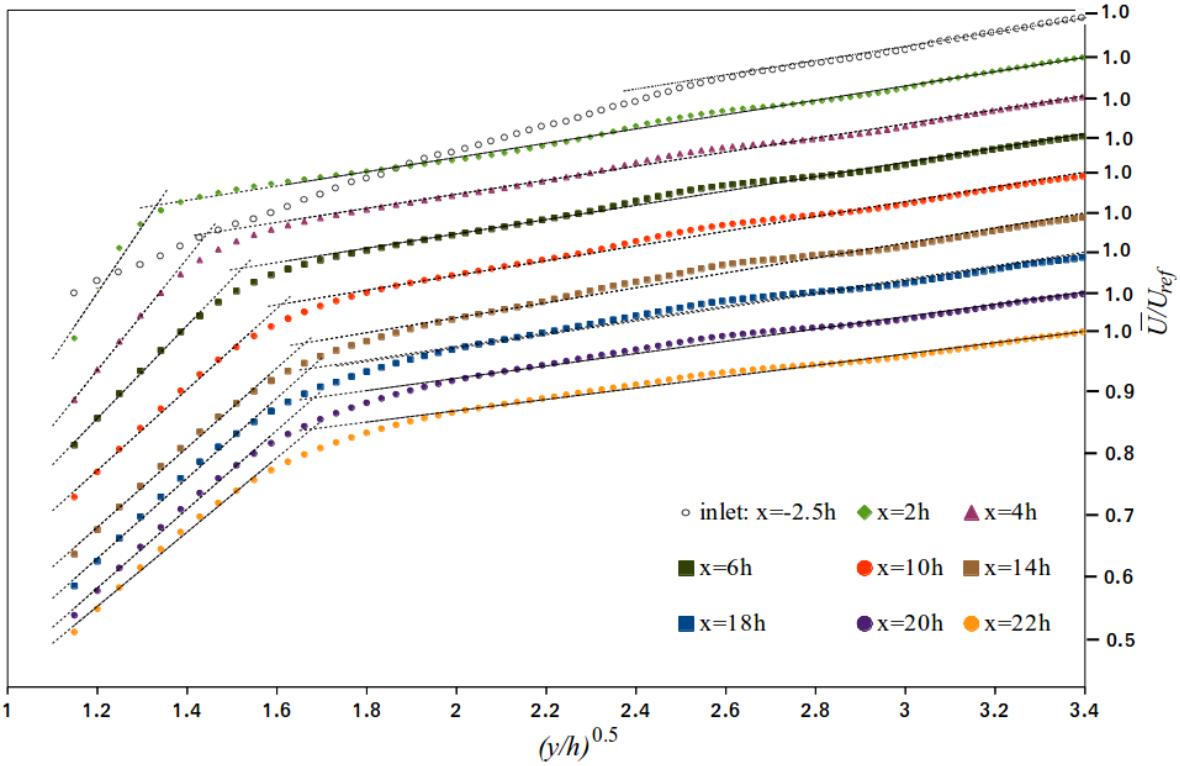

Figure 3.5: Laterally averaged mean velocity profiles in 9 streamwise locations: 1 upstream and 8 downstream of the leading edge (LE). The velocity profiles are shifted upwards to facilitate interpretation.

This study tests a method based on the wall–normal turbulent variance $\overline{v'v'}$, referred to as method III. Fig. 3.6 shows the vertical Reynolds stress profiles normalized by the friction velocity u^*, i.e. $\overline{v'v'}^+$, plotted against the height normalised by the domain height H, in a similar way to applying methods I and II. The Reynolds stress profiles for the external and IBL regions were linearly fitted to a residual error of less than 1%.

Fig. 3.7 shows the result of fitting the IBL depth data derived from the three methods to the Elliott (1958) power–law formula (Eq. 1.4). The residual error of the power–law fit for method I ($\overline{U}$) was less than 3% with exponent $P = 0.18$ and coefficient $a = 13.59$:

$$\frac{\delta_{IBL}}{y_{02}} = 13.59 \left(\frac{X}{y_{02}} \right)^{0.18}, \tag{3.7}$$

The residual error of the power–law fit for method II ($\overline{u'u'}$) was less than 6% with exponent $P = 0.22$ and coefficient $a = 12.42$:

$$\frac{\delta_{IBL}}{y_{02}} = 12.42 \left(\frac{X}{y_{02}} \right)^{0.22}. \tag{3.8}$$

Lastly, the residual error of the power–law fit for method III ($\overline{v'v'}$) was less than 2.5% with exponent $P = 0.21$ and coefficient $a = 12.71$:

$$\frac{\delta_{IBL}}{y_{02}} = 12.71 \left(\frac{X}{y_{02}} \right)^{0.21}. \tag{3.9}$$

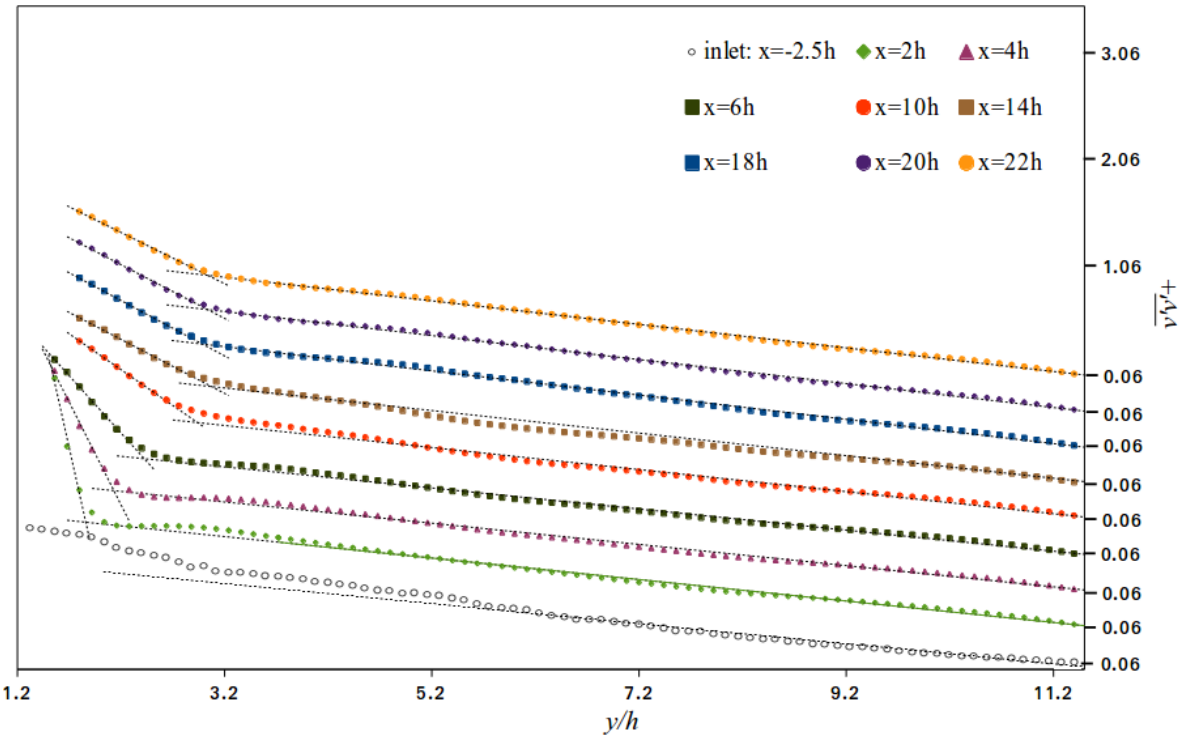

Figure 3.6: Laterally averaged vertical Reynolds stress profiles at 9 streamwise locations: 1 upstream and 8 downstream of the leading edge (LE). The stress profiles are shifted downwards to facilitate interpretation.

The fitted results (Eqs.3.7–3.9) from the three methods all confirmed that near the step change in roughness ($X/y_{02} < 300$) the exponent P of the power–law formula is much lower than the value $P = 0.8$ found in literature for $X/y_{02} > 1000$. Moreover, the estimated coefficient a is much higher than the range of values suggested by Elliott (1958). This is perhaps not surprising as the fitted results are dependent on the details of step change in roughness and the characteristics of the roughness elements.

The fitted results from the three methods are consistent. Of the three methods analysed here, the IBL heights derived from method III were fitted to the power–law formula with the lowest residual error. The coefficient $a = 12.71$ is not significantly different from $a = 10.56$ obtained in Cheng and Castro (2002), which studied the height of an internal boundary layer over an array of two-dimensional rib-type roughness elements at a range $X/y_{02} < 1000$. Nevertheless, the exponent $P = 0.21$ was significantly different from that $P = 0.33$ found by Cheng and Castro (2002). Again, this is owing to the difference of the roughness elements between the current study and Cheng and Castro (2002). We speculate that the

two-dimensional rib-type elements used in Cheng and Castro (2002) may yield a steeper IBL than that by using the three-dimensional cuboid type elements in the current study.

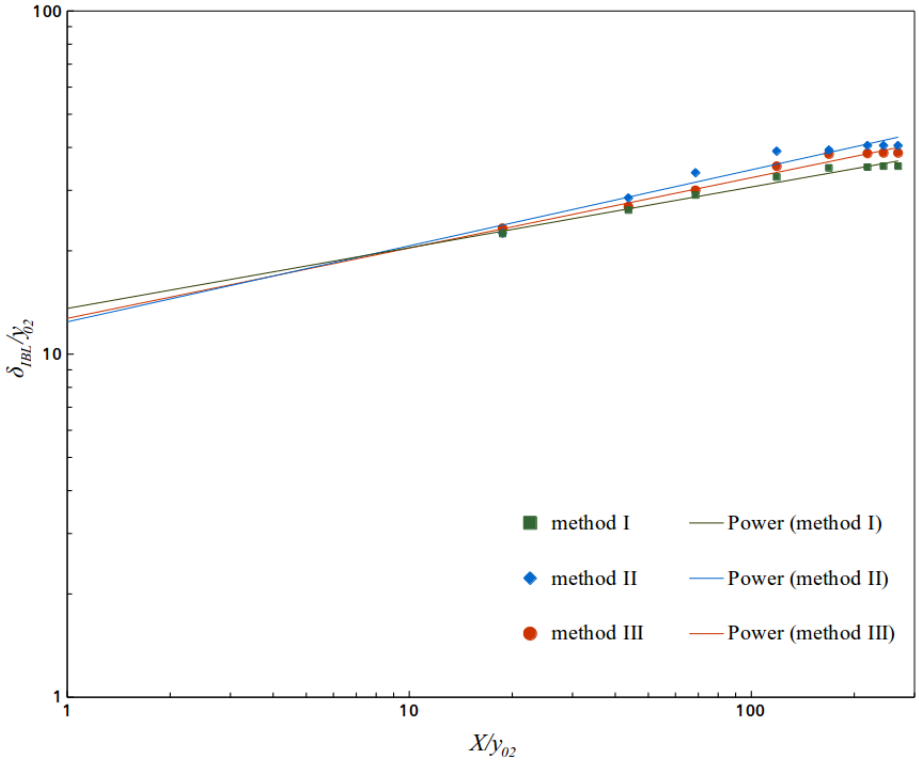

Figure 3.7: IBL depth δ_{IBL} derived by using the mean velocity $\overline{U}$ (method I, square green), the streamwise stress $\overline{u'u'}$ (method II, diamond blue) and the vertical stress $\overline{v'v'}$ (method III, circle red). These data fit to power–law profiles with lines respectively.

3.4.3 Point source dispersion

The point source dispersion was simulated by a source placed at point S in Fig. 3.1 at $x = 14h$ and $y = -1.5h$. Although the source size and location were similar in the experiment and LES simulations, the source shape was substantially simplified in the LES.

The mean scalar concentration $\overline{C}$ was normalized as follows:

$$\overline{C^*} = \overline{C}\frac{U_r L_{ref}^2}{Q} \tag{3.10}$$

where the characteristic length L_{ref} was the building height h and Q was the emission rate. Because LES predictions with inlet–outlet periodic boundary conditions differed from the experimental wind profile and turbulence statistics above $y \sim 3h$ (Castro et al., 2017), the mean velocity at $y = 3h$ and $x = -2.5h$ was chosen here as the reference velocity U_r. Similarly, the scalar variance $\overline{c'c'}$ was normalized as:

$$\overline{c'c'^*} = \overline{c'c'}\left[\frac{U_r L_{ref}^2}{Q}\right]^2. \tag{3.11}$$

Coceal et al. (2014) defined the near–field as being within a distance of $2 \sim 3h$ from the source. Within the near–field the results are likely to be affected by the source shape, size and location, but in the far–field ($> 3h$) turbulent mixing would be expected to show little memory of the source characteristics and the results are expected to be insensitive to the shape of the source.

The IBC LES concentration data were compared against the PBC LES and wind tunnel experiment data reported in Fuka et al. (2018). The first comparison was of data taken in the near-field along a lateral line at $x = 16h$ and $y = 0.5h$. For both sets of LES data the averaging process was long enough (180 flow–passes) to give fully converged results. The results for the dimensionless mean concentration and scalar variance are shown in Fig. 3.8a and Fig. 3.8b respectively. The wind tunnel standard error for the mean concentration $\overline{C}$ was 2%.

Both PBC and IBC results for mean concentration in the near–field (Fig. 3.8a) showed two non-symmetric peaks located in alignment with the corners of the upwind obstacle. Recalling that the source was located in the centre of the long 'street' (position $z = -1.5h$), the IBC highest peak was located on the right side of the source and the PBC highest peak on the left (when looking downwind). In contrast, the experimental data showed a peak on the right side of the source at $z = 0h$.

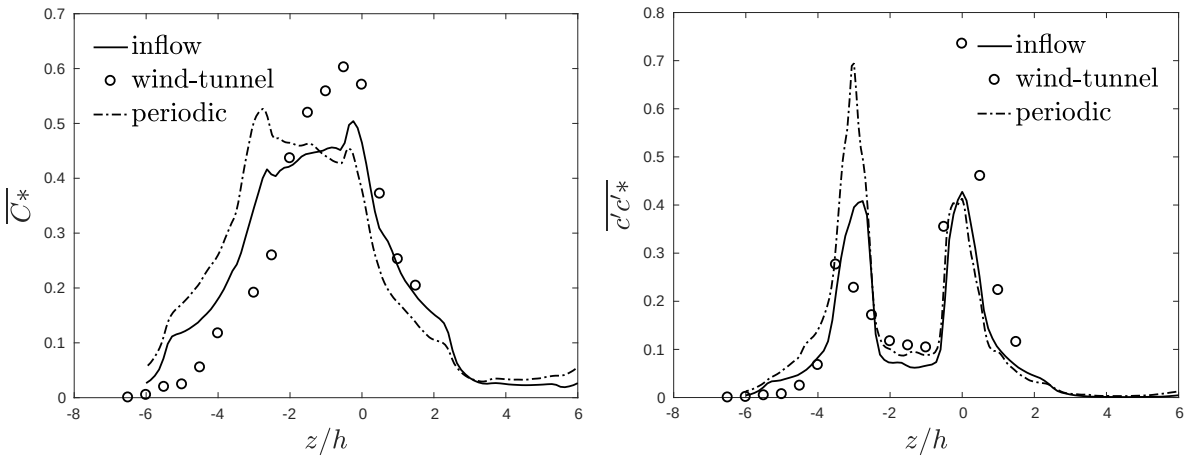

(a) (b)

Figure 3.8: (a) Inflow, periodic and wind tunnel normalized mean concentration values measured at $x = 16h$ and $y = 0.5h$, resulting from a source at $x = 14h$ and $z = -1.5h$. (b) Normalized mean scalar variance measured at $x = 16h$ and $y = 0.5h$.

The flow around the obstacle downwind of the source determines how the scalar plume divides into the left and/or right channels. In the experiment and the IBC case the plume was found to be mainly transported down the right-hand street, rather than the left. The

asymmetry in the experimental results was suspected to be due to imperfect alignment of the array and/or a small effective offset in the flow direction. The wind tunnel alignment error is expected to be of the order of 0.25° (Fuka et al., 2018).

The PBC LES simulation had periodic boundary conditions applied to the lateral sides of the domain, so symmetric results might be expected in the spanwise direction. That the results were found to be asymmetric was perhaps due to strong 3-dimensional anisotropic turbulence leading to non-zero spanwise velocity on the lateral boundaries.

Whether the peaks matched on either the right or left side close to the source was considered to be arbitrary, and of little importance to the results of any far–field analysis. The near-field LES and wind tunnel results were both sensitive to the local flow details at the 0° wind direction. Except for the peak alignment discrepancies discussed above, the LES with IBC simulation captured the lateral size of the plume and scalar peak mean values well.

Numerical predictions and measurements of the spanwise scalar variance at a height of $y = 0.5h$ and distance $x = 16h$ are compared in Fig. 3.8b. The experimental results again show a higher peak to the right of the source position, indicating that the plume drifted to the right, whereas the LES with PBC results show a higher peak to the left of the source. The LES with IBC shows two peaks which are almost symmetric about the source position. These results are consistent with those discussed above. As no standard error data are available for the experimental scalar variance measurements no further conclusions can be drawn.

Fig. 3.9a and Fig. 3.9b show a comparison of the spanwise variation in mean concentration and variance data above the canopy at $y = 2h$ and $x = 16h$. In this case some of the wind tunnel sampling stations might approach or cross the edge of the plume. If this was so, fluctuations in concentration and intermittency would make accurate agreement between modelling and experiment difficult to achieve. Fig. 3.9a also shows that the mean concentration profiles are not in a Gaussian shape. Nevertheless, the IBC results were found to be in fair agreement with the wind tunnel measurements, with both the magnitude and the lateral size of the plume being well predicted.

Although the alignment of both the IBC and experimental plumes on the same side is considered to be fortuitous, the higher peak is well captured and the lower peak only slightly underestimated. The double peak of the measured variance was also fairly well predicted by the IBC method. The PBC results were also in fair agreement with the wind tunnel measurements in terms of magnitude and the lateral size of the plume. In contrast to the experimental and IBC LES results, the PBC LES results show almost symmetric double peaks for the mean concentration, although there is more asymmetry in the variance. The IBC results were qualitatively closer to the experimental data than the PBC ones.

From the results above, it appears that based on the array geometry and locations examined, the IBC method leads to a superior prediction of scalar dispersion than the PBC one, in that it captures the asymmetry observed. This is believed to result from the better agreement between measurements of Reynolds stresses and IBC predictions immediately above the canopy § 3.4.1.

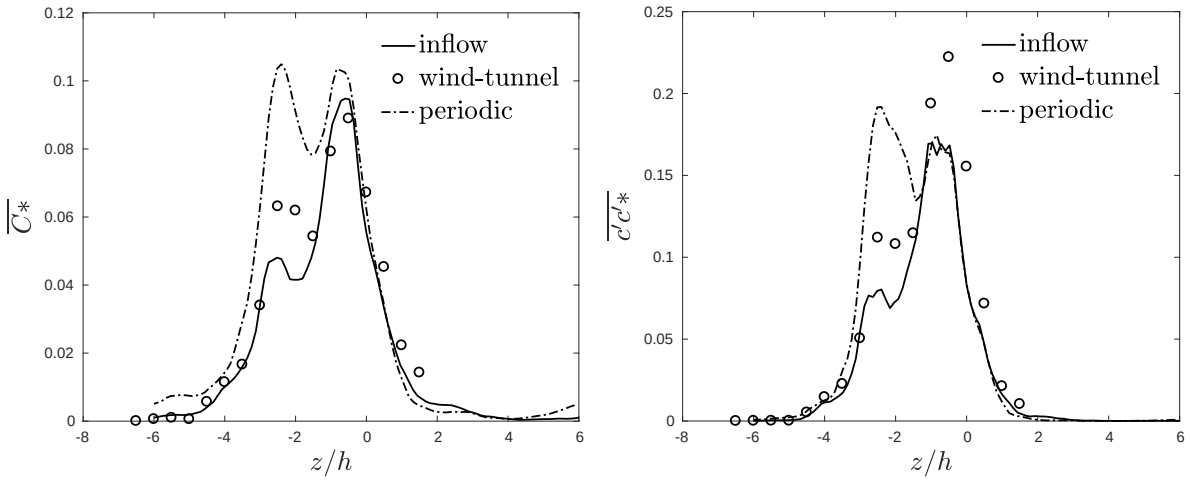

(a) (b)

Figure 3.9: (a) Inflow, periodic and wind tunnel normalized mean concentration data measured above the canopy at $x = 16h$ and $y = 2h$, for a source at $x = 14h$ and $z = -1.5h$. (b) Normalized mean scalar variance measured at $x = 16h$ and $y = 2h$.

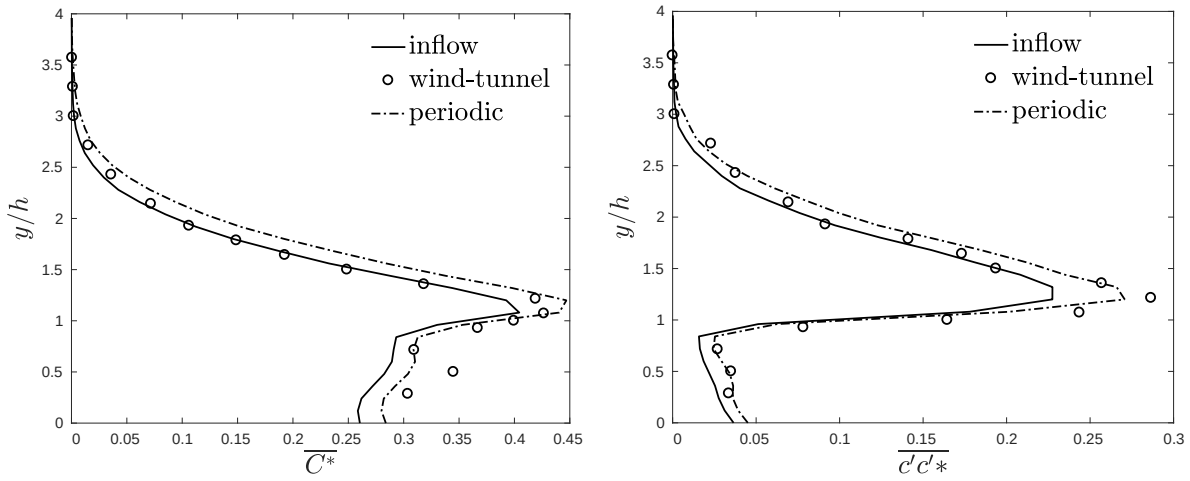

(a) (b)

Figure 3.10: (a) Inflow, periodic and wind tunnel normalized mean concentration measured at $x = 18h$ and $z = -1.5h$, resulting from source at $x = 14h$ and $z = -1.5h$. (b) Normalized mean scalar variance measured at $x = 18h$ and $z = -1.5h$.

Further comparisons were made between simulations and measurements of mean concentration and variance along a vertical line at $x = 18h$, $z = -1.5h$ (Fig. 3.10a and Fig. 3.10b). Examination of Fig. 3.10a shows that both LES IBC and PBC predictions for mean concentration and concentration variance are in fair agreement with the experimental results below $y = 1.5h$. However, the IBC predictions are consistently better than the PBC ones above $y = 1.5h$. Given the differences observed in the near-field, the similarity between these IBC and PBC far–field results confirms that beyond two rows downstream of the source, the effect of the difference in size and shape of the source becomes negligible and one can expect

more accurate comparisons.

3.4.4 Interface effects on dispersion

The mechanisms that affect dispersion below and above the urban canopy depend on the position of the source. For example, if the source is placed in the wake of an obstacle in a recirculation zone, the plume is effectively transported upwards either by the mean flow or by the turbulent Reynolds stresses (Fuka et al., 2018; Tomas et al., 2017; Brixey et al., 2009). The dimensionless vertical flux components were defined in Fuka et al. (2018) as follows:

$$\psi_{adv}^{v*} = \overline{V}\,\overline{C}\frac{h^2}{Q} \tag{3.12}$$

$$\psi_{turb}^{v*} = \overline{v'c'^*} = (\overline{VC} - \overline{V}\,\overline{C})\frac{h^2}{Q} \tag{3.13}$$

where v' and c' are the vertical velocity fluctuation and the scalar fluctuation respectively and $\overline{V}$ is the mean vertical velocity. It is these fluxes, the advective vertical concentration flux (Eq. 3.12) and the turbulent vertical concentration flux (Eq. 3.13), that determine the exchange of pollutants between the canopy flow and the boundary layer above.

In the wakes of obstacles the mean vertical velocity and the vertical velocity fluctuation are not negligible, and both flux components contribute to the upwards transport of the scalar. Above the canopy the mean vertical velocity decreases significantly because the flow is predominantly parallel to the array canopy, nevertheless, the vertical fluctuation component may still remain significant. This means though that the vertical turbulent concentration flux may contribute more than the advective flux to the upwards transport of the plume above the canopy and close to the IBL interface.

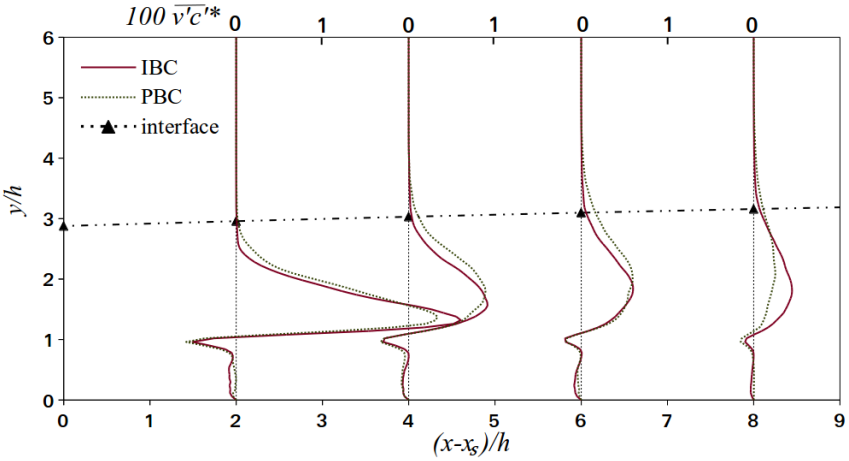

Figure 3.11: Turbulent vertical flux $\overline{v'c'^*}$ profiles scaled by 100 at four locations downstream of the source position ($x_s = 14h$ and $z_s = -1.5h$, Fig. 3.1). The black dashed line shows the IBL interface over the block array.

In Fig. 3.11, the vertical turbulent flux profile $\overline{v'c'^*}$ (Eq. 3.13) calculated by using LES IBC and LES PBC predictions is shown at four streamwise locations downstream of the source. The black dashed line represents the interface of the IBL as calculated in § 3.4.2 using method III. The vertical profiles in Fig. 3.11 suggest that the edge of the plume grew from the source and matched the interface after 2 rows of cuboids, as further downstream both the interface and the edge of the plume were found to be approximately at the same elevation.

The IBC turbulent flux profiles at all the x–locations analysed decayed sharply when approaching the IBL interface. Looking at the flux profiles at $(x - x_s) = 2h$, a much sharper decay is observed in the IBC profile as the interface is approached than in the PBC one. Similarly, at positions $(x - x_s) = 4h$ and $(x - x_s) = 6h$ the IBC flux profiles decay more rapidly than the PBC profiles when approaching the IBL interface. However, at position $(x - x_s) = 8h$, the IBC vertical flux was observed to be higher than the PBC flux below the interface, but lower above it. This trend shows that vertical transport of the scalar between the internal and external boundary layers is being constrained by the interface. Moreover, because the IBL interface is defined using method III, the distinct changes in vertical flux profile appear related to similar changes in the vertical Reynolds stress $\overline{v'v'}$ noted in § 3.4.2.

Dispersion from a ground–level point source is a $3D$ problem. In order to understand whether vertical constraint by the IBL interface enhanced the lateral spreading of the plume, the lateral turbulent fluxes were also analysed. The turbulent component of the lateral concentration flux was defined as follows:

$$\psi^{w*}_{turb} = \overline{w'c'^*} = (\overline{WC} - \overline{W}\,\overline{C})\frac{h^2}{Q} \tag{3.14}$$

where w' and c' are the lateral velocity fluctuations and scalar fluctuations respectively, and $\overline{W}$ is the mean lateral velocity. The lateral turbulent flux regulates the diffusion of the plume in positive or negative spanwise directions and determines the lateral extent of the plume.

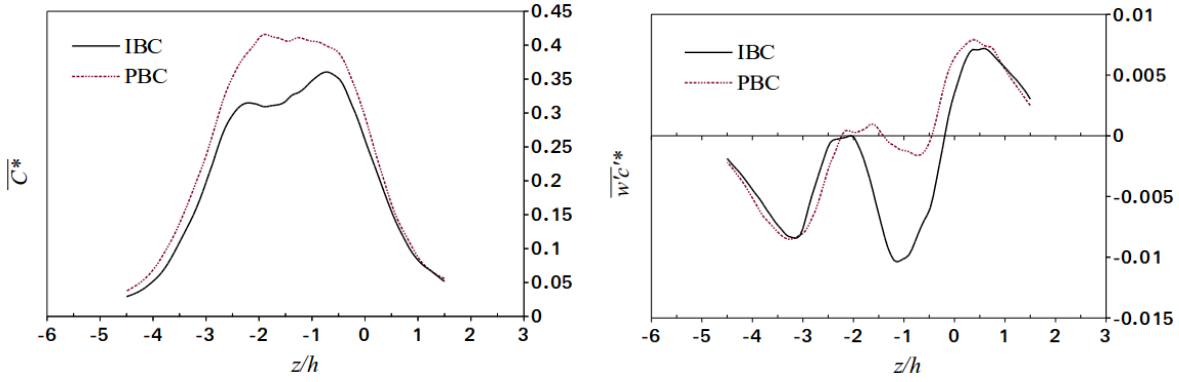

(a) (b)

Figure 3.12: (a) Spanwise normalized mean concentration predictions at $x = 18h$ and $y = 1.5h$. (b) Spanwise normalized lateral flux predictions at $x = 18h$ and $y = 1.5h$, resulting from a ground level source at $x = 14h$ and $z = -1.5h$.

Fig. 3.12a and 3.12b show the LES IBC and PBC mean concentration and lateral flux predic-

tions at $x = 18h$ (i.e. two rows downstream from the source) and $y = 1.5h$ in the spanwise direction. The spanwise location of the source is $z = -1.5h$, and the mean concentration is normalized as in Eq. 3.10.

In common with the results at $x = 16h$ and $y = 2h$ shown in Fig. 3.9a, the IBC mean concentration in Fig. 3.12a shows a higher peak located to the right of the source ($z = -0.5h$) and a lower peak on the left ($z = -2.5h$). Whereas the PBC mean concentration shows one symmetric peak close to the source's position. The double peak in the IBC mean concentration means that there are two zero–crossings of the IBC lateral flux (Fig. 3.12b). Between $z = -2.5h$ and $z = -0.5h$, the magnitude of the IBC lateral flux is much greater than that of the PBC flux. Outside of this range, the fluxes are very close in magnitude.

We fitted the mean concentration profiles to Gaussian distributions, and found that the width of the Gaussian profile for the IBC plume was slightly greater than that of the PBC. This is interesting given the greater lateral flux of the IBC. Fig. 3.4a shows that the mean streamwise velocity immediately above the canopy in the IBC simulation and the experiment are greater than that of the PBC, which yields a shorter convection time for the plume to develop. This might explain why the plume width above the canopy of the IBC is only slightly greater than that of the PBC.

Following the same approach, the mean concentration and the lateral turbulent flux were analysed at $x = 20h$ (three rows downstream) and $y = 1.5h$ over the spanwise direction (Fig. 3.13a and 3.13b, respectively). The peak PBC mean concentration in Fig. 3.13a is again greater than that of the IBC. The magnitude of IBC lateral flux in Fig. 3.13b is also again greater than the PBC flux near the core of the plume, and the width of the IBC plume was again found to be greater than that of the PBC. These findings are all consistent with those in Figs. 3.12a and 3.12b.

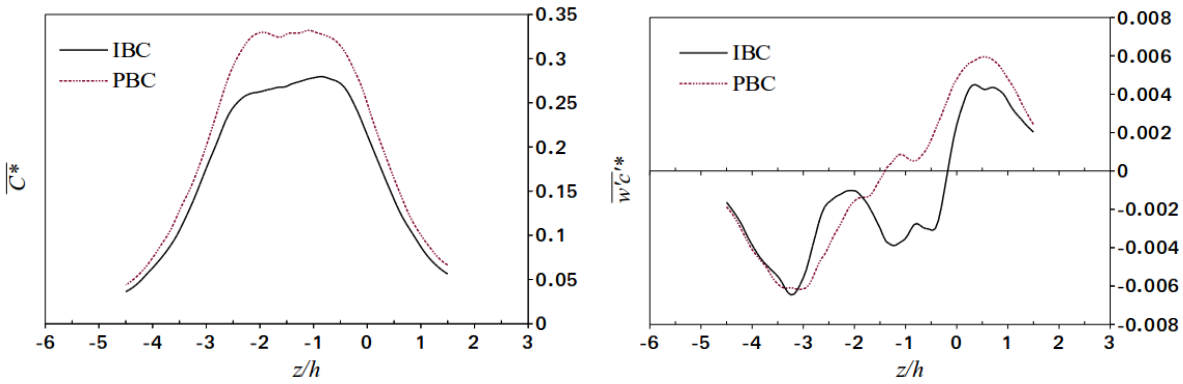

(a) (b)

Figure 3.13: (a) Normalized mean concentration prediction at $x = 20h$ and $y = 1.5h$. (b) Inflow and periodic normalized lateral flux predictions at $x = 20h$ and $y = 1.5h$, resulting from a source at $x = 14h$ and $z = -1.5h$.

The mean concentration and lateral turbulent flux profiles in Fig. 3.13a and Fig. 3.13b suggest that the lateral spread of the IBC plume is greater than that of the PBC plume. This is

consistent with the greater lateral Reynolds stresses observed in the IBC profile than in the PBC profile at $y = 1.5h$ shown in Fig. 3.4c.

In the IBC simulations vertical transport of the scalar between the internal and external boundary layers is constrained by the lower TKE above the interface. The vertical constraint on the vertical Reynolds stress and the enhancement of the lateral Reynolds stress lead to increased lateral spreading of the IBC plume. This results in the lower mean concentrations observed in the IBC simulation than in the PBC one in Fig. 3.12a and 3.13a.

Finally, in order to determine the position of the edge of the plume compared to the IBL interface, vertical profiles of the dimensionless mean concentration were taken downstream of the source in several streamwise locations at $z = -1.5h$ (Fig. 3.14). The results of both PBC and IBC simulations were normalized as in Eq. 3.10 and compared. The origin of the coordinate system was fixed at the source position.

As far as we are aware, there is no generally accepted definition of the plume's edge. Therefore, the edge of the plume was identified here by fitting with a power–law formula the 3% values of local–peak mean concentrations measured at the canopy height. The aim here was to evaluate whether or not the predicted development of the plume when using the IBC method differed from that using the PBC. Hence, the choice of the percentage at which to define the plume edge was not critical. Nevertheless, sensitivity tests made using 1%, 5% and 10% values of the local concentration peak all showed similar plume growth rates.

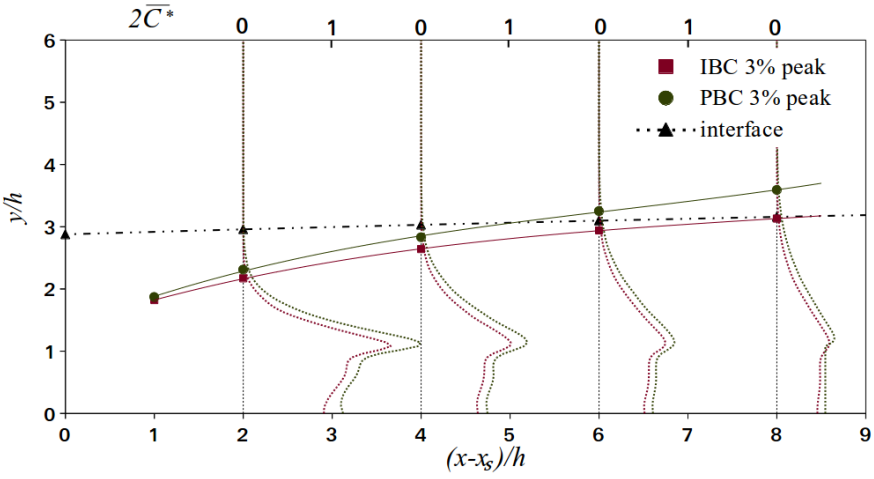

Figure 3.14: Dimensionless scalar concentration $\overline{C}^*$ scaled by 2 in four locations downstream of the source position ($x_s = 14h$, $z_s = -1.5h$, Fig. 3.1). The black dashed line shows the IBL interface. The plume edge is taken as 3% of the local peak in both LES simulations.

The development of the plume when using IBC was found to be visibly different from the one by using PBC. This is shown in Fig. 3.14, in which the plume edge in the IBC simulation appears to asymptote to the IBL interface. Whereas when inlet–outlet PBC are used, the roughness boundary layer grows indefinitely up to the top of the domain which allows the plume to continue to expand vertically. This is a result of the interface between the internal

and external boundary layers only existing when the inflow method is applied. Within the simulated LES domain, the plume development appears to be influenced by the IBL interface location which leads to trapping of the scalar in the IBL and greater lateral spreading.

3.5 Conclusions and discussion

LES with prescribed IBC was used to simulate a rural–to–urban transition region where the change in surface roughness generates an IBL at the leading edge of a regular array of cuboid elements. The LES with IBC was found to provide an accurate simulation of the flow which predicted the TKE to be greater below the interface of the IBL when compared to the TKE obtained from LES with inlet–outlet PBC.

To our best knowledge the growth rate of the IBL depth has been evaluated for the first time by analysing the vertical Reynolds stress profiles in several streamwise positions. The vertical Reynolds stress method was found to define the IBL interface more clearly than existing methods based on mean streamwise velocity and streamwise Reynolds stress. It was further found that the IBL growth rate derived from the vertical stress method followed the power–law formula with a similar coefficient a as that derived by Cheng and Castro (2002) in the near roughness transition region ($X/y_{02} < 1000$), but with a significantly lower exponent $P = 0.21$ compared to $P = 0.33$ derived by Cheng and Castro (2002). We speculate this is owing to the difference of characteristics of the roughness elements within a range $X/y_{02} < 1000$.

LES predictions of turbulence and dispersion from a ground–level point source were compared against wind tunnel measurements reported in Castro et al. (2017) and Fuka et al. (2018). The impact of the interface between the internal and external boundary layers on dispersion was then analysed by studying vertical and lateral profiles of dimensionless mean concentration and turbulent fluxes downstream of the source. The IBC vertical scalar turbulent flux profiles decayed more rapidly than the PBC profiles when approaching the IBL interface. We speculate that the distinct changes in IBC vertical flux profiles appear related to similar changes in the vertical Reynolds stress. Furthermore, the lateral spreading of the IBC plume was found to be greater than that of the PBC plume, this was found to be correlated with greater values of lateral turbulent Reynolds stress. These features led to the plume's upper edge in the IBC simulation differing distinctly from that obtained by using inlet–outlet PBC. It is concluded that the presence of the IBL constrains vertical spreading, and so leads to trapping of the scalar. The development of the interface between the internal and external boundary layers will also be affected by thermal stratification conditions, and further work should seek to quantify this.

4 Thermal stratification effects on turbulence and dispersion. *Sessa, Xie & Herring, 2019. Boundary Layer Meteorology, accepted*

A synthetic turbulence and temperature fluctuation generation method embedded in Large–Eddy Simulations (LES) was developed to investigate the effects of weakly stable stratification (i.e. with the Richardson number $Ri \leq 1$) on turbulence and dispersion following a rural–to–urban transition region. The work was based on firstly validating predictions of mean velocity, turbulent stresses and point–source dispersion against wind tunnel experiments of a stable boundary layer approaching a regular array of uniform cuboid elements at $Ri = 0.21$. The depth of the internal boundary layer (IBL) formed at the leading edge of the uniform array was determined using the method which we have previously proposed. Vertical profiles of wall–normal turbulent stress showed that the height and the growth rate of the IBL were sensitive to the thermal stability prescribed at the inlet. We found that the IBL height was reduced when the inflow turbulent kinetic energy (TKE) was reduced while maintaining the same stratification condition. Lastly, scalar fluxes and mean concentrations within and above the canopy from a ground–level line source were simulated and analysed. It was found that increasing the stable stratification level reduced the vertical transport of pollutant which increased the volume–averaged concentration within the canopy. For a given level of stable stratification, the effect on the total scalar fluxes within and above the canopy, and on the volume-averaged mean concentration within the lateral streets is more pronounced when the TKE is reduced.

4.1 Introduction

The effects of stable stratification on turbulence and dispersion are not negligible even under weakly stable conditions (e.g. Xie, Hayden, and Wood, 2013; Boppana, Xie, and Castro, 2014). The consumption of buoyancy energy in such conditions damps turbulence which affects ventilation and the concentration of pollutants at pedestrian level. When Cheng and Liu (2011) investigated stability effects at bulk Richardson numbers of 0.18 and 0.35 on the dispersion in $2D$ street canyons using LES, it was found that for a Richardson number greater than 0.25, turbulence was strongly suppressed at ground level. This meant that the pollutant tended to reside longer at pedestrian level than in the upper street canyon. Tomas, Pourquie, and Jonker (2016) showed that for a bulk Richardson number of 0.147 the area–averaged street concentration of a line source was 17% higher than in neutral conditions due

to decreased streamwise advection and trapping of pollutant by the IBL. Similar conclusions were reached in the LES study conducted by Xie, Hayden, and Wood (2013), who found that the stability effects induced at a bulk Richardson number of 0.21 increased mean concentrations by up to an order of magnitude when compared to neutral conditions. Moreover, Xie, Hayden, and Wood (2013) also found that turbulent fluctuations and mean velocities were not substantially affected either by a change of mean temperature profile below the canopy or inlet temperature fluctuations for a given Richardson number.

As far as we are aware, very few studies have examined the effects of stable stratification on dispersion within an IBL, and those that have have only considered weakly stable conditions. In our study we considered the effects of various stratification conditions up to a Richardson number 1.0 on turbulence and dispersion following a rural–to–urban transition. The objective was to use LES to answer the following three questions:

1. To what extent are stratification effects on flow and dispersion following a step change in roughness length dependent on the inflow turbulence intensity?

2. To what extent does increasing stratification affect the IBL thickness for bulk Ri numbers below 1?

3. To what extent does increasing stratification affect the ventilation of pollutant within and above the canopy for bulk Ri numbers below 1?

The governing equations are briefly described in Sect. 4.2. Details of numerical settings including geometry, mesh and inflow conditions are given in Sect. 4.3. LES validation, sensitivity tests on the ground temperature and turbulent kinetic energy at inlet are reported in Sect. 4.4.1. Stratification effects on the internal boundary layer are discussed in Sect. 4.5. The analysis of scalar fluxes and mean concentration results are reported in Sect. 4.6. Finally, the conclusions are summarised in Sect. 4.7.

4.2 Governing equations

In LES the filtered continuity and momentum equations for a buoyancy–driven flow are written as follows:

$$\frac{\partial u_i}{\partial x_i} = 0 \tag{4.1}$$

$$\frac{\partial u_i}{\partial t} + \frac{\partial u_i u_j}{\partial x_j} = -\frac{1}{\rho}\frac{\partial p}{\partial x_i} + f\delta_{i2} + \frac{\partial}{\partial x_j}\left(\frac{\tau_{ij}}{\rho} + \nu\frac{\partial u_i}{\partial x_j}\right) \tag{4.2}$$

where the filtered velocity and pressure fields are u_i and p respectively, ν is the kinematic molecular viscosity and ρ is the density. τ_{ij} is the subgrid–scale (SGS) Reynolds stress which was determined by using the mixed time–scale subgrid eddy viscosity model (Inagaki, Kondoh, and Nagano, 2005). $f\delta_{i2}$ is the body force due to thermal buoyancy and is calculated by using the Boussinesq approximation.

The filtered transport equation for a passive scalar is:

$$\frac{\partial C}{\partial t} + \frac{\partial u_j C}{\partial x_j} = \frac{\partial}{\partial x_j}\left[(K + K_r)\frac{\partial C}{\partial x_j}\right] + S \tag{4.3}$$

where C is the filtered scalar concentration and S is a source term. The second term on the left–hand side is the advection term and the first term on the right–hand side is the diffusion term. K is the molecular diffusivity and K_r is the subgrid-scale (SGS) turbulent diffusivity computed as:

$$K_r = \frac{\nu_r}{Sc_r} \tag{4.4}$$

where ν_r is the SGS viscosity and Sc_r is the subgrid Schmidt number. A constant Schmidt number of $Sc_r = 0.7$ was assumed.

The filtered transport equation of temperature is:

$$\frac{\partial T}{\partial t} + \frac{\partial u_j T}{\partial x_j} = \frac{\partial}{\partial x_j}\left[(D + D_r)\frac{\partial T}{\partial x_j}\right] \tag{4.5}$$

where T is the resolved–scale temperature. D is the molecular diffusivity of temperature, D_r is the subgrid turbulent diffusivity and is given by ν_r / Pr_r, where Pr_r is the subgrid Prandtl number was set to 0.9.

4.3 Numerical settings

The LES model was implemented within the open-source CFD package OpenFOAM version 2.1.1. A second-order backward implicit scheme in time and second–order central difference scheme in space were applied for the discretisation of the terms in Eqs. 4.2, 4.3 and 4.5. The domain was set as a half channel. An efficient inflow turbulence generation method (Xie and Castro, 2008) was used at the inlet, with periodic conditions at the lateral boundaries and a stress–free condition at the top of the domain ($y = 12h$, where $h = 70mm$ was the uniform height of the array element). The Reynolds number based on h and the free stream velocity $u_{ref} = 1.35m/s$ at $y = 12h$ was approximately $8,000$. The average CFL number was 0.2, based on a time step resolution of $0.0007s$. Flow and second-order statistics were initialized for 20 flow-passes and then averaged over 150 flow–passes.

For the purpose of validating the baseline study, the numerical settings (e.g. the geometry of the array, the point source, the approaching boundary layer and the thermal stratification conditions) were made as consistent as possible with experiments conducted by, i.e. Castro et al. (2017), Hertwig et al. (2018), Marucci, Carpentieri, and Hayden (2018) and Marucci and Carpentieri (2018a). The wind tunnel experiments were conducted using the meteorological wind tunnel at the University of Surrey, UK, which has a test section $20m$ (length)$\times 3.5m$ (width)$\times 1.5m$ (height). The wind tunnel is able to generate a 'simulated' atmospheric boundary layer representative of stable and unstable conditions by using Irwin's spires, two-dimensional roughness elements and adjusting the inlet and floor temperature. Propane was used as a passive tracer and its concentration was measured by using

a fast flame ionisation detector system (FFID). Velocities were measured by using a two-component laser-Doppler anemometry (LDA). Mean temperature and its fluctuations were measured using a fast-response cold-wire probe (CW). More generic details can be found in the above references. The numerical settings applied to simulate the flow and point source dispersion in neutral conditions were consistent with those in Castro et al. (2017) and Hertwig et al. (2018), respectively. For the studies in stable conditions, the numerical settings applied to the flow and point source dispersion were consistent with those in Marucci, Carpentieri, and Hayden (2018) and Marucci and Carpentieri (2018a), respectively. More specific details are given in the following sections.

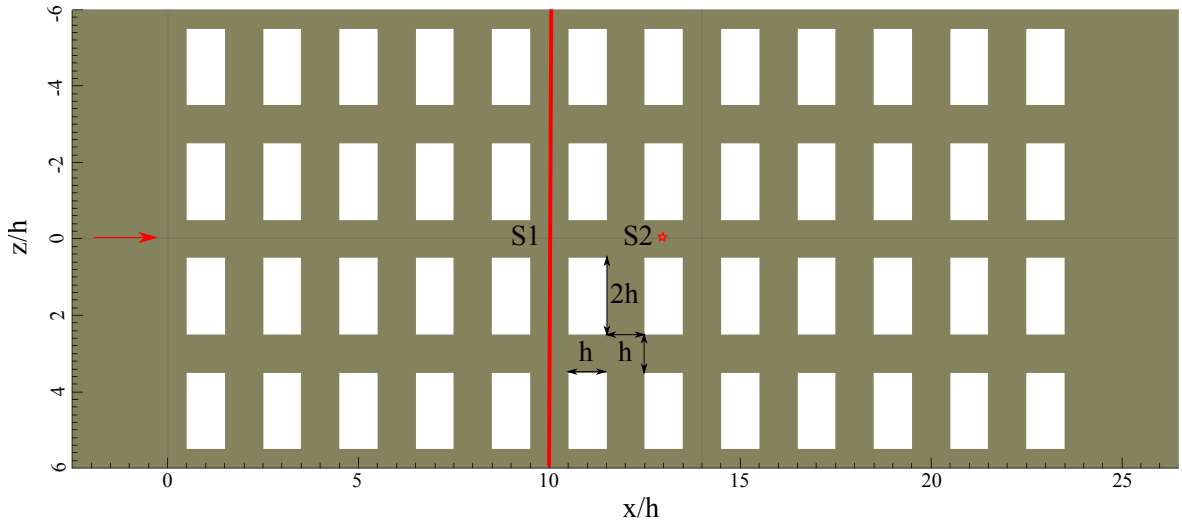

Figure 4.1: Plan view of the array configuration showing dimensions of buildings and streets, coordinate system, flow direction, and locations of line source $S1$ and point source $S2$.

4.3.1 Geometry, mesh and resolution

Again, the array of regular cuboid elements modelled in this paper represents part of a larger array used in the wind tunnel experiments of Castro et al. (2017) and Marucci and Carpentieri (2018a). This array was designed to simulate a neighbourhood scale region in which statistical homogeneities are assumed. The basic obstacle layout is identical to those described in Sessa, Xie, and Herring (2018) and in Fuka et al. (2018).

A plan view of the modelled array is shown in Fig. 4.1 where the street units parallel to the x axis are $1h$ long and referred to as 'short streets' hereinafter. Street units parallel to the z axis are $2h$ long and referred to as 'long streets'. The rectangular array comprised 48 aligned blocks with h spacing, which leads to a plan area density of $\lambda_p = 0.33$ when considering the single block unit.

The dimensions of the modelled domain were $31.5h \times 12h \times 12h$ within a uniform Cartesian grid of resolution $\triangle = h/16$. The top boundary was placed at $y = 12h$ to be very close to the experimental boundary layer height (Marucci and Carpentieri, 2018a). In order to

ensure the zero–gradient outflow boundary condition, the domain size was extended by $2.5h$ in x–direction compared to the domain used by Sessa, Xie, and Herring (2018) in Chap.3. Computations were made for the 0° wind direction by assuming that the mean wind flow was perpendicular to the front face of the cuboid elements as indicated in Fig. 4.1.

4.3.2 Scalar sources

A passive scalar was released from a ground–level point source ($S2$) and a ground–level line source ($S1$) within the array of cuboid elements. Because of the finite size of the grid, the shape of the point source only approximated the source used in the experiment. The shape and size of the point source was identical to that reported in Fuka et al. (2018). The diameter was represented by 4 cells and so measured $0.25h$, while the height was one cell ($h/16$). The point source was positioned in the middle of a short street within the seventh row of blocks (Fig. 4.1) in accordance with the experimental set–up of Marucci and Carpentieri (2020).

The line source was positioned on the ground between the fifth and sixth rows of blocks. The lateral extent of the line source was set equal to the entire width of the domain ($12h$) while the height and width of it were one cell ($h/16$) and four cells ($4h/16$) respectively. A constant scalar flux release rate was set for each cell inside the volume of both the point source and the line source.

4.3.3 Inlet conditions of temperature for LES

In order to analyse the effects of thermal stratification on flow and dispersion, LES simulations were conducted for various bulk Richardson numbers Ri, defined as:

$$Ri = \frac{gH(\overline{T}_{ref} - \overline{T}_0)}{\overline{T}_0 \overline{u}^2_{ref}} \tag{4.6}$$

where $\overline{u}_{ref}$ is the free-stream velocity at the inlet, g is the acceleration due to gravity, H is the domain height and $\overline{T}_0$ is the mean temperature on the ground. LES comparisons for increasing stable stratification were achieved in a similar manner to Boppana, Xie, and Castro (2013), by fixing $\overline{T}_{ref}$ and $\overline{T}_0$ and changing the value of g as shown in Tab. 4.1. The upstream boundary layer height was kept fixed at $H = 12h$ in the LES simulations for all values of Ri, as in the wind tunnel experiments of Marucci, Carpentieri, and Hayden (2018) in which the tendency towards reducing boundary layer height with increasing stability was overcome by the level of turbulence generated by the inlet spires.

The LES requires a continuous specification of turbulence in time at the inlet to simulate an evolving turbulent boundary layer. This was achieved by using the inflow turbulence method developed by Xie and Castro (2008) to generate a synthetic turbulent inflow with exponential–form correlations in time and space. This inflow method has been shown to provide a high fidelity reconstruction of the turbulence characteristics in both the energy–containing region and inertial sublayer of the spectra. Moreover, recent work by Bercin, Xie,

Table 4.1: LES variation of gravity g with Ri

Case	Ri	g
Ri=0	0.00	9.81
Ri=0.21	0.21	0.74
Ri=0.5	0.50	1.77
Ri=0.7	0.70	2.48
Ri=1	1.00	3.54
$Ri = 1^*$	1.00	3.54

and Turnock (2018) has shown that that the exponential form correlations provide a better approximation than the Gaussian ones.

Figure 4.2: Vertical profiles of prescribed integral length scales at the LES inlet $x = -2.5h$.

The turbulence generated by the inflow method satisfies the prescribed integral length scales and Reynolds stress-tensor values. The integral length scales L_x, L_y and L_z prescribed in the streamwise, vertical and lateral directions respectively are shown in Fig. 4.2. These were estimated from data presented in Marucci, Carpentieri, and Hayden, 2018 for an experiment simulating $Ri = 0.21$.

The estimated integral length scales can have considerable uncertainties due to the complexity of auto-correlation function, etc. Xie and Castro (2008) performed numerical sensitivity tests using different length scale combinations imposed at inlet (i.e. L_x, L_y and L_z factored by 0.5, 1 or 2). They found that the mean velocities and turbulent stresses within or immediately above the canopy were not sensitive to these variations provided the baseline length scales are not too different from the 'true' values. This suggested that it was not necessary to consider the effect of integral length scales in the current work.

The inflow turbulence method of Xie and Castro (2008) was also used to generate tempera-

ture fluctuations. The integral length scale of turbulence in the vertical direction L_y (Fig. 4.2) was chosen as the integral length scale of temperature fluctuations. Xie, Hayden, and Wood (2013) and Okaze and Mochida (2017) used similar approaches to generate flow temperature fluctuations, whereas Xie, Hayden, and Wood (2013) did not carry out a validation and Okaze and Mochida (2017) considered temperature as passive scalar. The prescribed mean temperature (Fig. 4.3a) and temperature variance (Fig. 4.3b) were obtained from the wind tunnel experiment at $Ri = 0.21$ reported in Marucci, Carpentieri, and Hayden (2018) where lateral homogeneity was checked. Marucci, Carpentieri, and Hayden (2018) fitted the mean temperature profile (Fig. 4.3a) for $Ri = 0.21$ in the usual log–law form,

$$T(y) - T_0 = \frac{T_*}{\kappa}\left[\ln(\frac{y-d}{y_{0h}}) + 16\frac{y-d-y_{0h}}{L}\right], \tag{4.7}$$

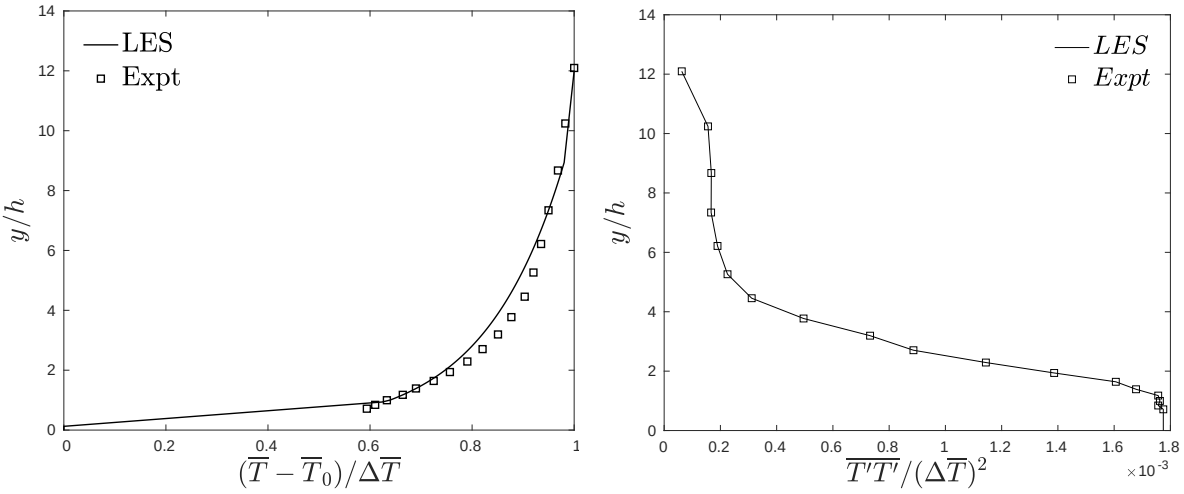

(a) (b)

Figure 4.3: (a) Vertical profiles of laterally averaged mean temperature from LES at inlet and prescribed mean temperature from experiments. (b) Vertical profiles of prescribed temperature variance at the LES inlet and experimental values.

where the von–Karman constant $\kappa = 0.41$, the roughness displacement height $d = 0$, the ratio of the boundary layer thickness to the Monin–Obukhov length $H/L = 1.13$, the scaling temperature $T_* = 0.34K$, the thermal roughness length $y_{0h} = 0.021mm$, and the maximum temperature difference $\Delta\overline{T}_{MAX}$ between the cooled floor $\overline{T}_0$ and the free stream flow $\overline{T}_{ref}$ was fixed as $16K$. Because of the experimental uncertainty in measuring temperature values close to the ground, Marucci, Carpentieri, and Hayden (2018) applied the least–squares fitting procedure to estimate the ground temperature $\overline{T_0}$ shown in Hancock and Hayden (2018).

Figure 4.3b shows the prescribed temperature variance at the LES inlet and the experimental values. A constant temperature variance was prescribed in the vicinity of the floor $(y/h \leq 1)$ where it is assumed there is a surface layer. The building walls, the streets and the ground were assumed to be adiabatic, as the inlet wind speed was high, the air pass–through time over the array was short, and the local heat transfer over the block surfaces was negligible

(i.e. less than 10% of the incoming heat from the upstream flow). This assumption was validated against data from the wind tunnel experiments of Marucci and Carpentieri (2018a) in Sec. 4.4.1.

4.3.4 Inlet conditions of velocities for LES

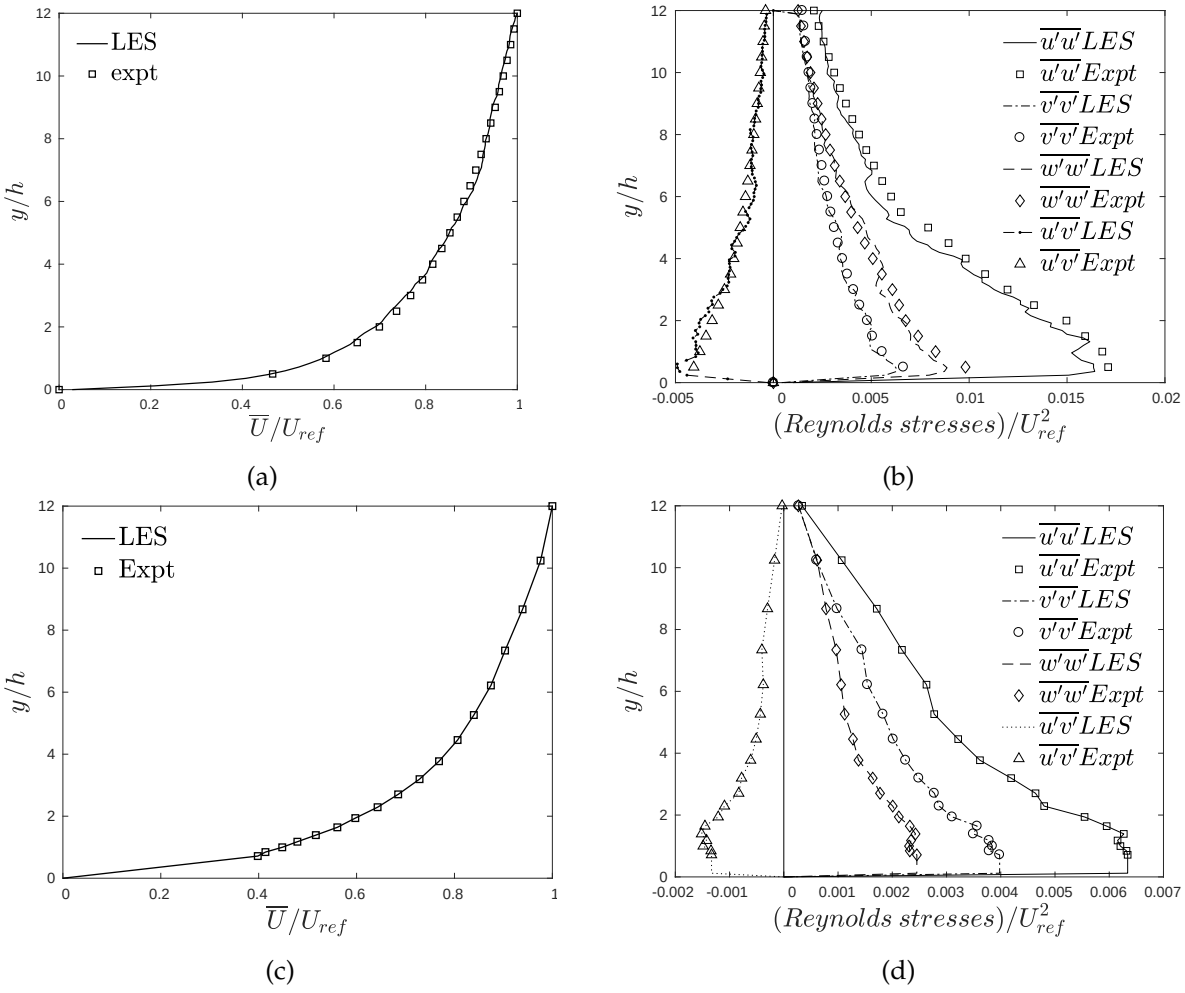

Figure 4.4: Vertical profiles of experimental and numerically prescribed inlet mean velocity and turbulent stresses. (a) mean velocity,$Ri = 0$; (b) turbulent stresses, $Ri = 0$; (c) mean velocity, $Ri = 0.21$; (d) turbulent stresses, $Ri = 0.21$.

Figure 4.4a and Fig. 4.4b show vertical profiles of experimental data (Marucci, Carpentieri, and Hayden, 2018) and numerically (Sessa, Xie, and Herring, 2018) prescribed inlet mean velocity and turbulent stresses in neutral condition $Ri = 0$, respectively. Figure 4.4c and Fig. 4.4d show vertical profiles of experimental data (Marucci, Carpentieri, and Hayden, 2018) and numerically prescribed inlet mean velocity and turbulent stresses respectively, at $Ri = 0.21$. The prescribed inlet mean velocity and turbulent stresses for the cases $Ri = 0.5, 0.7, 1$ (Table 4.1) were the same as those for the case $Ri = 0.21$. This was use-

ful for quantifying to which extent the thermal stratification alone impacted turbulence and dispersion, as in Xie, Hayden, and Wood (2013).

The case $Ri = 1^*$ (Table 4.1) was designed to quantify the effect of inlet TKE. The inlet mean velocity profile was prescribed to be the same as that of $Ri = 1$, while the turbulent stresses were estimated using a simple method. The ratios of the friction velocity to the free–stream velocity u_*/u_{ref} at $Ri = 0, 0.14, 0.21, 0.33$ reported in Marucci, Carpentieri, and Hayden (2018) were normalised by that at $Ri = 0.21$, and fitted to an exponential–function of Ri number (Fig. 4.5a).

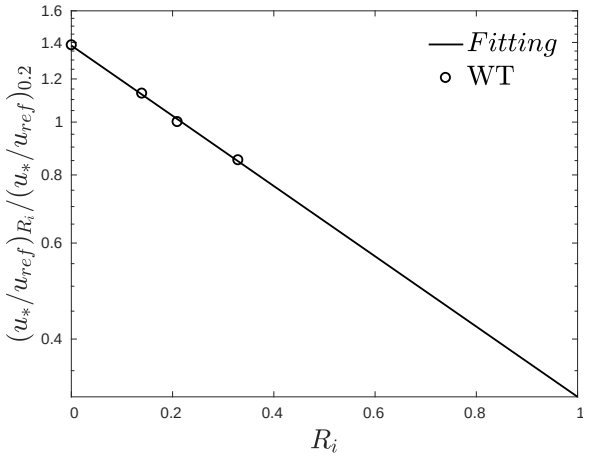

(a)

Figure 4.5: (a) The data of u_*/u_{ref} at $Ri = 0, 0.14, 0.21, 0.33$ in Marucci, Carpentieri, and Hayden, 2018 fitted to an exponential–function of Ri number, normalised by that at $Ri = 0.21$.

Marucci, Carpentieri, and Hayden (2018) found that the ratio of turbulent stresses to the friction velocity (i.e. $\overline{u'u'}/u_*^2$) did not change significantly in the vicinity of the wall in various weakly stable conditions. We therefore assumed that this ratio was constant between $Ri = 1$ and $Ri = 0.21$. The turbulent stresses for '$Ri = 1^*$' at the inlet were determined from the estimated friction velocity u_* obtained from Fig. 4.5. The estimated TKE prescribed at inlet for '$Ri = 1^*$' was about 10% of that for '$Ri = 0.21$'.

4.4 LES validation and verification

4.4.1 Validation

Predictions of turbulence, dispersion and mean temperature at $Ri = 0.21$ were validated against the wind tunnel (WT) data reported in Marucci, Carpentieri, and Hayden (2018) and Marucci and Carpentieri (2020). The standard error of the experimental measurements was around $\pm 1\%$ for mean velocity, $\pm 5\%$ for mean concentration and turbulent variances (Marucci, Carpentieri, and Hayden, 2018; Marucci and Carpentieri, 2020). Mean velocity

and temperature, streamwise and lateral turbulent stresses, mean concentration and concentration variance from the point source $S2$ were compared with wind tunnel data measured at $x = 16h$ and $z = 0$.

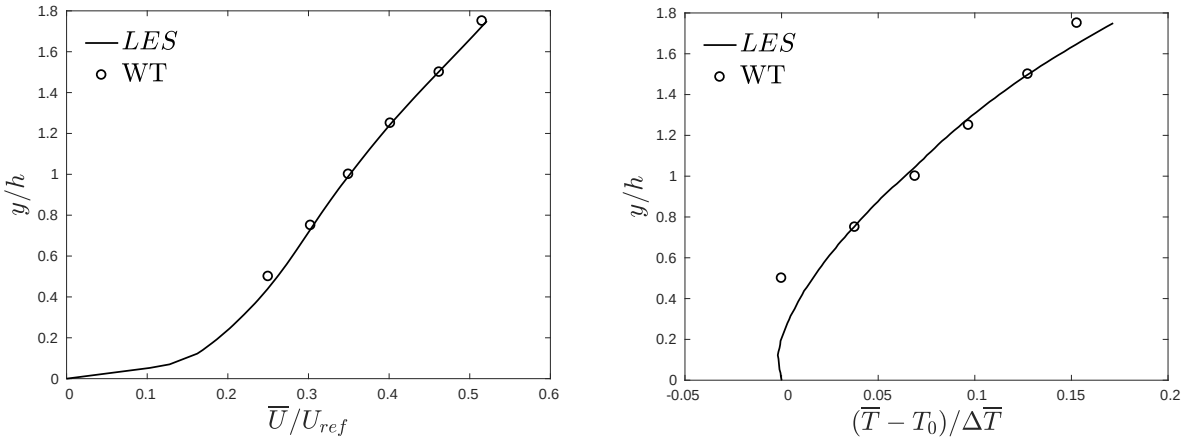

(a) (b)

Figure 4.6: (a) Vertical profiles of laterally averaged mean velocity from LES and experiments. (b) Vertical profiles of mean temperature from LES and wind tunnel (WT).

LES mean velocity (Fig. 4.6a) and mean temperature (Fig. 4.6b) were spatially averaged over four identical street intersections at $x = 16h$, whereas the experimental data were averaged in time only. The LES predictions of mean velocity were found to be in good agreement with experimental values below and immediately above the canopy (Fig. 4.6a). Similarly, the experimental profile of mean temperature was well captured by LES although the experimental uncertainty in temperature measurements close to the ground is not negligible.

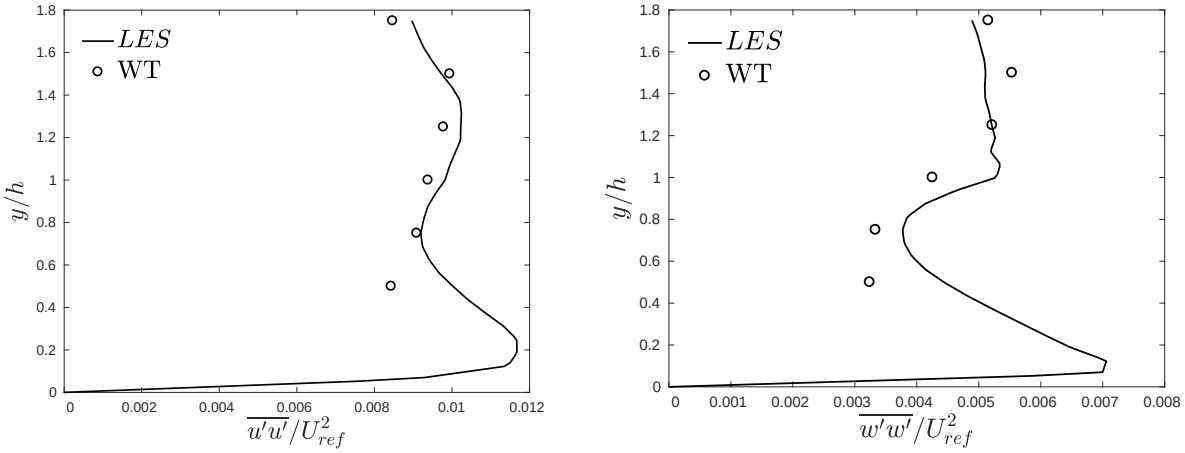

(a) (b)

Figure 4.7: (a) Vertical profiles of laterally averaged streamwise turbulent stress 6(a)and lateral turbulent stress 6(b) from LES and wind tunnel (WT).

Figure 4.7 presents comparisons between LES predictions of the mean streamwise and lateral

turbulent stresses again averaged over four identical street intersections at $x = 16h$ with the corresponding experimental data. The small differences between the second–order statistics in the LES and wind tunnel data in the figures demonstrate the success of the validation. The differences may reasonably be attributed to comparing spatial averages from the LES with a single sampling station in the experimental data.

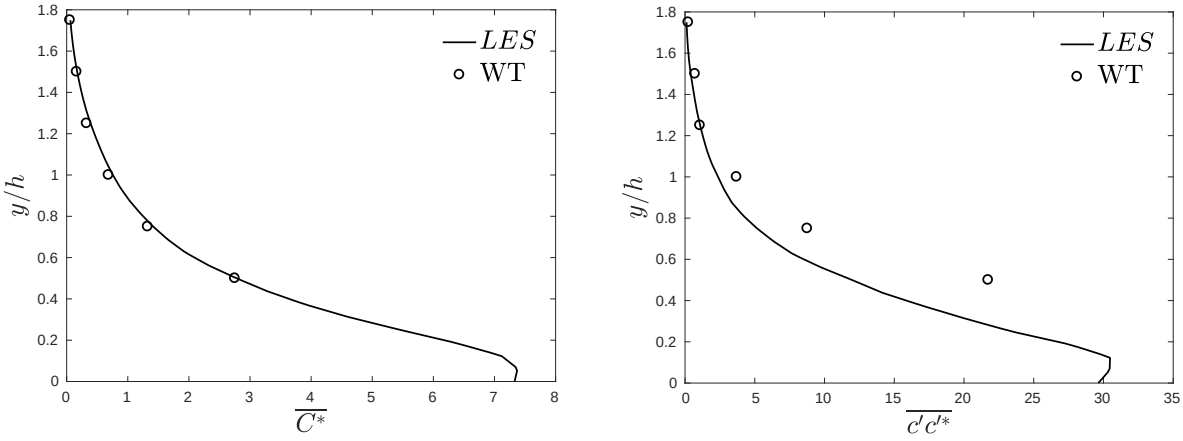

(a) (b)

Figure 4.8: (a) Vertical profiles of laterally averaged mean concentration (a) and vertical concentration variance (b) from LES and wind tunnel (WT).

The scalar concentration from the point source $S2$ was normalised following the method of Sessa, Xie, and Herring (2018) and Fuka et al. (2018):

$$\overline{C^*} = \overline{C}\frac{u_{ref}L_{ref}^2}{Q}, \tag{4.8}$$

where the characteristic length L_{ref} was the building height h and Q was the emission rate. Similarly, the scalar variance was normalized as:

$$\overline{c'c'^*} = \left[\frac{\sqrt{\overline{c'c'}}u_{ref}L_{ref}^2}{Q}\right]^2. \tag{4.9}$$

Laterally averaged LES mean concentration (Fig. 4.8a) and scalar variance (Fig. 4.8b) data were sampled at the main street intersection ($x = 16h$, $z = 0$) and compared with the experimental data. It can be seen that the LES accurately predicted the experimental mean concentration for $y \geq 0.5h$. The close agreement suggests that the predicted mean concentration at ground level should also be accurate. Figure 4.8b shows that the concentration variance was also well predicted above the canopy, but under-estimated within it. This difference may well be due to the uncertainties in measuring the concentration variance in the wind tunnel, and the source shape/size differences which affect the results in the near field (Sessa, Xie, and Herring, 2018).

4.4.2 Ground temperature sensitivity test

As discussed in Sec. 4.3.3, Marucci, Carpentieri, and Hayden (2018) used the least–square fitting method of Hancock and Hayden (2018) to obtain the upstream mean temperature profile and the temperature at the surface. From this they determined a good fit close to the ground. They then determined that the stability level in the wind tunnel was $Ri = 0.21$ by considering the maximum temperature difference $\Delta\overline{T} = 16K$ between the cooled floor $\overline{T_0}$ and the free stream flow $\overline{T}_{ref}$.

Although the temperature comparison was good, because of the experimental uncertainty in determining the surface temperature, the sensitivity of the derived value of Ri to this must be assessed. A ground surface temperature sensitivity study was therefore conducted to assess to what extent turbulence and dispersion within and above the canopy were affected by a small change in ground temperature at the inlet. One case was simulated using the inlet mean temperature profile shown in Fig. 4.3a but changing the temperature profile in the vicinity of the ground (i.e. for $y \leq 0.125h$) to be a constant which was $2K$ lower than $\overline{T}_0$ in Section 4.4.1.

The normalised total heat flux, $\psi^{u_*}_{h,tot}$, in the direction of flow resulting from the prescribed inlet temperature profile (Fig. 4.3a) can be estimated.

$$\psi^{u_*}_{h,tot} = \int_{y/h\in(0,12)} \frac{(\overline{U}\,\overline{T} + \overline{u'T'})}{u_* T_*} d\left(\frac{y}{h}\right), \tag{4.10}$$

where u' and T' are the velocity and temperature fluctuations respectively. As discussed above, the temperature in the vicinity of the ground was changed between the two LES cases for $y \leq 0.125h$ only. This meant that the incoming heat flux was only expected to change below $y = 0.125h$. It is to be noted that close to the ground the turbulent flux component $\overline{u'T'}$ in Eq. 4.10 is always very small or negative compared to the advective part $\overline{U}\,\overline{T}$ (Fuka et al., 2018; Goulart et al., 2019). Similarly, the advective component $\overline{U}\,\overline{T}$ in the vicinity of the ground is also very small as the mean velocity is nearly zero.

Vertical profiles of mean velocity and turbulent stresses were sampled at $x = 16h$ and laterally averaged over 60 locations. The mean concentration from point source $S2$ was sampled in the lateral direction at $x = 16h$ and $y = 0.5h$ below the canopy, and normalized as in Eq. 4.8. As expected, the mean velocity, turbulent stresses and normalised concentration values for the two cases were found to be in close agreement. This confirmed that small differences in incoming heat flux due to the measurement errors in ground surface temperature had a negligible effect on the downstream turbulence and dispersion within and above the canopy.

4.4.3 Inlet TKE sensitivity test

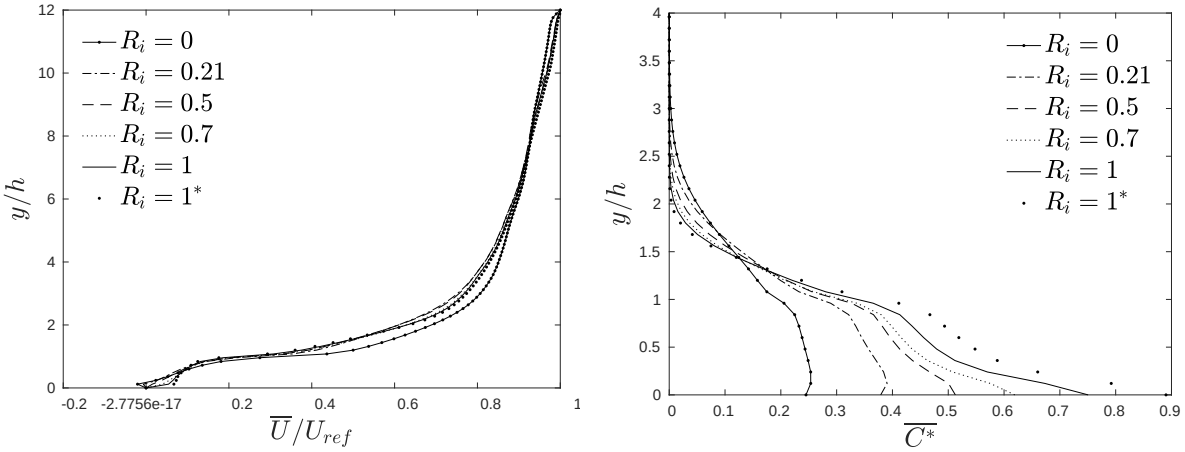

(a) (b)

Figure 4.9: Vertical profiles of mean velocity (a) and normalized concentration from the line source (b) measured at $x = 16h$ and laterally averaged over 60 locations.

Vertical profiles of mean velocity (Fig. 4.9a) and normalized mean concentration (Fig. 4.9b) were sampled at $x = 16h$ and laterally averaged over 60 locations. The effect of applying an inflow with a much lower TKE (i.e. '$Ri = 1^*$') on the mean velocity profile at $x = 16h$ was negligible. This shows that the difference between the mean velocity $x = 16h$ for $Ri = 0$ and the stable cases was mainly due to the small difference in the velocity profiles at the inlet (Fig. 4.4).

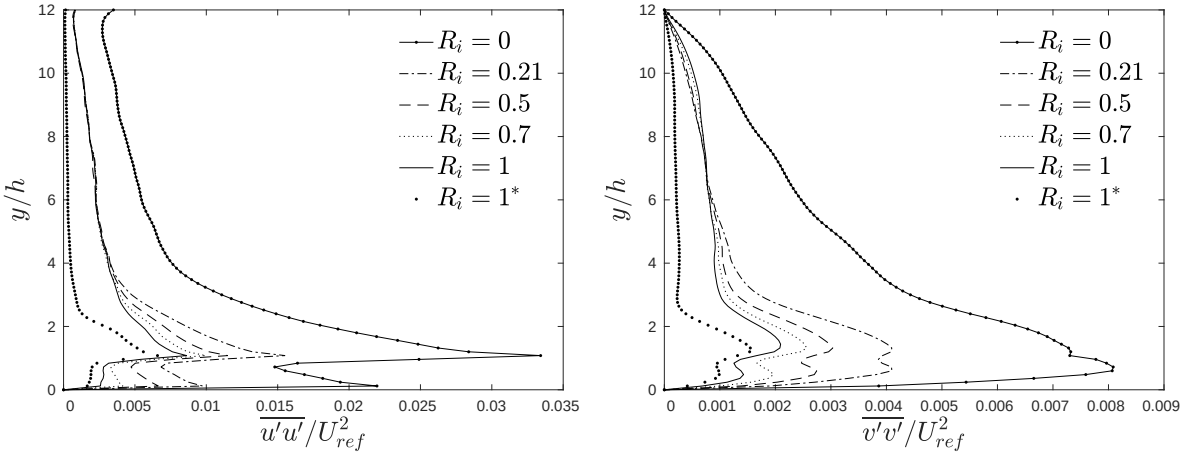

(a) (b)

Figure 4.10: Vertical profiles of streamwise (a) and vertical (b) turbulent stresses laterally averaged over 60 points at $x = 16h$.

Figure 4.9b shows vertical profiles of laterally averaged mean concentration at $x = 16h$ for the line source $S1$ at various stratification levels. It is to be noted that dispersion from the

line source is a quasi–2D problem where the plume is laterally homogeneous. Increasing stability yielded higher concentrations within the canopy and lower concentrations above it. These effects were found to be further enhanced by prescribing much lower TKE at the inlet. The increase in concentration below the canopy also demonstrates the impact of reduced vertical mixing above it.

Figures 4.10a and 4.10b respectively show vertical profiles of streamwise and turbulent stresses laterally averaged over 60 points at $x = 16h$. The effects of inflow TKE and thermal stability are clearly visible on both quantities. For $Ri = 0.2, 0.5, 0.7, 1$, both the streamwise and the vertical stresses were found to be reduced within and above the canopy by increasing stability. For the cases $Ri = 0.2, 0.5, 0.7, 1$, the differences above $\sim 6h$ were negligible due to the same inflow turbulence conditions being imposed at the inlet. On the contrary, for the cases $Ri = 0$ and '$Ri = 1^*$', the different turbulence conditions imposed at the inlet led to substantial differences in turbulent stresses at $x = 16h$ above the height $6h$ compared to the other cases. The evident differences in the $Ri = 0, 1$ and 1^* profiles demonstrate the importance of applying the correct inflow TKE for a chosen stability level.

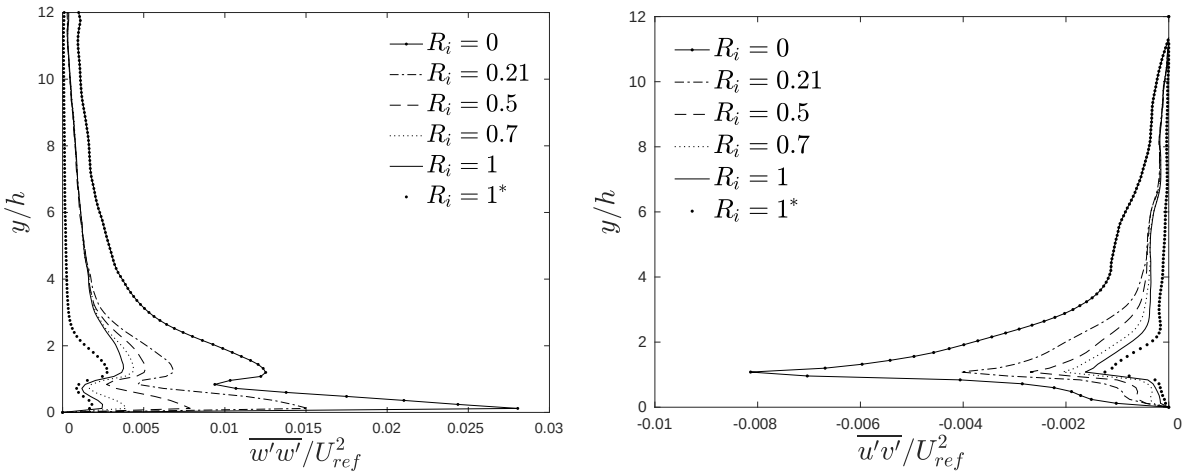

(a) (b)

Figure 4.11: Vertical profiles of lateral normal turbulent stress (a) and shear stress (b) measured at $x = 16h$ and laterally averaged over 60 locations. Estimated TKE at inlet for '$Ri = 1^*$'.

Figure 4.11 shows laterally averaged vertical profiles of lateral normal turbulent stress and turbulent shear stress at $x = 16h$. Similarly to the profiles of streamwise and vertical turbulent stresses in Fig. 4.10, both the lateral normal turbulent stress and turbulent shear stress profiles showed no visible differences above $\sim 6h$ for for $Ri = 0.2, 0.5, 0.7, 1$, while within and immediately above the canopy increasing stability damped the lateral normal turbulent stress and turbulent shear stress. For the '$Ri = 1^*$' case, both the turbulent stresses were lower than those for $Ri = 1$, due to the much lower TKE prescribed at the inlet, which was nearly zero above $4h$.

4.5 Stability effects on the internal boundary layer

The transition from the rough surface upstream of the array to the much higher roughness of the array itself causes an internal boundary layer IBL to develop from the leading edge of the array. In neutral stratification conditions, the IBL increases in depth as it develops downstream over the array and the flow within it has greater turbulent kinetic energy than that in the external boundary layer (e.g. Sessa, Xie, and Herring, 2018). Given that IBLs develop at rural to urban transitions etc., and affect the dispersion in urban areas, it is important to understand their characteristics and how these affect the dispersion of pollutants at various stability levels.

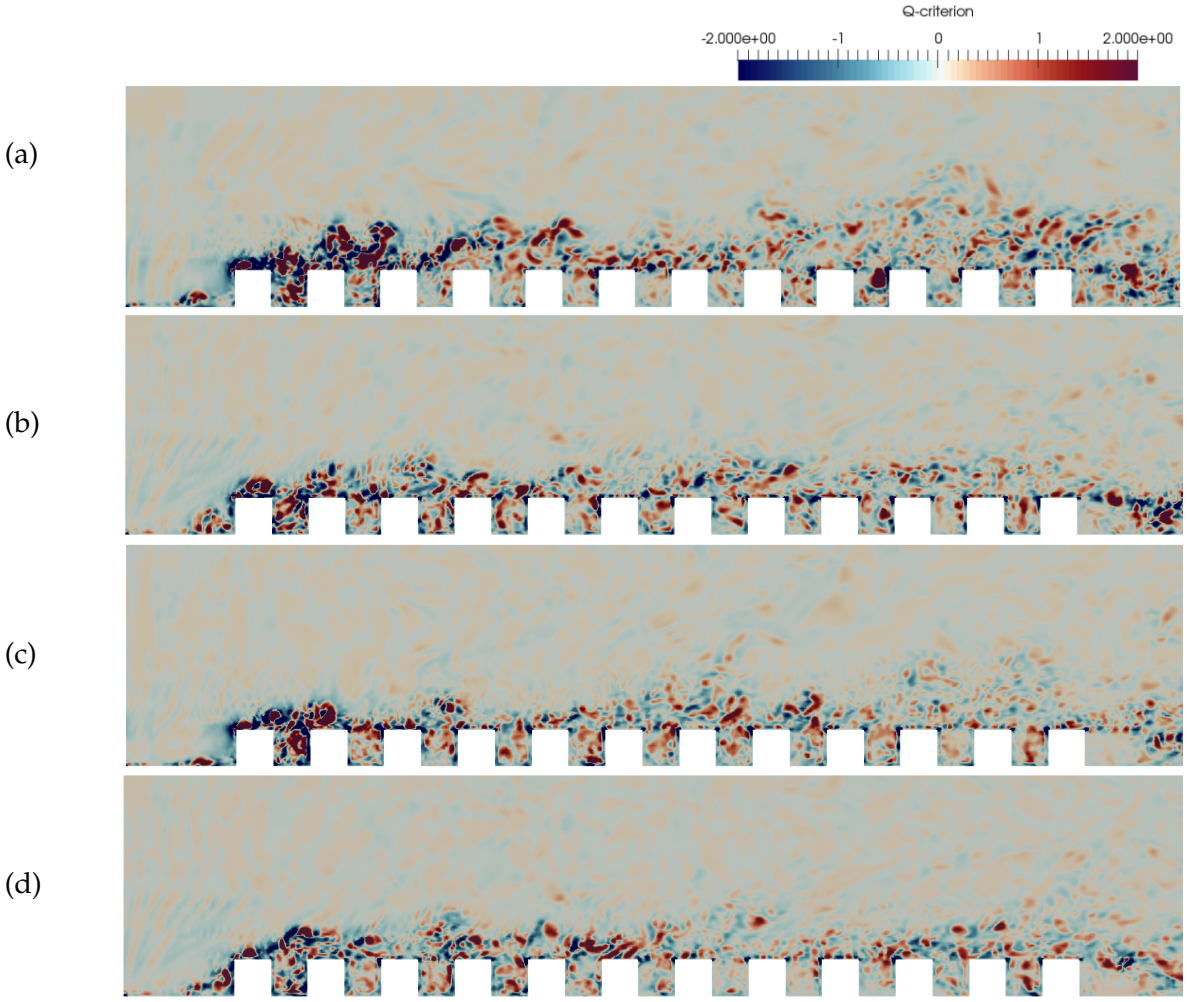

Figure 4.12: Q–criterion analysis of flow at $z = -1.5h$ for various stratification conditions and same inflow turbulence conditions. $Ri = 0.21$ (a), $Ri = 0.5$ (b), $Ri = 0.7$ (c), $Ri = 1$ (d).

The Q–criterion is defined as,

$$Q = 0.5(\Omega_{ij}\Omega_{ij} - S_{ij}S_{ij}), \tag{4.11}$$

where $\Omega_{ij} = 0.5(\frac{\partial u_i}{\partial x_j} - \frac{\partial u_j}{\partial x_i})$ and $S_{ij} = 0.5(\frac{\partial u_i}{\partial x_j} + \frac{\partial u_j}{\partial x_i})$. It is useful for highlighting flow regions in which rotation is dominant over the shear.

Figure 4.12 shows the results of Q criterion analyses for $Ri = 0.2$ (Fig. 4.12a), $Ri = 0.5$ (Fig. 4.12b), $Ri = 0.7$ (Fig. 4.12c) and $Ri = 1$ (Fig. 4.12d) cases. The IBL was shallower and of a lower growth rate compared to weaker thermal stratification. The Q–criterion analyses were repeated for several cross-sections in the lateral direction with similar results.

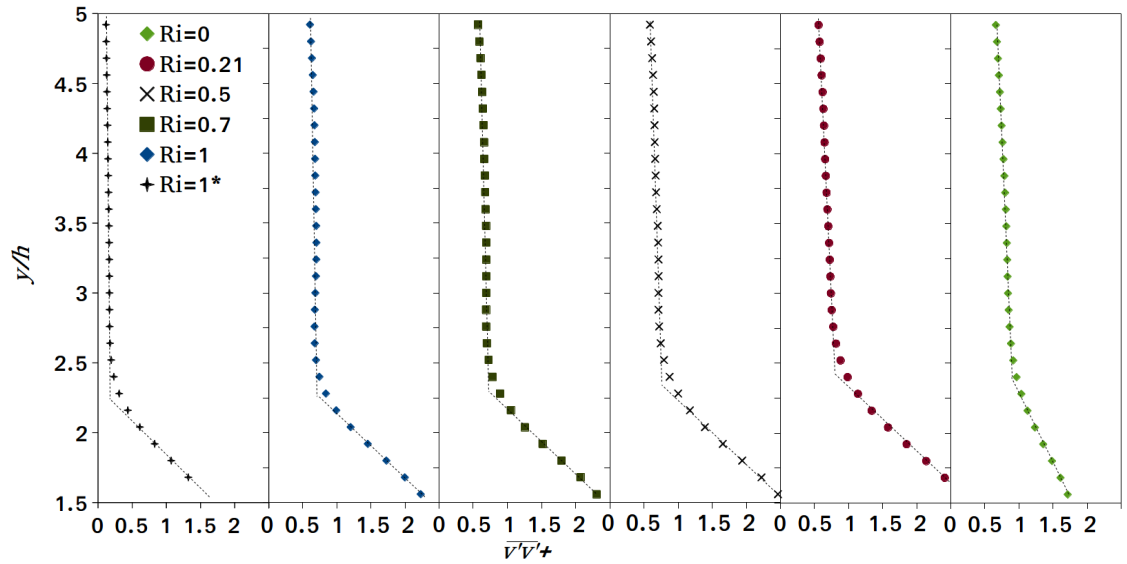

(a)

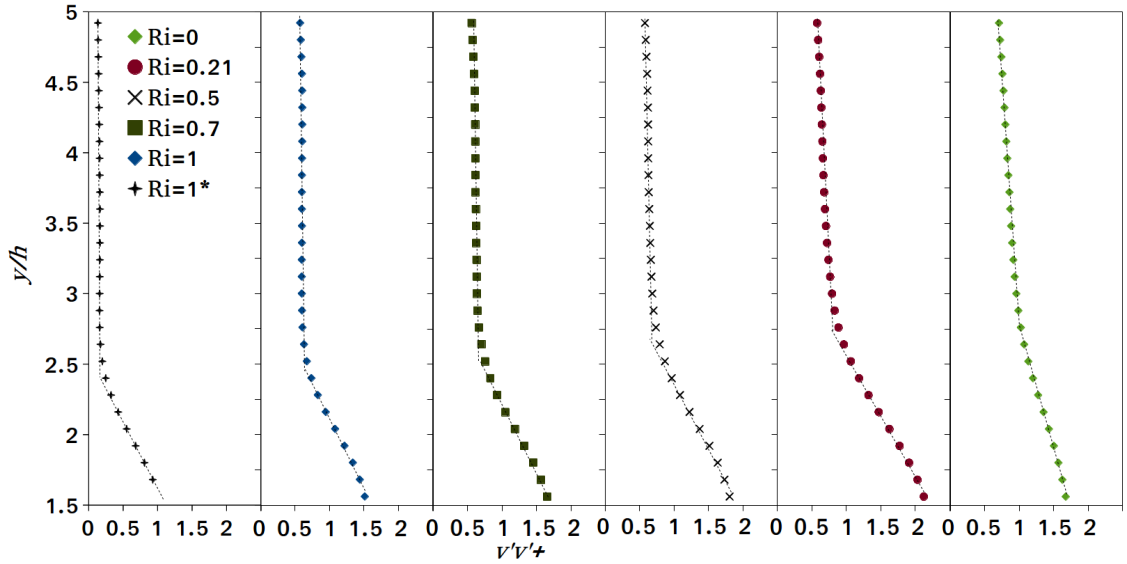

(b)

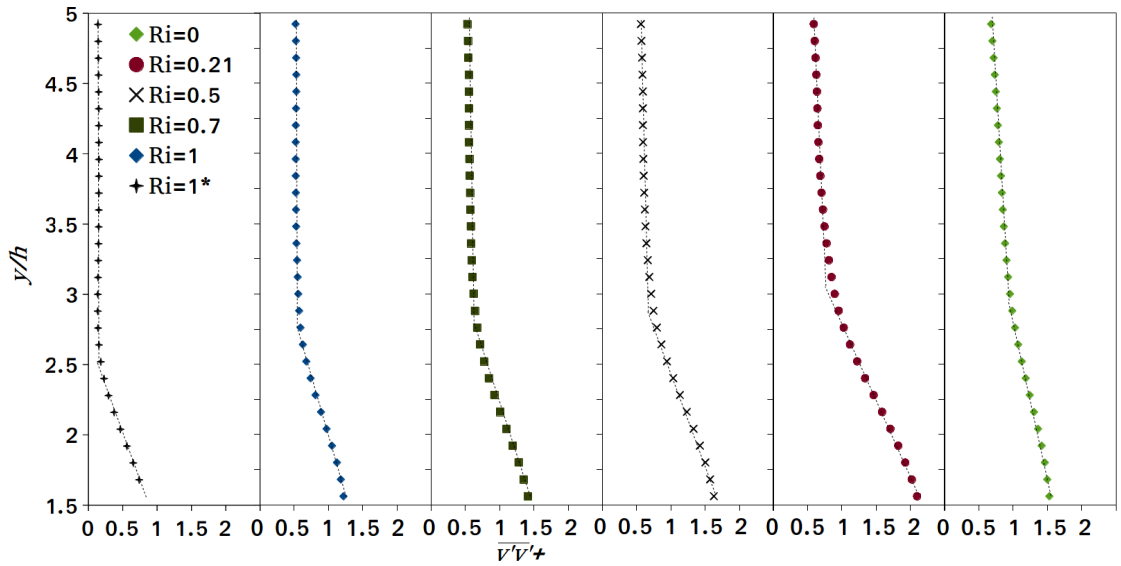

(c)

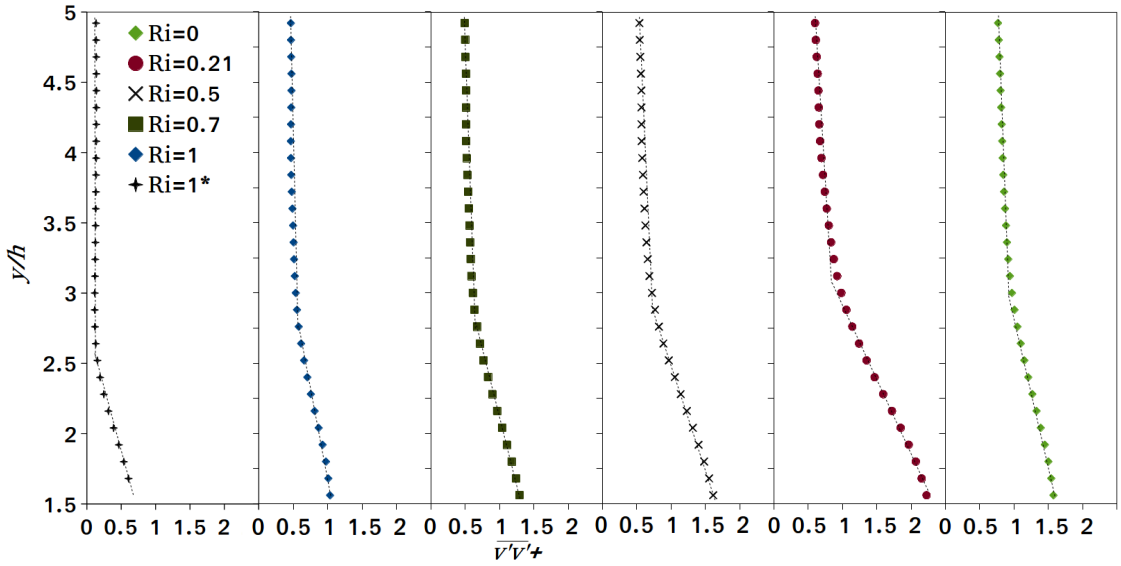

(d)

Figure 4.13: Vertical profiles of wall–normal turbulent stress $\overline{v'v'}^+$ at $x = 6h$ (a), $x = 10h$ (b), $x = 14h$ (c) and $x = 18h$ (d), averaged over 60 points in the lateral direction.

The method III (Sessa, Xie, and Herring, 2018) was used to process the data from each lateral street downstream of the leading edge of the array to locate the height of the IBL interface for various stability cases (Fig. 4.13). This involves deriving vertical profiles above the canopy by laterally averaging the dimensionless wall–normal turbulent stress $\overline{v'v'}^+$, and is easy to implement and provides a reasonable indication of the IBL development. Figure 4.13 plots vertical profiles of wall–normal turbulent stress immediately above the canopy, shows visible discontinuities in these profiles.

Fitting linearly these profiles to two straight lines yielded intersections (i.e. “knee" points). These were identified as the interface of the internal and external boundary layer, which was

consistent with the Q-criterion analyses shown in Fig. 4.12. This approach is in a similar manner to the methods of Antonia and Luxton (1972) and Efros and Krogstad (2011). The vertical stress profiles in the external and internal boundary layer regions were linearly fitted to a residual error of less than 2% in all cases.

Figure 4.13 shows that for the case '$Ri = 1^*$' the wall-normal turbulent stress was much smaller than the other cases because less TKE was prescribed at the inlet. On the contrary, for the $Ri = 0$ case, the wall–normal turbulent stress was greater than for the other stable cases because of the greater level of TKE defined at the inlet.

In Fig. 4.13a ($x = 6h$) the intersection of the two straight lines shows the height of the IBL interface was approximately the same for all the LES cases. This is due to a strong recirculation bubble formed at the leading edge, whose size was relatively insensitive to the inflow turbulence and thermal stability. At $x = 10h$ (Fig. 4.13b) and farther downstream $x = 14h$ and $18h$ (Figs. 4.13c and 4.13d), the effects of thermal stability on the depth of the IBL were more evident and the IBL was found to be shallower as the stratification was increased from $Ri = 0$ to $Ri = 1$.

These results confirm that increasing the thermal stratification damped the turbulence and mixing, and led to a thinner IBL. It is to be noted that the local mean temperature gradient within the IBL is much greater than that above it (Fig. 4.3a), resulting in a greater local stratification effect on the turbulence and mixing in the IBL and almost a step–change in normal Reynolds stress at the interface.

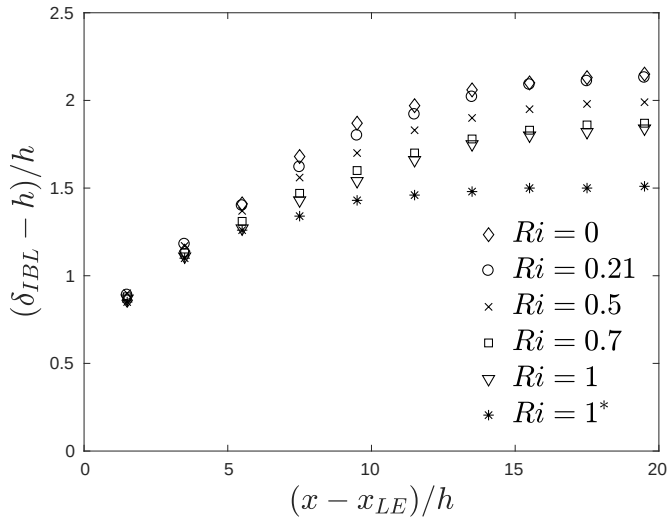

Figure 4.14: IBL height δ_{IBL} for different stratification conditions derived using the method of Sessa, Xie, and Herring (2018) based on vertical profiles of wall–normal turbulent stress $\overline{v'v'}^+$. x_{LE} is the streamwise coordinate of the leading edge of the array.

Figures 4.13a – 4.13d show that under the same stratification, lower incoming turbulence (i.e. '$Ri = 1^*$') yields a shallower IBL compared to greater incoming turbulence (i.e. '$Ri = 1$'). This suggests that an approaching boundary layer with lower turbulence intensity is more

susceptible to the effect of local thermal stratification over an urban area. This is consistent with the work of Williams et al. (2017) who found that the critical Richardson number for a rough wall was greater than for a smooth wall. This also emphasises the importance of modelling the non-linear interaction between the incoming turbulence and locally generated turbulence in thermally stratified conditions.

Figure 4.14 shows the IBL height δ_{IBL} for different stratification conditions derived by using the method of Sessa, Xie, and Herring (2018) based on vertical profiles of wall–normal turbulent stress $\overline{v'v'}^{+}$. It can be seen that the overall depth and growth rate of the IBL were sensitive to both the thermal stability and inflow turbulence conditions. Increasing stratification leads to a reduced IBL depth and a lower growth rate. A reduced TKE at the inlet ('$Ri = 1^{*}$') enhances these effects further compared to the case '$Ri = 1$'. The depth of the IBL varies by up to 30% within the studied range of thermal stratification conditions. Given that the present work has only considered weakly stably stratified conditions, we can conclude that both the depth of the IBL and the turbulence below and above it following a change in surface roughness are significantly affected by even small changes in thermal stratification.

4.6 Pollutant dispersion

The effects of stable stratification on pollutant dispersion were investigated by considering the emission of a passive scalar from a line source $S1$ (Fig. 4.1). This setup is useful for studying the effect of stratification on scalar concentration and scalar fluxes. As the periodic boundary conditions were used in the lateral direction, dispersion from the line source was a quasi–$2D$ problem because the scalar plume was laterally homogeneous.

Fig. 4.15 shows the instantaneous concentration of the line source $S1$ on a vertical plane at $z = -1.5h$ for $Ri = 0.21$ (a), $Ri = 0.5$ (b), $Ri = 0.7$ (c), $Ri = 1$ (d). The TKE prescribed at inlet was identical for cases (a), (b), (c) and (d) in order to isolate the effects of increasing stratification on pollutant transport downstream of the source's location. Although the contour's analysis of Fig. 4.15 only shows instantaneous concentrations, the effects were evident. From $Ri = 0.21$ (a) to $Ri = 1$ (d) the pollutant concentration was found to be increased below the canopy within the downstream lateral streets and consequently, the vertical transport and mixing was found to be reduced above the canopy. The qualitative plots confirm that the suppression of turbulence and the thinner IBL due to increasing thermal stratification ($Ri \leq 1$) lead to significant changes on dispersion mechanisms which are quantified in the following sections.

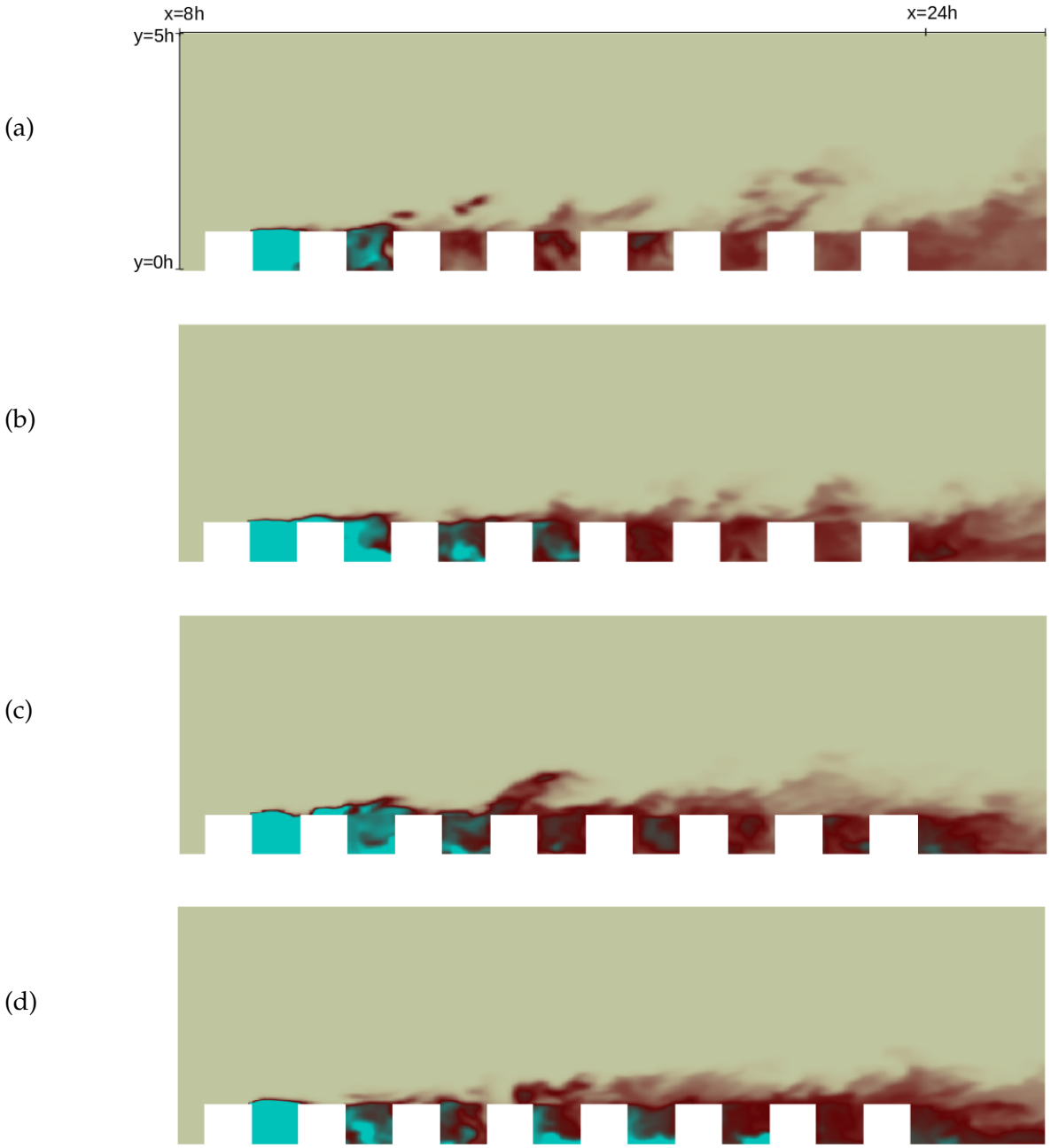

Figure 4.15: Instantaneous concentration contours of the line source $S1$ on a vertical plane at $z/h = -1.5h$ for $Ri = 0.21$ (a), $Ri = 0.5$ (b), $Ri = 0.7$ (c), $Ri = 1$ (d).

4.6.1 Stability effects on scalar fluxes

The total vertical flux $\psi^{v*}_{tot} = \psi^{v*}_{adv} + \psi^{v*}_{turb}$ includes contributions from both advective (Eq. 4.12) and turbulent (Eq. 4.13) scalar fluxes. The advective and turbulent vertical concentration fluxes transport pollutants from the canopy flow to the boundary layer above. The dimensionless advective and turbulent vertical flux components are defined respectively as follows (Fuka et al., 2018):

$$\psi_{adv}^{v*} = \overline{V}\,\overline{C}\frac{h^2}{Q} \tag{4.12}$$

$$\psi_{turb}^{v*} = \overline{v'c'^*} = (\overline{VC} - \overline{V}\,\overline{C})\frac{h^2}{Q} \tag{4.13}$$

where v' and c' are the vertical velocity and concentration fluctuations respectively and $\overline{V}$ is the mean vertical velocity.

Similarly, the total streamwise flux in the streamwise direction is defined as follows:

$$\psi_{tot}^{u*} = (\overline{U}\,\overline{C} + \overline{u'c'})\frac{h^2}{Q} \tag{4.14}$$

where u' is the streamwise velocity fluctuation and $\overline{U}$ is the mean streamwise velocity.

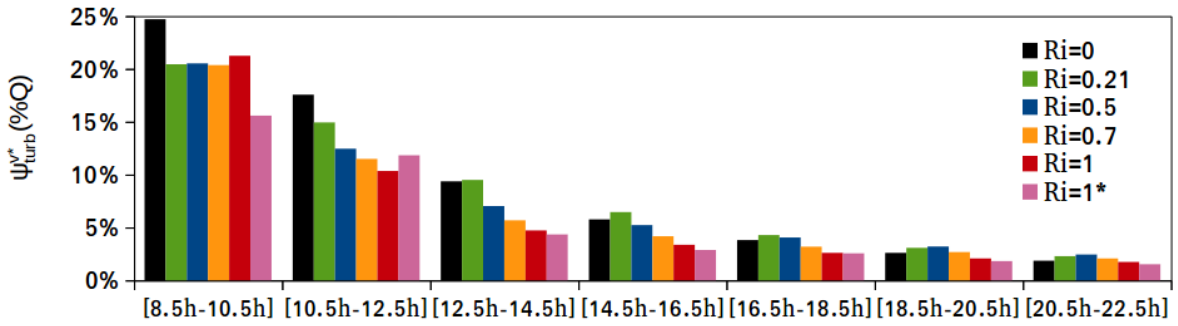

Figure 4.16: Integrated turbulent vertical concentration flux for horizontal planes $2h \times 12h$ at $y = 1h$ within 7 lateral streets for various stratification conditions. Line source placed at $x = 10h$.

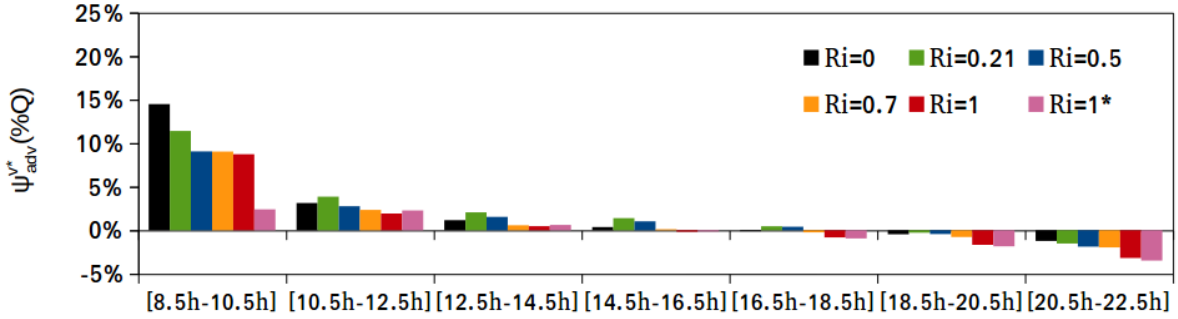

Figure 4.17: Integrated advective vertical concentration flux for horizontal planes $2h \times 12h$ at $y = 1h$ within 7 lateral streets for various stratification conditions. Line source placed at $x = 10h$.

The vertical turbulent (Fig. 4.16) and advective (Fig. 4.17) concentration fluxes from the line source $S1$ were integrated at the canopy height $y = 1h$ across the entire span $12h$, between each lateral street defined by two x coordinates separated by $2h$.

$$\psi^{a,b} = \int\int_{x/h\in(a,b),y/h=1} \psi^{v*} d\left(\frac{x}{h}\right) d\left(\frac{z}{h}\right). \tag{4.15}$$

Large positive turbulent and advective fluxes were found over the first interval ($x = 8.5h - 10.5h$) because the horizontal plane was above the source street ($x = 10h$). Further downstream, the turbulent and advective concentration flux components decreased significantly. Figures 4.16 and 4.17 show that the turbulent flux was generally greater in magnitude than the advective flux.

Both the turbulent and the advective fluxes generally decreased as Ri was increased from 0.2 to 1.0, given the same turbulent inflow conditions. This confirmed that increasing stratification reduced vertical transport of pollutant due to decreasing both the turbulent and advective scalar fluxes in the vertical direction. For $Ri = 0$, because of higher TKE prescribed at inlet, the general pattern was slightly different. For example, at the third downstream interval from the line source ($x = 14.5h - 16.5h$), the turbulent scalar flux (Fig. 4.16) was found to be lower than that for $Ri = 0.2$. This was due to higher turbulent kinetic energy near the source which yielded greater vertical transport above the canopies than that for $Ri = 0.2$.

For '$Ri = 1^*$', the much lower TKE at the inlet caused significantly low turbulent and advective scalar fluxes over the source street ($x = 8.5h - 10.5h$). As a result, the scalar plume for '$Ri = 1^*$' was strongly advected into the following lateral street ($x = 10.5h - 12.5h$), producing a so–called virtual secondary source. Figures 4.16–4.17 show that over the first two lateral streets both the turbulent and advective scalar fluxes for '$Ri = 1^*$' have almost the same magnitude. This again confirms the existence of the virtual secondary source in the 2^{nd} street.

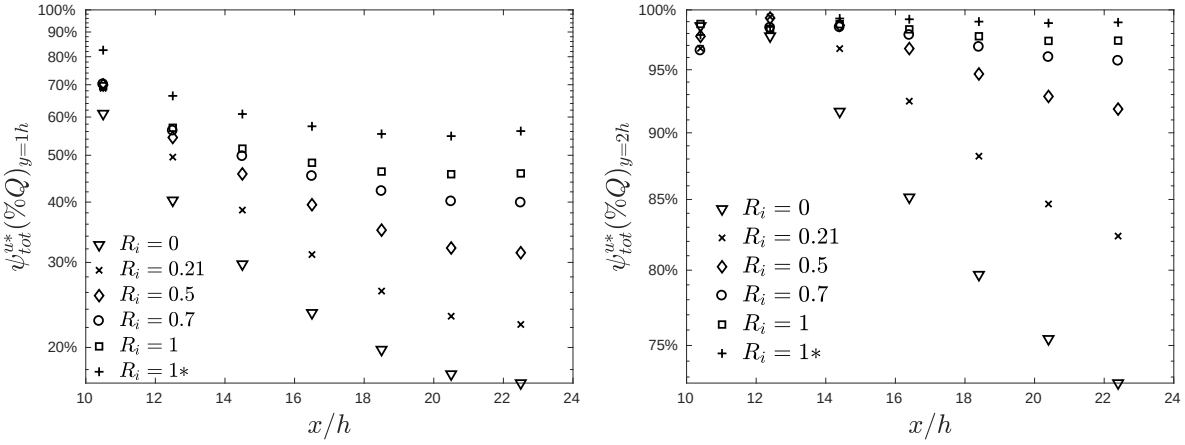

(a) (b)

Figure 4.18: Total streamwise flux over $1h \times 12h$ (a) and $2h \times 12h$ (b) vertical planes at 7 streamwise locations downstream of the line source (at $x = 10h$).

The streamwise total concentration flux (Eq. 4.14) of the line source $S1$ was integrated over vertical planes with dimensions ($1h \times 12h$) as shown in Fig. 4.18a and ($2h \times 12h$) as shown in Fig. 4.18b. The integration was performed between two constant y coordinates across the entire span. For example, at $x = 10.5h$, the total flux was computed as follows:

$$\psi^{a,b} = \int \int_{y/h\in(a,b),x/h=10.5} \psi^{u*} d\left(\frac{y}{h}\right) d\left(\frac{z}{h}\right). \tag{4.16}$$

Figure 4.18a shows the amount of pollutant transported in the streamwise direction below the canopy top. Near the line source, approximately 60% of the total emission Q for $Ri = 0$ was transported in the streamwise direction while $\sim$ 40% of the emission Q was transported vertically through the horizontal plane above the source street. Further downstream, the amount of pollutant transported in the streamwise direction dropped to less than 20% of the total flux for $x \geq 20h$.

From $Ri = 0.2$ to $Ri = 1$ a similar amount of pollutant was transported downstream at $x = 10.5h$ because the kinetic energy close to the source was similar in all cases. Away from the source, greater stability trapped more pollutant within the canopy layer. Within the range $Ri = 0.2$ to $Ri = 1$ the total concentration flux below the canopy increased by more than 25% at $x/h = 20$ which is 5 rows of bocks downstream from the line source. For the case '$Ri = 1^*$' with lower incoming TKE, the stratification effect is evidently stronger compared to the case $Ri = 1$.

Figure 4.18b shows the amount of pollutant transported through the vertical plane below $y = 2h$ in the streamwise direction. All of the profiles show a peak value at approximately $x = 12.5h$. The vertical plane at $x = 10.5h$ was very close to the line source at $x = 10h$, where the gradient of total streamwise flux, and consequently the error in integrated total streamwise flux through the plane was greatest. This might explain why the integrated total streamwise flux at $x = 10.5h$ shown in Fig. 4.18b is not 100%. Further downstream, the total streamwise flux through the vertical plane $y = 0 - 2h$ increases monotonically as the stratification level increases for the same incoming turbulence intensity, confirming again that the spreading of the plume is evidently affected by the stability level. Furthermore, reducing incoming turbulence resulted in an increase in total streamwise flux through the vertical plane $y = 0 - 2h$ at the same stratification.

4.6.2 Stability effects on mean concentration

As stated earlier in Sec. 4.6.1, within the LES simulations the dispersion from a ground–level constant line source can be considered to be laterally homogeneous, with spreading of the plume constrained in the lateral direction. The previous sections show that increasing Ri decreased the vertical scalar transport above the canopy and led to higher concentrations close to the ground. In this section, we quantify these effects on mean concentration.

The volume–averaged concentration was calculated within each lateral street up to the canopy height, starting from the source street which was located between $x = 9.5h$ and $x = 10.5h$. Mean concentration from the line source $S1$ was normalized as in accordance with Eq. 4.8 and averaged over a volume with dimensions $1h \times 1h \times 12h$:

$$< \overline{C^*} >^{a,b} = \int_{x/h\in(a,b)} \int_{y/h\in(0,1)} \int_{z/h\in(-6,6)} \overline{C^*} d\left(\frac{x}{h}\right) d\left(\frac{y}{h}\right) d\left(\frac{z}{h}\right). \tag{4.17}$$

Figure 4.19 shows that the volume–averaged concentration increased monotonically in all of the streets as the thermal stability was increased, and decreased with distance from the source at all stratification conditions. This is because increased stability suppresses turbulence resulting in reduced vertical mixing within and above the canopy (see Fig.4.13). Figure 4.19 also shows that the volume–averaged concentration was increased when a lower TKE was prescribed at the inlet in the case '$Ri = 1^{*}$' compared to that in the case $Ri = 1$. This is consistent with a reduction in vertical scalar flux in the case '$Ri = 1^{*}$' compared to that in the case $Ri = 1$ (Sec. 4.6.1).

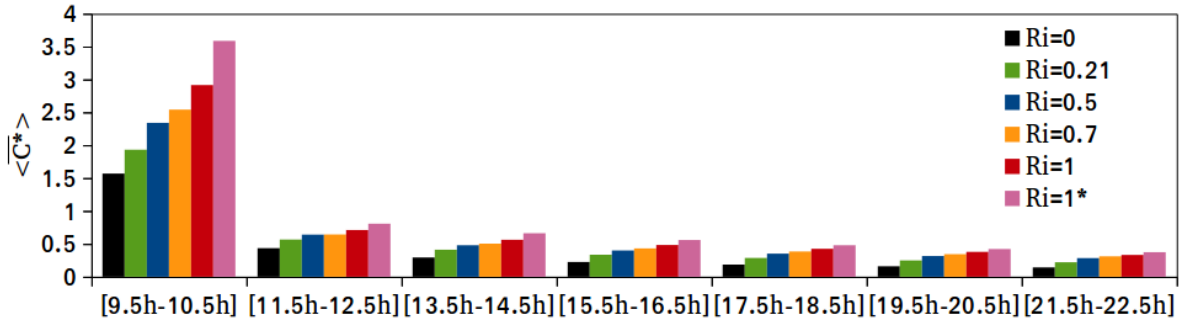

Figure 4.19: Volume–average of normalized mean concentration within lateral streets, from the ground to the canopy height $y = 1h$. The lateral source street is defined at $x = 9.5 - 10.5h$.

Figure 4.20 shows a monotonic increase in volume–averaged concentration within each lateral street for cases at $Ri \geq 0.2$ compared to that within the same street for case $Ri = 0$. This again confirms the effect of increasing thermal stratification and the lower TKE in the approaching flow for the $Ri = 1^{*}$ case shows a 20% increase in volume–averaged concentration.

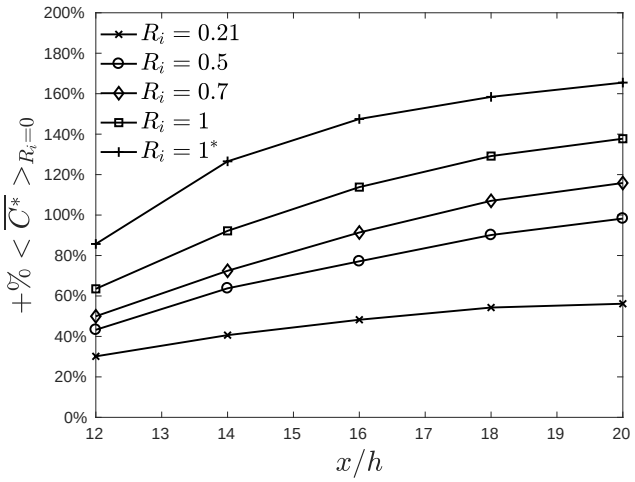

Figure 4.20: Increase (%) in volume–averaged concentration $< \overline{C^*} >$ for cases at $Ri \geq 0.2$ compared to $Ri = 0$ within lateral streets up to the canopy height.

4.7 Conclusions and discussion

In this study we have rigorously examined the effects of various levels of weakly stable stratification ($0 \leq Ri \leq 1$) on turbulence and dispersion over a rural–to–urban transition region using a high–fidelity large eddy simulation (LES) approach. Firstly we validated the LES predictions against wind tunnel measurements on a stratified boundary layer approaching a regular array of cuboid elements at $Ri = 0.21$. The validation suggested that our developed synthetic inflow generation method embedded in LES was able to accurately predict mean velocities, turbulent stresses, mean concentration and variance of concentration fluctuations from a ground–level line source in weakly stratified flows over a rough–to–very–rough transition region, such as from rural–to–urban region. It is to be noted that this is the first time we carried out assessment of synthetic generation of turbulence and temperature fluctuations for modelling a developing weakly stable atmospheric boundary layer.

A numerical sensitivity test was conducted to assess whether a small change of ground temperature upstream of the step change in roughness affected turbulence and dispersion further downstream. This was required to assess the potential impact of the non–negligible errors of measuring the ground temperature upstream of the step change in the experiments. We found that the differences in incoming heat flux due to changes in the surface temperature were negligible because the mean streamwise velocity was nearly zero in the vicinity of the ground. We conclude that the turbulence and dispersion downstream of the step change in roughness were insensitive to small changes of ground temperature upstream of the step change.

The transition from a rough surface to a much rougher surface composed of an array of regular cuboid elements generated an internal boundary layer (IBL) from the leading edge of the array. The method developed in Sessa, Xie, and Herring (2018) was used to evaluate the depth of the IBL for the different stratification conditions simulated (i.e. $0 \leq Ri \leq 1$) and different inflow turbulence intensities. We found that the IBL became shallower as the thermal stratification was increased. The greater local vertical temperature gradient within the IBL than in the external boundary layer led to a greater local stratification effect within the IBL and consequently a more pronounced step–change of normal Reynolds stress at the the interface of IBL.

It was also found that the IBL height was reduced as the level of TKE was reduced in the approaching flow for the same stratification condition. This suggests that an approaching boundary layer with less turbulence intensity is more susceptible to the effect of local thermal stratification over an urban area. This also suggests the importance of accurately modelling the non-linear interaction between the incoming turbulence and the locally generated turbulence in thermal stratification conditions.

The dispersion and scalar fluxes from a ground–level line source placed behind the fifth row of elements downstream of the leading edge were analysed extensively in various stratification conditions ($0 \leq Ri \leq 1$). The total vertical flux decreased above the lateral streets

whereas the horizontal total flux increased within the lateral streets as the thermal stratification was increased. This led to larger volume-averaged concentrations within streets with increasing stratification. If the TKE in the approaching boundary layer was reduced while maintaining the same level of thermal stratification, the effect on the total scalar fluxes within and above the canopy, and on the volume–averaged mean concentration within lateral streets was greater.

We conclude that even weakly stable stratification ($0 \leq Ri \leq 1$) in an approaching boundary layer significantly changes the concentration levels that result from material dispersing from point or line sources within an array of blocks. This is because of the suppression of the turbulence in the IBL, and the reduced vertical transport of pollutant above the canopy.

5 Wind direction effects on turbulence and dispersion

This chapter investigates wind direction effects on turbulence and dispersion over urban areas. The study examines the wind direction effects over an array of buildings with uniform height in neutral and weakly stable thermal conditions. Mean flow and turbulence were successfully validated against wind tunnel experiments for 15° ($Ri = 0$) and 45° ($Ri = 0.2$) wind directions. However, it was found that for the 45° wind direction, the experimental Reynolds stresses were slightly over–predicted by LES immediately above the canopy due to the differences between the wind tunnel settings and the LES model at the leading edge. Volume–averaged concentration below the canopy, vertical and horizontal total fluxes were analysed against LES of 0° wind direction in neutral ($Ri = 0$) and weakly stable ($Ri = 0.2$) thermal conditions. It was found that natural ventilation below the canopy was improved when the mean wind direction was inclined to a different angle (i.e. 45°) from the main streets. However, the mean concentration from a ground–level line source was found to be insensitive to small variations of wind direction (i.e. 15°). Furthermore, for $Ri = 0.2$ the effects of wind direction on turbulence and dispersion were found to be dominant over the effects of weak stable stratification.

5.1 Numerical settings of LES 15° wind direction

The LES model was implemented within the open-source CFD package OpenFOAM version 2.1. The simulated domain was identical to the one used in our previous studies (i.e. domain size, number of buildings, building's orientation etc., Chap. 3) with periodic lateral boundaries and stress-free condition at the top of the domain. The inflow turbulence method (Xie and Castro, 2008) was used at the LES inlet to generate a mean wind rotated by 15° in the clockwise direction from $z/h = 0$ (Fig. 5.2). The wind tunnel mean velocity and Reynolds stresses measured upstream of the leading edge in neutral conditions (Fig. 5.3, Marucci and Carpentieri (2020)) were converted at the LES inlet into the coordinates of the LES model following the code implementation below and as described in Fig. 5.1.

Assuming clockwise rotation ϕ on the plane (x, z) from the wind tunnel axes to the LES axes, the rotation vector R is defined as:

$$R(-\phi) = \begin{bmatrix} cos\phi & sin\phi \\ -sin\phi & cos\phi \end{bmatrix}$$

so that the mean velocity components $(\overline{u}, \overline{w})$ and the fluctuation terms (u', w') from the decomposition (Eq. 2.31) are obtained as follows:

$$\overline{u}_{LES} = \overline{u}_{WT} cos\phi + \overline{w}_{WT} sin\phi; \tag{5.1}$$

$$\overline{w}_{LES} = -\overline{u}_{WT} sin\phi + \overline{w}_{WT} cos\phi; \tag{5.2}$$

$$u'_{LES} = \Psi_1 \sqrt{\overline{u'u'}_{WT}} cos\phi + \Psi_3 \sqrt{\overline{w'w'}_{WT}} sin\phi : \tag{5.3}$$

$$w'_{LES} = -\Psi_1 \sqrt{\overline{u'u'}_{WT}} sin\phi + \Psi_3 \sqrt{\overline{w'w'}_{WT}} cos\phi; \tag{5.4}$$

where Ψ_j is the same of Eq. 2.31. The Reynolds stresses in the wind tunnel coordinate system $\overline{u'u'}$, $\overline{v'v'}$, $\overline{w'w'}$ and $\overline{u'v'}$ are respectively R_{11}, R_{22}, R_{33} and R_{21} in Eq. 2.32.

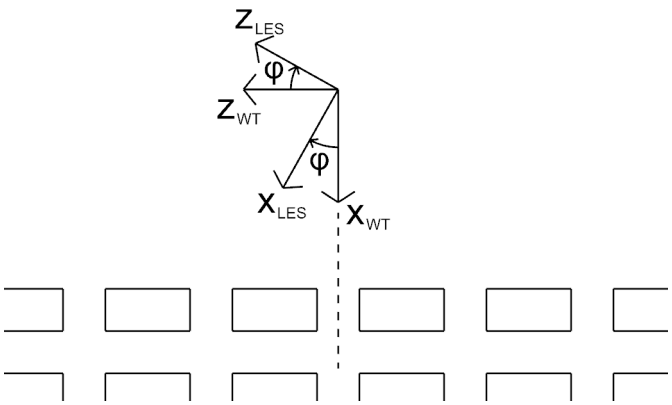

Figure 5.1: Rotation ϕ from the wind tunnel coordinates (WT) to the LES coordinates with cuboid elements oriented as in the LES model.

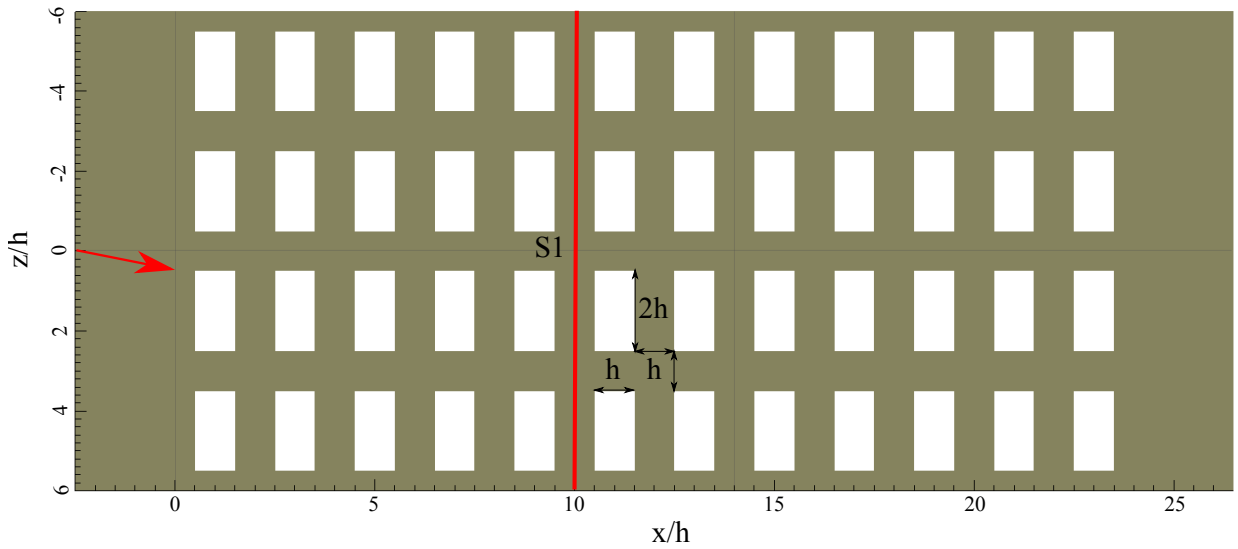

Figure 5.2: Plan view of the LES array configuration showing dimensions of buildings and streets, coordinate system, the flow direction rotated by 15° in the clockwise direction from $z/h = 0$, and the location of line source $S1$.

The synthetic turbulent velocities, converted in the LES coordinates, were generated in the wind tunnel coordinates by rotating the urban array by 15° in the anti–clockwise direction (i.e. see Fig. 5.3 for the 45° wind direction). This produced slightly different wind configuration at the leading edge of the urban array and further downstream, compared to that created in the LES model using periodic lateral conditions. A line source was positioned on the ground between the fifth and sixth rows of buildings. The lateral size of the line source was set equal to the entire width of the domain and a constant scalar flux release rate was set for each cell inside the volume of the line source.

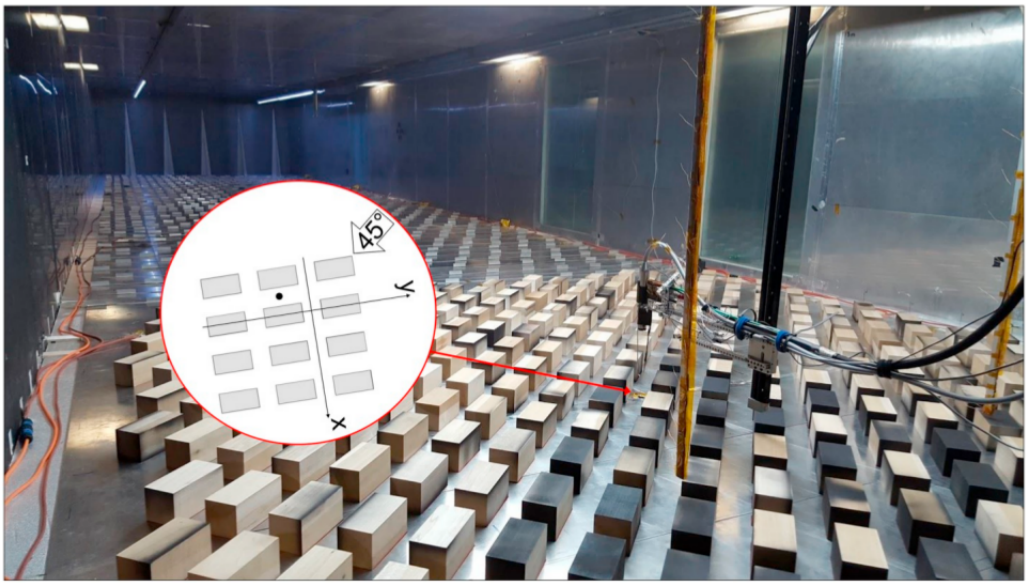

Figure 5.3: Picture of the experimental urban array rotated by 45° in the anti–clockwise direction from $z/h = 0$ assuming the wind direction parallel to the side walls of the wind tunnel (Marucci and Carpentieri, 2020).

5.2 Validation of turbulence and dispersion (15° wind direction)

Predictions of turbulence and dispersion produced using the inflow method for 15° wind direction were validated against data obtained in the environmental wind tunnel at University of Surrey (Marucci and Carpentieri, 2020). Mean velocity, streamwise and lateral turbulent stresses were averaged over four identical locations at $x = 17h$ (Fig. 5.2) in the middle of the short street. Mean concentrations produced by point source $S2$ (Fig. 4.1) were sampled at $x = 17h$ and $z = 0h$ and compared with wind tunnel measurements. The standard error of the experimental data was around $\pm 1\%$ for mean velocity, $\pm 5\%$ for mean concentration and turbulent variances.

The LES predictions of mean velocity (Fig. 5.4a) were found to be in good agreement with the experimental data below the canopy and up to $y = 2h$. Above that height, LES slightly over–predicted the wind tunnel data. Fig. 5.4c shows that the streamwise turbulent stress was marginally over–predicted below the canopy and under–predicted above. The peak

stress at the canopy height was again slightly over–predicted. Fig. 5.4d shows that the lateral turbulent stress was well captured by LES within and immediately above the canopy up to $y = 3h$. Above that height, LES under–predicted the experimental values. As mentioned above, the LES wind configuration at inlet was slightly different from the one of the wind tunnel and this caused small discrepancies from the experimental mean velocity and turbulent stresses. Furthermore, wind tunnel data were averaged in time (2.5min) only at a single location rather than four locations.

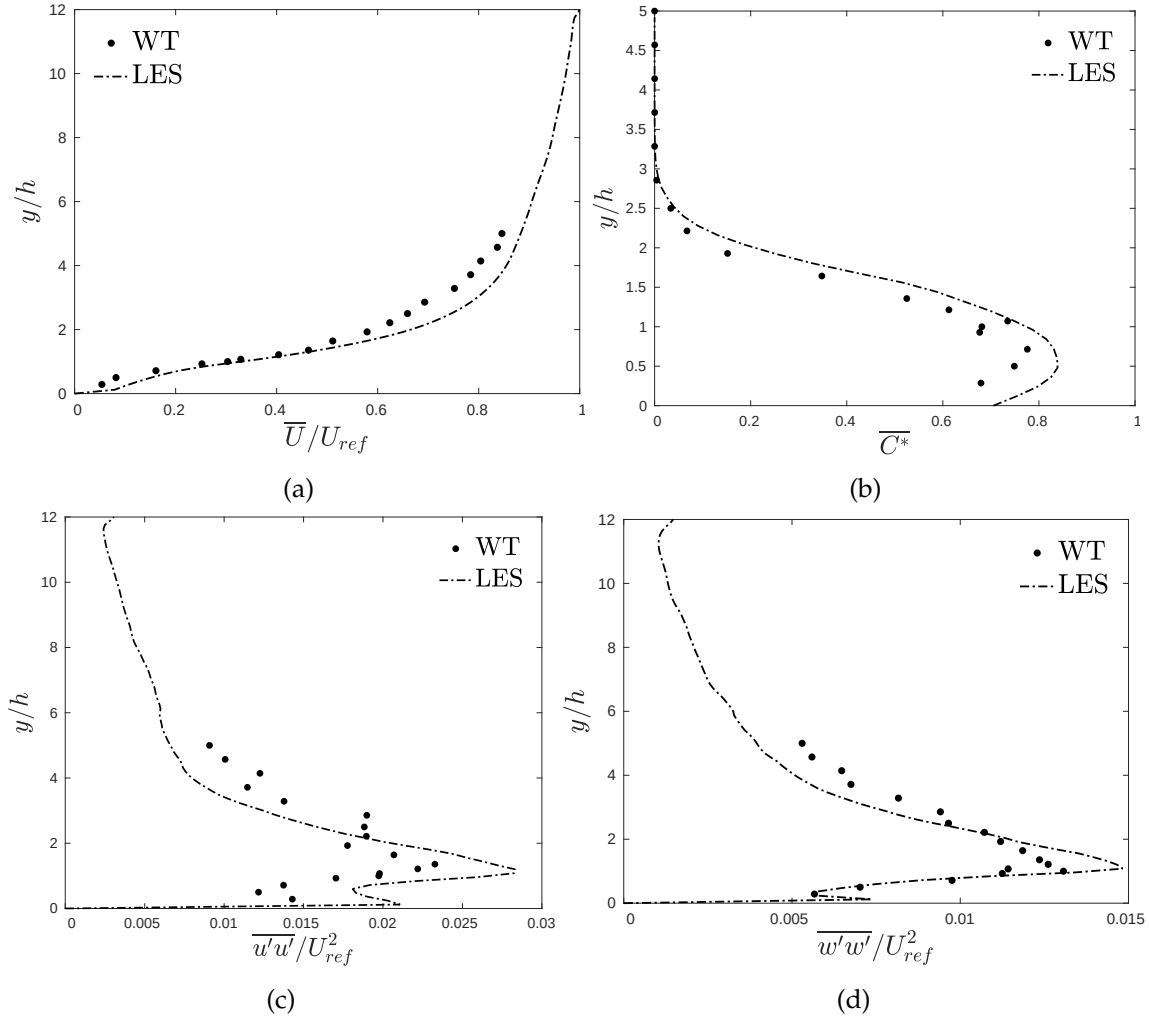

Figure 5.4: (a) LES and wind tunnel vertical profiles of mean velocity, (c) streamwise and (d) lateral turbulent stresses at $x = 17h$.(b) LES and wind tunnel vertical profile of mean concentration of the point source $S2$ at $x = 17h$ and $z = 0h$.

Fig. 5.4b shows the comparison between LES and wind tunnel mean concentration due to point source $S2$. The scalar concentration was normalized as in Eq. 3.10 and measured over a vertical line at $x = 17h$ and $z = 0h$. The comparison shows that LES provided an accurate prediction compared to the experimental mean concentration both below and immediately above the canopy.

5.3 Dispersion (15° wind direction)

Following the dispersion analysis described in Chap. 4, wind variation effects on the exchange of pollutant between the flow within the canopy and the boundary layer above were quantified by computing the total vertical and horizontal fluxes downstream of the line source location.

The vertical total flux is defined as follows (Fuka et al., 2018; Sessa, Xie, and Herring, 2018):

$$\psi_{tot}^{v*} = \overline{V}\,\overline{C}\frac{h^2}{Q} + \overline{v'c'}\frac{h^2}{Q} \tag{5.5}$$

where v' and c' are the vertical velocity fluctuation and the scalar fluctuation respectively, $\overline{V}$ is the mean vertical velocity, $\overline{C}$ is the mean concentration of the line source $S1$ and Q is the emission rate. Similarly, the horizontal total flux in x–direction is defined as in Eq. 4.14.

Fig. 5.5 shows the total vertical flux produced by line source $S1$ for 0° and 15° wind directions under neutral thermal conditions ($Ri = 0$). The flux was integrated at the canopy height ($y = 1h$) across the entire span ($12h$), between two x coordinates a distance of $2h$ apart:

$$\psi^{a,b} = \int\int_{x/h\in(a,b),y/h=1} \psi^{v*} d\left(\frac{x}{h}\right) d\left(\frac{z}{h}\right). \tag{5.6}$$

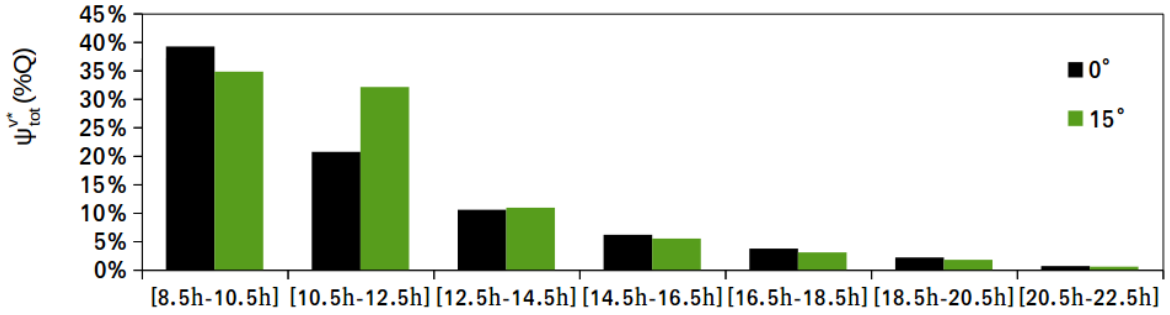

Figure 5.5: Vertical total flux over $2h \times 12h$ horizontal planes ($y = 1h$) in several streamwise locations for 0° and 15° wind direction ($Ri = 0$). The line source is placed at $x = 10h$.

Large vertical fluxes were found over the first location ($x = 8.5h - 10.5h$) because the horizontal plane was placed above the source street ($x = 10h$). However, the vertical transport of pollutant for 0° wind direction was slightly greater than that for 15° wind direction. This was due to the non–zero lateral component of flow direction which caused significant lateral transport of pollutant. As a consequence, the scalar plume for 15° was visibly more advected into the following lateral street ($10.5h - 12.5h$) causing the so–called virtual secondary source. In fact, the vertical transport of pollutant for 15° wind direction was slightly higher than the 0° within the second lateral street. Further downstream, the differences of vertical transport between 0° and 15° wind direction were found to be almost negligible.

Overall, for 15° wind direction the amount of pollutant removed from the canopy layer was found to be only slightly greater than that for 0° flow direction.

The amount of pollutant transported in the horizontal direction was quantified by computing the horizontal total flux in x–direction as in Eq. 4.14 and integrated across the entire span as in Eq. 4.16. Fig. 5.6a shows the amount of pollutant transported below the canopy top ($y = 1h$) in the streamwise direction as the percentage of emission rate Q for 0° and 15° wind direction. Near the line source ($x = 10h$), approximately $\sim 65\%$ of the total emission Q was transported horizontally for 15° wind direction while $\sim 61\%$ for 0°, consistently with Fig. 5.5. Away from the source, the amount of pollutant transported horizontally decreased faster for 15° wind direction compared to 0°. Again this was due to the amount of pollutant removed vertically from the first two lateral streets for 15° wind direction. Far from the source (i.e. $x \geq 16h$), the non–zero flow direction caused the total horizontal flux to decrease by approximately 4%.

Fig. 5.6b shows the total horizontal flux integrated over $2h \times 12h$ vertical planes for 0° and 15° wind direction. Near the line source almost the total emission Q was transported horizontally for $y \leq 2h$ and for both wind directions. Further downstream, the amount of pollutant trapped below $y = 2h$ decreased faster for 15° than for 0° wind direction. For $x \geq 16h$, the total horizontal flux was found to be reduced by $\sim 8\%$ when changing the flow direction by 15°.

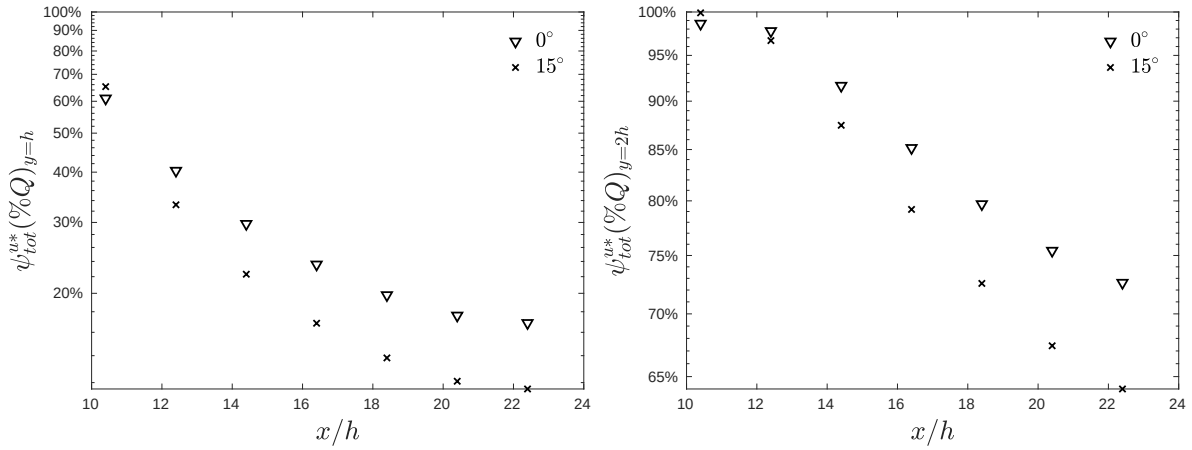

(a) (b)

Figure 5.6: Streamwise total flux over $1h \times 12h$ (a) and $2h \times 12h$ (b) vertical planes in several streamwise locations downstream of the line source (at $x = 10h$).

Fig. 5.7 and Fig. 5.8 show the time–averaged streamwise total flux (Eq. 4.14) over an horizontal plane at $y = 0.5h$ below the canopy, for the 0° and 15° wind direction cases. According to the above analysis, the contour plots show that the amount of pollutant transported at $y = 0.5$ is visibly lower for the 15° wind case compared to the 0°. The figures also suggest that most of the pollutant is transported along the main streets for the 0° wind case. For the non–zero flow direction, the channelling along the street is less evident and the additional

turbulence generated at the building's corner caused increased vertical transport within the near–source two lateral streets.

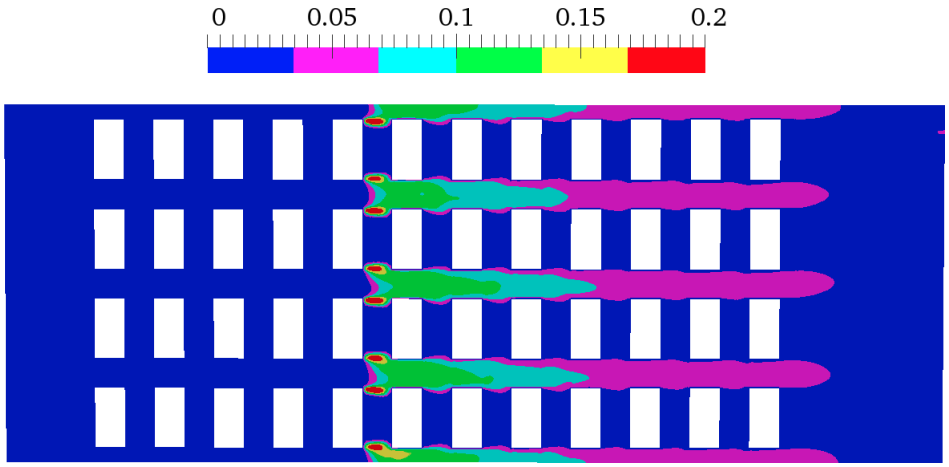

Figure 5.7: Streamwise total flux $\overline{UC}$ contours over an horizontal plane at $y = 0.5$ for 0° wind direction ($Ri = 0$).

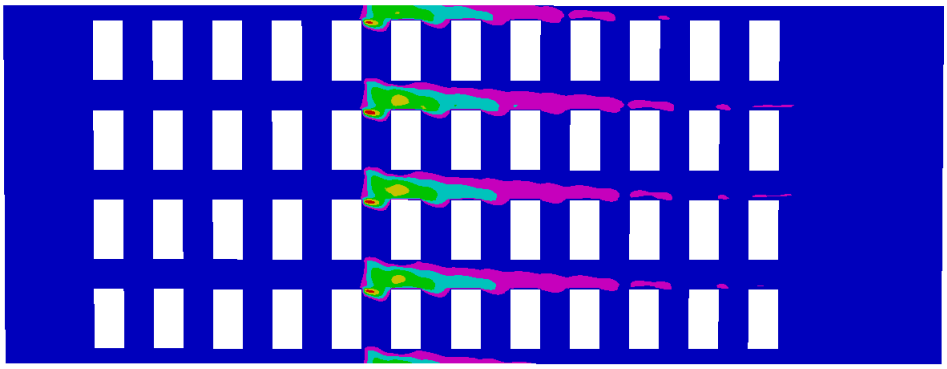

Figure 5.8: Streamwise total flux $\overline{UC}$ contours over an horizontal plane at $y = 0.5$ for 15° wind direction ($Ri = 0$).

As mentioned in Chap. 1, the surface drag can vary substantially if the prevailing wind direction is not in–line with the main streets of a regular array of cuboid elements (Britter and Hanna, 2003; Claus et al., 2012). The increase of surface drag leads to increasing turbulent kinetic energy which was found to be beneficial to pollutant ventilation within and immediately above the canopy.

The scalar concentration of the line source was normalized as in Eq. 4.8 and averaged over several volumes with dimensions $1h \times 1h \times 12h$ (Eq. 4.17). The volume–averaged concentration within the source street ($x = 9.5h - 10.5h$, Fig. 5.9) was found to be more or less similar for both wind directions, although slightly greater for 15°. On the contrary, the mean concentration for 15° was slightly lower than that of 0° within the following lateral street because more pollutant was removed vertically from the canopy layer (Fig. 5.6a). Further downstream, the volume-average concentration was found to be reduced by approximately 15% for 15° wind direction compared to 0°. We concluded that the volume–averaged con-

centration from a ground–level line source is slightly affected by a small variation of the mean wind direction.

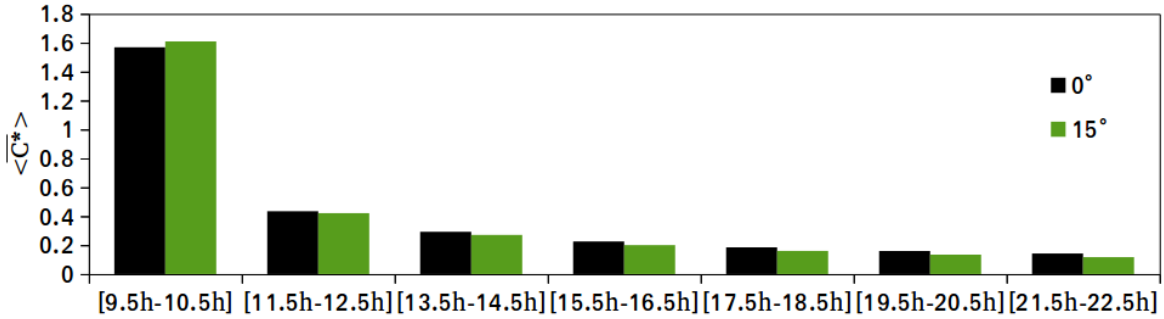

Figure 5.9: Volume–average of normalized mean concentration within lateral streets, from the ground to the canopy height $y = 1h$. The lateral source street is placed at $x = 9.5h - 10.5h$.

5.4 Numerical settings of LES 45° wind direction

The inflow turbulence method (Xie and Castro, 2008) was used at the LES inlet to generate a mean wind rotated by 45° in the clockwise direction from $z/h = 0$ (Fig. 5.10). Again, the experimental mean velocity measured upstream of the leading edge in weakly stable conditions ($Ri = 0.2$) (Marucci and Carpentieri, 2020) was rotated by 45° and prescribed with turbulent stresses at the LES inlet (Fig. 5.3). As in the previous case, the wind tunnel experiment of 45° wind direction was carried out by using a wind direction parallel to the side walls and by rotating the urban array of 45° in the anti–clockwise direction (Marucci and Carpentieri, 2020).

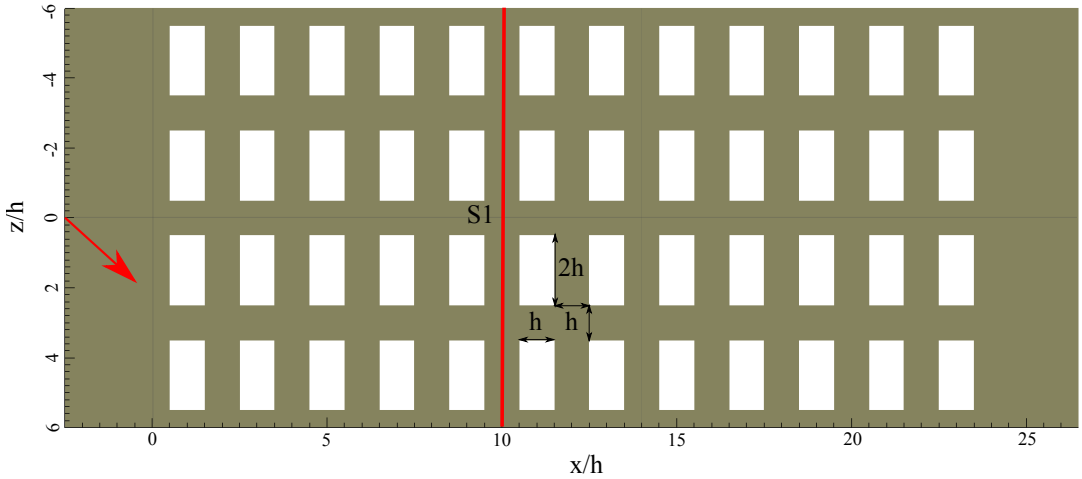

Figure 5.10: Plan view of the LES array configuration showing dimensions of buildings and streets, coordinate system, the flow direction rotated by 45° in the clockwise direction from $z/h = 0$, and locations of line source $S1$.

5.5 Validation of flow and turbulence (45° wind direction)

LES mean velocity and turbulent stresses for 45° ($Ri = 0.2$) wind direction were compared with experimental data obtained in the environmental wind tunnel at University of Surrey (Marucci and Carpentieri, 2020). Numerical results were averaged over four identical locations in the street intersections ($x = 16h$, Fig. 5.10). Wind tunnel measurements were sampled in the same locations and averaged over time ($2.5min$) only. The standard error of the experimental data was around $\pm 1\%$ for mean velocity and $\pm 5\%$ for turbulent variances.

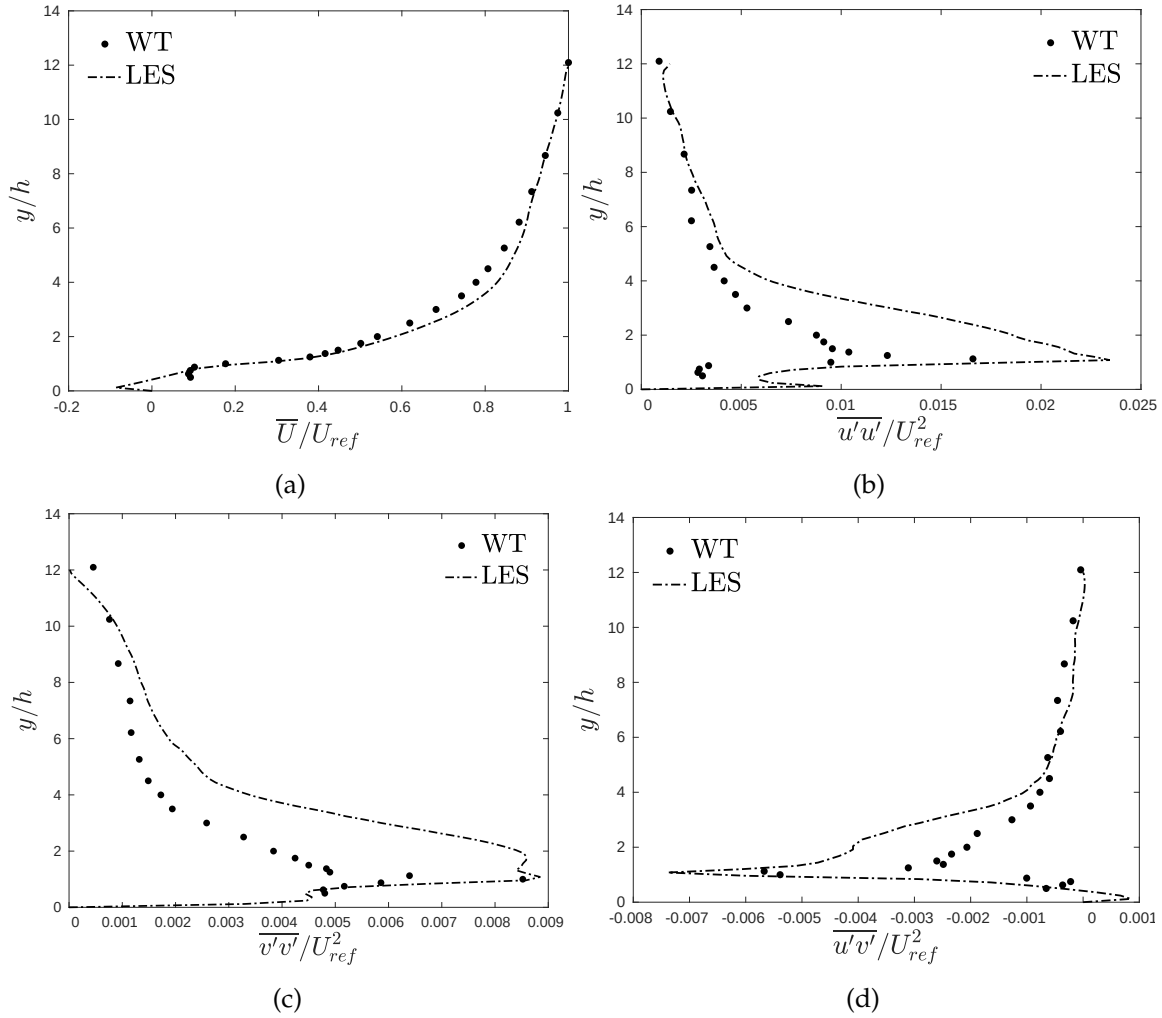

Figure 5.11: (a) LES and wind tunnel vertical profiles of mean velocity, (b) streamwise, (c) vertical and (d) turbulent shear stresses over street intersections at $x = 16h$.

Fig. 5.11a shows that the inflow method for the 45° wind direction predicted the experimental mean velocity with high accuracy below the canopy and well above it. However, experimental streamwise (Fig. 5.11b), vertical (Fig. 5.11c) and turbulent shear stresses (Fig. 5.11d) were visibly over–predicted immediately above the canopy. This was mainly due to the different wind configuration at the leading edge of the LES array compared to the wind tunnel (i.e. Fig 5.12).

In the experimental set–up of Marucci and Carpentieri (2020), the 45° wind direction was performed by assuming the wind flow parallel to the lateral walls of the wind tunnel and the original array (Castro et al., 2017) rotated by 45° in the anti–clockwise direction. The experimental array was trimmed at 45° to avoid flow separation at the upper–right corner and the leading edge (red line) is shown in Fig. 5.12. On the contrary, the 45° wind direction was simulated in the LES model by simply rotating the flow direction and assuming an infinitely–wide array. The CFD leading edge is shown with a blue line in Fig. 5.12.

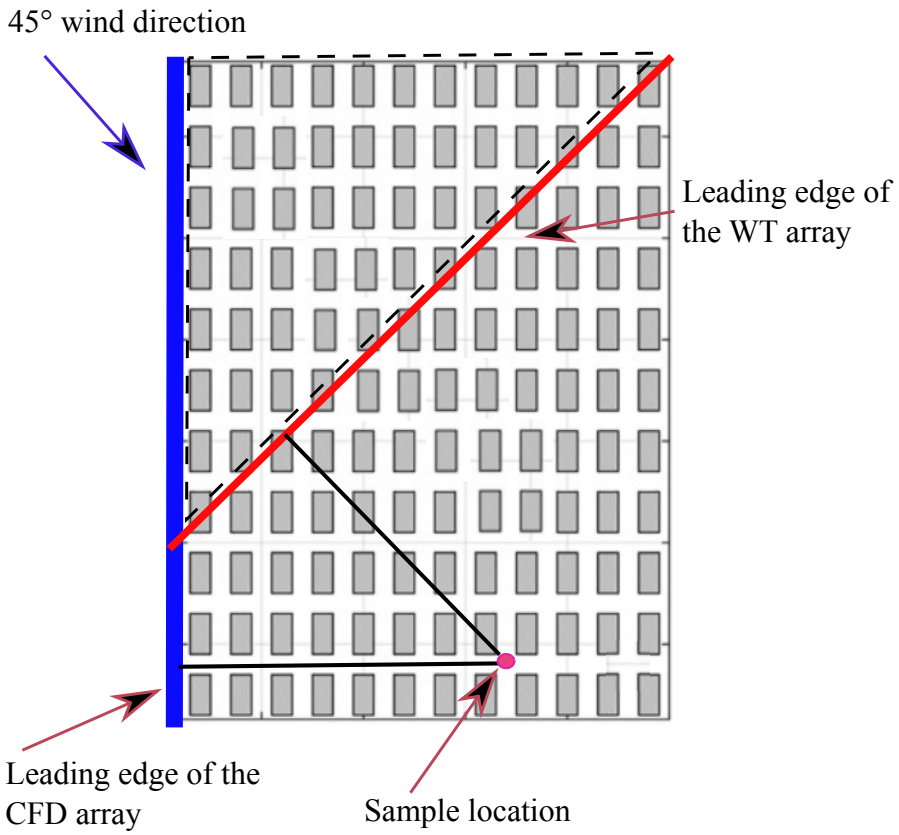

Figure 5.12: LES and wind tunnel configuration for the 45° wind direction. The CFD and wind tunnel leading edges are shown with blue and red lines respectively.

Although LES and experimental mean velocity and turbulent stresses (Fig. 5.11) were sampled at the same distance from the leading edge ($x = 16h$), the LES TKE immediately above the canopy was much greater than that of the wind tunnel experiment due to the additional rows of buildings on the upper–left side of the CFD model (dashed black line in Fig. 5.12). These rows of buildings were omitted in the wind tunnel configuration and as a result, the experimental Reynolds stresses were found to be evidently lower than those from LES. Moreover, Marucci and Carpentieri (2020) found that the plume centreline from the ground–level point source deviated from the 45° wind direction by a certain angle in the clockwise direction, indicating a strong flow within and immediately above the canopy along the long street. A finite width of the array constraints this flow to some extent and the effects of the missing upper rows of buildings would be more evident.

We claim that the LES wind configuration at inlet is more realistic than the wind tunnel approach as it is a better simulation of the idealised case of flow crossing an infinite discontinuity in surface at an angle. Assuming the successfully validation of LES with the inflow method against wind tunnel measurements for the 15° wind direction, the analysis of the 45° was used to investigate flow and dispersion mechanisms further.

The LES and wind tunnel comparison improved significantly above $y \sim 5h$ because, well above the canopy, the turbulence is mostly influenced by the inflow turbulent conditions rather than the array configuration. Below the canopy, mean flow and turbulence are driven by the mechanical mixing induced by the shape of the obstacles and street configuration. For this reason, LES turbulent stresses were found to be in good agreement with wind tunnel measurements below the canopy.

5.6 Dispersion (45° wind direction)

Wind direction effects on dispersion in weakly stable conditions were analysed by computing the total vertical flux produced by the line source in several streamwise locations. The vertical flux was integrated at the canopy height ($y = 1h$) across the entire span ($12h$) as in Eq. 5.6 for both 0° and 45° wind directions.

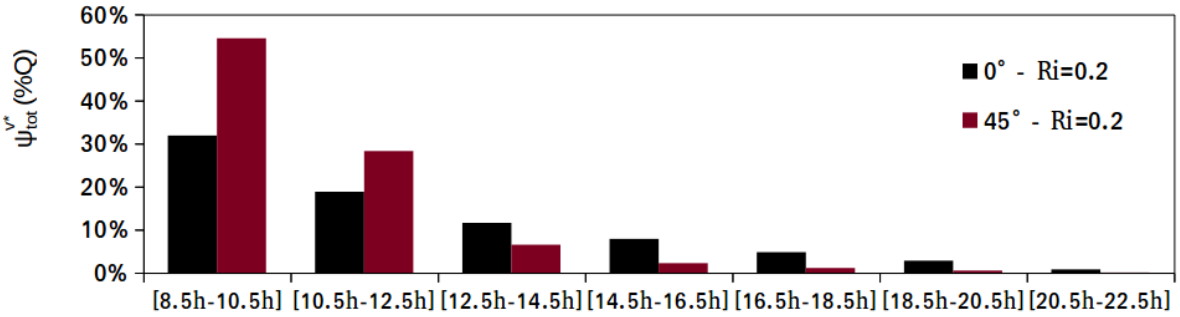

Figure 5.13: Vertical total flux over $2h \times 12h$ horizontal planes ($y = 1h$) in several streamwise locations for 0° and 45° wind direction ($Ri = 0.2$). Line source is placed at $x = 10h$.

Fig. 5.13 shows that within the source street ($z = 8.5h - 10.5h$) the amount of pollutant removed from the canopy layer increased by more than 20% for the 45° wind direction compared to 0°. Similarly, within the following lateral street ($x = 10.5h - 12.5h$) the percentage of total vertical flux increased by approximately 10%. Further downstream ($x \geq 12.5h$) the vertical flux for 45° wind direction was found to be lower than that of 0°. As mentioned above, for the 45° case the wind flow is inclined by a prominent angle which leads to additional flow separation at the upwind corner of the cuboid elements. As a result, the ventilation close to the source is enhanced by the increased turbulent kinetic energy. Fig. 5.13 shows that more than 80% of the total emission Q was removed from the first two lateral streets for the 45° wind direction case. This amount of pollutant was found to be more than 20%

greater than that of the 15° case in Fig. 5.5, although for a slightly different level of thermal stability. The results show that wind direction was the dominant factor in determining the exchange of pollutant between the canopy flow and the boundary layer above.

The total horizontal flux in the streamwise direction was again computed as in Eq. 4.14 and integrated across the entire span (Eq. 4.16). Fig. 5.14a shows the amount of pollutant transported below the canopy for both 0° and 45° wind directions. Because of the amount of pollutant removed vertically from the source street (Fig. 5.13), for 45° wind direction less than 50% of the emission Q was transported below the canopy into the following lateral street. Compared to 0° flow direction, the total horizontal flux of 45° was found to be $20\% - 30\%$ lower, downstream of the source street. In fact, for $x \geq 16h$ the total amount of pollutant below the canopy dropped to less than 10% of the emission Q.

Similarly, wind variations caused a substantial decrease of pollutant transported below the height $y = 2h$ (Fig. 5.14b). The effects were more visible away from the source (i.e. $x \geq 14h$) where the total horizontal flux for 45° wind direction was found to be approximately 20% lower than that of the 0° case. This again confirms the beneficial effects of wind variation on scalar ventilation below and immediately above the canopy.

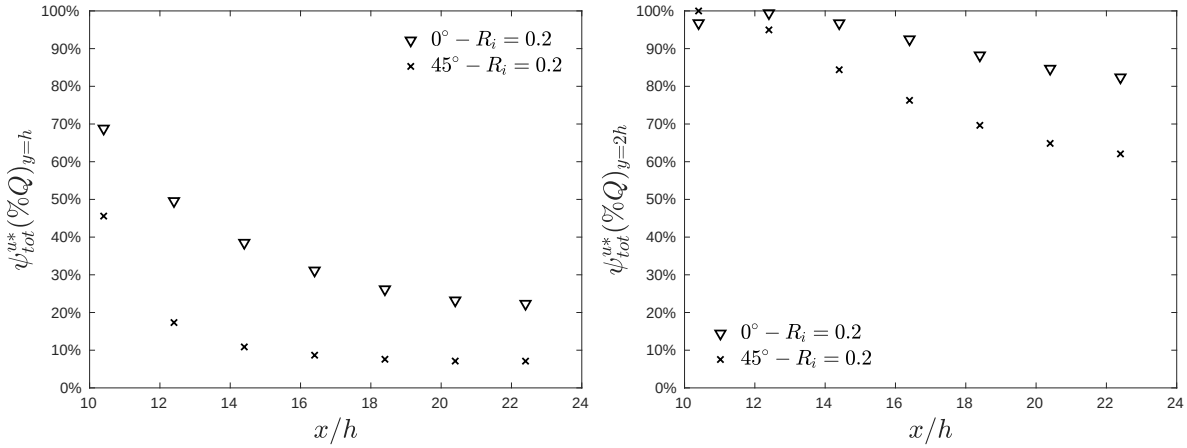

(a) (b)

Figure 5.14: Streamwise total flux over $1h \times 12h$ (a) and $2h \times 12h$ (b) vertical planes in several streamwise locations downstream of the line source (at $x = 10h$).

Hertwig et al. (2018) analysed point source dispersion over the same array of regular cuboid elements by using a combination of high–resolution large–eddy simulation and wind tunnel data. For 45° wind direction, it was found that the scalar plume was transported much faster above the canopy layer than below and at a distance of $4.5h$ from the source, a significant part of the plume was located outside of the urban canopy layer. In this study we were able to quantify the amount of pollutant removed from the urban canopy layer because line source dispersion is a quasi–$2D$ dimensional problem where the plume is laterally homogeneous and so easier to analyse compared to the $3D$ point source dispersion. For example, Fig. 5.14a shows that at $x = 4.5h$ from the source approximately 60% of pollutant was removed from the canopy layer.

Fig. 5.15 and Fig. 5.16 show the time–averaged streamwise total flux (Eq. 4.14) over an horizontal plane at $y = 0.5h$ below the canopy, for the 0° and 45° wind direction cases in weakly stable condtions ($Ri = 0.21$). As discussed above, the contour plots show that the amount of pollutant transported at $y = 0.5h$ is much lower for the 45° wind case compared to the 0°. Again, for the 45° wind direction the channelling along the streets is less evident and the additional turbulence generated at the building's corner caused increased vertical transport near the source. These effects are more evident than for the 15° wind direction (Fig. 5.8) although the thermal stratification conditions are slightly different.

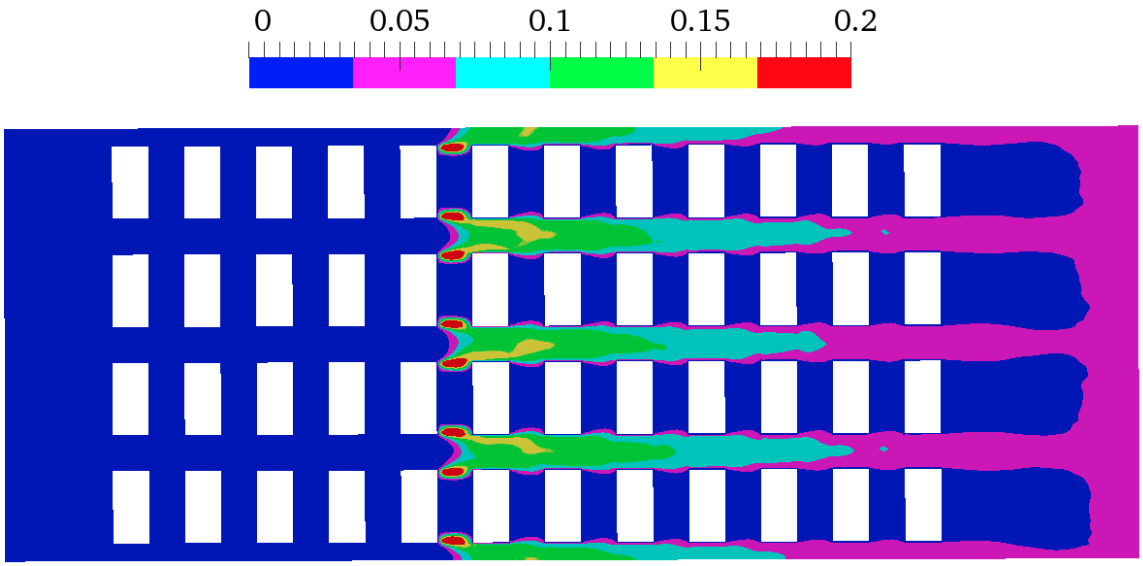

Figure 5.15: Streamwise total flux $\overline{UC}$ contours over an horizontal plane at $y = 0.5$ for 0° wind direction ($Ri = 0.2$).

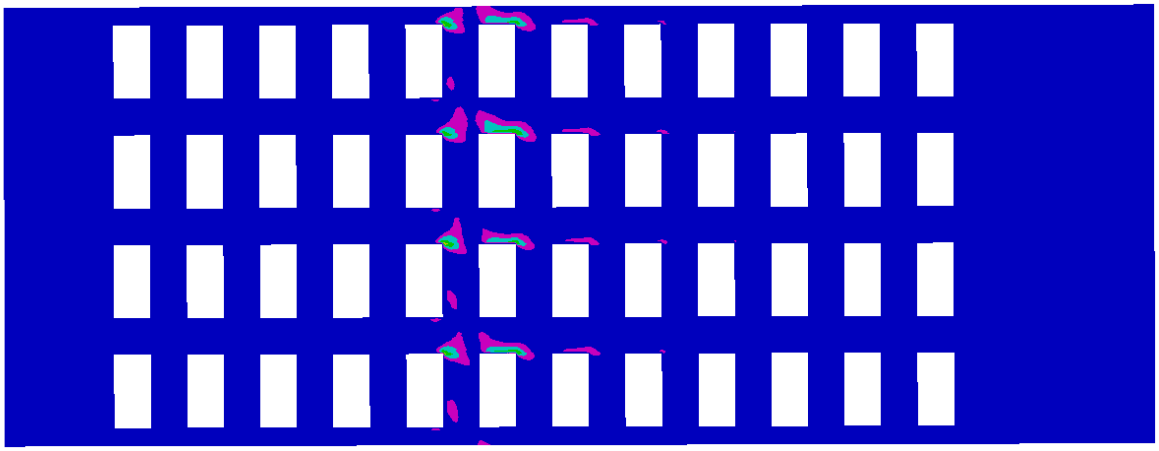

Figure 5.16: Streamwise total flux $\overline{UC}$ contours over an horizontal plane at $y = 0.5$ for 45° wind direction ($Ri = 0.2$).

Lastly, the mean scalar concentration of the line source was averaged over several volumes with dimensions $1h \times 1h \times 12h$ (Eq. 4.17) for 0° and 45° wind direction (Fig. 5.17). Within the source street ($x = 9.5h - 10.5h$) the volume–average concentration was found to be almost

insensitive to wind direction. The reason was due to the increased vertical flux for 45° (*i.e.* + 25%, Fig. 5.13) which was balanced by the reduced horizontal flux (*i.e.* − 25%, Fig. 5.14a), compared to the 0° wind direction. However, the wind variation effects were dominant away from the source. For example, within the fourth lateral street ($x = 15.5h - 16.5h$) the volume–average concentration decreased by approximately 40% below the canopy, and even more further downstream. As shown in Fig. 5.9, the 15° wind variation in neutral thermal conditions caused a decrease of $\sim$ 15% of volume–average concentration. Therefore, it was concluded that the increasing rotation of the flow direction up to 45° leads to a significant decrease of volume–average concentration below the canopy. Moreover, these conclusions were conservative because the 45° wind direction was simulated at $Ri = 0.2$ so the vertical exchange would be greater and mean concentrations reduced even further if it was at neutral conditions.

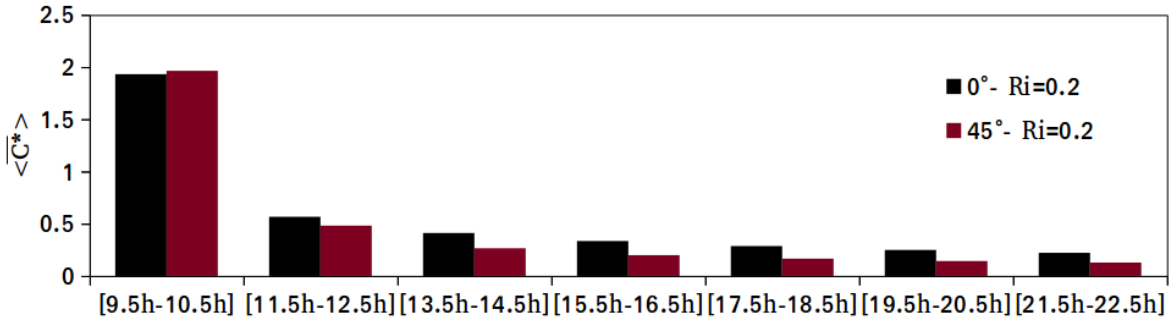

Figure 5.17: Volume–average of normalized mean concentration within lateral streets, from the ground to the canopy height $y = 1h$. The lateral source street is placed at $x = 9.5 - 10.5h$.

5.7 Conclusions and discussion

Wind direction effects on turbulence and dispersion were analysed by using LES with inflow turbulent conditions over a rural–to–urban transition region. LES mean flow and turbulent statistics were validated against wind tunnel experiments of 15° wind direction at $Ri = 0$ and 45° wind direction at $Ri = 0.2$. Compared to the 0° wind direction (Sec. 3.4.1), we found that rotation of the wind direction (i.e. 15° and 45°) led to less accurate agreement of turbulent statistics between LES and wind tunnel experiments in the region immediately above the canopy. The discrepancies were due to the lower turbulent kinetic energy produced by the experimental array of limited lateral dimensions compared to the LES array of periodic lateral conditions. The effects were considerable for the 45° wind direction.

Wind direction effects on dispersion were analysed by comparing LES vertical and horizontal total fluxes for 15° and 45° wind direction against LES of 0° at $Ri = 0$ and at $Ri = 0.2$ respectively. It was found that the amount of pollutant transported below the canopy was significantly reduced because the turbulence near the ground was enhanced for a mean wind direction inclined to a different angle from the main streets. The effects were greatest for the 45° wind direction. The comparison between LES of 15° against 0° suggested that the

volume–average concentration below the canopy was almost insensitive to small variations of wind direction. In contrast, the comparison between LES of 45° against 0° showed that the volume–averaged concentration below the canopy was evidently reduced. This confirmed that the natural ventilation below the canopy was greatly improved for the non–zero wind direction, even in weakly stratified thermal conditions. Further to previous studies, we were able to quantify the amount of pollutant removed from the urban canopy layer at any distance from the source and in neutral and weakly stable stratification conditions.

6 On the effects of wind velocity and direction on point source dispersion in rural environment

In this study, a field experiment of gas dispersion in a rural environment was modelled by using full–scale LES with turbulent inflow conditions. LES results of mean concentration were compared against real–field measurements and the predictions of the Urban Dispersion Model (UDM) (Guy and Herring, 2016). It was found that field measurements were sensitive to wind conditions, in fact similar wind directions but different wind speeds produced different dispersion scenarios in the real field. LES performed similar to the UDM model but predicted the lateral mean concentration better, although the accurate prediction of field measurements was hard to achieve. Lastly, it was found that LES dispersion over a relatively smooth surface (i.e. uniform mowed grass) was sensitive to source size differences in the near–field but not in the far–field.

6.1 Introduction

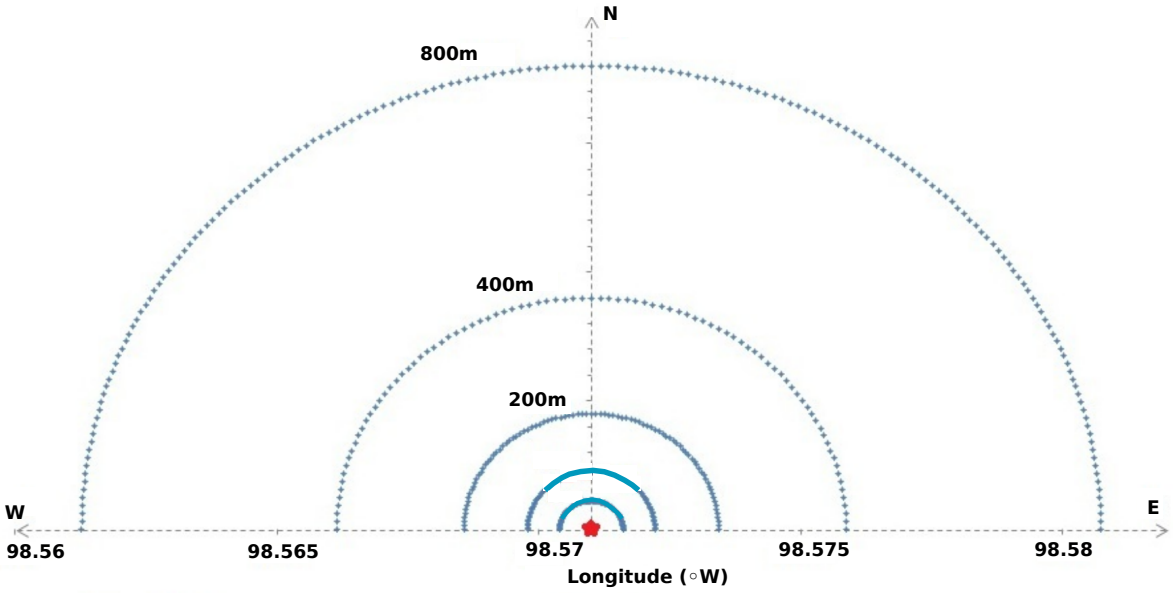

Figure 6.1: Illustration of source location (red star) and samplers at a height of 1.5m from the ground on arcs up to 800m downwind of the source (Guy and Herring, 2016).

In the summer of the 1956 one of the most comprehensive dispersion experiments with name 'Project Prairie Grass' was carried out in Nebraska (Barad, 1956). The experiment involved nearly 70 releases of SO_2 of 10 and 20 minutes durations with concentration sampled at a height of 1.5m on arcs up to 800m downwind of the source Fig. 6.1. During the experiment, SO_2 concentrations, wind, temperature and humidity profiles were measured and the large dataset has been used to assess and validate theories on dispersion mechanisms within the atmospheric boundary layer.

Guy and Herring (2016) conducted a study to assess the performance of the Urban Dispersion Model (UDM) against data from the Prairie Grass experiment. UDM is a Gaussian puff model which uses empirical relationships to predict dispersion in open terrain (Guy and Herring, 2016). A total of 52 concentration releases in unstable, neutral and stable thermal conditions were compared at a height of 1.5m on arcs up to 800m downwind of the source. It was found that the UDM dispersion model produced good predictions in neutral and nearly neutral conditions for wind speed above $5m/s$. However, the model performance decreased rapidly for wind speeds below $5m/s$, maybe due to less accurate prediction of scalar turbulent diffusion which dominates at low wind speeds.

In this section, LES with the inflow turbulent conditions was used to simulate the dispersion from a ground–level point source in a rural environment. The aim was to assess LES predictive performance against data produced by the UDM dispersion model (Guy and Herring, 2016) and field measurements (Barad, 1956) for different velocities and wind directions.

6.2 Numerical Settings

The biggest challenge of modelling the Prairie Grass study is to simulate dispersion from a $50.8mm$ diameter pipe source at a height of $0.46m$ within the atmospheric boundary layer over an area of $800m^2$ ($Re \propto 10^6$). Guy and Herring (2016), used a $1m$ diameter spherical source over an empty ground ($4000m \times 4000m$) with surface roughness length $y_0 = 0.006m$ and derived Monin–Obukhov lengths (Nieuwstadt and Ulden, 1978) for each release. The UDM dispersion model assumed SO_2 concentrations following a Gaussian distribution downwind of the source.

The wall model is an important issue for LES if the near–wall mesh is not fine enough to resolve the viscous sublayer. Although computational power is increasing rapidly, it is still impossible to reproduce a ground surface of mowed grass within the atmospheric boundary layer, therefore a rough–wall model has to be used. This LES study considered the Spalding rough–wall function (Launder and Spalding, 1974) implemented in OpenFOAM to model the ground surface by prescribing the roughness length y_0. This meant that it was assumed that the centroid of the cell next to the wall falls within the logarithmic region of the boundary layer:

$$u = \frac{u_*}{\kappa} ln \left[\frac{y}{y_0} \right], \tag{6.1}$$

where the von Karman constant was $\kappa = 0.41$ and the roughness length $y_0 = 0.006m$ was estimated over an empty ground area by UDM in Guy and Herring (2016). The friction velocity u_* was assumed to be constant near the ground and calculated for each wind scenario by substituting in Eq. 6.1 the field measurements (Barad, 1956) of $20min$–average wind velocity at $y = 2m$.

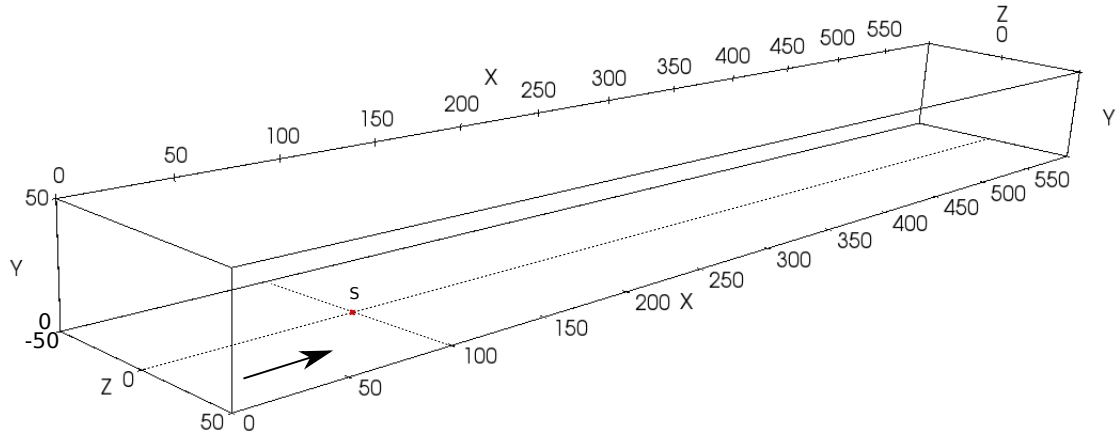

Figure 6.2: Schematic view of the modelling domain, including the size $600m \times 50m \times 100m$ and the location $X_S = 100m$ of the ground source S.

The inflow turbulent method developed by Xie and Castro (2008) was used at the inlet ($X = 0m$) of a plane channel flow of dimensions $600m \times 50m \times 100m$ (Fig. 6.2), with periodic conditions at the lateral boundaries and stress–free condition at the top of the domain ($H = 50m$). Because the point source S was positioned very close to the ground (i.e. $Y \leq 1m$, $X = 100m, Z = 0m$), the height of the domain was assumed to be conservative enough to capture the most important turbulent features near the wall (i.e. $Y = 1.5m$). The lateral and longitudinal size of the domain were chosen in order to capture the lateral spreading of the plume and to allow a fully developed turbulent flow respectively ($Re \propto 10^6$).

It has been widely shown that accurate LES predictions are achieved over regular urban and rural–to–urban geometries by using a grid resolution of $h/15$ (Cheng and Porte-Agel, 2016) or $h/16$ (e.g. Sessa, Xie, and Herring, 2018; Castro et al., 2017). Over more complex urban geometries which include building height and shape variations, finer resolution is typically required. For example, Xie and Castro (2009) found that a resolution down to $1m$ (i.e. $h/20$) was reasonable to produce sufficiently accurate LES predictions over a genuine urban geometry. However, Xie and Castro (2009) used an unstructured non–hexahedral mesh with separate region refinements in the streamwise and vertical directions.

In this study we used a Cartesian hexahedral mesh with grid refinements in the vertical and lateral directions. Uniform hexahedral meshes are known to be more accurate than polyhedral meshes due to the simpler approximation (i.e. linear) and higher efficiency. We

used a uniform grid resolution of $0.25m$ near the ground for our course–mesh cases ($LES1$ and $LES2$) which is much finer than the suggested value of $1m$ for accurate LES predictions over complex urban geometries. Moreover, the geometry simulated in this study represents an ideal rural surface where the flow features are less complex than urban–type flows.

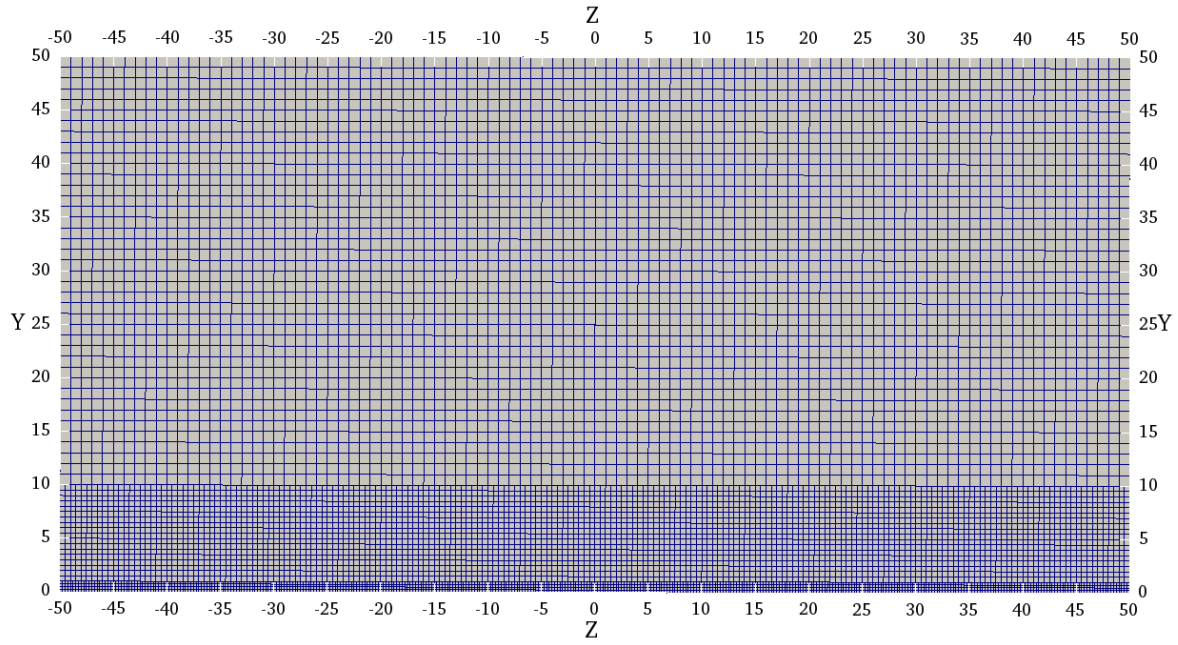

Figure 6.3: Cross–section of the first mesh configuration with three grid refinements: fine resolution $0.25m$ for $Y \leq 1m$, medium resolution $0.5m$ for $1m < Y \leq 10m$ and coarse resolution $1m$ for $10m < Y \leq 50m$.

This LES study was performed by using two different mesh configurations with similar numbers of cells (10^7). The first model used a uniform Cartesian mesh with three grid refinements in the vertical direction (cross–section in Fig. 6.3), whereas the second model used four mesh refinements, radial to the source location $Z = 0$ (Fig. 6.4). Within the first model, a fine resolution of $0.25m$ was applied up to the height of $Y = 1m$ from the ground in order to simulate the spherical source $S1$ with diameter $d_{S1} = 1m$ and centre height $h_{S1} = 0.50m$. A medium resolution of $0.50m$ was used from the height of $Y = 1m$ to $Y = 10m$ and a coarse resolution of $1m$ was used from the height of $Y = 10m$ to the top of the domain ($H = 50m$). The first mesh configuration was also used to simulate a second spherical source $S2$ with diameter $d_{S2} = 0.5m$ and centre height $h_{S2} = 0.5m$ in order to quantify the effects of reduced source size on dispersion, downwind of the source location.

The second mesh configuration (cross-section in Fig. 6.4) used a very fine resolution of $0.125m$ near the source from $Z = -5m$ to $Z = 5m$ and up to $Y = 1m$ from the ground. A fine resolution of $0.25m$ was then used radially from $Z = -10m$ to $Z = 10m$ and up to $Y = 5m$ from the ground, a medium resolution of $0.5m$ from $Z = -18m$ to $Z = 18m$ and up to $Y = 15m$ from the ground and lastly, a coarse resolution of $1m$ in the outer domain. The four mesh refinements were applied in the lateral direction only, so that semi–cylindrical re-

gions of increasing resolution were obtained from inlet ($X = 0m$) to outlet ($X = 600m$) (top view in Fig. 6.5). Within the second mesh configuration, a third spherical source $S3$ with diameter $d_{S3} = 0.25m$ and centre height $h_{S3} = 0.50m$ was simulated with LES. Dispersion predictions from the small source $S3$ ($LES3$) were compared against LES of the medium size source $S2$ ($LES2$) and LES of the big size source $S1$ ($LES1$).

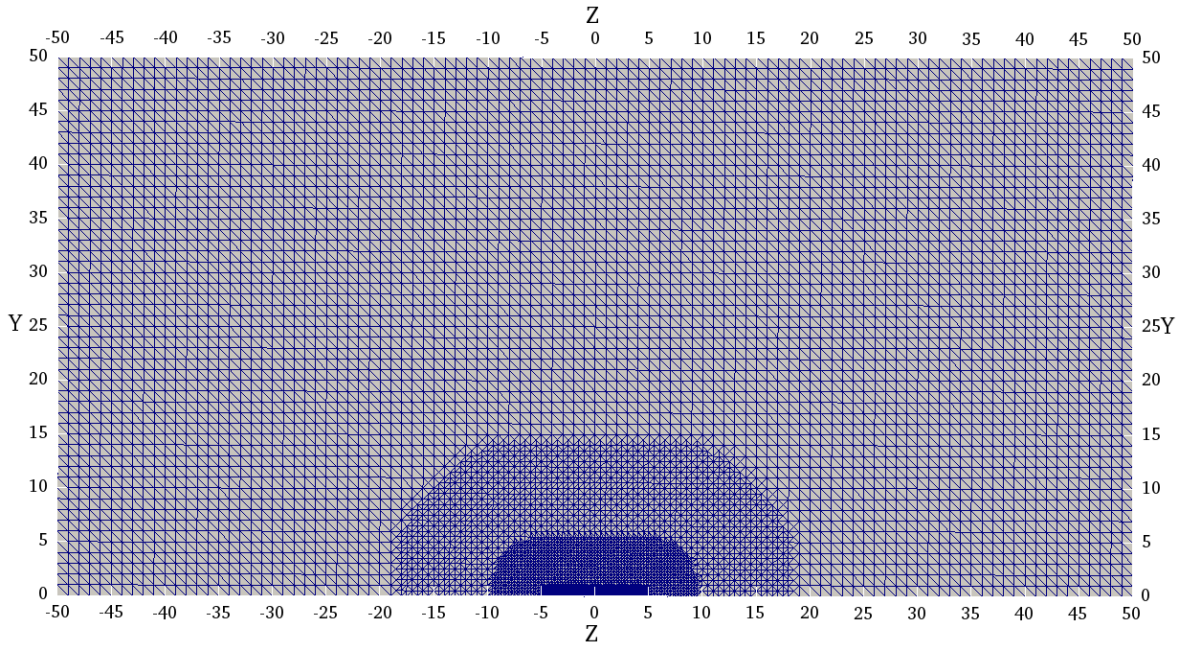

Figure 6.4: Cross–section of the second mesh configuration with four grid refinements: very fine resolution $0.125m$ for $Y \leq 1m$ and $-5m \leq Z \leq 5m$, radial fine resolution $0.25m$, medium resolution $0.5m$ and coarse resolution $1m$ up to the domain top $Y = 50m$.

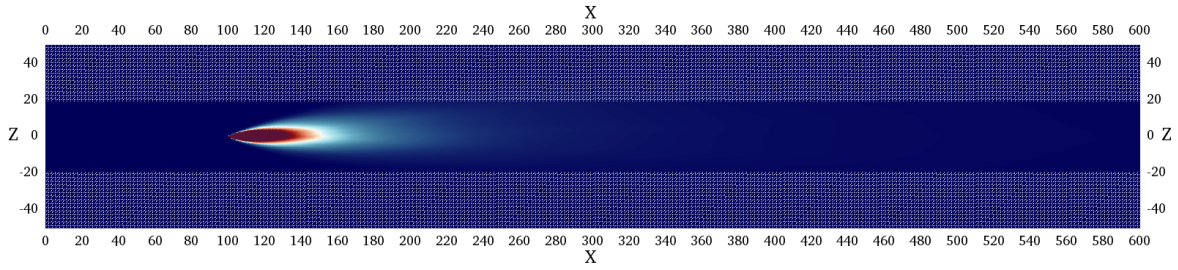

Figure 6.5: Top view of the second mesh configuration showing the lateral scalar spreading from the ground source S captured by the mesh refinement over the centreline.

6.3 Flow and turbulence

As mentioned above, the ground surface of mowed grass was modelled in LES by using the Spalding rough–wall function (Launder and Spalding, 1974) with prescribed roughness

length $y_0 = 0.006m$. The use of a rough–wall function is advisable when simulating the flow over spatially–homogeneous and very complex geometries with limited computational resources. However, the big issue for even the most recently–implemented rough–wall functions is that the turbulent kinetic energy prescribed at inlet decays rapidly within the domain because it is not properly sustained by the modelled ground surface.

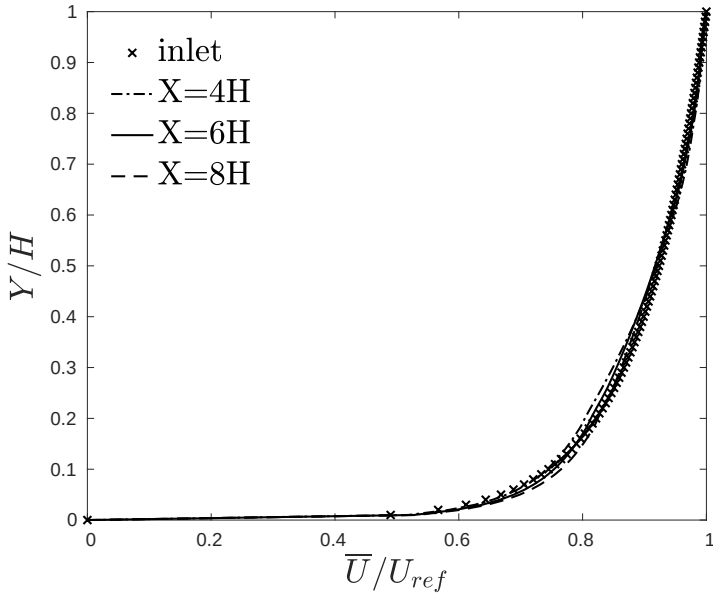

Figure 6.6: Vertical profiles of laterally averaged mean velocity prescribed at inlet and further downstream at $X = 0m$, $X = 4H$, $X = 6H$ and $X = 8H$, where $H = 50m$.

In this LES study we found that the Spalding rough–wall function implemented in OpenFOAM v.2.1 performed surprisingly well, providing an accurate prediction of the prescribed mean flow and second–order statistics, even far from the inlet.

Fig. 6.6 shows the comparison of mean velocity profile prescribed at inlet (Eq. 6.1) and mean velocity at the streamwise distances of $X = 4H, 6H, 8H$ where H is the height of the domain. The velocity profiles were laterally averaged over several points and normalized by the reference velocity $U_{ref} = 10.5m/s$ at the top of the domain. The comparison shows that within a distance of $X = 8H$ $(400m)$ from the inlet, the differences of laterally–averaged mean velocities were negligible. This confirmed that the mean flow was accurately sustained by the rough–wall model.

In order to evaluate the performance of the rough–wall function in more detail, the streamwise, vertical, lateral turbulent stresses and TKE were compared in Fig. 6.7. Because the turbulent stresses were not provided in the Prairie grass experiment, the prescribed turbulent stresses at inlet were estimated from wind tunnel experiments (Castro et al., 2017), scaled by the friction velocity and assumed to be constant near the ground surface. The mean vertical profiles of turbulent stresses were normalized by the reference velocity U_{ref} and laterally averaged over several points.

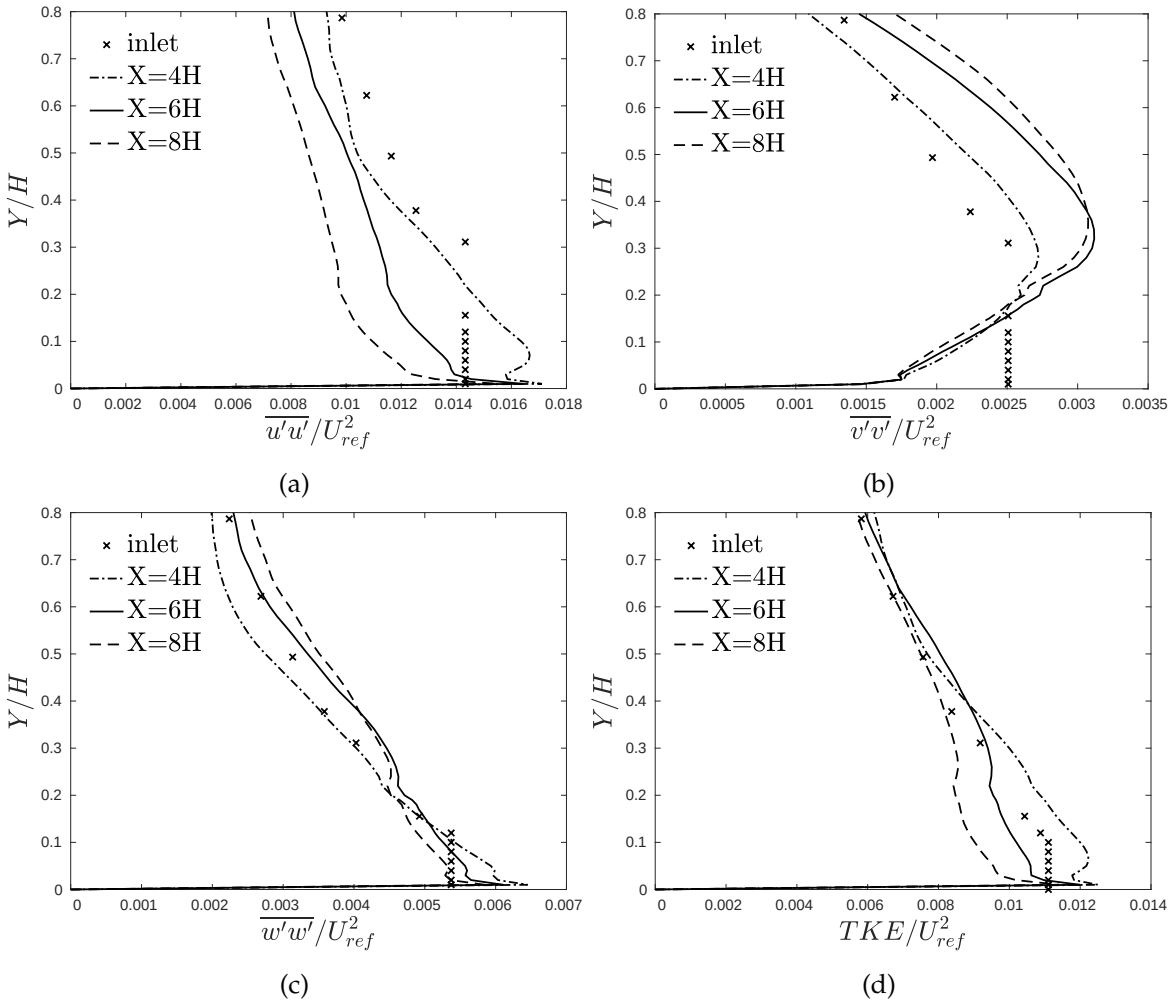

Figure 6.7: Vertical profiles of laterally averaged streamwise (a), vertical (b), lateral (c) and turbulent kinetic energy (d) prescribed at inlet and further downstream at $X = 0m$, $X = 4H$, $X = 6H$ and $X = 8H$, where $H = 50m$.

In Fig. 6.7a the streamwise turbulent stress at $X = 4H$ was found in good agreement with the prescribed stress at inlet although, the inlet profile was slightly over–estimated near the ground. Further downstream the turbulent stress decayed evidently in the vertical direction, nevertheless the peak stress near the ground was found to be approximately constant within a distance of $X = 8H$ from the inlet. Similarly, the vertical turbulent stress prescribed at inlet (Fig. 6.7b) was found to be well sustained by the rough–wall model at $X = 4H$, but differently from the streamwise stress, it was under–estimated near the ground surface. Further downstream, the vertical stress profiles were found to be visibly enhanced but in agreement below the height of $Y = 0.2H$ from the ground with constant peak stress localized at around $Y = 0.3H$.

In Fig. 6.7c, the lateral turbulent stress prescribed at inlet was found in good agreement with lateral stresses at $X = 4H, 6H, 8H$ near the ground surface and well above. Again, the peak stress near the ground surface was found to be approximately constant within a distance of $X = 8H$ from the inlet. Lastly, Fig. 6.7d summarise the turbulent kinetic energy

prescribed at inlet and further downstream at $X = 0m$, $X = 4H$, $X = 6H$ and $X = 8H$. The comparison shows that the wall model sustained the flow energy accurately. The turbulent kinetic energy at $X = 4H$, $X = 6H$ and $X = 8H$ was found in good agreement with the prescribed kinetic energy at inlet, near the ground and well above. This also confirmed that the size of the domain was reasonable and the mesh resolution was fine enough to preserve second–order statistics. Overall, it was found that the the Spalding rough–wall function performed well for second–order statistics. The above–described differences between the downstream stress profiles and the prescribed turbulent stresses at inlet were maybe due to not accurate turbulence assumptions made at inlet.

6.4 Results

Table 6.1: Analysed field measurements including the mean wind speed at $2m$ from the ground, wind direction (0°N) and the release rate from the source (kg/s).

Case	$\overline{U}$ (m/s)	Wind direction (0°N)	Release rate (kg/s)
6^*	6.8	0	0.0895
11	7.03	5	0.0959
20	8.6	12	0.1012
21	6.12	13	0.0509
22^*	6.42	10	0.0484
23	5.91	48	0.0409
24	6.22	34	0.0412
31	7.33	-24	0.0960
38	4.14	19	0.0454

The UDM and experimental $20min$–average concentration of SO_2 in several wind scenarios (neutral and weakly non–neutral thermal conditions) were normalized as in Eq. 3.10 and compared with predictions by LES. For each wind scenario the observed wind speed and direction were averaged in time ($20min$) and the reference velocity U_{ref} at $Y = 50m$ was obtained from Eq. 6.1, while the reference length was set to $L_{ref} = 1m$.

Because of the effects of the source size in the near–field, LES mean concentration was normalized by the average experimental peak mean concentration at $X - X_S = 50m$, where X_S is the source location. LES normalized mean concentration $\overline{C^*}$ from the source $S1$ (LES1, Fig. 6.8a), the source $S2$ (LES2, Fig. 6.8b) and the source $S3$ (LES3, Fig. 6.9) were compared against normalized mean concentration from the field experiment (Barad, 1956) and the UDM model (Guy and Herring, 2016) over the centreline. The figures below show the comparison in $\overline{C^*}$–to–$\overline{C^*}$ plots of LES against the field experiment (OBS), LES against the UDM and the UDM against OBS, measured at $X - X_S = 1H, 2H, 4H, 8H$. Table 6.1 shows the field measurements in neutral thermal conditions (Guy and Herring, 2016) used for the comparison with LES and UDM predictions in Fig. 6.8a, Fig. 6.8b and Fig. 6.9. Cases 6^* and 22^* were analysed further in Sec. 6.4.2 and Sec. 6.4.3 respectively.

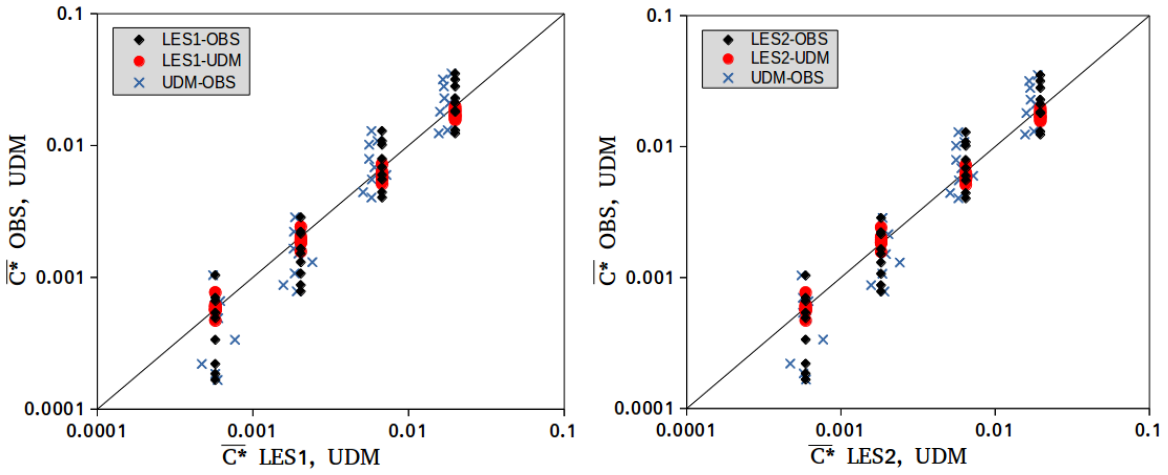

(a) (b)

Figure 6.8: Peak mean concentration comparison over the centreline at $X - X_S = 1H, 2H, 4H, 8H$ between $LES1$ of source $S1$ (a) and $LES2$ of source $S2$ (b) against field measurements (OBS) of Table 6.1 and UDM.

Fig. 6.8a shows that the normalized mean concentration of the big size source $S1$ (LES1) was found in good agreement with results of the UDM model far from the source (i.e. $X \geq 4H$, $\overline{C^*} \leq 0.003$). Near the source (i.e. $X \leq 2H$) UDM predictions were found to be slightly over–estimated by LES maybe due to turbulence differences which certainly affect dispersion near the source. On the contrary, field measurements were found to be well predicted near the source (i.e. $X \leq 2H$) but visibly over–estimated far from the source (i.e. $X \geq 4H$). In this case, good prediction near the source was expected because LES mean concentration was normalized by the field measurement of mean concentration at $X = 1H$ from the source. However, most of the experimental results were over–estimated in the far field because the size of the LES source $S1$ was significantly bigger than the experimental one. Fig. 6.8a as well as Fig. 6.8b and Fig. 6.9 also show a comparison between UDM and field measurements. According to Guy and Herring (2016), most of the field measurements were under–predicted by UDM near the source and over–predicted in the far–field, again due to the size of the UDM source which was significantly bigger than the experimental one.

Fig. 6.8b shows that the normalized mean concentration of the medium size source $S2$ (LES2) was found in good agreement with UDM results far from the source (i.e. $X \geq 4H$, $\overline{C^*} \leq 0.003$) and in fair agreement with those near the source (i.e. $X \leq 2H$). We found that the improvement of UDM prediction in the near–field was due to the reduced size of source $S2$ which led to lower concentrations compared to LES of source $S1$. As a consequence, the prediction of field measurements slightly improved in the far–field because the concentration from the medium size source $S2$ decayed more rapidly than the concentration from the big size source $S1$.

Lastly, Fig. 6.9 shows the comparison between the normalized mean concentration from the small source $S3$ with UDM and field measurements. To be noted that the second mesh configuration with four radial refinements was used for LES of source $S3$. Firstly, it was found

that the prediction of UDM mean concentration further improved near the source, whereas it was slightly over–estimated further downstream. In turn, field measurements in the far–field were found in better agreement with LES of source $S3$ compared to LES of source $S1$ and $S2$. This was due to greater resolution over the centreline and the further reduced size of source $S3$, more similar than $S2$ and $S1$ to the experimental one.

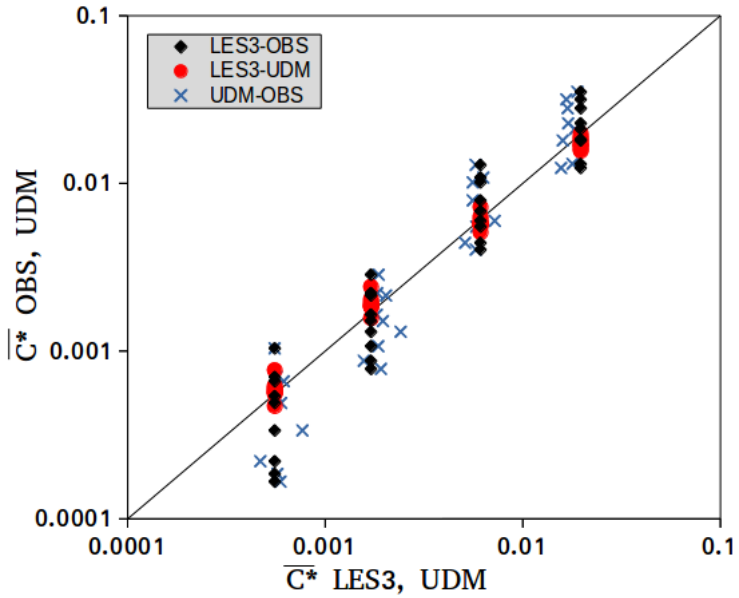

Figure 6.9: Peak mean concentration comparison over the centreline at $X - X_S = 1H, 2H, 4H, 8H$ between $LES3$ of source $S3$ against field measurements (OBS) of Table 6.1 and UDM.

To summarise, within the same mesh configuration it was found that the differences of source size slightly affected the prediction of experimental mean concentration in the far–field (Fig. 6.8a and Fig. 6.8b). Obviously, the prediction further improved for the second mesh configuration (Fig. 6.9) with high resolution in the region of interest (i.e. over the centreline). The above–described discrepancies between LES and experimental mean concentration were certainly affected by temporal variations of wind speed and direction within the $20min$–average window. In fact, small variations of wind direction in the real field may enhance lateral and vertical scalar spreading leading to lower concentration over the same monitoring point.

Fig. 6.10 shows the comparison of LES mean concentration over the centreline of source $S1$, $S2$ and $S3$ with UDM and field measurements (Tab. 6.1) downstream of the source location X_S. Again, experimental and UDM mean concentration were normalized as in Eq. 3.10 where LES mean concentration was normalized by the experimental peak value at $X - X_S = 50m$. The overall analysis of Fig. 6.10 suggests that LES mean concentration from the three sources were found to be within the range of field measurements and in good agreement with UDM predictions. The large scatter of experimental mean concentration was due to short–time variations of wind speed and direction (Kumar, Fennell, and Britter, 2008; Xie, 2011) which

were not accounted in the LES and UDM models. Most of the experimental mean concentrations were visibly over–estimated in the far–field (i.e. $(X - X_S) > 2H$) by LES and UDM, nevertheless, the reduced size of source $S2$ compared to source $S1$ caused lower concentrations in the near–field (i.e. $(X - X_S) \leq 2H$) and in the far–field, which slightly improved the prediction of field measurements, mainly at $(X - X_S) = 4H$. The second mesh configuration with high resolution over the centreline and small source $S3$ improved further the prediction of turbulence and dispersion leading to less overestimation of field measurements.

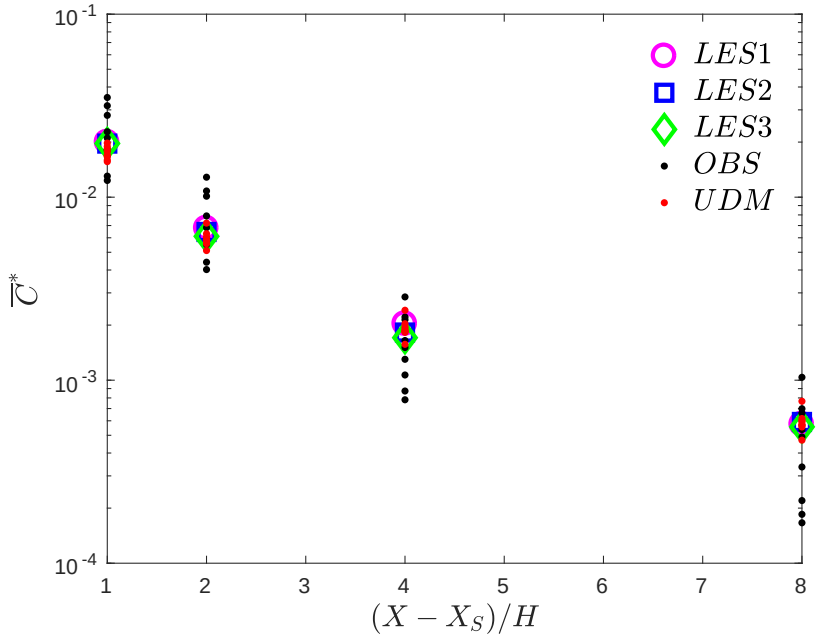

Figure 6.10: Peak concentration comparison over the centreline at $X - X_S = 1H, 2H, 4H, 8H$ between $LES1$ of source $S1$, $LES2$ of source $S2$ and $LES3$ of source $S3$ against field measurements (OBS) and UDM.

6.4.1 Quantitative comparison

Dimensionless validation metrics (Chang and Hanna, 2004; Britter and Schatzmann, 2007; Hertwig et al., 2018) were used to quantify the differences between LES and UDM models against the field experiment. The mean peak concentrations of pollutant from LES1, LES2 and LES3 (Fig. 6.10) were compared against the average peak concentrations of field data samples (Fig. 6.1) at a distance of $100m$, $200m$ and $400m$ from the source. Similarly, the average peak concentrations from the UDM model (Fig. 6.10) were compared against field measurements over the same locations. Because the LES peak concentration was normalized by the experimental concentration at a distance of $50m$ from the source, this location was not included in the comparison.

The validation metrics used for the comparison were the factor of two of observations (FAC2), the fractional bias (FB), the normalised root mean square error (NMSE), the geometric mean

bias (MG) and the geometric variance (VG), defined by Britter and Schatzmann (2007) as follows:

$$FAC2 = \frac{\overline{C}_{p,EXP}}{\overline{C}_p} \tag{6.2}$$

$$FB = 2\frac{(\overline{C}_p - \overline{C}_{p,EXP})}{(\overline{C}_p + \overline{C}_{p,EXP})} \tag{6.3}$$

$$NMSE = \frac{(\overline{C}_p - \overline{C}_{p,EXP})^2}{(\overline{C}_p \overline{C}_{p,EXP})} \tag{6.4}$$

$$MG = exp(ln\overline{C}_p - ln\overline{C}_{p,EXP}) \tag{6.5}$$

$$VG = exp((ln\overline{C}_p - ln\overline{C}_{p,EXP})^2) \tag{6.6}$$

where $\overline{C}_{p,EXP}$ is the average peak concentration of field data samples (target values) and $\overline{C}_p$ is the average peak concentration from the evaluated model (LES and/or UDM).

The tables below list the validation metrics for the mean peak concentration of the UDM model, LES1, LES2 and LES3 against the field data, which was assumed as the target values at a distance of 100m (Table 6.2), 200m (Table 6.3) and 400m (Table 6.4) from the source.

Table 6.2: Validation metrics for the mean peak concentrations of UDM, LES1, LES2 and LES3 at 100m from the source. The target values are given for a perfect agreement with the field data.

Model	$\overline{C}_p$	FAC2	FB	NMSE	MG	VG
Target value	–	1.0	0.0	0.0	1.0	1.0
EXP	0.0076	–	–	–	–	–
UDM	0.0059	1.2851	-0.2496	0.0633	0.7781	1.0650
LES1	0.0068	1.1245	-0.1172	0.0138	0.8893	1.0139
LES2	0.0065	1.1777	-0.1632	0.0268	0.8491	1.0271
LES3	0.0061	1.2437	-0.2172	0.0478	0.8041	1.0487

Table 6.3: Validation metrics for the mean peak concentrations of UDM, LES1, LES2 and LES3 at 200m from the source. The target values are given for a perfect agreement with the field data.

Model	$\overline{C}_p$	FAC2	FB	NMSE	MG	VG
Target value	–	1.0	0.0	0.0	1.0	1.0
EXP	0.0016	–	–	–	–	–
UDM	0.0019	0.8324	0.1830	0.0338	1.2014	1.0342
LES1	0.0020	0.7868	0.2387	0.0578	1.2710	1.0592
LES2	0.0018	0.8775	0.1305	0.0171	1.1397	1.0172
LES3	0.0017	0.9364	0.0657	0.0043	1.0679	1.0043

Table 6.4: Validation metrics for the mean peak concentrations of UDM, LES1, LES2 and LES3 at 400m from the source. The target values are given for a perfect agreement with the field data.

Model	$\overline{C}_p$	FAC2	FB	NMSE	MG	VG
Target value	–	1.0	0.0	0.0	1.0	1.0
EXP	0.00048	–	–	–	–	–
UDM	0.00059	0.8151	0.2037	0.0419	1.2268	1.0427
LES1	0.00057	0.8382	0.1761	0.0312	1.1931	1.0317
LES2	0.00059	0.8136	0.2056	0.0427	1.2291	1.0435
LES3	0.00056	0.8650	0.1447	0.0211	1.1560	1.0212

Acceptance criteria to assess good performance of urban dispersion models have been proposed by Chang and Hanna (2004): $FAC2 > 0.3$, $|FB| < 0.67$, $NMSE < 6$, $0.7 < MG < 1.3$ and $VG < 1.6$. These criteria are commonly applied to assess the model performance over the entire extent of the plume (e.g. Hertwig et al., 2018), although such thresholds are strongly case–specific and sensitive to the margin of errors of the investigated model.

All the validation metrics assessed in this study for the UDM and LES models satisfied the criteria proposed by Chang and Hanna (2004) over the analysed locations. The three LES cases performed better than UDM in each location except for 200m from the source where UDM performed slightly better than LES1 only. Close to the source's position (100m, Table 6.2), surprisingly, the big size source of LES1 provided the best agreement with field data, whereas LES2 performed better than LES3. However, plume dispersion near the source may vary substantially for different source dimensions and local turbulence intensity. Furthermore, LES peak concentration was normalized by the experimental peak concentration at 50m from the source therefore, the model comparison at 100m may be less reliable than further downstream.

At a distance of 200m from the source (Table 6.3), the effects of different source's size between LES1, LES2 and LES3 were visible. LES3 provided the best model performance with validation metrics, approaching the perfect agreement with target values. LES2 performed slightly worse than LES3 but better than LES1 and UDM. Lastly, far from the source (400m, Table 6.4) the three LES cases showed similar validation metrics with LES3 providing again the best agreement with field data. LES2 performed better than LES1 but with worse validation metrics compared to those at 200m.

Overall, the model comparison by using validation metrics showed good performance of both UDM and LES over the three analysed locations. LES performed systematically better than UDM with best agreement at a distance of 200m from the source. Further downstream, the LES performance of the three cases decreased although the criteria of good model performance (Chang and Hanna, 2004) were still satisfied. LES of the small size source (LES3) provided the best agreement with field data more frequently than LES1 and LES2.

6.4.2 0°N Wind direction

Guy and Herring (2016) compared UDM mean concentration with field measurements at a height of 1.5m on arcs up to 400m downwind of the source. For example, Fig. 6.11 shows a typical comparison between UDM and observations for the wind scenario 9 (Guy and Herring, 2016), where the wind direction was $-19°$N (0°N is the X axis ($Z = 0$), the emission $Q = 92g/s$ and the wind speed $U(Y = 2m) = 6.88m/s$. The comparison was useful to define regions of high concentrations near the source and the lateral size of the plume defined by the lowest concentration values detected by the measurement instruments (i.e. 10^{-7}).

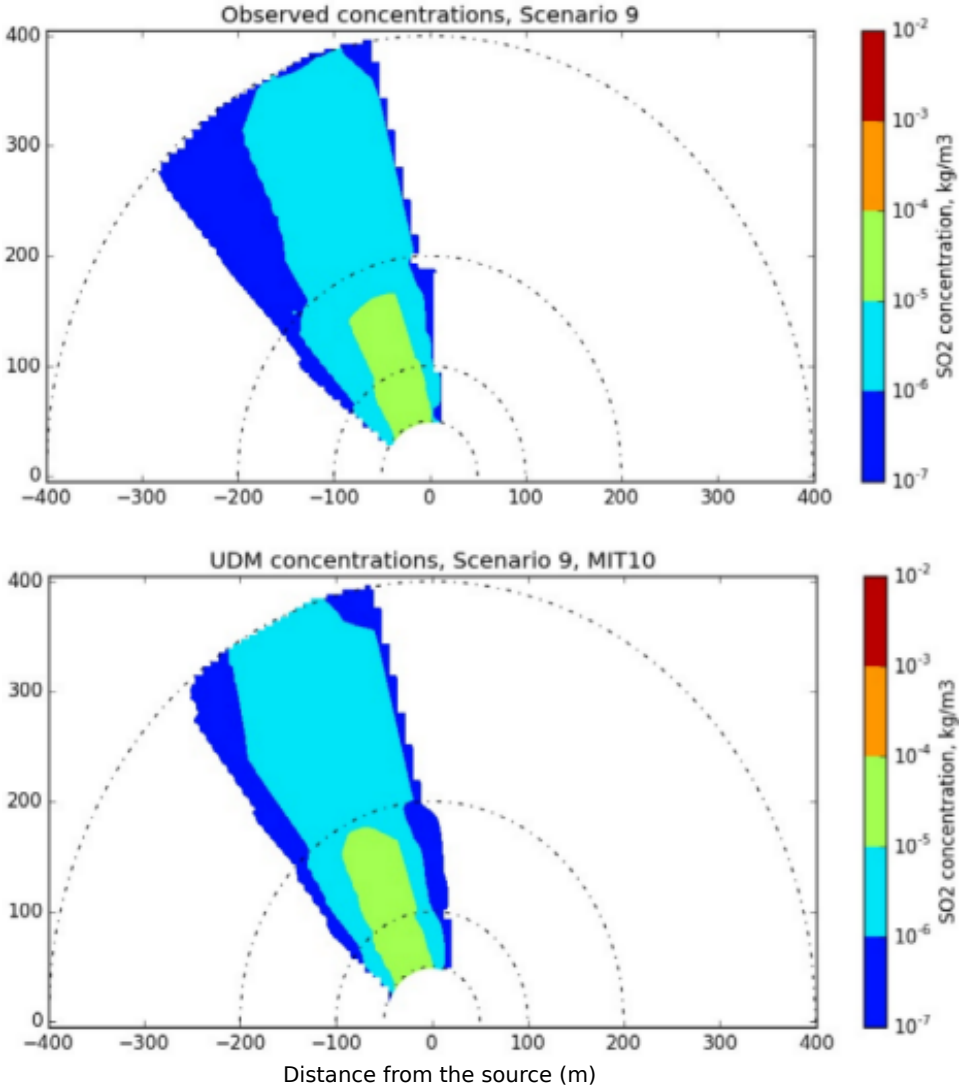

Figure 6.11: UDM and field measurements of SO_2 concentrations for wind scenario 9 (Guy and Herring, 2016), at a height of 1.5m on arcs up to 400m downwind.

A similar comparison was produced for the 0°N (CASE 6, Table 6.1) wind direction in Fig. 6.2 by using LES predictions of radial mean concentration at a height of 1.5m on arcs at 50m (Fig. 6.12a), 100m (Fig. 6.12b), 200m (Fig. 6.13a) and 400m (Fig. 6.13b) downwind

of the source. UDM and experimental mean concentration were again normalized as in Eq. 3.10 while LES mean concentration was normalized by the experimental peak value at $50m$ from the source. The comparison was used to determine the accuracy of LES predictions of peak location, peak magnitude and lateral size of the plume against UDM and field experiments.

Fig. 6.12a shows that at $X = 50m$ from the source, LES radial mean concentrations from source $S1$ and $S2$ agreed on the location of the concentration peak (0°N) and the lateral size of the plume. LES mean concentration from source $S3$ ($LES3$) agreed well with $LES1$ and $LES2$ on the peak location but the lateral size of the plume was found to be slightly wider and in better agreement with field measurements (OBS). This was mainly due to the high mesh resolution over the source centreline. UDM mean concentration at $X = 50m$ (Fig. 6.12a) agreed with the three LES on the peak location but not on the lateral size, which was found to be visibly wider than LES and field measurements on the left side of 0°N. Compared to LES and UDM, the peak concentration from the field measurements was found to be shifted by few degrees on the right side of 0°N, certainly due to short–time variation of wind direction in the real field. However, the lateral size of the experimental plume was well predicted by $LES3$.

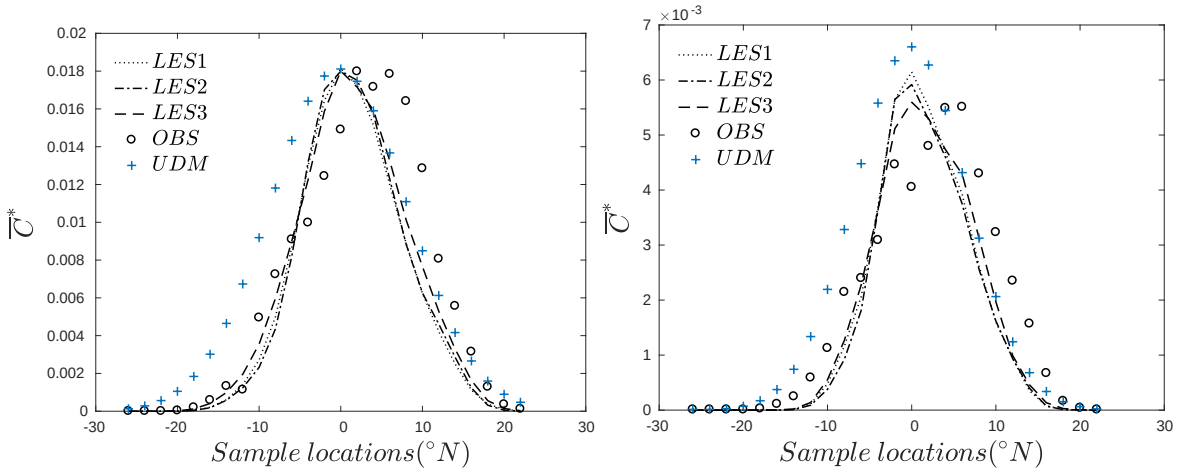

Figure 6.12: Radial mean concentration ($Y = 1.5m$) at $X = 150m$ (a) and $X = 200m$ (b) for 0°N wind direction ($Z = 0$) of field measurements (OBS), UDM, LES of source $S1$ ($LES1$), LES of source $S2$ ($LES2$) and LES of source $S3$ ($LES3$).

At $X = 100m$ from the source (Fig. 6.12b), radial mean concentration from $LES1$, $LES2$ and $LES3$ were found again in good agreement on the peak location and the lateral size of the plume although, the plume of $LES3$ was again slightly wider. In this case, the peak mean concentration of $LES3$ was found to be visibly lower than $LES2$, $LES1$ and UDM due to more accurate prediction of dispersion and enhanced spreading from the small source $S3$. The peak mean concentration from $LES3$ was found to be in better agreement with field measurements compared to $LES2$ and $LES1$, which was over–estimated by UDM substantially. However, the lateral size of the experimental plume was under–estimated by LES and

maybe in better agreement with UDM if matched by the concentration peak at 0°N.

At $X = 200m$ from the source (Fig. 6.13a), LES mean concentrations from source $S1$, $S2$ and $S3$ were found to be in good agreement on the location of the concentration peak. The LES lateral size of the plume was found to be increased for decreased size of the source (from $LES1$ to $LES3$) because of the enhanced scalar spreading due to source size differences in the near–field. In fact, the peak concentration was found to be the lowest for $LES3$ and the highest for $LES1$. Nevertheless, $LES3$ visibly over–predicted the field measurements although it was in better agreement than $LES1$, $LES2$ and UDM. The latter over–predicted the concentration peaks of both LES and field measurements quite significantly. Again, the location of the experimental concentration peak was found to be shifted to 5°N and the lateral size of the plume was under–predicted by LES and UDM. It can be said with some confidence that the effects of the variations to the mean wind speed and direction in the real field were found to be relevant in the accurate prediction of scalar dispersion at $X = 200m$ from the source.

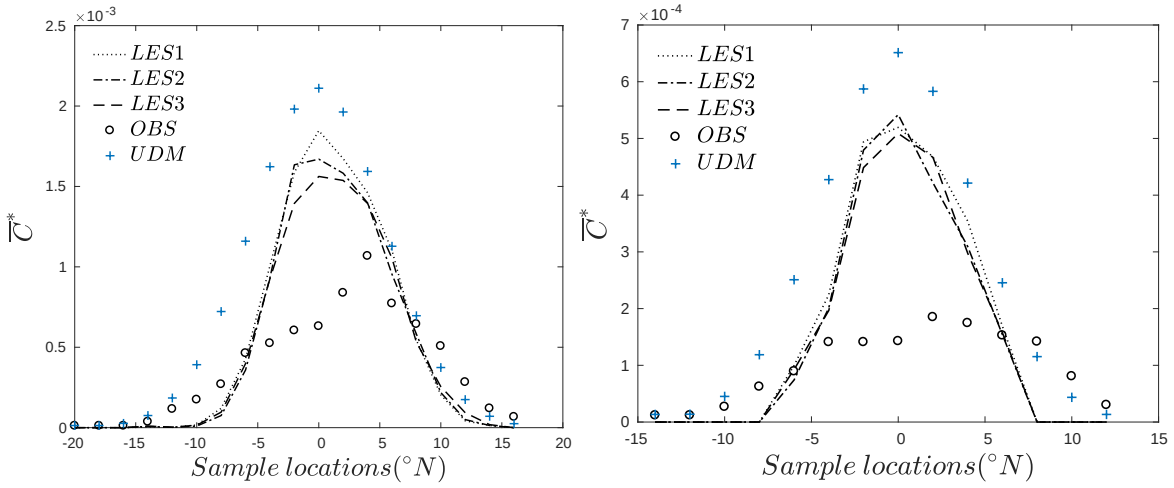

(a) (b)

Figure 6.13: Radial mean concentration ($Y = 1.5m$) at $X = 300m$ (a) and $X = 500m$ (b) for 0°N wind direction of field measurements (OBS), UDM, LES of source $S1$ ($LES1$), LES of source $S2$ ($LES2$) and LES of source $S3$ ($LES3$).

Lastly, at $X = 400m$ from the source (Fig. 6.13b), the concentration peak, the peak location and the lateral size of the plume were found to be similar for all LES cases. So that the source size differences in the far–field were found to be negligible. UDM predicted the same peak location of LES at 0°N but with a greater peak value and a wider lateral size of the plume. Both UDM and LES over–predicted the experimental peak concentration and under–predicted the lateral size of the plume. Although LES showed a slight improvement in the prediction of field measurements than UDM, the comparison in the far–field was found to be inaccurate. The lateral spread of the plume in the real field was certainly enhanced by short–time variation of wind direction so the experimental peak concentration was found to be much lower than those from UDM and LES.

Below, the normalized mean concentration $\overline{C^*}$ from source $S3$ is shown over an horizontal plane at the height of $Y = 1.5m$ from the ground (Fig. 6.14) and over a vertical plane at $Z = 0m$ (Fig. 6.15). Fig. 6.14 suggests that at $Y = 1.5m$ the maximum lateral size of the plume was $\sim 50m$ at about $200m$ from the source's location. At the same distance from the source, the vertical size of the plume approached the maximum value of $10m$. These plume's dispersion characteristics agree with our definition of near–field region within $200m$ from the source and far–field region beyond, over the analysed rural geometry.

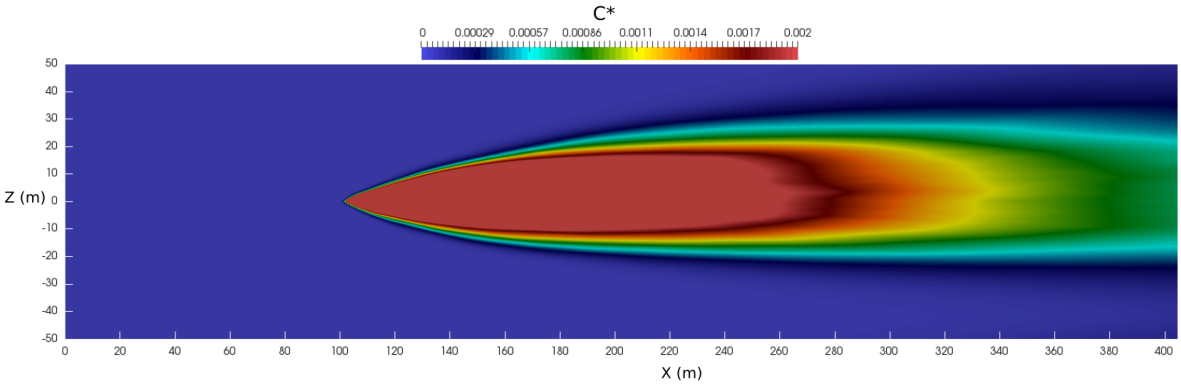

Figure 6.14: Normalized mean concentration $\overline{C*}$ of source $S3$ over an horizontal plane at the height of $Y = 1.5m$ from the ground.

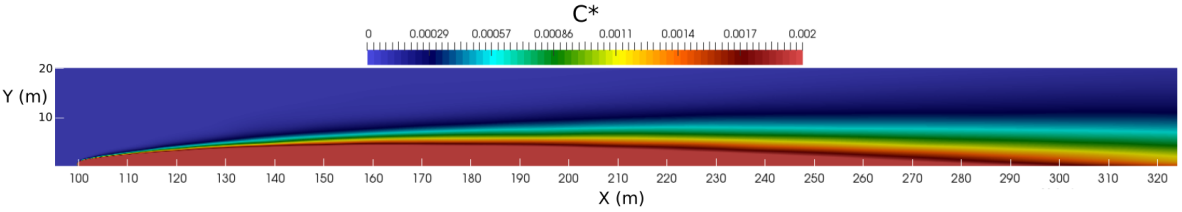

Figure 6.15: Normalized mean concentration $\overline{C*}$ of source $S3$ over a vertical plane at $Z = 0m$.

6.4.3 10°N Wind direction

The LES predictions of radial mean concentration at a height of $1.5m$ on arcs at $50m$ (Fig. 6.16a), $100m$ (Fig. 6.16b), $200m$ (Fig. 6.17a) and $400m$ (Fig. 6.17b) downwind of the source were compared against UDM and experimental mean concentration for the 10°N wind direction (CASE 22, Table 6.1). To be noted that the comparison was made along the mean wind direction (e.g. the centreline) so the previous LES case was used again for comparison. UDM and experimental mean concentrations were again normalized as in Eq. 3.10 while LES mean concentration was normalized by the experimental peak value at $50m$ from the source.

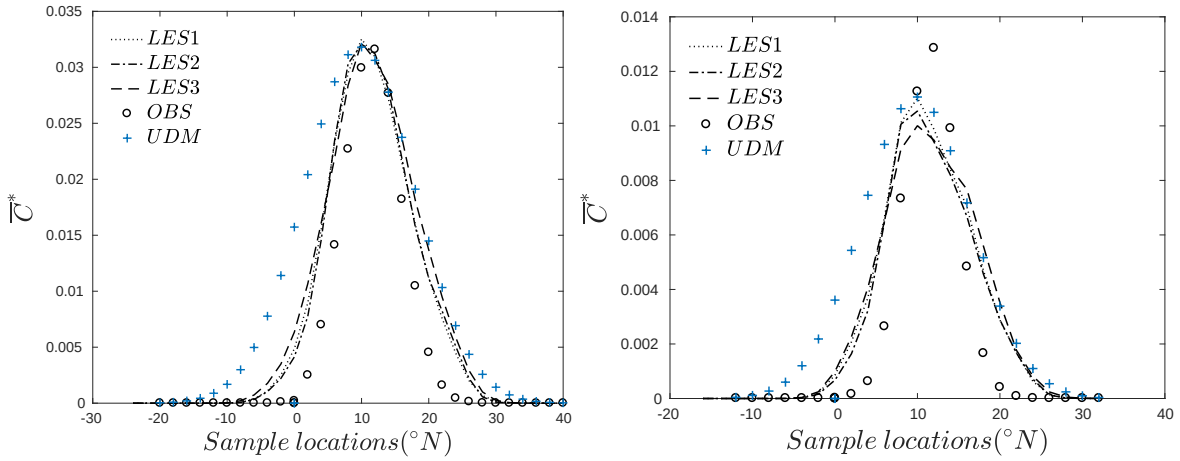

Figure 6.16: Radial mean concentration ($Y = 1.5m$) at $X = 150m$ (a) and $X = 200m$ (b) for 10°N wind direction of field measurements (OBS), UDM, LES of source $S1$ ($LES1$), LES of source $S2$ ($LES2$) and LES of source $S3$ ($LES3$).

Fig. 6.16a shows that at $X = 50m$ from the source, UDM and all LES predicted the experimental peak location at 10°N successfully. While the LES lateral size of the plume was found in fair agreement with field measurements, UDM slightly over–predicted on the left side of 10°N. Although LES of source $S1$ ($LES1$) and UDM modelled the same source size ($d = 1m$), the former produced more accurate prediction than the latter.

At $X = 100m$ from the source (Fig. 6.16b), UDM and all LES were found again in agreement with the experimental peak location at 10°N. The experimental peak value was predicted slightly better by UDM than LES, whereas the lateral size of the plume was found to be over–estimated by UDM and in good agreement with LES. Similarly to the previous case for 0°N wind direction, the LES peak concentration was found to be the lowest for $LES3$ and the highest for $LES1$ but in this case, LES of the big source $S1$ ($LES1$) was found in better agreement with field measurements than $LES2$ and $LES3$. This confirmed that dispersion predictions are sensitive to source size differences in the near–field.

Not surprisingly, the field measurements showed a rapid change of dispersion scenario at $X = 200m$ from the source (Fig. 6.17a). The experimental peak location was found shifted by few degrees on the right side of 10°N wind direction. The experimental peak value was found in this location in better agreement with LES (in particular with $LES3$) than UDM. The latter over–predicted the experimental peak value and the lateral size of the plume on both sides of 10°N. The lateral size of the experimental plume was found slightly over–predicted also by LES. Again, this was due to the significant difference of source size between the LES and the field experiment.

Lastly, at $X = 400m$ from the source (Fig. 6.17b) the experimental peak location was found shifted by 13°N and the peak value in better agreement with UDM than LES. The lateral size of the experimental plume was found to be visibly over–predicted by both LES and UDM, although LES provided some improvements. The effects of different source size and mesh

configuration between $LES1$, $LES2$ and $LES3$ were found to be very small in the far–field, in fact the three LES cases showed similar predictions of peak location, magnitude and lateral size of the plume.

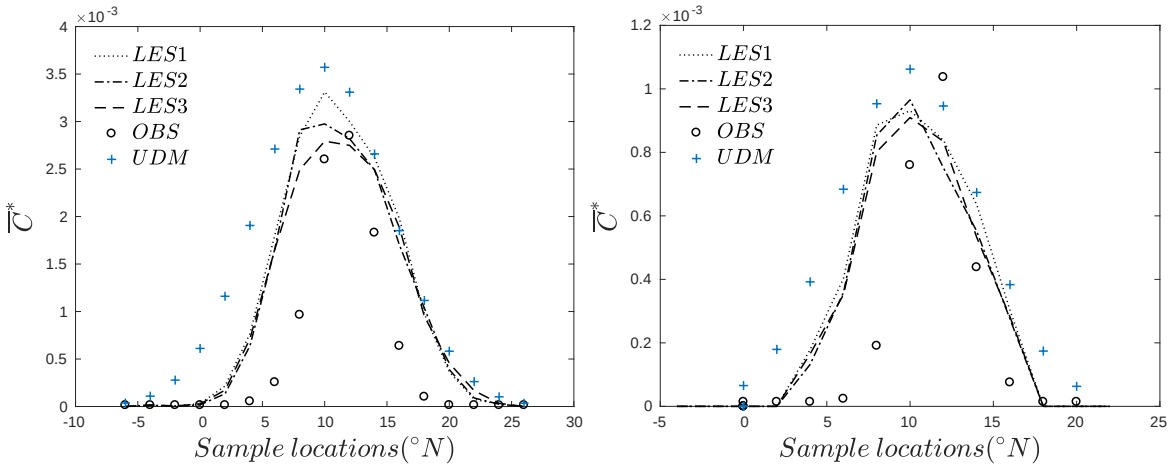

Figure 6.17: Radial mean concentration ($Y = 1.5m$) at $X = 300m$ (a) and $X = 500m$ (b) for 10°N wind direction of field measurements (OBS), UDM, LES of source $S1$ ($LES1$), LES of source $S2$ ($LES2$) and LES of source $S3$ ($LES3$).

Regardless of the above–described discrepancies, LES and UDM in the far–field were found to be in better agreement with field measurements for the 10°N wind direction compared to 0°N wind direction (Sec. 6.4.2). This was due to the uncertainties and the short–time variations in the mean wind speed and direction in the real field which produced two different dispersion scenarios (i.e. Fig. 6.13b and Fig. 6.17b), even for similar mean wind direction. Therefore, it was concluded that uncertainties from mean wind speed and direction should be taken into account in order to achieve a significant improvement in dispersion prediction in the far–field.

6.5 Conclusions and discussion

LES with inflow turbulent conditions were used to simulate a field experiment of gas dispersion (Barad, 1956) in a rural environment under real wind conditions. This LES study successfully validated a rough–wall function and assessed source size sensitivity on dispersion by using a very fine resolution down to $0.125m$ near the ground to simulate a full–scale very–high Reynolds–number flow. LES radial mean concentration was compared against the measurements and the predictions of the Urban Dispersion Model on arcs up to $400m$ downwind of the source. It was found that LES performed similar to UDM but predicted the lateral mean concentration from the field experiment better than UDM. The study showed that dispersion was sensitive to the source size in the near–field only and that more accurate predictions may be achieved by simulating the real–field source dimensions. Furthermore,

it was found that field measurements were influenced by changes in the wind conditions over the sampling period which caused large dispersion differences in the far–field. For example, the experimental peak of mean concentration in the far–field was never aligned with the mean wind direction. It was concluded that short–time variations of wind conditions (i.e. direction and speed) should be included in the model in order to achieve more realistic predictions of dispersion in a rural environment. As suggested by Xie (2011), wind measurements should be filtered by using an integral time scale of approximately 1 minute and the wind data should be processed as 60s and 30s averages to generate inflow conditions to drive LES simulations.

7 Final Conclusions

This PhD research aimed to improve understandings of mechanism of turbulence and dispersion over a rural–to–urban transition region under different meteorological conditions. The main achievement of this study was the development of a robust predictive tool which proved high accuracy through extensive validation. This tool and the large amount of data produced can be used for future applications such as model validations, dispersion/turbulence analysis, and prediction studies over more complex geometries.

The first topic investigated during this study was the development of the Internal Boundary Layer (IBL) formed at the leading edge of a regular array of cuboid buildings. For the first time the depth and growth rate of the IBL were evaluated by analysing the vertical Reynolds stress profiles in several streamwise positions. The proposed method (Sessa, Xie, and Herring, 2018) was found to define the IBL interface more clearly than existing methods. The IBL growth rate derived from the vertical stress method followed the power–law formula with a similar coefficient a as that derived by Cheng and Castro (2002) in the near roughness transition region ($X/y_{02} < 1000$), but with a significantly lower exponent $P = 0.21$ compared to $P = 0.33$ derived by Cheng and Castro (2002).It was emphasised that this was due to the different characteristics of the roughness elements within a range $X/y_{02} < 1000$.

The following objective of this study was to prove whether or not the development of the IBL affects ground–source dispersion. The impact of the interface between the internal and the external boundary layers on point–source dispersion was analysed by studying vertical and lateral profiles of dimensionless mean concentration and turbulent fluxes downstream of the source. Distinct changes in vertical flux profiles appeared related to similar changes in the vertical Reynolds stress leading to the plume's upper edge differing visibly from that obtained by using inlet–outlet periodic conditions. It was concluded that the presence of the interface between the internal and the external boundary layers constrains vertical spreading, and so leads to trapping of the pollutant.

Because of the difficulties of studying non–neutral conditions in the laboratory and the field, atmospheric stratification is usually neglected and there are many uncertainties on quantifying its effects. This research advanced from the current knowledge by analysing IBL mutations due to different incoming turbulence and thermal stratification. The effects of IBL mutations on ground–source dispersion were then quantified.

The LES model was thus developed to account for various levels of weakly stable stratification ($0 \leq R_i \leq 1$). For the first time the synthetic generation of turbulence and temperature fluctuations was assessed and used to model a developing weakly stable atmospheric boundary layer.

The successful validation against wind tunnel measurements suggested that the developed synthetic inflow generation method embedded in LES was able to accurately predict mean velocities, turbulent stresses, mean concentration and variance of concentration fluctuations from a ground–level line source over a rough–to–very–rough transition region. To assess the potential impact of the non–negligible errors of measuring the ground temperature upstream of the change in roughness in the experiments, a numerical sensitivity test was performed on the incoming temperature near the ground. It was found that the differences in incoming heat flux due to small changes of ground temperature were negligible and unable to affect turbulence and dispersion downstream of the change in roughness.

The depth of the IBL generated at the transition between the rough surface and the very rough surface was evaluated for different stratification conditions (i.e. $0 \leq R_i \leq 1$) by using the method developed in Sessa, Xie, and Herring (2018). It was found that the local vertical temperature gradient was greater within the IBL than in the external boundary layer, leading to a more pronounced step–change of normal Reynolds stress and shallower IBL as the thermal stratification increased. Moreover, the IBL height was found to be reduced as the TKE level of the approaching flow was reduced, suggesting that a boundary layer with less turbulence intensity is more sensitive to the effect of local thermal stratification over an urban area.

Because of the suppression of the turbulence in the IBL, the vertical transport of pollutant above the canopy decreased as the thermal stratification increased. This led to larger volume–averaged concentrations within streets with increasing stratification. If the TKE in the approaching boundary layer was reduced while maintaining the same level of thermal stratification, the effect on the total scalar fluxes within and above the canopy, and on the volume–averaged mean concentration within lateral streets was greater.

The last topic of this research focussed on the effects of wind direction on pollutant dispersion for different thermal stratification conditions. The predictive capabilities of the developed numerical model were finally assessed against the widely–used urban dispersion model (UDM) and a real–field experiment.

The LES study of wind direction effects showed that the mean wind direction inclined to a different angle from the main streets of the urban array enhanced the turbulence within the canopy, leading to increased vertical transport of pollutant above the canopy and reduced concentration levels below. It was found that the volume–averaged concentration below the canopy was almost insensitive to small variations of wind direction (i.e. 15°). In contrast, the comparison between LES of 45° against 0° showed the volume–averaged concentration to be drastically reduced (about 40%) so that the natural ventilation below the canopy was greatly improved for the non–zero wind direction, even in weakly stratified thermal conditions. The effects of wind direction on turbulence and dispersion were found to be dominant over the effects of weak stable stratification. Compared to previous studies, the amount of pollutant removed from the urban canopy layer was quantified at any distance from the source and in neutral and weakly stable stratification conditions.

The numerical simulations of a real–field experiment of gas dispersion required additional model developments. This LES study successfully validated a rough–wall function and used a full–scale fine resolution down to $0.125m$ near the ground to assess source size differences for a very high Reynolds–number flow. Measurements of mean concentration under real wind conditions were compared against the results of the LES model and the predictions of the UDM model (Guy and Herring, 2016). LES performed similar to UDM for the location and magnitude of the peak mean concentration but better for the prediction of the lateral mean concentration from the field experiment. The study confirmed the dominant influence of wind direction on pollution dispersion and highlighted that changes over the sampling period may cause large dispersion differences, even in the far–field of a rural environment.

7.1 Future works

During this research it was not possible to address all the emerging questions. Hence, some ideas and suggestions for future work are outlined in this sections.

To achieve more accurate CFD predictions for real urban scenarios, future works should firstly use the capability developed during this work to generate predictions which can be compared with experimental data from arrays which include building height and shape variations.

Under low–speed wind conditions, local thermal effects from the building walls might be non–negligible on pollutant dispersion at the street scale region. Therefore, more accurate boundary conditions should be used for the building walls and additional atmospheric parameters (i.e. incident solar radiation) should be considered. For example, a solar shading analysis should be conducted on the wall boundaries and heat flux should be set on those boundaries according to the ratio of direct fraction.

Lastly, real wind flows are hardly constant in direction and magnitude and our last study showed that dispersion mechanisms in the real field are greatly sensitive to small wind variations. In order to further improve CFD predictions of real wind scenarios, short–time variations of wind direction and magnitude are to be included in the developed inflow turbulent method. For example, Xie (2011) suggested to filter wind measurements by using an integral time scale of approximately 1 minute and to process the wind data as $60sec$ and $30sec$ averages to generate inflow conditions to drive LES simulations. Furthermore, it would be interesting to use the proposed method (Sessa, Xie, and Herring, 2018) to analyse the development of the IBL for different wind directions and its effect on dispersion from a ground–level line source.

Bibliography

Antonia, R. A. and R. E. Luxton (1972). "The response of a turbulent boundary layer to a step change in surface roughness. Part 2. Rough-to-smooth". In: *Journal of Fluid Mechanics* 53.4, pp. 737–757.

Antoniou, N., H. Montazeri, H. Wigo, M. Neophytou, B. Blocken, and M. Sandberg (2016). "CFD and wind-tunnel analysis of outdoor ventilation in a real compact heterogeneous urban area: Evaluation using air delay". In: *Building and Environment* 126, pp. 355–372.

Baker, J., H. L. Walker, and X. Cai (2004). "A study of the dispersion and transport of reactive pollutants in and above street canyons – a large eddy simulation". In: *Atmospheric Environment* 38.39, pp. 6883 –6892.

Balsley, B. B., G. Svensson, and M. Tjernstr (2008). "On the Scale-dependence of the Gradient Richardson Number in the Residual Layer". In: *Boundary-Layer Meteorology* 127.1, pp. 57–72.

Barad, M. (1956). "Project Prairie Grass, A Field Program in Diffusion". In: *Geophysical Research Papers* I - II,59.

Barlow, J. F. (2014). "Progress in observing and modelling the urban boundary layer". In: *Urban Climate* 10, Part 2. ICUC8: The 8th International Conference on Urban Climate and the 10th Symposium on the Urban Environment, pp. 216 –240.

Barlow, J. F. and O. Coceal (2008). *A review of urban roughness sublayer turbulence*. Technical Report. Met Office.

Batten, P., S. Chakravarthy, and U. Goldberg (2004). "Interfacing Statistical Turbulence Closures with Large-Eddy Simulation". In: *AIAA Journal* 42, pp. 485–492.

Belcher, S. E. (2005). "Mixing and transport in urban areas". In: *Philosophical Transactions of the Royal Society of London A: Mathematical, Physical and Engineering Sciences* 363.1837, pp. 2947–2968.

Bercin, K. M., Z.-T. Xie, and S. R. Turnock (2018). "Exploration of digital-filter and forward-stepwise synthetic turbulence generators and an improvement for their skewness-kurtosis". In: *Computers & Fluids* 172, pp. 443 –466.

Bezpalcova, K. (2007). "Physical modelling of flow and diffusion in urban canopy". In: *PhD Thesis, Charles University in Prague*, p. 193.

Boppana, V. B. L., Z.-T. Xie, and I. P. Castro (2014). "Thermal Stratification Effects on Flow Over a Generic Urban Canopy". In: *Boundary-Layer Meteorology* 153.1, pp. 141–162.

Boppana, V. B. L., Z.-T. Xie, and I. P. Castro (2010). "Large-Eddy Simulation of Dispersion from Surface Sources in Arrays of Obstacles". In: *Boundary-Layer Meteorology* 135.3, pp. 433–454.

Boppana, V. B. L., Z. T. Xie, and I. P. Castro (2013). "Large-Eddy Simulation of Heat Transfer from a Single Cube Mounted on a Very Rough Wall". In: *Boundary-Layer Meteorology* 147.3, pp. 347–368.

Bottema, M. (1997). "Urban roughness modelling in relation to pollutant dispersion". In: *Atmospheric Environment* 31.18, pp. 3059 –3075.

Bradley, E. F. (1968). "A micrometeorological study of velocity profiles and surface drag in the region modified by a change in surface roughness". In: *Quarterly Journal of the Royal Meteorological Society* 94.401, pp. 361–379.

Britter, R and M Schatzmann (2007). "Model evaluation guidance and protocol document". In: *COST Action 732*.

Britter, R. E. and S. R. Hanna (2003). "Flow and dispersion in urban areas". In: *Annual Review of Fluid Mechanics* 35.1, pp. 469–496.

Brixey, L. A., D. K. Heist, J. Richmond-Bryant, G. E. Bowker, S. G. Perry, and R. W. Wiener (2009). "The effect of a tall tower on flow and dispersion through a model urban neighborhood Part 2. Pollutant dispersion". In: *J. Environ. Monit.* 11 (12), pp. 2171–2179.

Cao, S. and T. Tamura (2007). "Effects of roughness blocks on atmospheric boundary layer flow over a two-dimensional low hill with/without sudden roughness change". In: *Journal of Wind Engineering and Industrial Aerodynamics* 95, pp. 679–695.

Castro, I. P. and A. G. Robins (1977). "The flow around a surface-mounted cube in uniform and turbulent streams". In: *Journal of Fluid Mechanics* 79 (02), pp. 307–335.

Castro, I. P., H. Cheng, and R. Reynolds (2006). "Turbulence Over Urban-type Roughness: Deductions from Wind-tunnel Measurements". In: *Boundary-Layer Meteorology* 118.1, pp. 109–131.

Castro, I. P., Z. T. Xie, V. Fuka, A. G. Robins, M. Carpentieri, P. Hayden, D. Hertwig, and O. Coceal (2017). "Measurements and Computations of Flow in an Urban Street System". In: *Boundary-Layer Meteorology* 162.2, pp. 207–230.

Chang, J. and S. Hanna (2004). "Air quality model performance evaluation". In: *Meteorology and Atmospheric Physics* 87, pp. 167–196.

Chavez, M., B. Hajra, T. Stathopoulos, and A. Bahloul (2011). "Near field pollutant dispersion in the built environment by CFD and wind tunnel simulations". In: *Journal of Wind Engineering and Industrial Aerodynamics* 99.4. The Fifth International Symposium on Computational Wind Engineering, pp. 330 –339.

Cheng, H. and I. P. Castro (2002). "Near-Wall Flow Development After A Step Change In Surface Roughness". In: *Boundary-Layer Meteorology* 105.3, pp. 411–432.

Cheng, W.-C. and F. Porte-Agel (2016). "Large-eddy simulation of flow and scalar dispersion in rural-to-urban transition regions". In: *International Journal of Heat and Fluid Flow* 60, pp. 47 –60.

Cheng, W. and C.-H. Liu (2011). "Large-eddy simulation of turbulent transports in urban street canyons in different thermal stabilities". In: *Journal of Wind Engineering and Industrial Aerodynamics* 99.4. The Fifth International Symposium on Computational Wind Engineering, pp. 434 –442.

Clarke, J., J. Ching, F. Binkowski, and J. Godowitch (1978). "Turbulent structure of the urban surface boundary layer (St.Louis, Missouri)." In: *Proc. 9th international technical meeting on air pollution modeling and its application, Toronto, August 1978*. Ed. by C. Morawa. NATO Committee on the Challenges of Modern Society, Brussels; Report 103, pp. 187–196.

Claus, J., O. Coceal, T. G. Thomas, S. Branford, S. E. Belcher, and I. P. Castro (2012). "Wind-Direction Effects on Urban-Type Flows". In: *Boundary-Layer Meteorology* 142.2, pp. 265–287.

Coceal, O., E. V. Goulart, S. Branford, T. G. Thomas, and S. E. Belcher (2014). "Flow structure and near-field dispersion in arrays of building-like obstacles". In: *Journal of Wind Engineering and Industrial Aerodynamics* 125, pp. 52 –68.

Counehan, J. (1971). "Wind tunnel determination of the roughness length as a function of the fetch and the roughness density of three-dimensional roughness elements". In: *Atmospheric Environment (1967)* 5.8, pp. 637 –642.

Cushman-Roisin, B., C. Gualtieri, and D. Mihailovic (2008). "Environmental fluid mechanics: current issues and future outlook". In: *Fluid Mechanics of Environmental Interfaces*. Ed. by Taylor and Francis. Chap. 1, pp. 1–13.

Cushman-Roisin, B. and J.-M. Beckers (2005). *Introduction to Geophysical Fluid Dynamics - Physical and Numerical Aspects*. Academic Press.

Cybyk, B., J. Boris, J. Theodore Young, M. Emery, and S. Cheatham (2001). "Simulation of fluid dynamics around complex urban geometries". In: *39th Aerospace Sciences Meeting and Exhibit*.

Davenport, A., C. Grimmond, T Oke, and J Wieringa (2000). "Estimating the roughness of cities and sheltered country". In: *15th conference on probability and statistics in the atmospheric sciences/12th conference on applied climatology, Ashville, NC, American Meteorological Society*, pp. 96–99.

Davidson, M. J., W. H. Snyder, R. E. Lawson, and J. C. R. Hunt (1996). "Wind tunnel simulations of plume dispersion through groups of obstacles". In: *Atmospheric Environment* 30.22, pp. 3715 –3731.

Drew, D. R., J. F. Barlow, and S. E. Lane (2013). "Observations of wind speed profiles over Greater London, UK, using a Doppler lidar". In: *Journal of Wind Engineering and Industrial Aerodynamics* 121, pp. 98 –105.

Efros, V. and P.-A. Krogstad (2011). "Development of a turbulent boundary layer after a step from smooth to rough surface". In: *Experiments in Fluids* 51.6, pp. 1563–1575.

Elliott, W. P. (1958). "The growth of the atmospheric internal boundary layer". In: *Eos, Transactions American Geophysical Union* 39.6, pp. 1048–1054.

Flores, O. and J. Riley (2011). "Analysis of Turbulence Collapse in the Stably Stratified Surface Layer Using Direct Numerical Simulation". In: *Boundary-Layer Meteorology* 139, pp. 241–259.

Fuka, V., Z. T. Xie, I. P. Castro, P. Hayden, M. Carpentieri, and A. G. Robins (2018). "Scalar Fluxes Near a Tall Building in an Aligned Array of Rectangular Buildings". In: *Boundary-Layer Meteorology* 167.1, pp. 53–76.

Garratt, J. (1994). *The Atmospheric Boundary Layer*. Cambridge Atmospheric and Space Science Series. Cambridge University Press.

Germano, M., U. Piomelli, P. Moin, and W. H. Cabot (1991). "A dynamic subgrid-scale eddy viscosity model". In: *Physics of Fluids A: Fluid Dynamics* 3.7, pp. 1760–1765.

Giometto, M. G., A. Christen, C. Meneveau, J. Fang, M. Krafczyk, and M. B. Parlange (2016). "Spatial Characteristics of Roughness Sublayer Mean Flow and Turbulence Over a Realistic Urban Surface". In: *Boundary-Layer Meteorology* 160.3, pp. 425–452.

Golder, D. (1972). "Relations among stability parameters in the surface layer". In: *Boundary-Layer Meteorology* 3.1, pp. 47–58.

Goulart, E., N. Reis, V. Lavor, I. Castro, J. Santos, and Z. Xie (2019). "Local and non-local effects of building arrangements on pollutant fluxes within the urban canopy". In: *Building and Environment* 147, pp. 23 –34.

Grachev, A. A., E. L. Andreas, C. W. Fairall, P. S. Guest, and P. O. G. Persson (2008). "Turbulent measurements in the stable atmospheric boundary layer during SHEBA: ten years after". In: *Acta Geophysica* 56.1, pp. 142–166.

Gualtieri, C., F. Martinez-Solano, P. Iglesias-Rey, and P. López-Jiménez (2010). "Modelling flow and concentration field in a 3D rectangular water tank". In: p. 12.

Guy, H. and S. Herring (2016). *Validation of UDM Against Data from Project Prairie Grass*. Technical Report DSTL/TR92221. Defence Science and Technology Laboratory.

Hancock, P. E. and P. Hayden (2018). "Wind-Tunnel Simulation of Weakly and Moderately Stable Atmospheric Boundary Layers". In: *Boundary-Layer Meteorology* 168.1, pp. 29–57.

Hanna, S., S Tehranian, B Carissimo, R. Macdonald, and R Lohner (2002). "Comparisons of model simulations with observations of mean flow and turbulence within simple obstacle arrays". In: *Atmospheric Environment* 36.32, pp. 5067 –5079.

Hanson, R. E. and B. Ganapathisubramani (2016). "Development of turbulent boundary layers past a step change in wall roughness". In: *Journal of Fluid Mechanics* 795, pp. 494–523.

Hertwig, A., L. Soulhac, V. Fuka, T. Auerswald, M. Carpentieri, P. Hayden, A. Robins, Z. Xie, and O. Coceal (2018). "Evaluation of fast atmospheric dispersion models in a regular street network". In: *Environ. Fluid Mech.* 18, pp. 1007–1044.

Horiuti, K. (1993). "A proper velocity scale for modeling subgrid-scale eddy viscosities in large eddy simulation". In: *Physics of Fluids A: Fluid Dynamics* 5.1, pp. 146–157.

Hsu, T.-J. and P. Liu (2004). "Toward modeling turbulent suspension of sand in the nearshore". In: *J. Geophys. Res.* 109, p. 14.

Huang, J. and E. Bou-Zeid (2013). "Turbulence and Vertical Fluxes in the Stable Atmospheric Boundary Layer. Part I: A Large-Eddy Simulation Study". In: *Journal of the Atmospheric Sciences* 70.6, pp. 1513–1527.

Inagaki, M., T. Kondoh, and Y. Nagano (2005). "A Mixed-Time-Scale SGS Model With Fixed Model-Parameters for Practical LES". In: *Journal of Fluids Engineering* 127.1, pp. 1–13.

Jackson, N. A. (1976). "The propagation of modified flow downstream of a change in roughness". In: *Quarterly Journal of the Royal Meteorological Society* 102.434, pp. 924–933.

Kanda, I. and Y. Yamao (2016). "Passive scalar diffusion in and above urban-like roughness under weakly stable and unstable thermal stratification conditions". In: *Journal of Wind Engineering and Industrial Aerodynamics* 148, pp. 18–33.

Kanda, M., R. Moriwaki, and F. Kasamatsu (2004). "Large-Eddy Simulation of Turbulent Organized Structures within and above Explicitly Resolved Cube Arrays". In: *Boundary-Layer Meteorology* 112.2, pp. 343–368.

Keating, A., U. Piomelli, E. Balaras, and H.-J. Kaltenbach (2004). "A priori and a posteriori tests of inflow conditions for large-eddy simulation". In: *Physics of Fluids* 16.12, pp. 4696–4712.

King, M., H. Gough, C. Halios, J. Barlow, A. Robertson, R. Hoxey, and C. Noakes (2017). "Investigating the influence of neighbouring structures on natural ventilation potential of a full-scale cubical building using time-dependent CFD". In: *Journal of Wind Engineering and Industrial Aerodynamics* 169, pp. 265–279.

Kumar, P., P. Fennell, and R. Britter (2008). "Effect of wind direction and speed on the dispersion of nucleation and accumulation mode particles in an urban street canyon". In: *Science of The Total Environment* 402.1, pp. 82 –94.

Launder, B. and D. Spalding (1974). "The numerical computation of turbulent flows". In: *Comput. Meth. Appl. Mech. Eng.* 3, pp. 269 –289.

Lienhard V, J. H. and C. W. Van Atta (1990). "The decay of turbulence in thermally stratified flow". In: *Journal of Fluid Mechanics* 210, pp. 57–112.

Lilly, D. K. (1992). "A proposed modification of the Germano subgrid-scale closure method". In: *Physics of Fluids A: Fluid Dynamics* 4.3, pp. 633–635.

Lim, H. C., I. P. Castro, and R. P. Hoxey (2007). "Bluff bodies in deep turbulent boundary layer: Reynolds number issues". In: *Journal of Fluid Mechanics* 571, pp. 97 –118.

Lund, T. S., X. Wu, and K. D. Squires (1998). "Generation of Turbulent Inflow Data for Spatially-Developing Boundary Layer Simulations". In: *Journal of Computational Physics* 140.2, pp. 233 –258.

Macdonald, R. (2000). "Modelling The Mean Velocity Profile In The Urban Canopy Layer". In: *Boundary-Layer Meteorology* 97, pp. 25–45.

MacDonald, R., R. Griffiths, and S. Cheah (1997). "Field experiments of dispersion through regular arrays of cubic structures". In: *Atmospheric Environment* 31.6, pp. 783 –795.

Marucci, D. and M. Carpentieri (2018a). "Wind tunnel study on the effect of atmospheric stratification on flow and dispersion in an array of buildings". In: ICUC10 10th International Conference on Urban Climate, 6 - 10 August, 2018, New York, USA.

Marucci, D., M. Carpentieri, and P. Hayden (2018). "On the simulation of thick non-neutral boundary layers for urban studies in a wind tunnel". In: *International Journal of Heat and Fluid Flow* 72, pp. 37 –51.

Marucci, D. and M. Carpentieri (2020). "Dispersion in an array of buildings in stable and convective atmospheric conditions". In: *Atmospheric Environment* 222, p. 117100.

Michioka, T., A. Sato, H. Takimoto, and M. Kanda (2011). "Large-Eddy Simulation for the Mechanism of Pollutant Removal from a Two-Dimensional Street Canyon". In: *Boundary-Layer Meteorology* 138.2, pp. 195–213.

Monin, A. S. and A. Obukhov (1954). "Basic laws of turbulent mixing in the surface layer of the atmosphere". In: *Contrib. Geophys. Inst. Acad. Sci. USSR* 151. Monin1954, pp. 163–187.

Nieuwstadt, F. and A. V. Ulden (1978). "A Numerical Study on the Vertical Dispersion of Passive Contaminants from a Continuous Source in the Atmospheric Surface Layer". In: *Atmospheric Environment* 12(11), pp. 2119 –2124.

Ohya, Y. (2001). "Wind-Tunnel Study Of Atmospheric Stable Boundary Layers Over A Rough Surface". In: *Boundary-Layer Meteorology* 98.1, pp. 57–82.

Okaze, T. and A. Mochida (2017). "Cholesky decomposition-based generation of artificial inflow turbulence including scalar fluctuation". In: *Computers & Fluids* 159, pp. 23 –32.

Pahlow, M., M. B. Parlange, and F. Port-Agel (2001). "On Monin–Obukhov Similarity In The Stable Atmospheric Boundary Layer". In: *Boundary-Layer Meteorology* 99.2, pp. 225–248.

Pardyak, E. R., P. Monti, and H. J. S. Fernando (2002). "Flux Richardson number measurements in stable atmospheric shear flows". In: *Journal of Fluid Mechanics* 459, pp. 307 –316.

Park, S.-B. and J.-J. Baik (2013). "A Large-Eddy Simulation Study of Thermal Effects on Turbulence Coherent Structures in and above a Building Array". In: *Journal of Applied Meteorology and Climatology* 52.6, pp. 1348–1365.

Pendergrass, W. and S. Arya (1984). "Dispersion in neutral boundary layer over a step change in surface roughness. Mean flow and turbulence structure". In: *Atmospheric Environment (1967)* 18.7, pp. 1267 –1279.

Piomelli, U. (2008). "Wall-layer models for large-eddy simulations". In: *Progress in Aerospace Sciences* 44.6. Large Eddy Simulation - Current Capabilities and Areas of Needed Research, pp. 437 –446.

Piomelli, U., E. Balaras, H. Pasinato, K. D. Squires, and P. R. Spalart (2003). "The inner-outer layer interface in large-eddy simulations with wall-layer models". In: *International Journal of Heat and Fluid Flow* 24.4, pp. 538 –550.

Pope, S. B. (2000). *Turbulent flows*. Reimpressions (avec des corrections) : 2001, 2003, 2005, 2008, 2010. Cambridge: Cambridge University Press.

Reible, D. (2017). *Fundamentals of Environmental Engineering*. CRC Press.

Schlichting, H. and J Kestin (1979). *Boundary-layer theory*. English. 7th ed. New York : McGraw-Hill.

Schofield, W. H. (1975). "Measurements in adverse-pressure-gradient turbulent boundary layers with a step change in surface roughness". In: *Journal of Fluid Mechanics* 70.3, pp. 573–593.

Sessa, V., Z.-T. Xie, and S. Herring (2018). "Turbulence and dispersion below and above the interface of the internal and the external boundary layers". In: *Journal of Wind Engineering and Industrial Aerodynamics* 182, pp. 189 –201.

Silva, I. D., A Brandt, L. Montenegro, and H. Fernando (1999). "Gradient Richardson number measurements in a stratified shear layer". In: *Dynamics of Atmospheres and Oceans* 30.1, pp. 47 –63.

Sini, J.-F., S. Anquetin, and P. G. Mestayer (1996). "Pollutant dispersion and thermal effects in urban street canyons". In: *Atmospheric Environment* 30.15, pp. 2659–2677.

Smits, A. J. and D. H. Wood (1985). "The Response of Turbulent Boundary Layers to Sudden Perturbations". In: *Annual Review of Fluid Mechanics* 17.1, pp. 321–358.

Snyder, W. H. and I. P. Castro (2002). "The critical Reynolds number for rough-wall boundary layers". In: *Journal of Wind Engineering and Industrial Aerodynamics* 90.1, pp. 41 –54.

Stull, R. B. (1988). *An Introduction to Boundary Layer Meteorology*. The Netherlands: Kluwer Academic Publishers.

Sutton, O. G. (1932). "A Theory of Eddy Diffusion in the Atmosphere". In: *Proceedings of the Royal Society of London. Series A, Containing Papers of a Mathematical and Physical Character* 135.826, pp. 143–165.

Theurer, W., E. Plate, K. Hoeschele, and hh (1996). "Semi-empirical models as a combination of wind tunnel and numerical dispersion modelling". In: *Atmospheric Environment* 30.21, pp. 3583 –3597.

Tolias, I., N. Koutsourakis, D. Hertwig, G. Efthimiou, A. G. Venetsanos, and B. J.G. (2018). "Large Eddy Simulation study on the structure of turbulent flow in a complex city". In: *Journal of Wind Engineering and Industrial Aerodynamics* 177, pp. 101–116.

Tomas, J. M., M. J. B. M. Pourquie, and H. J. J. Jonker (2016). "Stable Stratification Effects on Flow and Pollutant Dispersion in Boundary Layers Entering a Generic Urban Environment". In: *Boundary-Layer Meteorology* 159.2, pp. 221–239.

Tomas, J. M., H. E. Eisma, M. J. B. M. Pourquie, G. E. Elsinga, H. J. J. Jonker, and J. Westerweel (2017). "Pollutant Dispersion in Boundary Layers Exposed to Rural-to-Urban Transitions: Varying the Spanwise Length Scale of the Roughness". In: *Boundary-Layer Meteorology* 163.2, pp. 225–251.

Townsend, A. A. (1965). "Self-preserving flow inside a turbulent boundary layer". In: *Journal of Fluid Mechanics* 22.4, pp. 773–797.

Uehara, K., S. Wakamatsu, and R. Ooka (2003). "Studies on critical Reynolds number indices for wind-tunnel experiments on flow within urban areas". In: *Boundary-Layer Meteorology* 107, pp. 353–370.

Vasaturo, R., I. Kalkman, B. Blocken, and van Wesemael P.J.V. (2018). "Large eddy simulation of the neutral atmospheric boundary layer: performance evaluation of three inflow methods for terrains with different roughness". In: *Journal of Wind Engineering and Industrial Aerodynamics* 173, pp. 241–261.

Venayagamoorthy, S. and J. Koseff (2016). "On the flux Richardson number in stably stratified turbulence". In: *Journal of Fluid Mechanics* 798.

Vincont, J.-Y., S. Simoens, M. Ayrault, and J. M. Wallace (2000). "Passive scalar dispersion in a turbulent boundary layer from a line source at the wall and downstream of an obstacle". In: *Journal of Fluid Mechanics* 424, 127–167.

Wang, R., B. Chen, S. Qiu, Z. Zhu, Y. Wang, Y. Wang, and Z. Song (2018). "Comparison of Machine Learning Models for Hazardous Gas Dispersion Prediction in Field Cases". In: *International Journal of Environmental Research and Public Health* 15, p. 1450.

Wieringa, J. (1992). "Updating the Davenport roughness classification". In: *Journal of Wind Engineering and Industrial Aerodynamics* 41.1, pp. 357 –368.

Williams, O., T. Hohman, T. Van Buren, E. Bou-Zeid, and A. J. Smits (2017). "The effect of stable thermal stratification on turbulent boundary layer statistics". In: *Journal of Fluid Mechanics* 812, pp. 1039–1075.

Wood, C. R., A. Lacser, J. F. Barlow, A. Padhra, S. E. Belcher, E. Nemitz, C. Helfter, D. Famulari, and C. S. B. Grimmond (2010). "Turbulent Flow at 190m Height Above London During 2006–2008, A Climatology and the Applicability of Similarity Theory". In: *Boundary Layer Meteorology* 137.1, pp. 77–96.

Wood, D. H. (1982). "Internal boundary layer growth following a step change in surface roughness". In: *Boundary-Layer Meteorology* 22.2, pp. 241–244.

Wu, X. (2017). "Inflow Turbulence Generation Methods". In: *Annual Review of Fluid Mechanics* 49.1, pp. 23–49.

Xie, Z.-T. (2011). "Modelling Street-Scale Flow and Dispersion in Realistic Winds—Towards Coupling with Mesoscale Meteorological Models". In: *Boundary-Layer Meteorology* 141.1, pp. 53–75.

Xie, Z. T. and I. P. Castro (2008). "Efficient Generation of Inflow Conditions for Large Eddy Simulation of Street-Scale Flows". In: *Flow, Turbulence and Combustion* 81.3, pp. 449–470.

Xie, Z.-T. and I. P. Castro (2009). "Large-eddy simulation for flow and dispersion in urban streets". In: *Atmospheric Environment* 43.13, pp. 2174 –2185.

Xie, Z.-T., P. Hayden, and C. R. Wood (2013). "Large-eddy simulation of approaching-flow stratification on dispersion over arrays of buildings". In: *Atmospheric Environment* 71, pp. 64 –74.

Xie, Z. and I. P. Castro (2006). "LES and RANS for Turbulent Flow over Arrays of Wall-Mounted Obstacles". In: *Flow, Turbulence and Combustion* 76.3, pp. 291–312.

Xie, Z., P. Hayden, P. R. Voke, and A. G. Robins (2004). "Large-eddy simulation of dispersion: comparison between elevated source and ground level source". In: *Journal of Turbulence* 5.31, pp. 1–23.

Yassin, M., S. Kato, R. Ooka, T. Takahashi, and R. Kouno (2005). "Field and wind-tunnel study of pollutant dispersion in a built-up area under various meteorological conditions". In: *Journal of Wind Engineering and Industrial Aerodynamics* 93.5, pp. 361 –382.

Zhang, J., A. Tejada-Martínez, and Q. Zhang (2016). "Rapid Analysis of Disinfection Efficiency Through Computational Fluid Dynamics". In: *American Water Works Association* 108, p. 13.

Zoumakis, N. M. and A. G. Kelessis (1991). "The dependence of the bulk Richardson number on stability in the surface layer". In: *Boundary-Layer Meteorology* 57.4, pp. 407–414.